Studies of Antarctic ice shelf stability: surface melting, basal melting, and ice flow dynamics

by

Karen E. Alley

B.A., Colgate University, 2012

A thesis submitted to the
Faculty of the Graduate School of the
University of Colorado in partial fulfillment
of the requirement for the degree of
Doctor of Philosophy
Department of Geological Sciences
2017

This thesis entitled:
Studies of Antarctic ice shelf stability:
Surface melting, basal melting, and ice flow dynamics
written by Karen E. Alley
has been approved for the Department of Geological Sciences

_____
James White

_____
Ted Scambos

Date_____

The final copy of this thesis has been examined by the signatories, and we find that both the content and the form meet acceptable presentation standards of scholarly work in the above-mentioned discipline.

Alley, Karen Elizabeth (Ph.D., Department of Geological Sciences)
Studies of Antarctic ice shelf stability: Surface melting, basal melting, and ice flow dynamics
Thesis directed by Senior Research Scientist T.A. Scambos and Professor J.W.C. White

Abstract:

Floating extensions of ice sheets, known as ice shelves, play a vital role in regulating the rate of ice flow into the Southern Ocean from the Antarctic Ice Sheet. Shear stresses imparted by contact with islands, embayment walls, and other obstructions transmit “backstress” to grounded ice. Ice shelf collapse reduces or eliminates this backstress, increasing mass flux to the ocean and therefore rates of sea level rise. This dissertation presents studies that address three main factors that regulate ice shelf stability: surface melt, basal melt, and ice flow dynamics. The first factor, surface melt, is assessed using active microwave backscatter. Combined with measurements of annual melt, backscatter values provide insights into the state of the upper layers of the ice shelf, indicating whether melt ponds, which can destabilize ice shelves, are likely to form on the ice shelf surface. We present a map of the relative vulnerability of ice shelves to hydrofracture collapse caused by surface melt ponding. As many authors have recently performed large-scale assessments of basal melt, the second factor is addressed at a smaller scale, through the study of channels that form on the undersides of ice shelves. These basal channels are mapped using visible-band imagery, and shown statistically to be related to the presence of warm ocean water. Landsat imagery and ICESat laser altimetry provide evidence that basal channels can in some cases change very rapidly and cause weakening of ice shelf structures. The final study addresses the calculation of surface strain

rates from velocity fields. This common calculation, which is integral to understanding of flow patterns and stresses on both grounded and floating ice, can be achieved using a variety of approaches. We examine two commonly used algorithms and the differences in results produced by the different methods. We also present a Matlab code for calculating strain rates and a data product of strain rates across the Antarctic continent. All three studies contribute to the knowledge needed to comprehensively assess ice shelf stability; proposed future studies that continue toward this goal are discussed in the final chapter.

Acknowledgments

The years of work represented by this dissertation would not have been possible without the unwavering support of many family, friends, and colleagues.

First, I would like to thank both of my advisors, Ted Scambos and Jim White, who have supported me generously through their time, advice, and funding over the last five years. My sincere gratitude also goes to all my committee members. To Bob Anderson, for being an outstanding professor and keeping me excited about everything to do with science. To Waleed Abdalati, for helping me to become a better teacher and communicator. And to Helen Fricker, for inspiring me and helping to guide me through meetings and publications. I have also received considerable support from Dr. Hari Rajaram at CU Boulder and Dr. Doug MacAyeal at the University of Chicago, who gave me confidence to learn how to apply math and coding to my science.

I am indebted to several fellow CU Boulder grad students/post-docs who kept me going throughout the process: To Mike MacFerrin, for leading an outstanding Greenland field season and giving freely of friendship and help with research afterwards; to Mahsa Moussavi for her kindness and advice and great listening ear; and to Allen Pope, who was the main factor in keeping me sane during many stressful moments.

I would also like to acknowledge my family, who got me to where I am today. To my sister and life coach Janet Jones, whose Skype conversations keep me in touch with reality; to my mother Cindy Alley who inspires my creativity and encourages me every step of the way; and to my father, Richard Alley: Your enthusiasm and ability to communicate science brought me inexorably into the field of glaciology, and inspire me every single day to pass on that excitement to others.

Finally, I would like to thank my husband Alex, who has shown me love and support beyond anything I could have imagined, and who has probably heard more about this dissertation than he could have imagined.

CONTENTS

TABLES

FIGURES

Chapter 1:

Introduction

1.1: Ice shelves and their role in the cryosphere

When the Larsen B Ice Shelf collapsed on the Antarctic Peninsula in 2002, the world's attention was caught by the rapidity of change revealed by the stunning satellite imagery that recorded the event. In just a few weeks, ice covering an area the size of Rhode Island, which had remained solid for thousands of years, disintegrated into a loose mélange of blue glacial ice. Scientists who had long monitored the region turned their attention and their instruments to the ice flowing into the now-empty embayment, documenting dramatic increases in ice speed and in the volume of ice delivered to the ocean [e.g. *Rignot et al.*, 2004; *Scambos et al.*, 2004]. Thanks to the high visual impact of the satellite images and the undeniable, dramatic changes, the Larsen B served as a wake-up call to many that the impacts of climate change are important and perhaps much more immediate than often perceived.

Ice shelves are both sensitive indicators of climate change and important regulators of glacial response to a warming climate. They are extensions of ice sheets, where ice has flowed into the ocean and begun to float while still remaining attached to ice grounded on the continent. Ice shelf ice flows much like glacial ice, but generally at faster rates due to the lack of basal resistance. Ice shelves move up and down with the tides and provide feedbacks to local

ocean circulation patterns. At the same time as interfacing with the ocean, they also interface with the atmosphere. As ice shelf elevations are confined close to sea level, they experience some of the warmest air temperatures affecting ice sheets and therefore are often among the earliest ice masses to respond perceptibly to climate warming.

Beyond serving as evidence for climate change, ice shelves are important regulators of ice sheet contribution to sea level. Coupled numerical models of ice sheet/ice shelf systems [e.g. *Dupont and Alley*, 2005; *Gudmundsson*, 2013] reveal that ice shelves transmit an important "buttressing" effect to the grounded ice feeding the shelves. Ice shelves are frequently in contact with embayment walls, and often locally ground on islands or bedrock bumps, forming ice rumples and rises. The stress transmitted upstream from ice shearing at these contact points is known as "backstress." If ice shelf buttresses are removed, the pressure gradients that cause ice to flow become unbalanced, leading to easier spreading and increased flow speeds [*Fürst et al.*, 2016]. Models show that this causes a greater discharge of ice into the ocean and therefore increases rates of sea level rise. Observational studies, including many following the collapse of the Larsen B Ice Shelf [e.g. *Rignot et al.*, 2004; *Scambos et al.*, 2004], confirm the modeled predictions that ice shelf loss can lead to ice discharge increase.

Aside from a few small ice shelves remaining in the Canadian Arctic, ice shelves are mostly found fringing the world's two great ice sheets. Some of Greenland's largest outlet glaciers have floating ice tongues that are very important to their stability [e.g. *Joughin et al.*, 2004]. However, by far the largest percentage of ice shelf area is found in Antarctica, where ice shelves surround about three quarters of the coastline. These ice shelves help regulate the flow of the largest volume of ice in the world, capable of causing sea level rise that would be

catastrophic to our present civilization. It is therefore of utmost importance, to the advancement of science and to the well-being of humanity, to thoroughly understand ice shelves and their stability.

1.2: Dissertation goals and outline

This dissertation is a small piece of the very large effort at the intersections of glaciology, oceanography, and atmospheric sciences to understand the present stability of ice shelves and how that stability might change in the future. Ice shelf stability is regulated by three broad factors: surface melt, basal melt, and ice flow dynamics. Each study presented in this thesis investigates a topic related to a single one of these factors. The thesis concludes with a discussion of future research that will build on the studies presented here, including assessments that combine factors in a more comprehensive manner.

The thesis begins in Chapter 2 with a large-scale investigation of ice shelf surface melt and its effects on the upper firn layer. The study relies on active microwave backscatter data, which is validated using field data from a 2013 campaign in Greenland, to assess the concentration of ice lenses in the porous firn on all Antarctic ice shelves. Ice shelves with ice-saturated firn layers can support melt ponding at the surface, which can lead to the loss of the ice shelf through hydrofracture. The study presents a vulnerability index, built on the relationship between average annual melt days and backscatter, that represents how likely an ice shelf is to be affected by hydrofracture in the relatively near future. The chapter includes a literature review that examines the utility of scatterometry in understanding snow and ice characteristics and its limitations in cryospheric sciences.

Many recent studies have assessed rates of ice shelf melt [*Rignot et al.*, 2004; *Pritchard et al.*, 2012; *Depoorter et al.*, 2013], which are accelerating in some areas of Antarctica [*Paolo et al.*, 2015]. Chapter 3 addresses a small-scale aspect of ocean-driven ice shelf melt: the presence and evolution of basal channels. Although there is currently relatively little literature addressing these features directly, interest in basal channels within the glaciology and oceanography communities has grown in recent years, and it is likely that many more studies examining their importance will be completed in the future. Chapter 3 presents an overview study that depends on remote sensing data and statistical analysis to map basal channels around the continent and describe their general characteristics. It also documents rapid change on a large basal channel on the Getz Ice Shelf, and demonstrates that basal channel migration toward ice shelf shear margins is a potential contributor to ice shelf weakening. A comprehensive literature review of the growing resources on basal channels is included at the beginning of the chapter.

Chapter 4 explores in detail the calculation of a fundamental measure of ice flow for both floating and grounded ice: surface strain rates. The early part of the chapter explores the applications of strain rates represented in the glaciological literature. Strain rate calculations are then derived following Nye (1959), as well as using an alternative, direct differencing method for calculating strain rates. A Matlab code for calculating strain rates from satellite-derived velocity grids by adapting Nye's field-based methods is developed and included in the Appendix to Chapter 4. A strain rate data product for the entire Antarctic Ice Sheet is presented, which is built on a new velocity mosaic derived from Landsat image pairs [*Fahnestock et al.*, 2016] and honors varying viscous length scales caused by large ice thickness

variations. The final section in the chapter demonstrates the importance of strain rates in the calculation of basal melt through mass conservation equations.

Chapter 5 presents overall conclusions drawn from the studies comprising the dissertation, and suggests research directions to advance ice shelf understanding in the future. Each individual study in this dissertation has raised new questions and offered opportunities for further inquiry into each topic. The sections of Chapter 5 outline some specific ideas, proposing new research that builds on the knowledge advanced by each study in the dissertation and combines it into more comprehensive future assessments.

Chapter 2:

Surface melt and Antarctic ice shelf stability

2.1: Scatterometry and its applications to snow and ice

Scatterometers are active satellite sensors that gather earth data in microwave frequencies. Scatterometry missions were originally designed to measure wind speeds over the oceans; however, the data they collect can also be applied to assessments of surface characteristics and evolution on land. Microwave frequencies are valuable because their long wavelengths interact very little with particles in the atmosphere, making it possible to image the earth surface at almost any time, regardless of light availability or cloud cover.

Both passive and active instruments can operate in microwave frequencies. Passive microwave sensors, often referred to as radiometers, measure the strength of the microwave signal that is emitted or reflected naturally from the earth's surface. Because this is a relatively weak signal, passive radiometers rely on a very coarse spatial resolution to gather enough microwaves to make an accurate measurement. In contrast, active sensors (called radars) send synthetically produced waves to the surface and measure the signal that is returned to the sensor. Active sensors using microwave frequencies include radar altimeters, Doppler radar, synthetic aperture radar (SAR), and scatterometers. Each sensor type has advantages and disadvantages that make them most suitable to certain applications.

Radar altimeters send their signal to a small area on the surface and measure the time it takes for the signal to return to the sensor. The surface elevation can then be calculated based on the return time. Doppler radars are designed to detect small shifts in the frequency of the returned signal that are caused by movement of the target, which can be useful in a variety of applications including aviation and meteorology [*Ulaby and Long*, 2014].

SAR instruments and scatterometers both measure the power of the signal returned to the sensor, in a similar manner to passive microwave radiometers. SAR instruments achieve a particularly high spatial resolution by simulating a very large antenna using the movement of the satellite through its orbit. Though the data can be analyzed in the same manner as scatterometer data, the higher resolution and accordingly low temporal resolution makes it difficult to carry out analyses over large areas using SAR data [*Ulaby and Long,* 2014].

Scatterometers operate at a similar spatial resolution to passive microwave sensors. The coarse spatial resolution makes it possible to image the whole earth frequently, which makes the measurements especially valuable for the original purpose of measuring wind direction and speeds over the ocean. The active nature of the sensors allows for control over the incidence angle of the signal. These characteristics also make scatterometers valuable for monitoring many aspects of the Cryosphere [*Ulaby and Long*, 2014]. The following sections briefly review available scatterometry data and applications of scatterometry to the study of snow and ice. This is not an exhaustive review; it instead strives to describe in general terms the major snow and ice applications covered in the literature, with emphasis on recent articles published on each topic.

2.1.1: Available scatterometer data

The first satellite scatterometers were flown as part of NASA's Skylab missions in 1973 and 1974. These missions demonstrated that scatterometers could become a successful component of Earth observation systems. Since then, several scatterometers have been launched by space agencies in many countries. A brief summary of instruments that have been or currently are part of a major scientific mission is included in table 5.1.

Table 2.1 | Summary of available scatterometer data*

Instrument	Agency	Operational period	Band	Spatial resolution
Seasat-A Satellite Scatterometer System (SASS)	NASA	July-September 1978	Ku	50-100 km
ESCAT onboard European Space Agency's Earth Remote Sensing satellite 1 (ERS-1)	ESA	July 1991-March 2000	C	25-50 km
ESCAT on ERS-2	ESA	April 1995-July 2011	C	25-50 km
NASA Scatterometer (NSCAT)	NASA	August 1996-June 1997	Ku	25-50 km
SeaWinds on the Quick Scatterometer satellite (QuikSCAT)	NASA	June 1999-November 2009	Ku	25 km
Advanced Scatterometer (ASCAT)	EUMETSAT	May 2007-present	C	25-50 km
Oceansat-2 Scatterometer (OSCAT)	ISRO	September 2009-April 2014	Ku	25 km

* RapidScat is a scatterometer currently flown by NASA on the International Space Station. Because it does not cover polar latitudes, it is not included in this discussion.

Websites with sensor information:

SASS: https://nsidc.org/data/docs/daac/scatterometer_instrument.gd.html
ERS-1/2: https://earth.esa.int/web/sppa/mission-performance/esa-missions
NSCAT: https://winds.jpl.nasa.gov/missions/nscat/
QuikSCAT: http://winds.jpl.nasa.gov/missions/quikscat/
ASCAT: http://www.eumetsat.int/website/home/Satellites/CurrentSatellites/Metop/MetopDesign/ASCAT/index.html
OSCAT: http://manati.star.nesdis.noaa.gov/products/OSCAT.php
RapidScat: http://winds.jpl.nasa.gov/missions/RapidScat/

Scatterometers generally transmit pulses in one of two frequency ranges: C-band (4-8 GHz) or Ku-band (12-18 GHz). These bands have slightly different sensitivities to snow properties, as well as differences in penetration depth, which make it challenging to make direct comparisons between sensors that operate in different bands. C-band microwaves can penetrate much more deeply into snow than Ku-band, with penetration depths of ~10 m or more in dry snow. Ku-band sensors penetrate dry snow on the order of a few meters [*Rott et al.*, 1993]. There are many other specifications relevant to each sensor, such as the look angles, polarizations, and available sensing modes. Further information is available from the websites listed below Table 2.1.

2.1.2 Scatterometer measurements of sea ice

Scatterometers are valuable for monitoring sea ice in both the Arctic and Antarctic. Their high temporal resolution makes it possible to track change in ice pack characteristics and sea ice drift throughout the year. They are also increasingly being used to monitor sea ice extent.

Because microwaves penetrate a small distance into snow and ice, sea ice backscatter values are determined both by volume scattering and surface scattering from the overlying snow and the sea ice itself. In addition, surface characteristics that change continuously throughout the year, such as salinity and grain size, can change backscatter values considerably [*Haas*, 2001]. Many characteristics evolve with predictable seasonal patterns, which makes it possible to broadly monitor sea ice conditions by examining annual backscatter fluctuations. Willmes et al. (2011) also noted that, in addition to seasonal cycles, Antarctic sea ice exhibits

spatial variations, with some areas showing particularly high backscatter due to the presence of refrozen ice lenses in overlying snow.

The seasonal pattern of backscatter over Antarctic sea ice is very different from that found in the Arctic. In general, the Arctic tends to experience warmer air temperatures, and therefore more intense surface melt on sea ice. The melt amounts are too large and the snow too warm to allow for rapid refreezing, which results in wetted snow. This significantly increases the dielectric constant of the surface, and therefore decreases the backscatter signal. This means that summer backscatter values on Arctic sea ice in general tend to be lower than winter values. In contrast, Antarctic sea ice stays relatively cold, and any summer surface melt tends to percolate into the snow cover and refreeze as ice lenses. Discontinuous ice lenses tend to scatter microwaves efficiently, leading to higher backscatter values in the summer than in the winter [*Perovich et al.*, 2007; *Haas,* 2001].

Sea ice packs move in response to surface winds and ocean currents, and the high temporal resolution of scatterometer measurements makes it possible to track sea ice drift. Cross-correlation techniques can be automated to track the displacement of spatial features seen in backscatter data between image pairs, yielding estimates of the direction and velocity of sea ice movements [e.g. *Haarpaintner*, 2006]. The accuracy of drift measurements can be improved using resolution enhancements techniques, but some precision is sacrificed with loss of temporal resolution due to combining images from multiple passes [*Haarpaintner*, 2006]. More complete records may be produced by combining sea ice drift estimates from scatterometer records with passive microwave data [*Girard-Ardhuin and Ezraty*, 2012].

Scatterometers can also be used for classification of sea ice as first-year ice (sea ice that has formed during the current season) or multi-year ice (sea ice that has persisted through at least one melt season). Sea ice properties that evolve over time, such as surface roughness, porosity, and brine inclusion, cause multi-year ice ice to have higher backscatter values than first-year ice. Empirically-derived backscatter thresholds may be applied to maps derived from scatterometer data to identify areas of each type of ice [*Swan and Long*, 2012; *Lindell and Long*, 2016].

As scatterometers and radiometers operate in similar wavelengths, they are both useful in detecting sea ice extent. Most sea ice extent monitoring is currently carried out using passive microwave detectors such as the Special Sensor Microwave/Imager (SSM/I), due to the continuous record available from 1978 through today [*Meier and Stroeve*, 2008]. Except for the brief operation of SASS, scatterometer data did not become available until the 1990s, and differences in sensor wavelength and sensitivity create challenges for developing a continuous record from available data. However, it is likely that scatterometers will continue to fly, creating valuable records into the future.

Many scatterometer sea ice extent algorithms rely on the ratio between backscatter from beams that are either horizontally or vertically polarized, which interact very differently with open ocean and sea ice. Some also utilize estimates of backscatter dependence on incidence angle [*Long and Drinkwater*, 1999; *Remund and Long*, 2000; 2014]. Scatterometer resolution enhancement algorithms, such as the SIR algorithm [*Long et al.*, 1993], provide scatterometry data at significantly higher spatial resolutions than passive microwave, which can increase the accuracy of sea ice edge estimates. However, this also tends to add noise to the

data. Still, analysis suggests that passive microwave data and scatterometry perform similarly in sea ice edge detection, and that a blended product in the future could provide valuable insights on sea ice extent to both scientists and ships operating in areas prone to sea ice [*Meier and Stroeve*, 2008].

2.1.3 Scatterometer measurements of snow

Snow cover extent is generally monitored using visible-band products such as those derived from MODIS, while passive microwave data is often used for deriving snow water equivalent [*Brown et al.*, 2007; *Foster et al.*, 2011]. Though scatterometers are not as easily applied to these basic analyses, scatterometry data does fill important niches in the broad monitoring of Earth's snow cover. For example, particularly with resolution-enhanced products, scatterometers can track changes in physical processes within the snow pack, documenting evolution throughout the season [*Nghiem and Tsai*, 2001]. This is very similar to the physical processes detected in the overlying snow on sea ice discussed in section 2.1.2.

In accumulation zones on glaciers and ice sheets, where annual layers of snow are deposited, scatterometers can also be valuable for measuring rates of snow accumulation. Scatterometry studies show that, in general, backscatter decreases as accumulation rates increase because a lower density of layers decreases volume scattering and increases penetration depth [*Rotschky et al.*, 2006]. Empirical relationships that rely on this interaction can be created using ground-truthing data to estimate accumulation rates over the past several years on ice sheets [*Drinkwater et al.*, 2001; *Rotschky et al.*, 2006]. Snow accumulation can also be estimated empirically in a more precise time frame if a large melt event has left refrozen

meltwater, in the form of discontinuous ice lenses, near the surface. These lenses initially raise backscatter values following the melt event. As snow accumulates and the ice layer is buried, backscatter values begin to decrease. Assessment of the rate of backscatter decrease can make it possible to estimate snow accumulation in the years since the melt event [*Nghiem et al.*, 2005; 2007].

Recently, numerical models have been developed that may lead to more accurate, physically-based estimates of snow accumulation in some areas [*Dierking et al.*, 2012]. Radiative transfer models use estimates of grain size, snow temperature, depth-density relations, and accumulation rates to estimate radar backscatter. In turn, given radar backscatter from a satellite dataset, these calculations can be inverted for accumulation rates. So far, these models have been most effective in dry snow zones with low accumulation rates, where empirical parameters are most easily estimated [*Dierking et al.*, 2012].

2.1.4 Scatterometer melt detection

Microwave backscatter is strongly affected by the dielectric constant of the scattering surface. Even a small amount of meltwater increases the dielectric constant of snow dramatically, lowering volume scattering and increasing surface absorption [*Trusel et al.*, 2012]. The result is a marked decrease in backscatter measured by the sensor, a change that can be exploited to document surface melt on ice sheets, glaciers, and seasonal snow. As in other applications, the short records provided by many scatterometers make the creation of a long-term record of seasonal snow melt challenging. However, many studies exist that document snow melt over relatively short time periods over many parts of the earth.

Melt detection typically uses methods that rely upon a threshold of change in backscatter values. The most common threshold method to measure melt onset uses a moving window to detect a drop in backscatter that exceeds background average changes over a few days [*Drinkwater and Liu*, 2000; *Smith et al.*, 2003; *Wang et al.*, 2005; 2008; *Trusel et al.*, 2012]. Sometimes these methods are combined with an absolute threshold, where liquid water is reliably considered to be present. Accuracy, as well as the estimation of meltwater volume or intensity, can be improved by combining a threshold approach with a geophysical model that takes into account the scattering properties of layers of wet and dry snow [*Hicks and Long*, 2011]. As threshold methods use empirically-determined threshold values, they rely on validation data such as modeled energy fluxes from atmospheric reanalyses [*Drinkwater and Liu*, 2000], observations from other satellites [*Hall et al.*, 2009], or ground measurements from automatic weather stations or other instruments that log air temperature or surface energy balance [*Smith et al.*, 2003; *Wang et al.*, 2005; *Hicks and Long*, 2011]. Some algorithms also rely on thresholds of diurnal backscatter change, which is possible in areas where snow refreezes at night and where a scatterometer passes over the areas twice in one day [*Hall et al.*, 2009].

As noted previously, many scatterometers use radar signals that are polarized horizontally or vertically. These signals in general yield very similar results, but the two polarizations have slightly different sensitivities to liquid water presence. Therefore, melt onset and freeze-up algorithms can be built that rely on the polarization ratio between horizontally and vertically polarized measurements taken concurrently. Applications of this technique have been carried out on Antarctic ice shelves [*Kunz and Long*, 2006], where validation using passive microwave-derived brightness temperatures demonstrates its reliability.

Melt detection algorithms have also been successfully applied to sea ice, where surface melt tends to be common even in polar areas due to its low elevations and maritime climates. Antarctic sea ice [*Drinkwater and Liu*, 2000] generally shows much less surface melt than Arctic sea ice [*Winebrenner et al.*, 1994]. Annual melt records have also been produced for the Antarctic [*Trusel et al.*, 2012] and Greenland [*Hall et al.*, 2009; *Hicks and Long*, 2011] Ice Sheets, as well as on ice caps and terrestrial snow in the Arctic [*Smith et al.*, 2003; *WANG et al.*, 2005; 2008].

2.1.5 Other scatterometer measurements of ice sheets and glaciers

The health of ice sheets and glaciers is often monitored in part through tracking areal changes in accumulation and ablation zones. These zones are sometimes further divided into ice "facies," which are categories based on physical characteristics of the upper layers of ice, firn, and snow [*Benson*, 1962]. Because microwave signals are sensitive to snow characteristics such as the concentration of ice lenses and the specularity of refrozen meltwater surfaces, scatterometers can accurately map snow facies. This capability is especially useful in mapping facies on the Greenland Ice Sheet, which has both a large areal extent and a relatively predictable pattern of ice facies [*Jezek et al.*, 1994; *Long and Drinkwater*, 1994; 1999]. Some understanding of related categories can be gained through similar methods in Antarctica, though Antarctic ice facies are not as easily defined or predictably identified [*Rott and Rack*, 1995; *Long and Drinkwater*, 1999]. Similar analyses of ice facies have been made using SAR data [e.g. *Fahnestock et al.*, 1993], though these studies have generally been limited by difficulties in covering entire ice sheets using instruments with such high spatial resolutions.

It is worth noting that most of the measurements discussed in this review make the assumption that the surface is isotropic, meaning that the azimuth of the signal does not affect the measurement. This makes it possible to use all the data from sensors that have multiple beams arranged at multiple look angles, as well as to use satellite passes from multiple directions. While this is generally a good assumption, there are regions on the Greenland and Antarctic Ice Sheets that exhibit significant azimuthal variations [*Bingham and Drinkwater*, 2000; *Ashcraft and Long*, 2001; *Lindsley and Long*, 2016]. These variations, often caused by persistent winds creating preferentially oriented sastrugi, must be taken into account in some large-scale analyses of the ice sheets.

2.1.6 Strengths and limitations of scatterometry in cryospheric science

The sections above give brief overviews of a wide variety of scatterometer applications. These applications generally rely strongly on the broad spatial coverage and high temporal resolution of available scatterometry data. The ability of active microwave sensors to penetrate through clouds and operate at any time make the data particularly useful for continuous monitoring of seasonal and interannual changes in the cryosphere.

However, the wide variety of applications also illustrates a severe drawback of scatterometry data: the sensitivity of microwave backscatter to a very large number of variables. Scatterometry data is generally based on a single measurement: the power of the signal that reaches the sensor. Within this single measurement are the effects of a wide variety of variables on a snow or ice surface. For example, scatterometry is sensitive to grain size, surface roughness, and snow and ice salinity. Refrozen ice lenses in snow and firn can raise the

backscatter signal. The presence of liquid meltwater lowers it drastically. Penetration into surface snow alters based on accumulation rates. Strong directional scattering features such as sastrugi can bias the results from a given perspective of the satellite.

As it can be very difficult to tease apart the individual variables, scatterometry results are associated with a large amount of uncertainty. The combination of scatterometry with ground-truthing data, other satellite results, and physical modeling can significantly increase confidence in its application. Scatterometers can also be broadly applied where a single variable dominates the surface response, creating recognizable cycles or trends. The study presented in the following sections is an example of this broad analysis approach.

2.2 Submitted paper on ice shelf vulnerability to hydrofracture

Section 2.2 presents the text of a paper that we plan to submit to *Earth and Planetary Science Letters* in May of 2017. The paper relies on a novel use of scatterometer data that utilizes relative data values, rather than absolute numbers. This allows us to compare data from sensors that operate in different bands, and to extrapolate conclusions drawn from Greenland to the ice shelves of Antarctica. Section 2.3 comprises the supplementary information submitted alongside the paper.

Statement of contribution: K. E. Alley led the planning, analysis, and writing of the following study, including assembling data, applying statistical techniques, creating figures, and participating in the collection of Greenland field data presented in Figure 2.1. The study was based on a pilot study led by T. Scambos. J. Z. Miller provided the annual melt days data. D. Long processed and distributed the backscatter data. M. MacFerrin led the led the Greenland

field work and contributed Figures 2.1c and 2.6. All authors participated in writing and editing the paper.

Quantifying vulnerability of Antarctic ice shelves to hydrofracture

K. E. Alley[1], T. A. Scambos[1], J. Z. Miller[2], D. Long[3], M. MacFerrin[1]

[1]University of Colorado Boulder, Boulder, Colorado, USA,

[2]Ohio State University, Columbus, Ohio, USA,

[3]Brigham Young University, Salt Lake City, Utah, USA

Abstract

Recent ice shelf disintegrations on the Antarctic Peninsula and subsequent increases in ice sheet mass loss have highlighted the importance of tracking ice shelf stability with respect to surface melt ponding and hydrofracture. In this study, we use active microwave scatterometry to assess melt season duration and the relative concentration of refrozen ice lenses in Antarctic ice shelf firn. We demonstrate a physical relationship between melt days and backscatter using scatterometry and field data from Greenland, and apply the observed relationship to derive and map a vulnerability index across Antarctica's ice shelves. The index reveals that some remaining Antarctic Peninsula ice shelves have already reached a firn state that is vulnerable to hydrofracture. We also show that the progression of an ice shelf toward vulnerability is affected by many factors, such as surface mass balance and ice shelf geometry.

1 Introduction

Atmospheric warming can lead to ice shelf disintegration through hydrofracture [*Scambos et al.*, 2000; 2003; *Rott et al.,* 1996; *Hughes*, 1983]. Hydrofracture on glaciers and ice shelves occurs when water infiltrates crevasses, filling them to a level at which water pressure at the crack tip exceeds the fracture toughness of the ice as well as any compressive stresses transverse to the fracture orientation. For the fracture to continue to propagate, the crevasse tip pressure must continue to increase to offset increasing lithostatic pressure. This is facilitated by a surface reservoir of water that drains into the propagating fracture. Ponding of meltwater on the surface of ice shelves is an effective reservoir for hydrofracture. With closely-spaced fractures, fractured blocks may then topple, initiating a runaway disintegration effect [*MacAyeal et al.*, 2003].

Not all ice shelves are vulnerable to hydrofracture. In regions with high winter snow accumulation or permeable, porous firn, any meltwater produced during summer months percolates into the upper firn and refreezes. To support surface ponds, the firn layer must be sufficiently saturated with refrozen meltwater to prevent efficient downward percolation. Modeling studies and observations confirm that ice shelves that have collapsed on the Antarctic Peninsula in the past had very little firn air thickness preceding disintegration [*Holland et al.,* 2011; *Berthier et al.*, 2012; *Munneke et al.*, 2014].

Scambos et al. (2003) performed a pilot study investigating the utility of active microwave scatterometry for assessing firn ice-lens content. Using selected areas from several ice shelves, they demonstrated a relationship between winter backscatter and ice shelf melt season duration. They interpreted this relationship as reflecting the ice-saturation state of the

firn layer, based on a study linking radar scattering and ice sheet facies in Greenland [*Fahnestock et al.*, 1993]. On most shelves, backscatter increases with average annual melt days, because small ice lenses and other small refrozen structures are efficient diffuse scatterers. However, at high numbers of melt days, when ice lenses form large, nearly-continuous, and relatively smooth layers in the firn, specular reflections direct the microwave signal away from the sensor and backscatter values decrease. As large, continuous ice lenses also impede meltwater percolation, promoting melt pond formation, shelf areas with lowered backscatter values at high numbers of annual melt days are inferred to be the areas most susceptible to hydrofracture.

In this study, we use gridded scatterometry data to assess the relative firn-ice concentration for all Antarctic ice shelves using a relationship between annual melt days and average winter backscatter. We first conduct a validation of the expected relationship using scatterometry, ground-penetrating radar, and shallow firn cores in Greenland, where ice sheet facies are relatively well-mapped. We then show that the melt days-backscatter relationship exists for all areas of Antarctica's ice shelves, and use it to develop an index to assess vulnerability to surface-melt-induced hydrofracture collapse.

2 Data

The backscatter data used in this study come from four sensors: the C-band (5.7 cm wavelength) scatterometers ESCAT onboard the European Space Agency's (ESA's) Earth Remote Sensing (ERS) satellites 1 (1990-1995) and 2 (1995-1999); NASA's Ku-band (2.2 cm) Seawinds instrument on the QuikSCAT satellite (2000-2009); and ESA's C-band Advanced Scatterometer

(ASCAT) aboard the MetOp-A satellite (2009-2013). All scatterometry data were provided by Brigham Young University's Microwave Earth Remote Sensing Laboratory Scatterometer Climate Record Pathfinder. We restricted our backscatter data analysis to austral winter months (June, July, and August) in order to avoid liquid meltwater, which significantly lowers backscatter values [*Long and Drinkwater*, 1994]. A detailed description of the backscatter data is provided in supporting text S1.

We used 10-year averages of two passive microwave datasets in Greenland and Antarctica to document annual melt days for the periods leading up to each scatterometer dataset [*Mote et al.,* 2014, *Picard and Fily,* 2006]. We chose this time scale to establish a relatively long-term average while avoiding biases from melt season effects buried below scatterometer penetration depths. We also created a third, higher-resolution dataset for Antarctic surface melt derived from QuikSCAT backscatter following the technique presented in Hicks and Long (2011). Additional validation data for the subsurface physical processes that drive the backscatter-melt days relationship come from ground-penetrating radar and firn cores collected during a field campaign in southwest Greenland in 2013 [*Machguth et al.*, 2016].
All Antarctic data were provided as continent-wide datasets. Subsetting of ice shelf regions was carried out using the MODIS Mosaic of Antarctica (MOA) 2009-derived coastline and grounding line [*Scambos et al.*, 2007]. Modifications were made to the outlines of the Ross and Filchner-Ronne ice shelves for ERS-1 and -2 to exclude large no-data regions near the pole.

3 Backscatter/melt days relationship development and validation

The physical relationship presented by Scambos et al. (2003) is essentially a microwave-based documentation of snow facies for Antarctic ice shelves. The observed categories are most easily identified and described in Greenland. Benson (1962) divided the Greenland ice sheet into four snow facies (the dry snow, percolation, wet snow, and bare ice zones) based on their physical characteristics using *in situ* summer observations. Fahnestock et al. (1993) observed these same facies using winter SAR backscatter and discussed the physical features causing the distinctive backscatter response. Similar results have been presented in other studies [e.g. *Jezek et al.*, 1993; *Long and Drinkwater*, 1994]. At the highest elevations, in the dry snow zone, little or no melt occurs throughout the year, and backscatter values are typically very low due to penetration and absorption of microwave energy in the firn. At slightly lower elevations, in the percolation zone, summer melt is more significant and cooler subsurface temperatures cause meltwater to refreeze within the firn column, forming small, discontinuous ice lenses and pipes. These are efficient scatterers of microwave energy [*Jezek et al.*, 1994; *Partington*, 1998; *Hall et al.*, 2000; *Haas et al.*, 2001; *Willmes et al.*, 2011], and as summer melt intensity increases (with decreasing elevation on the ice sheet, among other factors), the winter backscatter signal rises. At lower elevations, in the wet snow zone, the entire upper firn column is wetted by melt and refreezes in winter to form large ice lenses, or (lower still) a nearly uniform ice layer in the superimposed ice zone. The bare ice zone at the lowest elevations is formed where summer melt removes the entire winter snow column, leaving smooth glacial ice. In contrast to the increasing backscatter values with decreasing elevation observed through the percolation zone, the shift at lower elevations to large, continuous layers of ice

creates a specular surface for microwave radiation, buried under dry snow in winter. Specular reflections redirect the active microwave signal primarily away from the sensor, causing a decrease in measured backscatter.

We infer that similar processes affect the firn column on Antarctic ice shelves, with analogous effects on backscatter. Cool-summer ice shelf areas have no significant summer melting, analogous to the dry snow zone in Greenland. Some areas receive a little melt, and have small, discontinuous ice lenses in the firn, similar to Greenland's percolation zone. A few areas receive significant amounts of melt that lead to the formation of superimposed ice capable of specular reflection of microwave energy. However, unlike in Greenland, where summer melt intensity is strongly correlated with elevation, snow facies on Antarctic ice shelves are more closely tied to local summer climate, and vary spatially around the continent.

Therefore, to explore the graphical relationship between ice lens content and backscatter, we examine backscatter characteristics and mean melt season duration for two transects in Greenland that together span all four facies (Figure 2.1). We extracted a 100 km-wide transect of passive microwave melt days data [*Mote et al.,* 2014] and ASCAT backscatter data from Summit Station to Kangerlussuaq. A second, more southern transect from the central ice divide west to the ice edge spans a region of extensive field work. Summit Station experiences surface melting very rarely and is well within the dry snow facies [*Benson*, 1962; *Fahnestock et al.,* 1993]. The field work region spans the lower percolation and upper wet snow and superimposed ice zones, and Kangerlussuaq is at the base of the ice sheet in the ablation zone with melt occurring on more than 50 days during a typical summer.

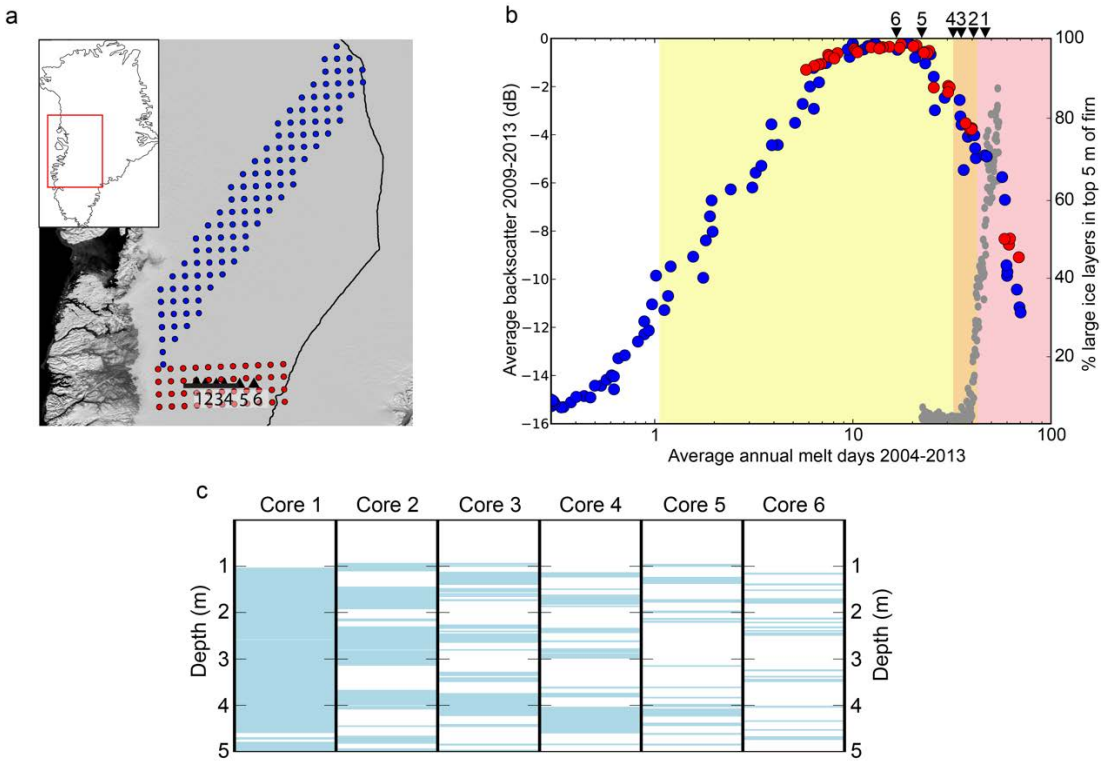

Figure 2.1 | Backscatter/melt days relationship in Greenland.
a. Transect from Summit Station to Kangerlussuaq (blue dots) and Greenland's central ice divide to the ice edge (red dots). Black line within red transect traces a ground-penetrating radar (GPR) transect in 2013, with numbered black triangles representing firn cores. b. Blue and red dots correspond to transects in (a). Backscatter data are from ASCAT, melt days data re from Mote et al. 2014. Black triangles are corresponding firn core locations. Gray dots show the percent by volume of large ice lenses (> ~0.8 m) in the top 5 m of firn from GPR (Figure 2.6). Yellow shading represents percolation zone, orange is deep percolation [*Machguth et al.*, 2016], and red is the runoff zone observed in 2013. c. Ice lenses (blue) in the top five meteres of firn cores collected in 2013 along the GPR transect shown in (a).

The distinctive shape of the graph illustrated in both transects (Figure 2.1b) reflects the expected relationship [*Fahnestock et al.*, 1993] based on backscatter response to the progression of snow facies. The field data show that progression up the backscatter-melt days relationship is accompanied by an increase in ice lenses in the firn that ultimately leads to surface-supported meltwater features in summer. The clear decrease in backscatter, representing a shift to specular reflections, occurs at slightly fewer melt days than the zone where GPR data and firn cores begin to show a significant fraction of large ice lenses. The GPR

data (Figure 2.6, supporting text S2) were processed to detect ice lenses > ~0.8 m thick, but as specular reflections are primarily a surface scattering response [*Carsey*, 1992], reduced backscatter should be observable with the much thinner, yet widespread, ice lenses observed in the firn cores above the superimposed ice zone. The thickest ice lenses near the surface in Core 5, close to the decrease in backscatter, are 25 cm or less. The point at which backscatter decreases also occurs at elevations significantly above areas where melt water is typically visible on the surface in summer. ASCAT is a C-band instrument and, although penetration depths vary widely in polar firn, the C-band frequency can penetrate ~10 m or more in areas of dry snow [*Rott et al.*, 1993]. In this study, data are limited to the winter season when very little liquid water is present. Therefore, ASCAT should be sensitive to extensive ice layers that are formed deep enough that more porous firn above the layer could store meltwater during summer and prevent visible ponding.

We utilized the Ku-band instrument QuikSCAT for our Antarctic analysis because it has a much lower penetration depth [*Rott et al.*, 1993] and therefore responds to lenses that are closer to the surface and much more likely to cause melt ponding. However, it would not be reasonable to compare QuikSCAT data to 2013 field data in Greenland, because QuikSCAT failed before the anomalously large 2012 melt event that significantly impacted the field data [*Machguth et al.*, 2016]. We show in the next section that the physical relationship demonstrated in Greenland is present in the shapes of the curves in Antarctica, regardless of sensor, band, or time period. This consistency, along with the fundamentally relative nature of our vulnerability index, allows us to utilize QuikSCAT data for Antarctic analysis of hydrofracture susceptibility.

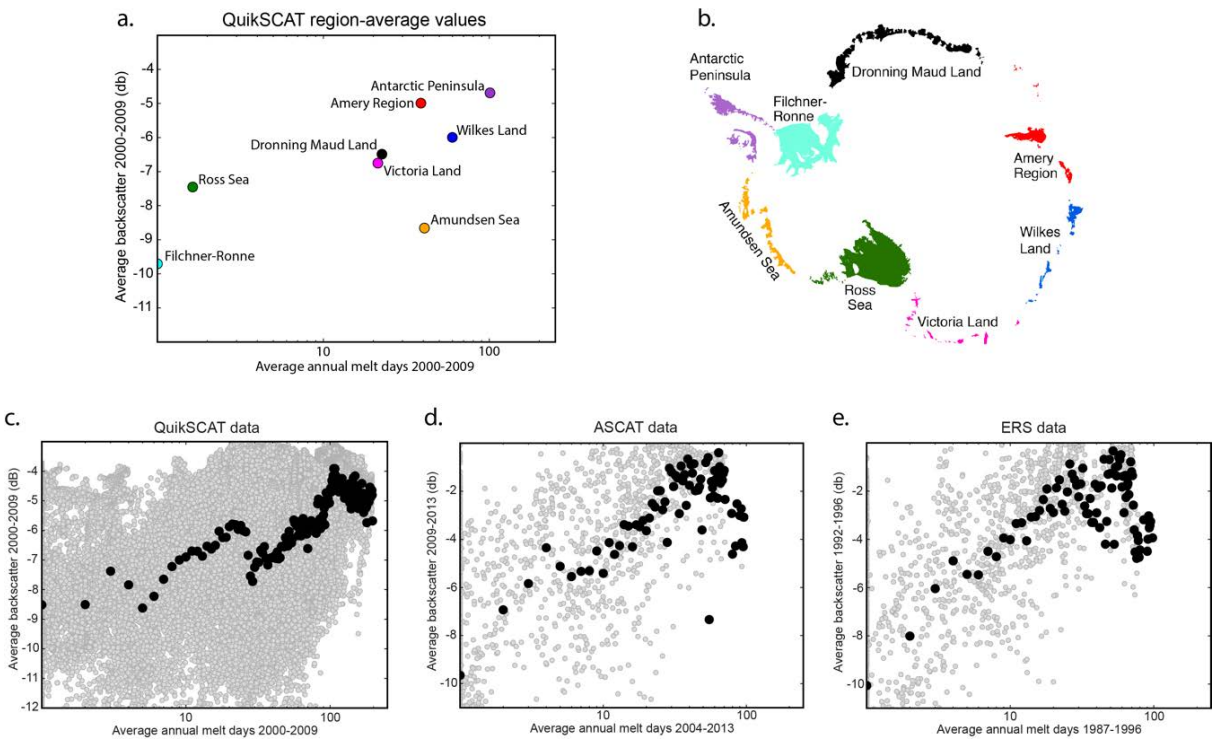

Figure 2.2 | Backscatter/melt days relationship in Antarctica.
a) Region-average values for all Antarctic ice shelves, with colors corresponding to regions shown in b. Both melt day count and backscatter are derived from QuikSCAT. Related plots in Figures 2.9-2.16. c) Same data used in a, binned and averaged by integer melt day (black) and shown without averaging (grey). d) Same as c, but with backscatter from ASCAT and melt days from Picard and Fily (2006). e) Same as d, but with backscatter from ERS.

4 Backscatter/melt days relationship in Antarctica

We expect to see the same backscatter response to ice lenses displayed by the distinct shape of the Greenland relationship in our analysis of Antarctic ice shelves. Figure 2.2 explores the relationship using data from all Antarctic ice shelves, with region-average values displayed in 2.2a providing a broad indication of where various geographic areas fall on the facies progression. Despite a significant amount of scatter in the raw data, backscatter values averaged within integer melt day bins, shown in black in Figures 2.2c-e, reveal a shape similar to that shown by our Greenland analysis. All scatterometry datasets considered show generally

increasing backscatter with increasing melt days, and a clear decrease in backscatter at high melt day values. Differences between sensors and detection bands cause backscatter values to vary between plots. Therefore, absolute variable values are not directly comparable between plots, although the shared physical relationship makes the shapes of the plots analogous. We continue our analysis exclusively using QuikSCAT data, because the long continuous record allows the extraction of annual melt days data directly from resolution-enhanced backscatter products. Therefore, the QuikSCAT analyses and maps can be produced at a much higher spatial resolution than those produced from ERS or ASCAT data.

Figure 2.3 shows that much of the scatter found in the raw QuikSCAT data may be explained by differences in surface mass balance over ice shelf areas that experience the same number of annual melt days. Using surface mass balances from RACMO2.3 [*Van Wessem et al.*, 2014], we separated the data into three mass balance categories. Ice shelves in a low mass balance category exhibit higher backscatter for each annual melt days value, and the drop in backscatter representing specular reflection is reached at a lower number of melt days than in the higher mass balance categories (in the highest mass balance category, the drop in backscatter is not present). Because the backscatter decrease is caused by the saturation-state of the firn with refrozen meltwater, this threshold, and the overall backscatter/melt days relationship, is determined by the ratio between annual surface melt and accumulation rate [*Pfeffer et al.*, 1991; *Braithwaite et al.*, 1994]. Ice shelves that receive large amounts of snowfall, for example, must experience more melt to fill the large amount of air space being replenished each year. Statistical tests show a significant, negative relationship between backscatter and surface mass balance in 100 out of 137 integer melt day categories with at

least 30 samples (supporting text S3), supporting the graphical evidence in Figure 2.3 that differences in surface mass balance cause divergence in backscatter values that appear as random scatter in the raw data.

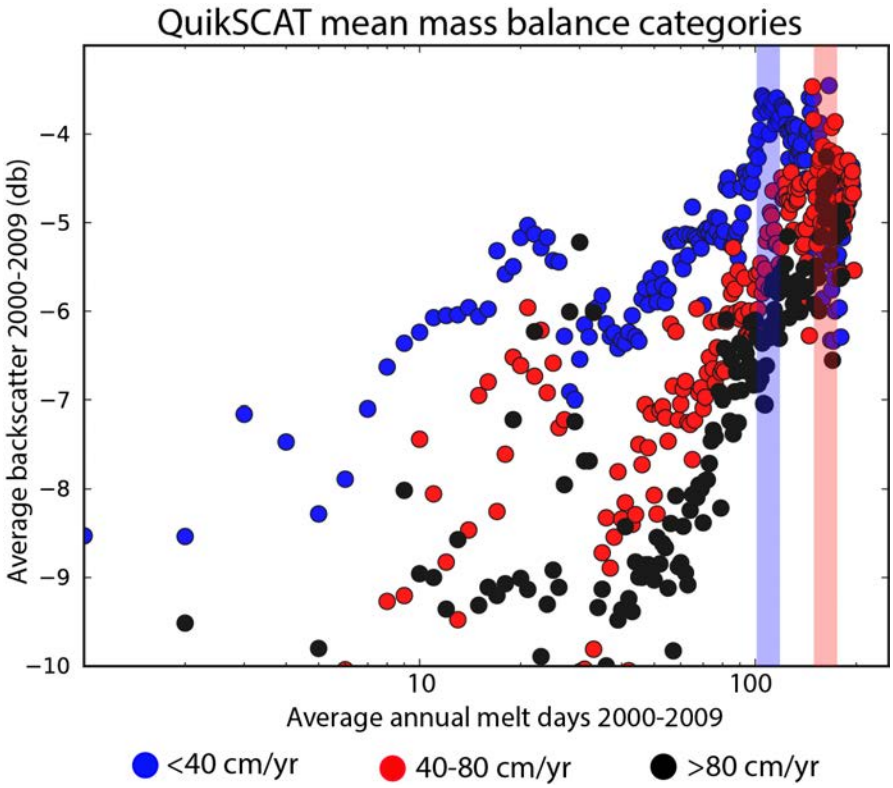

Figure 2.3 | Backscatter/melt days relationship for QuikSCAT.
Data separated by surface mass balance category [*Van Wessem et al.,* 2014] and averaged per integer melt day. Blue vertical line marks the decrease in backscatter at high annual melt days in the lowest surface mass balance category; red vertical line corresponds to the decrease in the middle surface mass balance category. No decrease in backscatter was observed in the highest surface mass balance category.

Backscatter values are also affected by other variables relevant to the Antarctic ice sheet. For example, heavily crevassed regions may create anomalously high backscatter values for a given number of annual melt days. We did not attempt to mask these areas in our study; however, they comprise only a small fraction of the shelf areas, and the similarity between the

shapes of the average Antarctic curve and the well-constrained Greenland curve indicate that they are not strongly influencing the averages. Another factor that might add scatter to the relationship is the presence of firn aquifers, which hold liquid water year-round [*Forster et al.,* 2014]. Further analysis would be required to assess the magnitude of the impacts of these and other factors.

5 Development of vulnerability index and error estimation

We use the mean relationships present in the QuikSCAT mass balance categories (Figure 2.3) to create a relative index that shows ice shelf vulnerability to surface-melt-induced collapse via hydrofracture. The index relies upon the assumption that the ice shelf backscatter/melt days relationship represents the temporal evolution that an ice shelf might experience under changing climate conditions (the 'space for time' substitution), and that any ice shelf may evolve to higher/lower positions on this relationship if temperatures in Antarctica warm/cool.

Two different approaches are used simultaneously to create this index. First, ice shelf areas with high annual melt days and reduced backscatter are classified as vulnerable to collapse, as the reduced backscatter observed indicates a significantly ice-saturated firn layer that could support melt ponding. For the QuikSCAT data, the selected threshold is at 119 average annual melt days in the lowest surface mass balance category, and 185 in the middle category (thresholds shown as blue and red vertical lines in Figure 2.3). These thresholds were determined by fitting a quadratic curve to the upper half of the averaged backscatter/melt days relationship and identifying the peak. Second, after data points above the threshold are removed, we carry out a simple, two-dimensional principal component analysis within each

mass balance category, which places an axis (the first principal component, Figure 2.17) along the direction of maximum variability, using information from both the backscatter and melt days data. The index is created by transforming each pixel to its location along the first principal component axis, and then scaling the values between zero and one. The result is a relative ranking of ice shelf vulnerability to hydrofracture, without explicit dependence on absolute backscatter or annual melt day values.

As shown in the graphs in Figure 2.2, the non-averaged relationship between backscatter and annual melt days contains a large amount of scatter. Because principal component analysis inherently reduces the two-dimensional relationship to one variable, error quantification must be performed along the principal component axis, rather than across an axis where a simple calculation of standard deviation would be relevant. In addition, error analysis must account for the differing thresholds used in the surface mass balance categories.

Due to these limitations, we chose an empirical Monte Carlo-type simulation to assess the impacts of data scatter on the calculated vulnerability index. For 100 iterations within each surface mass balance category, we built a vulnerability index with a small but significant percentage (10%) of the data points removed. For the lower two mass balance categories, we fit a quadratic function to the upper half of the data, which we used to identify a peak that was considered to be the ice-saturation threshold. The data for each iteration were then transformed to a vulnerability index as described above. We calculated the standard deviation for each point, as well as the standard deviation of the threshold values. Finally, we created maps of upper and lower estimates for the vulnerability index, which are equal to our best estimate for the index plus or minus two standard deviations as determined by the Monte Carlo

simulations. The results for the vulnerability index and the upper and lower error bounds are shown in Figure 2.4. The spread between the upper and lower bounds was typically between 5% and 40% of the calculated index values.

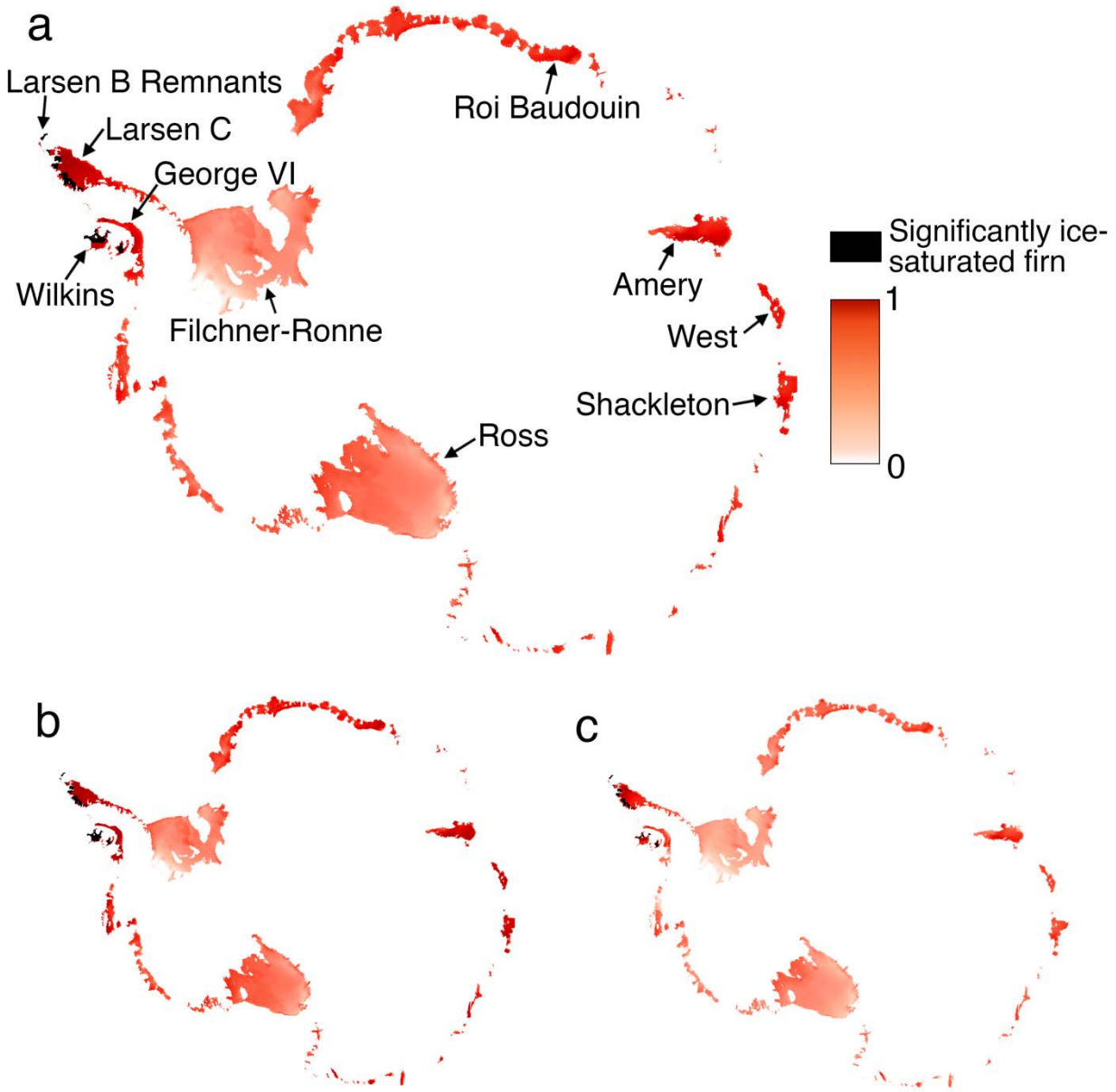

Figure 2.4 | Vulnerability index results.
a. Vulnerability index derived from the QuikSCAT data divided into surface mass balance categories as plotted in Figure 2.3. Labeled shelves are mentioned in the text. b. Vulnerability index plus two standard deviations. c. Vulnerability index minus two standard deviations.

6 Discussion of vulnerability index results

The results of the vulnerability index and the upper- and lower-bound error estimates are shown in Figure 2.4. Antarctica's largest ice shelves, the Ross and the Filchner-Ronne, plot relatively low on the vulnerability index, and thus we infer that they are in no immediate danger of surface-melt-induced collapse. Some shelves, like the Amery (Figure 2.5a), West, Shackleton, and Roi Baudouin (Figure 2.5b), have areas with very high vulnerability indices. These areas experience localized high annual melt rates, in many cases due to persistent, warm föhn or katabatic winds that travel down large slopes near the grounding line [*Cape et al.*, 2015; *Lenaerts et al.*, 2016]. Some areas on the Roi Baudouin Ice Shelf (Figure 2.5b) may show artificially low vulnerability due to the presence of liquid water in some measurements, which causes very large decreases in backscatter. Several ice shelves with high vulnerability areas support melt ponds annually (e.g., Roi Baudouin Ice Shelf in Dronning Maud Land, Figure 2.5a) [*Lenaerts et al.*, 2016], but are prevented from disintegration by either high compressive stresses due to pinning points downstream from the pond region, or very limited melt pond extent.

The areas identified as currently most vulnerable to collapse, plotting above the specular reflection threshold, are found on the Antarctic Peninsula. These include remnants of the Larsen B, parts of the Larsen C (Figure 2.5c), and much of the Wilkins and Bach Ice Shelves. These areas are interpreted to have the potential to support melt ponding given the right future climatic conditions; however, not all these areas currently exhibit melt ponding. Similarly, some areas that currently support melt ponds, such as the grounding line region of the Roi Baudouin Ice Shelf in Queen Maud Land, fall below this threshold. These plot at very

high values on the index, and are likely to contain a large proportion of smaller ice lenses that do not cause strong specular reflections but still impede downward meltwater percolation.

We checked the validity of our index in two ways. First, we generated a lower-resolution mapping of vulnerability using ASCAT data and temporally coincident melt days data generated from a passive microwave record (Figure 2.18) [*Picard and Fily,* 2006]. The mapped vulnerability index is nearly identical for the two determinations, indicating that our approach yields consistent results. Small differences between the indices may represent differences in the penetration depth of the sensors used, or they may be related to real firn layer evolution that occurred between the different time periods represented. Second, we compared the patterns in our results to those of Holland et al. (2011), who used an independent method relying on radio-echo sounding to estimate the air content of the firn on the Larsen C Ice Shelf. As shown in Figures 2.5c and 2.5d, the qualitative patterns in our vulnerability index match closely with the Holland et al. (2011) results, showing the highest vulnerability near the grounding line to the northwest where firn air thickness is lowest, and moving towards lower vulnerabilities towards the southeast corner as firn air content increases. A pixel-by-pixel correlation between the two assessments yields a Spearman's rho of -.60 and a p-value of 0.000. More recent *in situ* data has documented extensive, thick ice lenses in some of the locations we have marked as ice-saturated [*Hubbard et al.*, 2016], and Holland et al. (2015) documented a continuing loss of firn air thickness in the same regions.

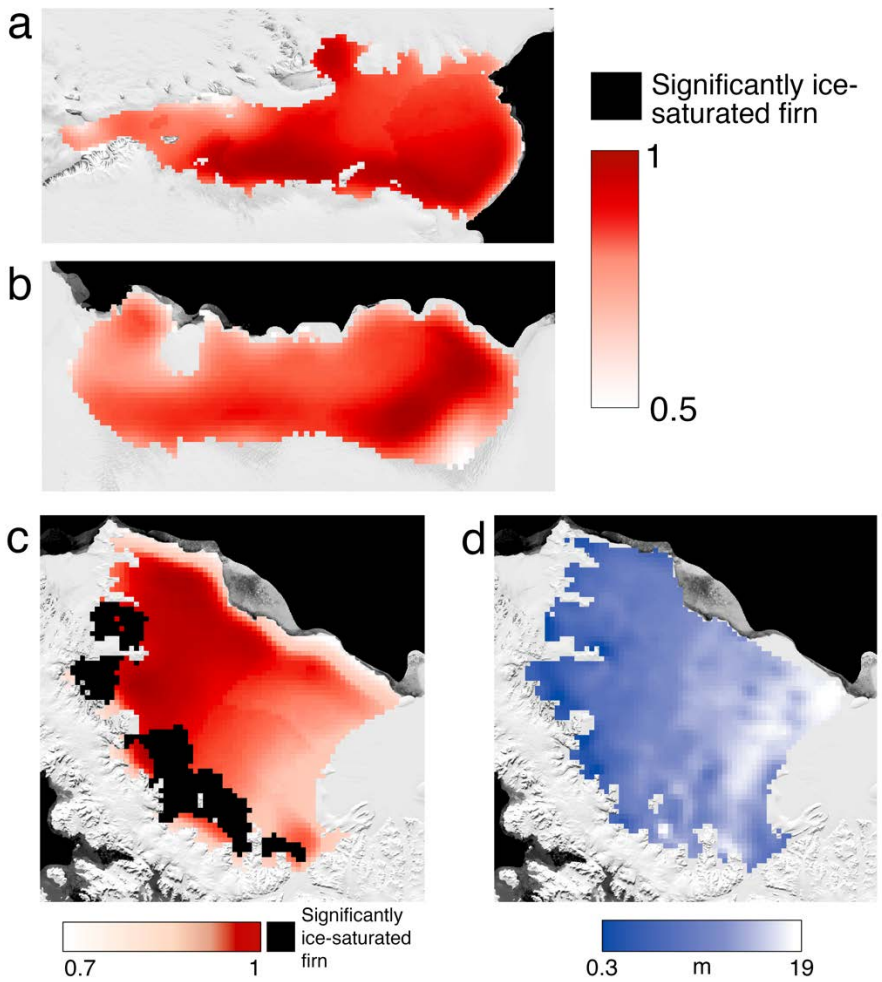

Figure 2.5 | Vulnerability index details.
a-b. Vulnerability index for the Amery and Roi Baudouin Ice Shelves, which are labeled in Figure 2.4. The index for both shelves is plotted using the colorbar to the right. c. Vulnerability index for the Larsen C ice shelf on the Antarctic Peninsula. d. Firn air thickness on the Larsen C ice shelf from Holland et al. (2011).

The map also suggests another important factor in the likelihood of an ice shelf to be affected by surface-melt-induced instability: ice shelf geometry. Some studies indicate that ice shelf flow is only stable in certain configurations, with a "compressive arch" at the ice front keeping the ice flow in balance [*Doake et al.*, 1998; *Fürst et al.*, 2016]. Breaching of the compressive arch and runaway disintegration due to capsizing ice blocks [*MacAyeal et al.*, 2003] are possible in part due to ice shelf geometry. The Larsen B, for example, flowed freely in

a relatively wide embayment with few pinning points to stabilize the middle of the shelf. An ice shelf like the George VI is unlikely to be as vulnerable to a hydrofracture collapse mechanism because it is tightly confined by its embayment [*Scambos et al.*, 2000; *Munneke et al.*, 2014]. And although the Wilkins Ice Shelf has a widely saturated firn layer according to our index and many visible surface melt ponds, its large number of pinning points could help stabilize the shelf. The advanced position of the Larsen C Ice Shelf on the vulnerability index and its relatively unconfined geometry make it a critical shelf to monitor in the future.

7 Conclusions

The relationship between active microwave backscatter and annual melt days reveals important information about the evolution of firn on ice shelves. A transect from Greenland, where snow facies are well-documented, compared with field data, demonstrates that backscatter increases with increasing mean annual melt days until specular reflections due to large, continuous ice lenses in the firn layer at high melt days causes the backscatter to decrease. Although less obvious because of large amounts of scatter in the data, this relationship is nonetheless also present in the mean backscatter relationship plotted from all Antarctic ice shelves. The scatter in the raw data is primarily explained by differences in surface mass balance and its effects on the air content of the firn within areas that would be classified as the same snow facies. The consistency of the relationship across sensors and time periods allows us to use it as the basis for a vulnerability index, identifying which ice shelves are currently or may soon be vulnerable to hydrofracture. Several ice shelves on the Antarctic

Peninsula have areas of significantly ice-saturated firn layers. The likelihood of an ice shelf with an ice-saturated firn layer to collapse is modulated by the geometry of the ice shelf.

Acknowledgments

The completion of this study was supported by NASA through a NASA Earth Science Student Fellowship (NNX14AK82H). Greenland field data were collected with the support of a NASA Cryospheric Sciences award (NNX10AC76G). The authors declare no financial conflicts of interest in the completion of the manuscript. We would like to thank P. Holland for providing data and helpful comments in the preparation of this manuscript. All data are available through the Brigham Young University Microwave Earth Remote Sensing Laboratory Scatterometer Climate Record Pathfinder (http://www.scp.byu.edu) and by contacting the authors directly.

2.3. Supporting information

Text S1. Detailed description of backscatter data

All backscatter data were processed using the Scatterometer Image Reconstruction (SIR) algorithm [*Long et al.,* 1993], which uses multiple days of scatterometry data to create gridded, resolution-enhanced products. The algorithm assumes a linear model that relates the normalized radar cross-section, σ^o, which is measured in decibels, and the signal incidence angle:

$$\sigma^o = A + B(\theta - 40)$$

The model normalizes the incidence angle to 40˚. This creates two images: an A image, which contains the normalized backscatter values and has units of dB, and a B image, which represents the dependence of backscatter on incidence angle and has units of dB/˚. In this study, we utilize the A images.

When applied to ERS data, the algorithm combines passes from multiple orbits, which requires the assumption that backscatter is independent of azimuth. Products are provided on a 25 km grid, with an estimated effective resolution of 25-30 km. ERS images are obtained using a vertically polarized microwave signal. In this study, data between 1991 and 1996 were used, a time period that includes maximum coverage consistency in the available data. ERS-1 and -2 are both C-band scatterometers, with an operating wavelength of 5.7 cm.

C-band (5.7 cm) ASCAT data were obtained for both Greenland and Antarctica for the time period 2009-2013. These images also combine multiple passes, and are vertically polarized. Data are provided on 4.45 km grids, with an estimated resolution of 12-15 km. In this

study, ASCAT data were down-sampled to match the 25 km resolution of passive microwave melt days datasets.

Ku-band QuikSCAT data are available as a variety of products, including both vertical and horizontal polarization, and also combine multiple passes. Data are provided on a 4.45 km grid, with an effective resolution of 8-10 km. Because ten years of continuous data are available (2000-2009), we were able to use these data to create a relatively long-term record of average annual melt days following the methods of Hicks and Long (2011). Since the backscatter and melt days data are derived from the same dataset, we leave the data on its original 4.45 km grid.

Text S2. Derivation of ice content from ground-penetrating radar (GPR)

Figure 2.6 displays a 108 km segment of GPR data collected along an uphill transect in southwest Greenland's lower accumulation zone (black line in Figure 2.1a), and the total ice content detected in the GPR data at each point along the same transect. We collected the GPR data with an 800 MHz shielded Tx/Rx antenna from Malå Geosciences during a Spring 2013 field campaign. After data collection, we combined the raw radar traces to form a continuous transect, resampled traces for constant 1.5 meter spacing, pre-processed the data with standard de-wow and exponential gain filters, and used a 3x13 moving window to determine the local variance of each sample, as described in detail by Machguth et al. (2016). The GPR signal contains more scatter in regions of porous firn than in volumes of solid ice, and the log-transform of local signal variance shows distinct patterns that correlate very well with ice lenses in coincident cores. Log-variance values of 4.75 or less (blue regions of the GPR plot) correlate best with thick ice lenses retrieved from coincident cores (Machguth et al., 2016). The depth-

integrated ice content in the top 5 meters of GPR are plotted above the main transect. The resolution of the radar and the nature of the post-processing allow us to detect thick (>~ 0.8 m vertical) and continuous (> ~20 m horizontal) ice lenses, while thinner lenses (such as those seen in cores #3-6, Figure 2.1c) are typically unresolved in the GPR signal.

Text S3. Correlation methods between backscatter and surface mass balance

Figure 2.3 shows a separation in backscatter values between pixels in different surface mass balance categories. We further demonstrate an established relationship between accumulation rate and firn ice lens content (or, conversely, firn air content [*Pfeffer et al.*, 1991; *Braithwaite et al.*, 1994]) by providing statistical correlations between surface mass balance and backscatter within sub-datasets that have pixels with the same number of average annual melt days. The results are very similar to what would be achieved using multiple linear regression, but apply better to the non-linear nature of the backscatter/melt days relationship.

First, we grouped the backscatter and accumulation values that correspond to the pixels that experience each integer melt day value. For example, all pixels that experience a rounded 1 melt day per year are placed in a single category. Then, any array comprising less than thirty pixels was removed because these would not yield robust statistical results. This left 137 integer melt day categories.

Within each category, we performed a Spearman's correlation between backscatter and accumulation. Of the 137 categories, 100 had a significant negative correlation at the 95% confidence level, meaning that higher surface mass balance rates lead to lower backscatter values for pixels that experience approximately the same amount of melt each year.

Figure 2.6 | Supplementary figure: Ice lens detection through ground-penetrating radar. Ground-penetrating radar transect (bottom) showing percentage of large ice lenses (~>0.8 m, top). Radar transect location shown in main text Figure 2.1a; distance along transect goes from east to west.

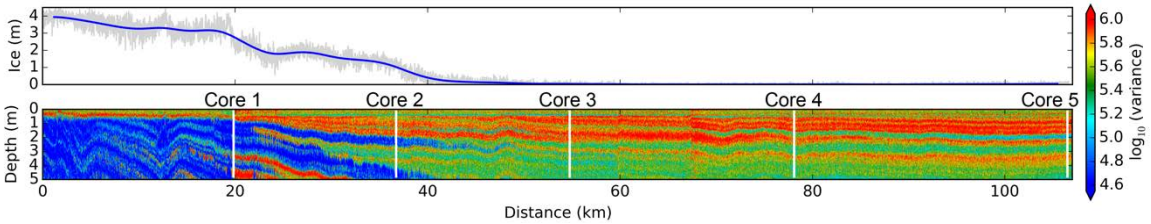

Figure 2.7 | Supplementary figure: QuikSCAT backscatter and melt days values averaged within the areas of Antarctic ice shelves.

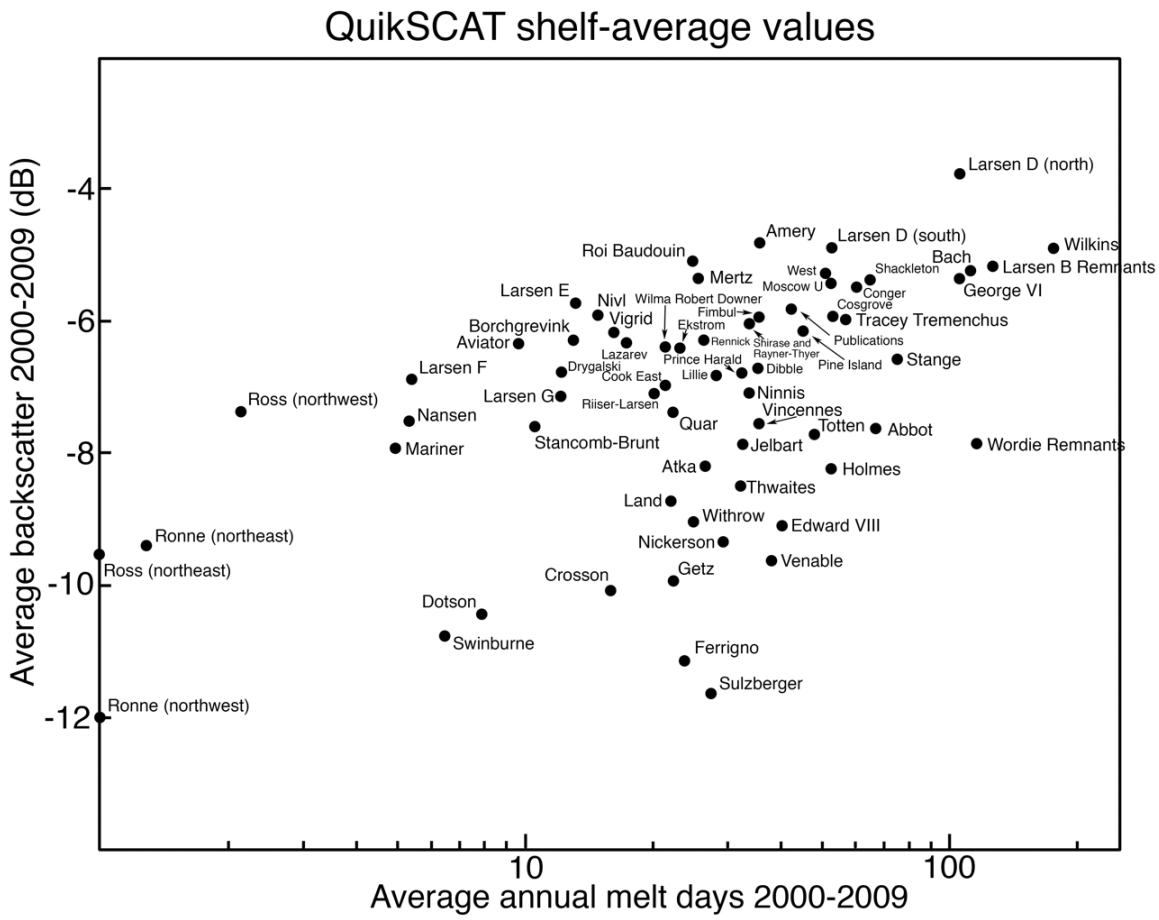

Figure 2.8 | Supplementary figure: Ice shelf regions.
Regions are averaged in Figure 2.7 and shown in Figures 2.9-2.16.

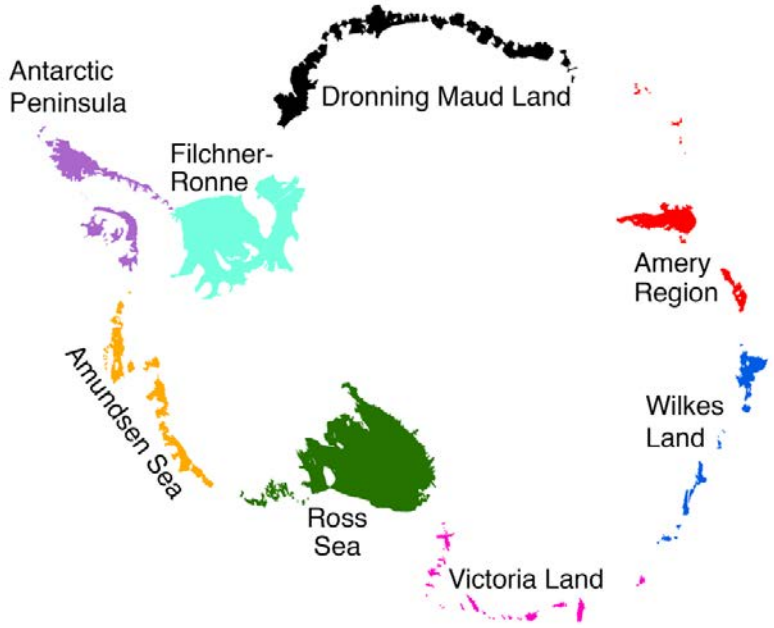

Figure 2.9 | Supplementary figure: QuikSCAT pixel-by-pixel backscatter and average annual melt days data for the Antarctic Peninsula region.
Raw data are shown in purple; data averaged within integer melt day bins shown in black.

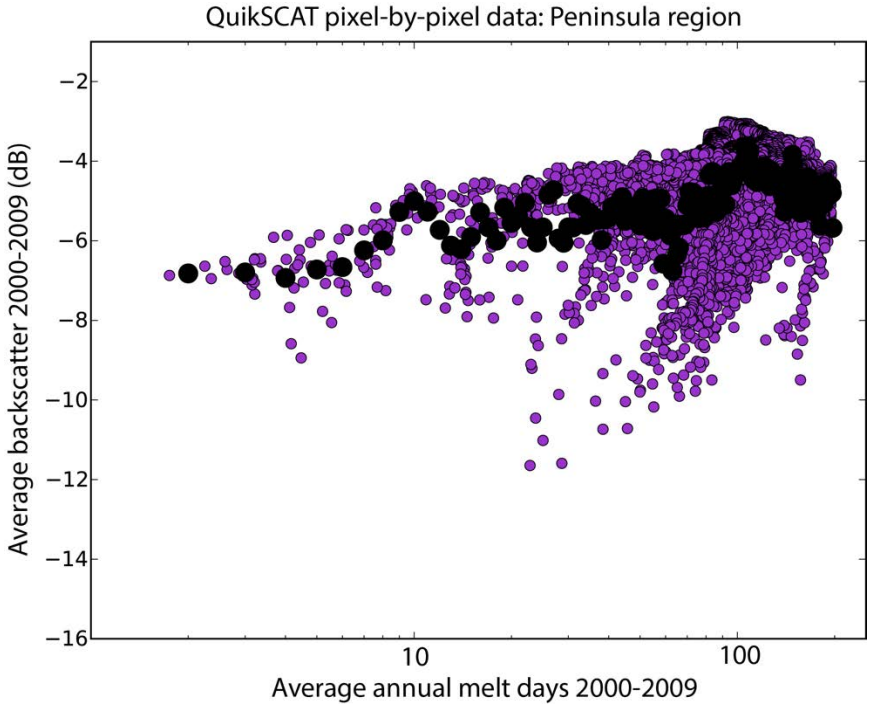

Figure 2.10 | Supplementary figure: QuikSCAT pixel-by-pixel backscatter and average annual melt days data for the Amundsen Sea region.
Raw data are shown in gold; data averaged within integer melt day bins shown in black.

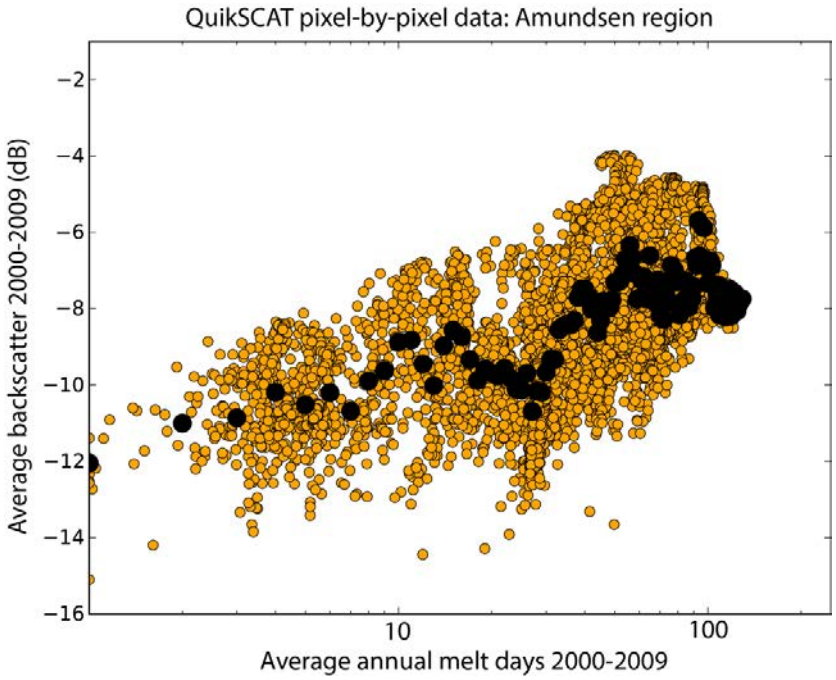

Figure 2.11 | Supplementary figure: QuikSCAT pixel-by-pixel backscatter and average annual melt days data for the Ross region.
Raw data are shown in green; data averaged within integer melt day bins shown in black.

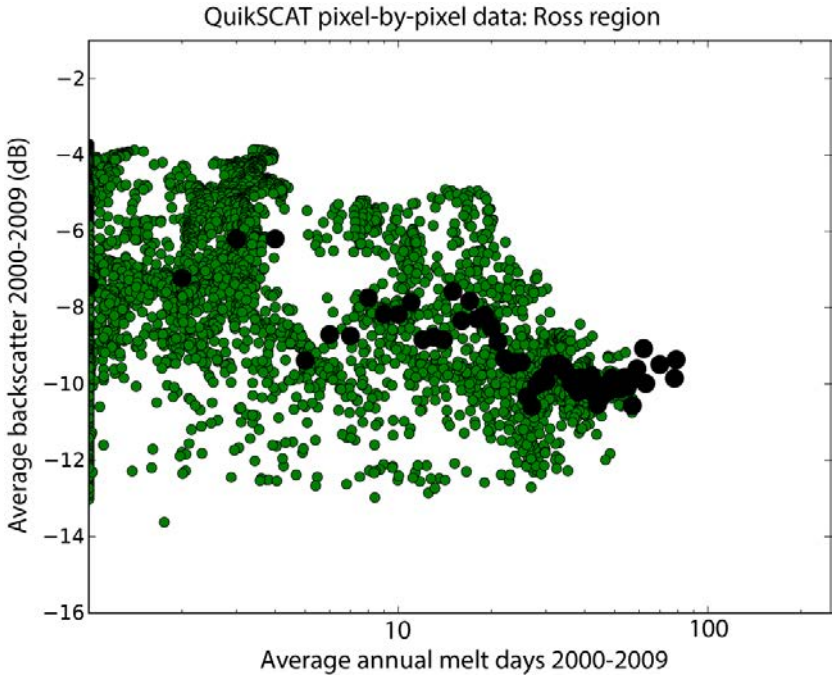

Figure 2.12 | Supplementary figure: QuikSCAT pixel-by-pixel backscatter and average annual melt days data for the Victoria Land region.
Raw data are shown in magenta; data averaged within integer melt day bins shown in black.

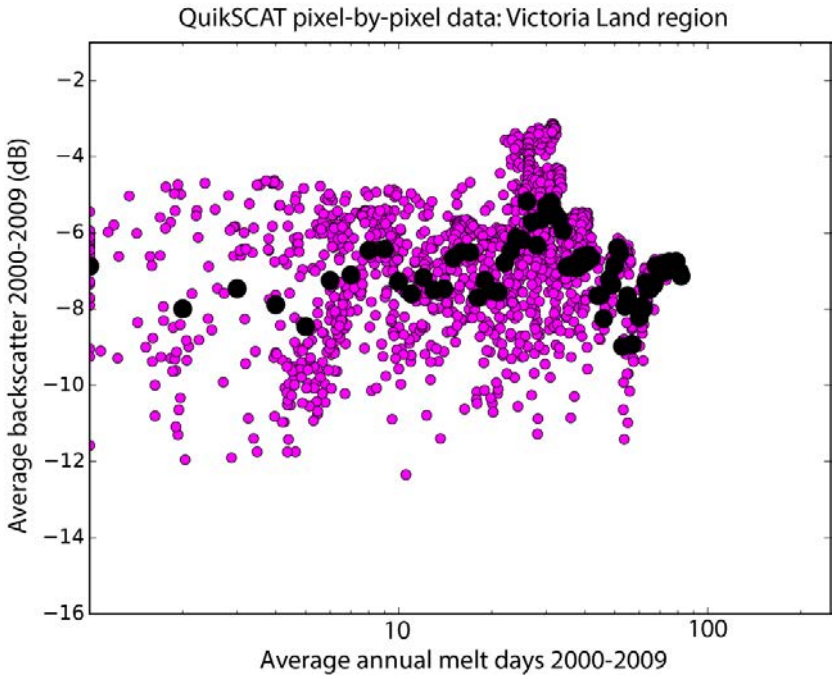

Figure 2.13 | Supplementary figure: QuikSCAT pixel-by-pixel backscatter and average annual melt days data for the Wilkes Land region.
Raw data are shown in blue; data averaged within integer melt day bins shown in black.

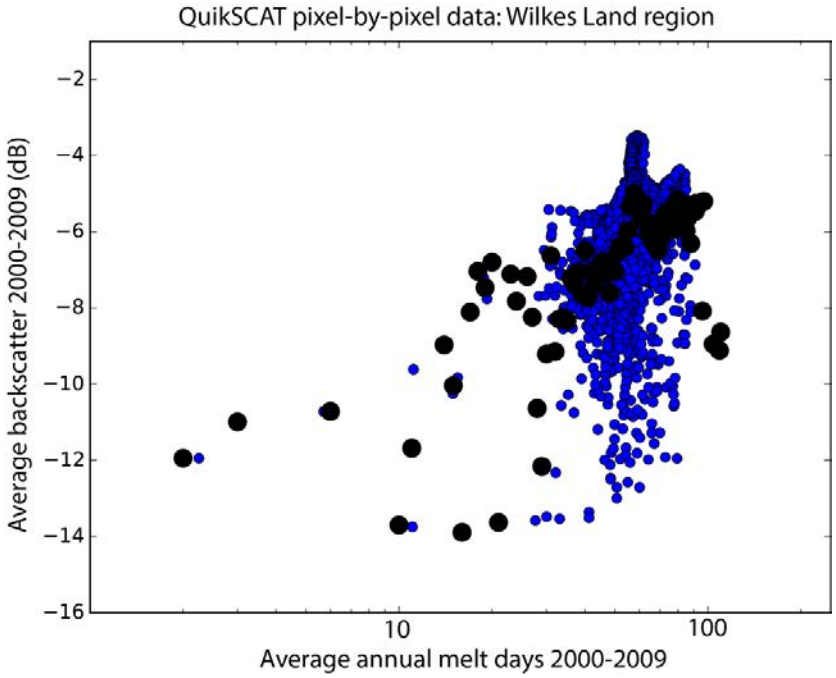

Figure 2.14 | Supplementary figure: QuikSCAT pixel-by-pixel backscatter and average annual melt days data for the Amery region.
Raw data are shown in red; data averaged within integer melt day bins shown in black.

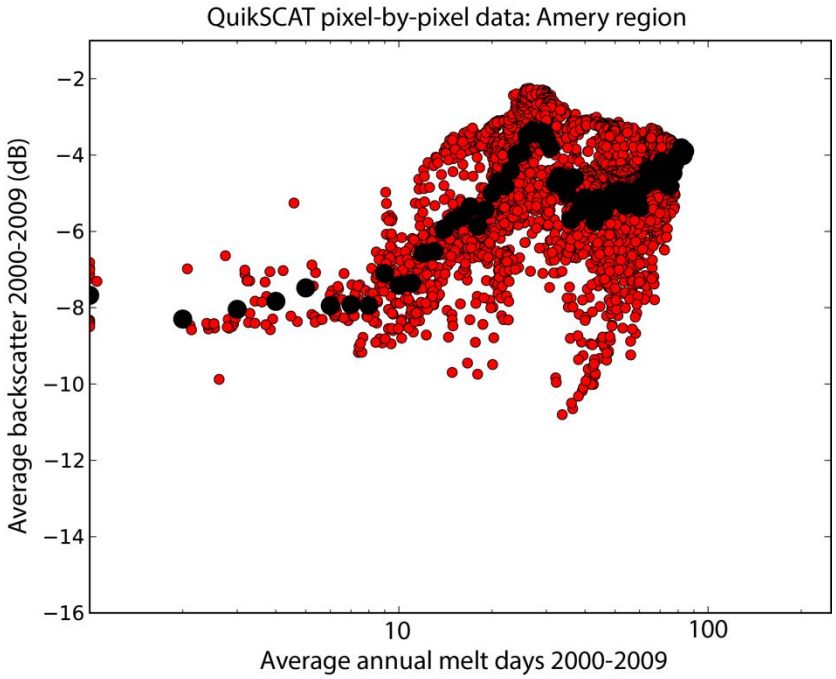

Figure 2.15 | Supplementary figure: QuikSCAT pixel-by-pixel backscatter and average annual melt days data for the Dronning Maud Land region.
Raw data are shown in grey; data averaged within integer melt day bins shown in black.

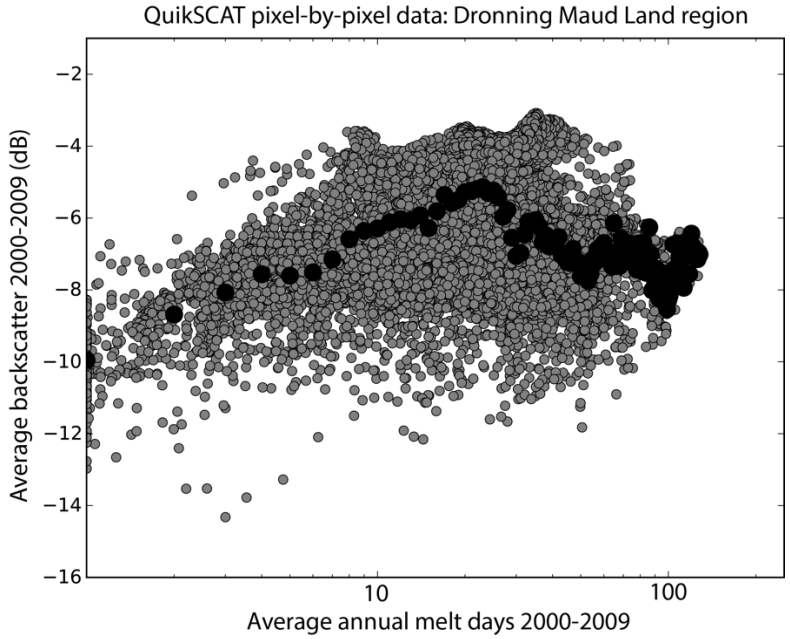

Figure 2.16 | Supplementary figure: QuikSCAT pixel-by-pixel backscatter and average annual melt days data for the Filchner-Ronne region.
Raw data are shown in cyan; data averaged within integer melt day bins shown in black.

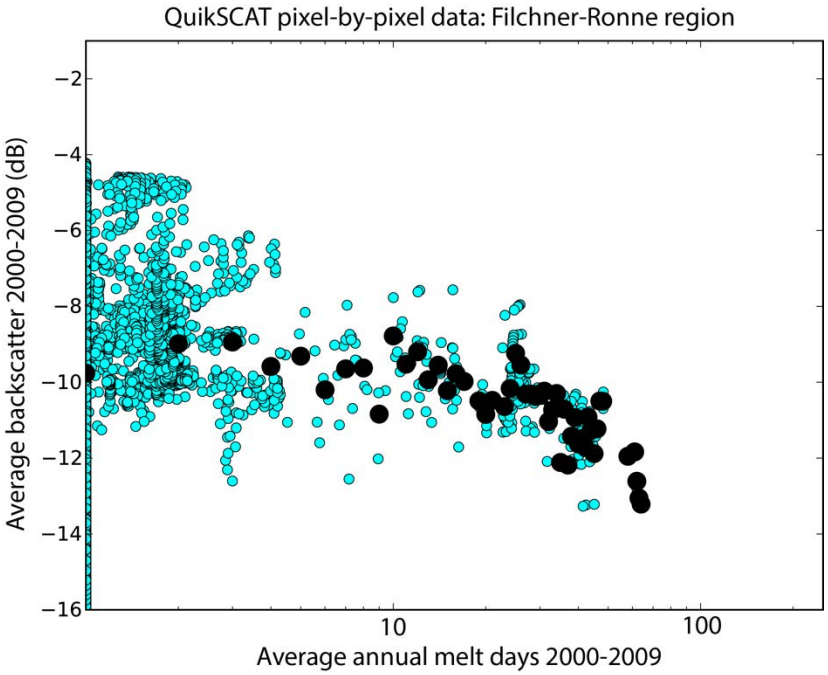

Figure 2.17 | Supplementary figure: QuikSCAT integer-average mass balance categories.
Categories as shown in Figure 2.3, with dotted lines representing the trajectories of the first principal component axes used to create the vulnerability index in Figure 2.4.

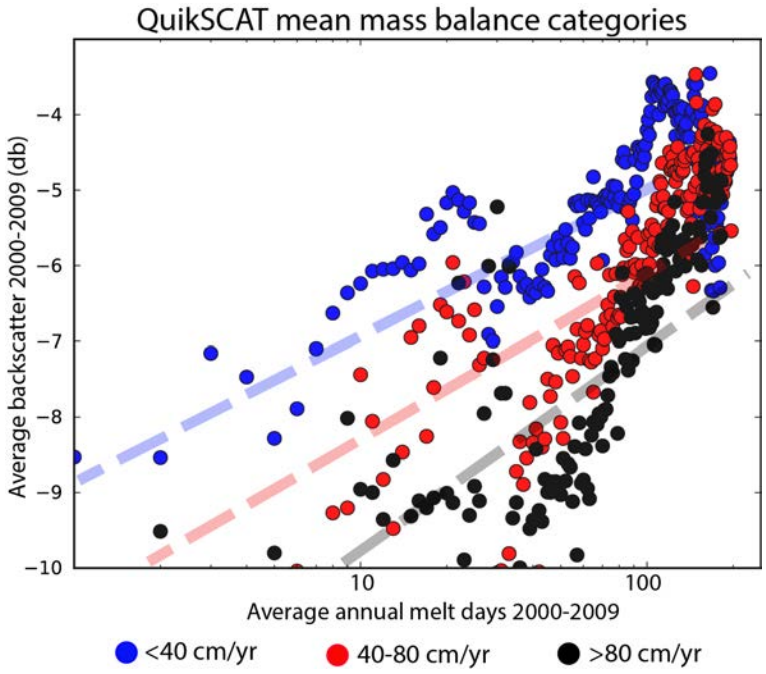

Figure 2.18 | Supplementary figure: ASCAT vulnerability index.
Vulnerability index created using the averaged ASCAT relationship shown in Figure 2.2d.

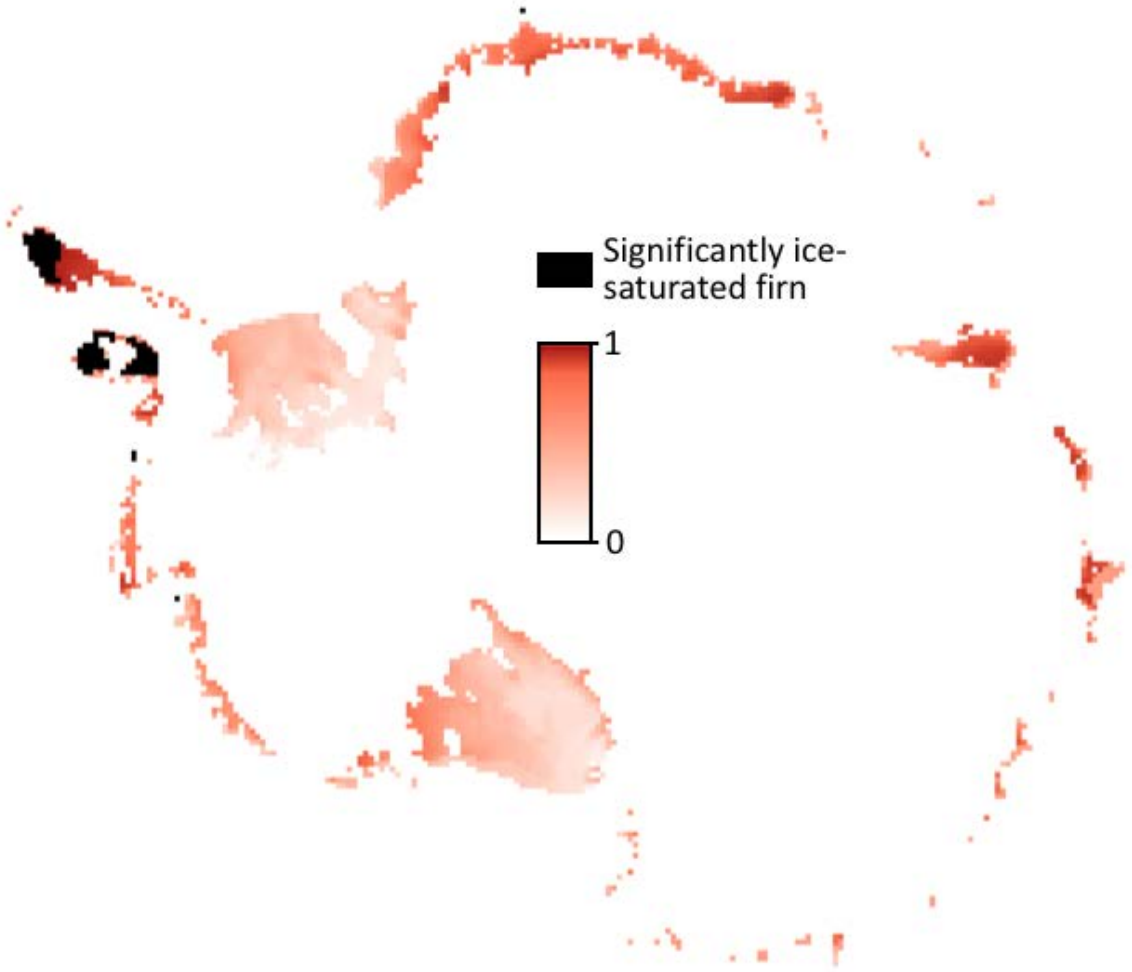

Chapter 3:

Basal channels and Antarctic Ice Shelf Stability

3.1: Introduction

Unlike surface melt, which contributes a relatively small fraction of ice shelf mass loss and is only significant on some ice shelves, basal melt has a strong impact on all floating ice. Though some ice shelf areas float in super-cooled water and experience accretion of marine ice, most areas thin as they interact with ocean water at or above the freezing point. Ice shelves often experience high melt rates near the grounding line, where they are thickest. Steady-state melt continues to thin any given ice column as it flows through an ice shelf, ultimately creating a typically concave profile with steep slopes near the grounding line and a more horizontal orientation near the ice edge (for a schematic, see Figure 3.8).

While ice shelves experience basal melt in steady-state, many ice shelves are experiencing unusually high rates of basal melt and are consequently thinning. Many important studies have documented various aspects of basal melting over the satellite record. Pritchard et al. (2012) produced a comprehensive map of ice shelf thinning using ICESat laser altimetry between 2003 and 2008, and linked patterns of thinning to the presence of warm ocean water. Rignot (2013) carried out a similar analysis, and used those data along with modeled surface mass balance and observed flow velocities to calculate basal melt rates (see sections 4.3 and

4.9). Depoorter et al. (2013) assessed ice fluxes to assess the partition in mass loss due to basal melt and iceberg calving on Antarctic ice shelves. Finally, Paolo et al. (2015) created the most comprehensive map of Antarctic ice shelf thinning available to date by reconciling measurements from altimeters spanning an 18-year record. All of these studies, along with more specific studies of individual shelves or regions, show that some ice shelves, particularly in the Amundsen Sea Region, are far from steady-state and are thinning at very high rates.

The large-scale assessments of basal melt discussed above have been undertaken recently and already utilize most of the relevant data currently available. These will play important roles in a future overall assessment of ice shelf stability. To advance understanding of the role of basal melt in the potential destabilization of ice shelves, we therefore chose to focus on a smaller-scale aspect that has received less attention at a comprehensive scale: the formation and development of basal channels.

3.2: Basal channels in the literature

Basal channels are features that are carved on the undersides of ice shelves. Because they float in water that is generally above the freezing point, ice shelves can experience significant amounts of basal melt. The relatively fresh meltwater that is produced is more buoyant than the surrounding saltwater, and therefore begins to rise along the ice shelf's sloping base, entraining ocean water as the plume ascends. Just as water moving down a slope on land has a tendency to channelize as it flows, the meltwater moving up the slope of the ice shelf base can also carve channel features. These "upside-down rivers" are common and are important factors in the stability of ice shelves. The remainder of this section will review the

current understanding of basal channels as represented in scientific literature. Sections 3.3 and 3.4 present an original study on basal channels, their characteristics and distribution, and their capacity for change.

3.2.1: Basal channel distribution

Basal channels are found beneath ice shelves in both Greenland and Antarctica. A high density of channels has been studied beneath the floating portion of Petermann Glacier (PG), a large outlet glacier in northwest Greenland that melts rapidly due to the presence of warm ocean water [*Rignot and Steffen*, 2008; *Dutrieux et al.*, 2014a]. The floating tongue of Pine Island Glacier (PIG) in West Antarctica, which is similarly affected by the presence of warm water, also exhibits abundant basal channels [*Bindschadler et al.*, 2011; *Mankoff et al.*, 2012; *Dutrieux et al.*, 2013; 2014a].

However, basal channel presence is not limited to shelves that are melting from below at such anomalously high rates. The Roi Baudouin Ice Shelf in East Antarctica, which experiences some warm water influence, exhibits an extensive network of channels [*Drews* 2015]. The nearby Fimbul Ice Shelf floats on ocean water that is very near the freezing point, but nonetheless has a complex array of small basal channels [*Langley et al.*, 2014]. Basal channels may also be formed by the release of subglacial meltwater, either in floods from draining subglacial lakes or as the result of a more consistent drainage pattern, with examples of these channels observed on the Ross, Filchner-Ronne, Roi Baudouin, and other small East Antarctic Ice Shelves [*Le Brocq et al.*, 2013; *Marsh et al.*, 2016]. Finally, it is also likely that

preexisting features, such as three prominent suture zones on the Amery Ice Shelf, may help channel water circulating beneath ice shelves [*Fricker et al.*, 2009].

Because significant attention has been focused on the basal channels of PG and PIG, this review will address those studies separately. Then basal channels that are found on ice shelves that are melting more slowly (the Roi Baudouin, Fimbul, and shelves with channels caused by subglacial meltwater release) are reviewed. The final section explores the ice and ocean models that have been used to date to understand the formation, evolution, and impacts of basal channels.

3.2.2: Basal channels beneath the Petermann Glacier ice shelf

Petermann Glacier (PG), on the northwest coast of Greenland, is one of the largest outlet glaciers in the northern part of the continent. It experiences extremely high melt rates, with 80% of ice mass lost to melt before reaching the terminus [*Rignot and Steffen*, 2008]. Current understanding of basal channels beneath PG is mainly derived from ground-based radar, GPS stakes, and instrumentation placed beneath the shelf through boreholes [*Rignot and Steffen*, 2008; *Dutrieux et al.*, 2014a].

Ground-based radar on the PG Ice Shelf reveals deep channels of approximately 1-2 km wide and 200-400 m deep spaced regularly on the underside of the ice shelf at ~5 km intervals. Channel alignment follows the ice flow direction very closely. Though channels originate near the grounding line, their cause is attributed solely to oceanic processes because channel features cannot be traced above the grounding line [*Rignot and Steffen,* 2008].

Analysis of ocean circulation beneath the shelf suggests that buoyant meltwater flows upwards along the channel sides, which are the areas of steepest slope. Water is then advected downstream through the center of the channel. The high water velocities at the channel apex may encourage vertical channel growth [*Rignot and Steffen,* 2008]. However, a higher-resolution analysis of melt rates within a PG channel shows that the highest melt rates are found on the channel edges, where the steepest slopes occur. The apex of the channel is protected from melt by a ~40 m-thick, relatively cold mixed layer [*Dutrieux et al.*, 2014a]. In addition, the channel sides are probably not smooth slopes. Instead, channels are formed as flat terraces with steep slopes in between. Melt rates tend to be relatively consistent on the terraces, and change discontinuously from one terrace to the next [*Dutrieux et al.*, 2014a].

It is hypothesized that the presence of these deep channels negatively affects the stability of PG. GPS measurements show that bending of the shelf around the basal channels is large enough to cause measurable ice divergence over channel keels and convergence over channel crests [*Dutrieux et al.*, 2014a]. Dutrieux et al. (2014) noted a crevasse ~100 m deep at the apex of one studied channel, a morphology that has also been observed on PIG and in numerical modeling studies [*Vaughan et al.*, 2012a]. Rignot and Steffen (2008) also note that the surfaces over some channels are currently only a few meters above sea level, and that seawater infiltrates to the surface at some locations. Only a small increase in melt rates or mechanical forcings would be needed to cause disintegration of the ice shelf along these channels.

3.2.3: Basal channels beneath the Pine Island Glacier ice shelf

The floating ice shelf at the terminus of Pine Island Glacier (PIG) in the Amundsen Sea sector of West Antarctica exhibits a similar density of basal channels to PG, and is evolving quickly. The presence of relatively warm Circumpolar Deep Water (CDW), which accesses the ice through deep troughs carved in the continental shelf, is causing rapid basal melt and grounding line retreat. It is possible that PIG is currently in an unstable configuration and may have begun a slow, irreversible retreat and disintegration, concurrent with other large glaciers in the Amundsen Sea region [*Joughin et al.*, 2014; *Rignot et al.*, 2014]

The CDW melting the ice shelf base is also responsible for the extensive network of large basal channels. Ice-penetrating airborne radar [*Vaughan et al.*, 2012a] shows 3-4 km wide, 100-200 m deep basal channels that roughly follow the ice flow direction. These channels have also been detected by inverting surface topography from SPIRIT DEMs [*Dutrieux et al.*, 2013] and using acoustic swath mapping from the underwater vehicle Autosub 3 [*Dutrieux et al.*, 2014a]. These channels are similar in size and morphology to those on PG, though they tend to be more sinuous. Vaughan et al. (2012) suggest that this may be due to the cavity geometry beneath the Pine Island Ice Shelf, which is wider than the cavity beneath the floating tongue of PG.

Channel morphology includes basal crevasses at the apices of melt channels, similar to those observed on PG [*Vaughan et al.*, 2012a; *Dutrieux et al.*, 2014a]. These basal crevasses are accompanied by swarms surface crevasses between channel crests, which are formed due to bending over the water-filled channel voids [*Vaughan et al.*, 2012a]. Dutrieux et al. (2013) also noticed deviation of velocity patterns on the ice shelf due to the topography induced by basal

channel presence, and PIG basal channels also exhibit terraces of the type described on PG [*Dutrieux et al.*, 2014a].

Several datasets indicate that warm water is being funneled through these basal channels. Stanton et al. (2013) were able to place oceanographic instruments within the channels by drilling through the Pine Island Ice Shelf. Their observations show very high melt rates within the channels, with much less melt outside the channels. Payne et al. (2007) used a plume model to predict areas where warm water was likely to emerge from beneath the shelf. Their model predicted three main outflow locations. Mankoff et al. (2012) and Bindschadler et al. (2011) noted channels and polynyas corresponding to each of these outflow locations. The polynyas, which are small areas of persistent open water at the shelf-edge terminus of a basal channel, are visible in satellite imagery when fast ice is present. Oceanographic data show that the polynyas are characterized by the presence of modified CDW, suggesting that the basal channels funnel a mixture of CDW and shelf meltwater to the ice shelf front [*Mankoff et al.*, 2012]. The heat and meltwater content of the channeled water is sufficient for it to rise to the surface at the shelf front, preventing fast ice formation [*Bindschadler et al.*, 2011]. In addition, the signature of warm water at these outflow locations is sometimes visible in Landsat thermal infrared imagery [*Bindschadler et al.*, 2011; *Mankoff et al.*, 2012].

Thus far, this section has focused on the large, sinuous channels that roughly follow the ice flow direction. However, PIG has a second set of features that have sometimes been identified as smaller versions of the large basal channels on the central ice tongue (see Figure 3.6). Near the southern edge of the shelf, a line of short features 1-2 km wide and 50 m deep are aligned obliquely to the ice flow direction [*Dutrieux et al.*, 2013]. These features were

closely examined by Bindschadler et al. (2013). The features form roughly parallel to the grounding line, and their amplitudes correlate positively with ocean heat transport to the grounding line. The authors suggest that a feedback exists between increased melt at the grounding line and shelf acceleration or extension, which leads to the formation of basal crevasses parallel to the grounding line. These crevasses are then enlarged by the anomalously high ocean heat content. Thus, it is possible that these features are not channelizing melt like the longitudinal channels on Pine Island and Peterman Glaciers, but are simply crevasses greatly enlarged by ocean melt. In contrast, the longitudinal channels are believed to be initiated by irregularities at the grounding line and/or are due to subglacial melt on grounded ice [*Dutrieux et al.*, 2013], and clearly channelize warm water as discussed above.

3.2.4: Basal channels in other locations

The basal channels found beneath PG and PIG are both extreme examples, where very large channels completely dominate the basal topography of the ice shelves. These areas are anomalous because they are exposed to exceptionally warm ocean waters compared to the temperatures experienced by most ice shelves in Greenland and Antarctica. However, basal channels also form in areas that are not so anomalous.

Some warm water influences the Roi Baudouin Ice Shelf in Dronning Maud Land, East Antarctica, but basal melt rates are significantly lower than those on PG or PIG [*Rignot et al.*, 2004; *Pritchard et al.*, 2012; *Paolo et al.*, 2015]. However, basal channels have been observed in surface morphology using satellite imagery and in basal topography using ice-penetrating radar. Many of these channels start near the grounding line and extend roughly in the direction of ice

flow. Though they are large enough to see easily in satellite imagery, and visibly affect the ice flow patterns around them, bridging stresses prevent them from attaining complete hydrostatic equilibrium. Drews (2015) studied these channels through GPS, satellite, and ice-penetrating radar observations, as well as numerical modeling, and suggest that they could be caused by the extension of grounding line irregularities into basal channels through the action of warm water. However, they may also be caused in part by the influence of subglacial meltwater from grounded ice [*Le Brocq et al.*, 2013].

The formation of channels on the nearby Fimbul Ice Shelf is also attributed to the action of the ocean, but in a very different environment. Ocean temperatures beneath the Fimbul Ice Shelf are very near the local freezing point. However, ground-penetrating radar reveals an extensive network of narrow channels (300-500 m wide and 50 m high) [*Langley et al.*, 2014]. These channels are much smaller than those reported on the PG, PIG, and Roi Baudouin Ice Shelves, though they still exhibit the predicted crevasse pattern (basal crevasses at channel apices, surface crevasses between channels) that has been observed on other shelves [*Vaughan et al.*, 2012a]. They are only faintly visible in satellite imagery of the surface morphology, as bridging stresses play a significant role in keeping them from achieving complete hydrostatic equilibrium. In addition, prevailing winds cause preferential snow accumulation within the channels that also makes them less visible on the surface. However, this does make them detectable to satellites such as Terra SAR-X, which are sensitive to accumulation rates. The presence of basal channels on the Fimbul Ice Shelf suggest that these features may be much more widespread than previously believed, even if they are not easily visible at the surface. This

has important implications for understanding small-scale ice-ocean interactions beneath ice shelves.

The formation of basal melt channels has also been attributed to the release of subglacial meltwater [*Le Brocq et al.*, 2013; *Marsh et al.*, 2016]. Like the channels on the Fimbul Ice Shelf, these channels have been identified on shelves that are not strongly influenced by warm water, such as on the Ross and the Filchner-Ronne, as well as many other shelves. A subglacially-sourced meltwater origin of the channels is suspected because channel features are frequently found to begin precisely at the locations of modeled subglacial hydrologic outflow [*Le Brocq et al.,* 2009]. The theory is that the buoyant meltwater released at the base of the shelf rises along the shelf slope, entraining relatively warm ocean water. The buoyant plume is also turbulent, which increases the rate of heat transfer from the ocean water to the ice and melts a channel. These channels typically follow the ice flow direction very closely, though abrupt shifts in channel path are interpreted to represent reorganizations of subglacial hydrology. It is likely that other outflow events, such as the drainage of subglacial lakes, play a role in the genesis of some of these features [*Marsh et al.*, 2016]. It is also likely that some channels are affected by both subglacial meltwater and ice-ocean interaction. For example, some of the channels on the Roi Baudouin Ice Shelf, modeled in Drews et al. (2015) as caused by ocean melt, also correspond to locations of subglacial hydrologic outflow. Channels driven by a sub-glacial meltwater origin can experience extremely high melt rates, such as those measured using phase-sensitive radar on the Ross Ice Shelf [*Marsh et al.*, 2016].

Basal channel origin from grounding line features has been suggested in many contexts. Basal channels may form at the grounding line as the result of subglacial hydrologic outflow [*Le*

Brocq et al., 2013]. They may also be the result of the amplification of grounding line irregularities [*Gladish et al.*, 2012]. In addition, basal channels may form in a location because a basal groove is already present. The Amery Ice Shelf, which is the third largest ice shelf in Antarctica, is fed by input from several distinct glaciers and regions. At suture zones between these regions, ice thickness is not as large as surrounding ice. It is likely that features such as these are also acting to channelize meltwater from beneath the ice shelf, regardless of additional forcings that could cause basal channel formation [*Fricker et al.*, 2009].

3.2.5: Basal channel modeling

Modeling studies that address basal channels seek to answer many questions. For example, how do these channels form and dissipate? Do they alter ice flow patterns? Can they affect the stability of floating ice shelves? These questions are addressed using a range of model types and approaches.

Drews (2015) carried out a modeling study specifically designed to understand ice dynamics related to the formation of basal channels. For this reason, the model used is a three-dimensional, transient, full-Stokes model, which provides a lot of detail in the results. The model confirms that melting is a feasible formation mechanism for basal channels. However, channels can persist for many tens of kilometers downstream if melting is not sustained, so the presence of a morphological channel feature does not guarantee actively high melt rates. After channel formation, transverse ice flow begins to fill in the channel, which means that a channel can disappear in the absence of basal ice accretion. The impacts on the local flow field also mean that it may be possible to identify melt channels using satellite-derived velocity fields.

The model also demonstrates scenarios where bridging stresses over narrow channels can prevent complete hydrostatic equilibrium.

Other studies use more simplified ice models in order to couple ocean models and gain a greater understanding of oceanic influence on basal channel evolution. Gladish et al. (2012) used coupled a buoyancy-driven mixed-layer model with the Glimmer Community Ice Sheet Model to investigate the formation of basal channels and their impact on ice shelf basal melt rates by using an idealized version of the PG ice shelf in Greenland. Their model shows that irregularities in basal topography caused by bedrock bumps near the grounding line are enlarged by oceanic melting. The addition of subglacial meltwater discharge at the grounding line deepens the channels that are formed. The melt rates are also sensitive to ocean temperatures. Their model shows that an ice shelf with basal channels has a lower overall melt rate than a shelf without channels, suggesting that basal channels can actually help protect a shelf from destabilization due to basal melt.

However, the ocean model used by Gladish et al. (2012) was simple enough that the causes of the reduced melt could not be pinpointed. Millgate et al. (2013) therefore followed this study by using the MIT General Circulation Model, which is a full, three-dimensional ocean model capable of identifying these mechanisms. Again, the study used an idealized geometry for PG. Rather than couple the ocean model to an ice flow model, the authors simply created a static ice shelf morphology with varying numbers of basal channels. Without any basal channels, sub-ice-shelf circulation is dominated by a single geostrophic boundary current, with the strongest flow on the right-hand side of the embayment, consistent with Coriolis influences. The strongest melt occurs where the strongest currents form.

When large channels are introduced, individual geostrophic currents form within each channel. Between the channels are large regions (keels) where there is very little water flow. The introduction of these “no-flow” regions lowers overall melt rates. The authors find that melt rates decline as the number of channels increase, though the melt rates plateau when more than four channels are present. There is a lower sensitivity when many narrow channels are involved, because the circulation shifts to an overturning pattern. The authors agree with the conclusions offered by Gladish et al. (2012), which state that the presence of basal channels lowers melt rates overall. Millgate et al. (2013) also note that the shelf may be further preserved by the relative distribution of melt across the base of the shelf, rather than concentrating melting in a single band at the right-hand margin of the embayment when a single geostrophic current is present without basal channel influence.

Sergienko (2013) created an idealized model of PIG using a shallow ice shelf model fully coupled to a two-layer, modified plume model. Payne et al. (2007) had previously modeled outflow from beneath PIG in three distinct regions. The Sergienko (2013) model also produces basal channels, but the idealized geometry does not allow for exact comparison.

The Sergienko (2013) model supports the possibility that channels can be initiated due to irregularities in topography at the grounding line, but also notes that the initial perturbations were not necessarily preserved downstream. The model also offers another basal channel formation mechanism: spontaneous formation due to transverse variations in ice shelf thickness. If the ice shelf base slopes transversely, plumes will accelerate along the steepest parts, which causes enhanced melt at these locations. The enhanced melt steepens the slopes, creating a positive feedback. Once a basal channel forms, the stresses due to its presence

deform other parts of the shelf, and the resulting undulations may themselves become basal channels. The author also observes morphological effects of Coriolis, which make the left sides of channels much steeper in the southern hemisphere because melting on this side is enhanced by Coriolis-induced plume acceleration. The spontaneous formation of large, longitudinal channels was accompanied by the formation of smaller channels oblique to the ice flow direction, similar to those noted on PIG, which offers an alternative explanation of their formation to that put forward by Bindschadler et al. (2011).

Basal curvature near shelf margins is controlled by the amount of shearing that occurs along shelf boundaries. Because there is frequently curvature here, channels have a tendency to form at lateral boundaries. Modeled plume fluxes near margins are almost two orders of magnitude greater than the areal average. Stresses over all channels are elevated, but stresses over channels at the lateral boundaries are, by order of magnitude, large enough to cause shelf fracture [*Sergienko*, 2013].

Vaughan et al. (2012) were also interested in stress magnitudes over basal channels on PIG. They used a simple finite element model on a 2-dimensional, vertical ice shelf section. The authors instantaneously added basal channels similar in size to those found on PIG. Subsequent hydrostatic relaxation of the shelf raised stresses on the shelf base over the channels and on the shelf surface adjacent to the channels enough to cause fracture. This fracture pattern has been observed on PIG [*Vaughan et al.*, 2012a; *Dutrieux et al.*, 2014a], while the basal crevasses at channel apices have also been seen on PG [*Dutrieux et al.*, 2014a] and the Fimbul Ice Shelf [*Langley et al.*, 2014]. Thus, the work of Sergienko (2013) and Vaughan et al. (2012) support the idea that basal channels can weaken an ice shelf.

These varied models offer an incomplete and sometimes conflicting picture of the various features that characterize basal channels. In particular, the models disagree as to whether or not basal channels are likely to weaken an ice shelf or help preserve it from ocean-melt-induced disintegration. Studies that model melt indicate that the presence of basal channels reduces overall melt rates and preserve ice shelves [*Gladish et al.*, 2012; *Millgate et al.*, 2013b]. Studies that can resolve stresses within the ice show that the presence of basal channels can raise stresses high enough to cause ice shelf fracture, weakening the shelf [*Vaughan et al.*, 2012a; *Sergienko*, 2013]. Further modeling and observations are required to determine which of these effects is more important to the long-term evolution of ice shelves and basal channels in Greenland and Antarctica.

3.3: Article published in Nature Geoscience, March 2016

The current section, along with section 3.4, comprise an observational study that provides further evidence that some basal channels weaken ice shelves, as well as presenting a map of basal channel locations and detailed discussion of basal channel characteristics. The paper was published in Nature Geoscience in March 2016. The current section includes the main text of the paper as it appeared in publication. Section 3.4 presents most of the supplementary information that was published alongside the paper. A series of detailed figures of polynyas and an extensive data table documenting channel statistics, originally printed with the supplementary information, are provided in the Appendix to Chapter 3 (hereafter Appendix 3). The polynya figures are also relevant to section 5.2, which describes a proposed study on details of their sizes, locations, and temporal evolution.

Statement of contribution: K. E. Alley led the planning, analysis, and writing of the following paper, including data collection and image analysis, statistical procedures, and the creation of figures. M. R. Siegfried and H. A. Fricker provided the corrected ICESat data presented in Figure 3; K. E. Alley carried out additional error analysis on these data. All authors contributed to the writing and editing of the paper.

Impacts of warm water on Antarctic ice shelf stability through basal channel formation

Karen E. Alley[1*], Ted A. Scambos[1], Matthew R. Siegfried[2], Helen Amanda Fricker[2]

[1] National Snow and Ice Data Center, University of Colorado Boulder, Boulder, CO

[2] Scripps Institution of Oceanography, University of California San Diego, La Jolla, CA

Antarctica's ice shelves provide resistance to the flow of grounded ice towards the ocean. If this resistance is decreased due to ice shelf thinning or disintegration [*Scambos et al.,* 2003*]*, acceleration of grounded ice can occur, increasing rates of sea level rise. Loss of ice shelf mass is accelerating, especially in West Antarctica where warm seawater is reaching ocean cavities beneath ice shelves [*Paolo et al.*, 2015]. Here we use satellite imagery, airborne ice-penetrating radar, and satellite laser altimetry spanning the period from 2002 to 2014 to map extensive basal channels in the ice shelves surrounding Antarctica. The highest density of basal channels is found in West Antarctic ice shelves. Within the channels, warm water flows northward, eroding the ice shelf base and driving channel evolution on annual to decadal timescales. Our observations show that basal channels are associated with the

development of new zones of crevassing, suggesting that these channels may cause ice fracture. We conclude that basal channels can form and grow quickly due to warm ocean water intrusion, and that they can structurally weaken ice shelves, potentially leading to rapid ice shelf loss in some areas.

Basal channels in floating ice shelves have been observed in both Greenland and Antarctica, with varying attributed origins. Channels dominate the basal topography of several ice shelves influenced by warm ocean water, including ice shelves in northwest Greenland [*Rignot and Steffen*, 2008; *Dutrieux et al.*, 2014b], the Amundsen Sea sector, West Antarctica [*Bindschadler et al.*, 2011; *Mankoff et al.*, 2012; *Vaughan et al.*, 2012b; *Dutrieux et al.*, 2013; 2014b], and Queen Maud Land, East Antarctica [*Drews*, 2015]. However, small channels have also been observed on the Fimbul Ice Shelf, where ocean temperatures are near the freezing point [*Langley et al.*, 2014]. In addition, channel formation at some locations has been associated with the release of subglacial meltwater [*Le Brocq et al.*, 2013; *Marsh et al.*, 2016], and with suture zones on the Amery Ice Shelf [*Fricker et al.*, 2009].

We have mapped and documented characteristics of basal channels in ice shelves around Antarctica (Figure 3.1A) using satellite imagery from the Moderate Resolution Imaging Spectroradiometer (MODIS) Mosaics of Antarctica [*Scambos et al.*, 2007] and Landsat 8. Identifying basal channels using surface features visible in satellite imagery requires that the ice shelf surface over the channel is near hydrostatic equilibrium, creating a surface depression of at least a few meters; therefore, our method captures only relatively large channels, typically ~1-5 km across and incised ~5-25 m in the surface (~50-250 m in the ice shelf base). For channels surveyed by NASA's Operation IceBridge, we use ice thickness data from radio-echo

sounding (RES) to show that the observed surface features correspond to channels deeply incised in the ice-shelf base (Supplementary Section 3.4.1).

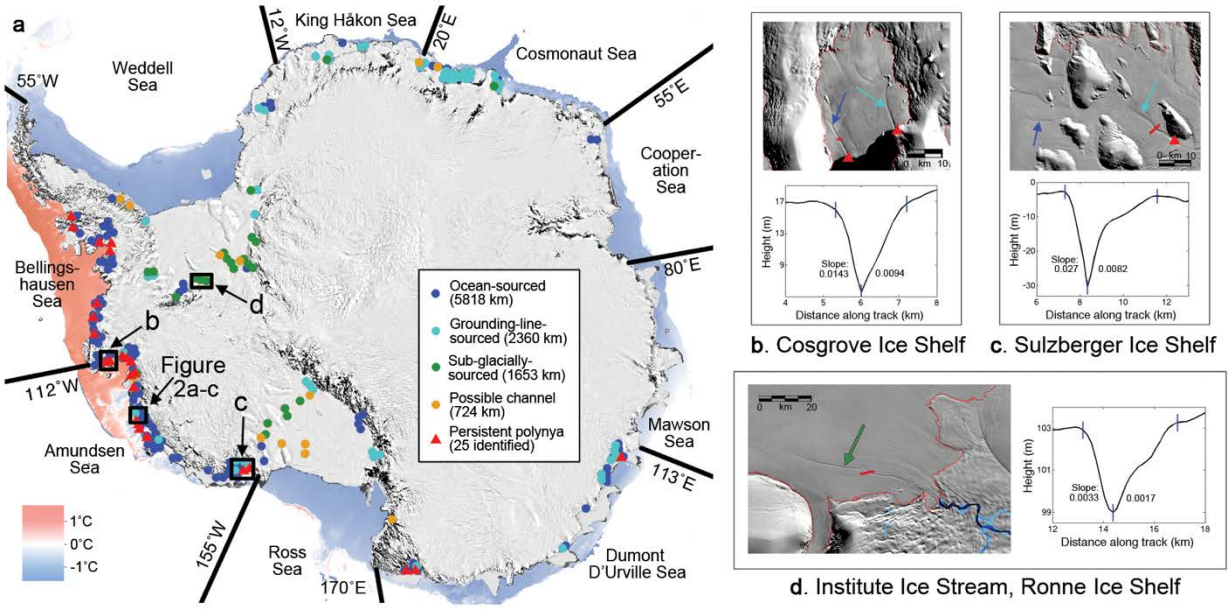

Figure 3.1 | Distribution and examples of basal channel types around the Antarctic continent.
a, Distribution of basal channels. Each dot represents 50 km of channel length. Red triangles mark persistent polynyas. Background is the MOA 2009 image. Colour fringe shows seafloor ocean temperatures for depths shallower than 1,500 m [*Schmidtko et al.*, 2014]. **b**–**d**, Arrows mark examples of channel types, with colours matching the legend in **a**. MOA 2009 grounding line shown in red. Modelled hydrologic outflow [*Brocq et al.*, 2009] shown in blue in **d**. Straight red line segments across channels are ICESat profiles shown in corresponding graphs. Blue vertical lines on graphs show limits of slope calculations.

Our analysis yielded three channel categories (a to c) based on whether the channels intersect the grounding line, and whether they are coincident with modeled subglacial outflow [*Brocq et al.*, 2009]: (a) "ocean-sourced" channels (Figure 3.1B and C) do not intersect the grounding line; (b) "subglacially-sourced" channels (Figure 3.1D) begin immediately at the grounding line at a location where subglacial meltwater drainage is predicted; (c) "grounding-line-sourced" channels (Figure 3.1B and C) intersect the grounding line but do not correspond

to a modeled subglacial outflow point. A fourth category, (d) “possible channels”, includes features that could not be confirmed as channels given the available data (Supplementary Section 3.4.1).

Each channel category has a different formation mechanism (Supplementary Section 3.4.2). Subglacially-sourced channels are formed by buoyant freshwater outflow from beneath the ice sheet, which carves channels through ocean-water entrainment and turbulent heat transfer [*Le Brocq et al.*, 2013; *Marsh et al.*, 2016]. These channels are typically deeply incised at the grounding line and dissipate along flow. Because ocean-sourced and grounding-line-sourced channels do not correspond to locations of subglacial outflow, we assume that oceanic processes control their formation. These two channel types share a typical morphology that deepens along flow.

Satellite laser altimetry profiles from the Ice, Cloud and land Elevation (ICESat) mission show that all three channel categories exhibit a common surface cross-sectional morphology, with steeper slopes on the western side (Figure 3.1 B-D, Figure 3.2 D). We infer that this is related to northward water flow in the channels and the Coriolis effect: enhanced melt occurs on the western flanks as a result of faster flow there, as predicted by numerical models [*Sergienko*, 2013]. This suggests that all three channel types are caused by basal melting from incision by currents flowing seaward; that flow within the channels is fast enough to be significantly deflected by the acting influence of Coriolis; and that fast flow concentrated on the western flanks leads to deeper or more rapid incision on that side.

To further investigate the origins of ocean- and grounding-line-sourced channels, we carried out statistical analyses using a “basal channel density” parameter, defined as the total

basal channel length over the corresponding ice shelf area (Supplementary Section 3.4.3). We found a significant positive correlation between basal channel density and basal melt rate [*Rignot et al.*, 2013] for all ice shelves ($p<0.01$), suggesting that warm water plays an important role in the formation of these large features. The Amundsen/Bellingshausen Sea (AB) sector, a region with generally high basal-melt rates due to Circumpolar Deep Water (CDW) presence [*Pritchard et al.*, 2012], has a statistically higher density of basal channels than any other sector (Supplementary Section 3.4.3). Within this sector, there was also a significant positive correlation between basal channel density and maximum grounding line depth (calculated from the MOA 2009 grounding line and Bedmap2 [*Fretwell et al.*, 2012], $p<0.05$). This correlation implies that CDW is the water mass creating these basal channels, as it is a mid-depth ocean water mass [*Jacobs et al.*, 2012] that mainly affects ice shelves with deep ice drafts. Because warm ocean water can flow through previously-formed subglacially-sourced channels (Supplementary Section 3.4.3), it was not possible to isolate the channel categories in statistical analyses; however, we note that only 57 km of the 4,250 km of basal channels in the AB region are subglacially-sourced and 254 km are grounding-line-sourced, leading us to conclude that the origin of ocean-sourced channels in this region is most strongly linked to CDW.

Formation of basal channels by warm water is also supported by the coincidence of ocean-sourced and grounding-line-sourced channels with persistent small ($<\sim10$ km^2) ice-front polynyas within areas of sea ice anchored to ice shelf fronts ("fast ice"; Supplementary Section 3.4.4). Previous studies have shown the presence of anomalously warm ocean surface water within these polynyas [*Bindschadler et al.*, 2011; *Mankoff et al.*, 2012], suggesting that a buoyant plume of warm water exits these basal channels, supplying sufficient heat to locally

prevent formation of fast ice. We identified 25 polynyas of this type around Antarctica: 22 were collocated with the termini of ocean-sourced channels, one was collocated with a grounding-line-sourced channel, and only two were not associated with any detectable channels. Twenty-two of the polynyas were in the AB sector. Two of the three polynyas outside the AB sector were in front of the Lillie Ice Shelf, which had the second highest channel density of all ice shelf regions, and one was in front of the Totten Ice Shelf, in a region with the highest channel density of any ice shelf region (Supplementary Section 3.4.3).

Although our statistical correlations and polynya presence firmly link both the ocean-sourced and grounding-line-sourced channels to oceanic forcings, they do not explain why grounding-line-sourced channels initiate at the grounding line and ocean-sourced channels initiate offshore. Several processes may contribute to determining the locations where channels form (Supplementary Section 3.4.2). One possible differentiating forcing is the degree of interaction with warm water. It is likely that ocean-sourced channels form on ice shelves with vigorous interactions with warm water, because they have a deep ice draft and/or a thick sub-ice-shelf layer of warm water. Conversely, grounding-line-sourced channels may form only on ice shelves that have weak interactions with warm water, due to either a shallow ice draft at the grounding line, or a thin layer of warm water near the seabed that migrates to the grounding line due to a shoreward slope of the bed. Another controlling factor is the size of any homogeneous mixed zone, formed by tidal processes, which shields the grounding line ice from direct interaction with warm intruded water [*Holland*, 2008]. More observations of sub-ice-shelf bathymetry and grounding-line-proximal oceanic properties are required to draw positive conclusions regarding these formation mechanisms.

Our observations also show that basal channels are capable of rapid change. Several channels on the Getz Ice Shelf have extended upstream in recent years, with a maximum measured growth of ~20 km towards the grounding line between 1986 and 2014 (Figure 3.2, Supplementary Section 3.4.5). We used repeated elevation profiles along ICESat tracks to infer melt rates for 2004-2007 in the most rapidly changing channel (Methods, Supplementary Section 5). The highest incision rates (8.8-14.7 m/yr) were found near the head of the channel, where channel extension is actively occurring (Figure 3.2d).

Ocean-sourced and grounding-line sourced channels tend to migrate towards edges of islands and peninsulas that confine an ice shelf. This relationship could result from a positive feedback caused by ice topography, which has been shown through numerical modelling [*Sergienko*, 2013] (Supplementary Section 3.4.6). Ice shelves are thinner close to shear margins [*Griggs and Bamber*, 2011; *Sergienko*, 2013], and the basal slope guides and accelerates density-driven water plumes toward thinner ice along islands and peninsulas [*Sergienko*, 2013]. This enhances melt along the shear margins, initiating a positive feedback cycle that further thins the marginal region.

Previous studies have not agreed on whether basal channels stabilize or weaken an ice shelf: some suggest that an abundance of basal channels can reduce overall melt rates [*Gladish et al.*, 2012; *Millgate et al.*, 2013a], leading to stabilization; others [*Rignot and Steffen*, 2008; *Vaughan et al.*, 2012b; *Sergienko*, 2013] focus on the importance of structural weakening effects due to basal channel presence. We identified two locations where the presence of basal channels appears to have led to structural weakening: (i) the margin of the Roi Baudouin Ice

Shelf (Supplementary Section 3.4.6, Figure 3.10), where the ice shelf has split along a basal channel; and (ii) the shear margin of the Getz Ice Shelf (Figure 3.3), where crevasses have recently formed at the tip of the Scott Peninsula. An IceBridge RES transect reveals deep basal channels on either side of the Scott Peninsula (Figure 3.3a), and a crevassed region has developed recently at their confluence (Figures 3.3b and c).

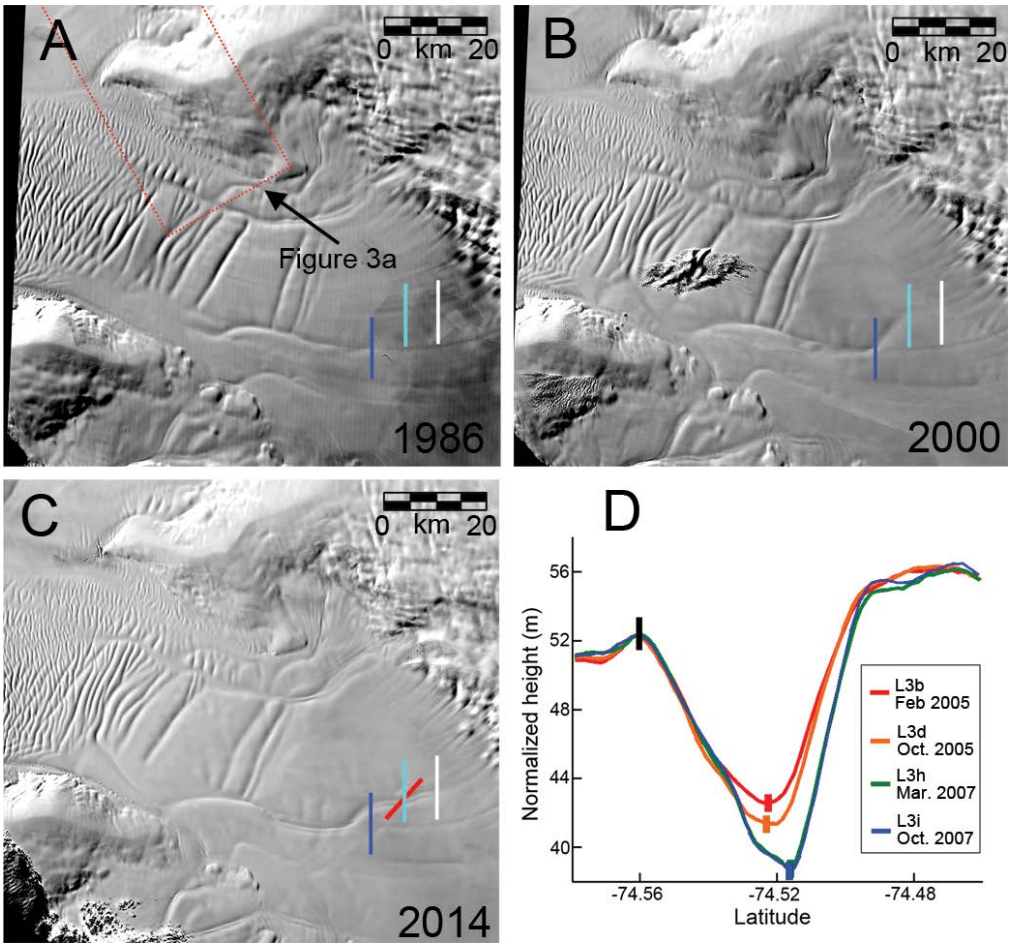

Figure 3.2 | Growing channel on the Getz Ice Shelf.
a–**c**, Landsat image series (ice flow approximately right to left). Vertical lines are in the same position in each panel, marking the approximate head of the channel in 1986 (blue), 2000 (cyan) and 2014 (white). **d**, Data from four repeats along a segment of ICESat Track 0348 across the channel (see red line on **c** for location). Vertical black line marks the location where track heights were normalized to remove background thinning rates. Error bars are the average plus one standard deviation of the topographic relief at the channel base.

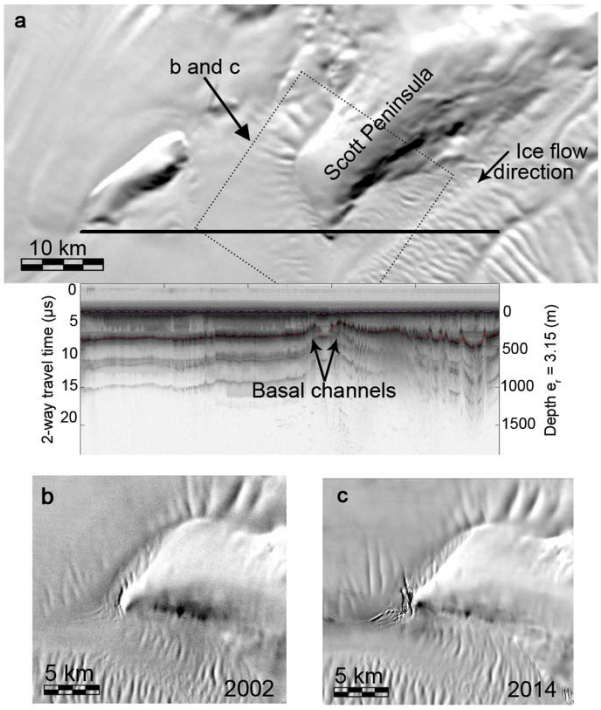

Figure 3.3 | Ice shelf fracture at the tip of the Scott Peninsula, Getz Ice Shelf.
a, A portion of the Getz Ice Shelf including the Scott Peninsula. Black line shows the location of a 3 November 2011 IceBridge flight line, with corresponding RES profile shown below. Two deep channels are visible on the base of the shelf in the radar segment on either side of the peninsula. **b**,**c**, Landsat image pair showing the development of crevasses at the tip of the Scott Peninsula.

Our association between basal channels and crevassing does not prove causation, as other dynamic processes could be causing rifting. Our observations of the Roi Baudouin and Getz ice shelves, however, are consistent with modeling studies [*Vaughan et al.*, 2012b; *Sergienko*, 2013], which show that the presence of basal channels can increase effective stresses sufficiently to cause ice shelf fracture, especially near shear margins. Before and during the collapse of the Larsen B Ice Shelf, extensive fracturing was seen along shear zones [*Khazendar et al.*, 2007] emphasizing the vulnerability of these regions and their importance to ice shelf stability. The prevalence of basal channels along shear margins (Supplementary Section 3.3.6), particularly in the AB region, justifies future studies of basal channel effects on large-scale ice shelf stability under forcing from warm ocean water.

Our data demonstrate the widespread presence of large basal channels on Antarctic ice shelves, with the highest density occurring in West Antarctica. We show that channels tend to

align with shear margins, that many are coincident with persistent polynyas at the ice front, and that they are associated with new zones of crevassing. Our observations and statistical correlations between channel density, basal melt rate, and grounding line depth suggest that ocean-source and grounding-line-sourced basal channel formation is primarily driven by CDW, and that the channels can evolve on short timescales. The presence and growth of channels can cause structural ice-shelf-weakening [*Rignot and Steffen*, 2008; *Vaughan et al.*, 2012b; *Sergienko*, 2013] along already-vulnerable shear zones [*Khazendar et al.*, 2007], which leads us to suggest a possible future scenario in which ice-shelf basal channels could lead to large-scale destabilization through the reduction of ice-shelf backstress. With increased access of warm water beneath ice shelves and further incision of channels along shear margins, a tipping point could be reached where an ice shelf margin becomes disrupted enough to lead to increased calving, reduced ice shelf area, increased grounded ice flux, and accelerated sea level rise. While basal melting at the grounding line has already been shown to lead to increased ice flux, the implied additional mechanism of shear-margin weakening by basal channels could further accelerate grounded ice loss, a feedback that requires significant further exploration.

Acknowledgements:

This study was supported by NASA through a NASA Earth Science Student Fellowship (NNX14AK82H) and grant NNX13AP60G, and by USGS contract G12PC00066. We thank A. Le Brocq for providing subglacial hydrology data, and S. Schmidtko and L. Padman for ocean temperature data. We would also like to acknowledge assistance with figures from A. Pope, and helpful suggestions from O. Sergienko, R. Alley, and C. Shuman.

Methods:

We identified and mapped channels mapped using the Moderate Resolution Imaging Spectroradiometer (MODIS) Mosaic of Antarctica (MOA) 2004 and 2009 data sets (https://nsidc.org/data/moa/) [*Scambos et al.*, 2007] and 95 Landsat 8 images (http://earthexplorer.usgs.gov), based on a set of criteria detailed in Supplementary Section 1. Basal channel presence was confirmed by inspecting browse images of radar data from the Operation IceBridge Multichannel Coherent Radar Depth Sounder (MCoRDS, http://nsidc.org/icebridge/portal/). We used images from the NSIDC MODIS Antarctic Ice Shelf Image Archive (https://nsidc.org/data/iceshelves_images/index_modis.html) to map ice-shelf-front polynyas, identified as small open ocean regions at the ends of channels within fast ice. Summer images between 2002 and 2014 were inspected from all 26 regions, encompassing all Antarctic ice shelves (390 images; Supplementary Section 3.4.4).

For statistical analyses, we divided larger ice shelves into sub-areas for more detailed analysis (Supplementary Section 3.4.3). Channel densities exhibited a non-normal distribution, necessitating the use of non-parametric tests. A Wilcoxon signed-rank test was used to check for statistical significance of anomalously high basal channel densities in each region of interest. Two correlation tests, Kendall's τ and Spearman's ρ, were recorded to identify any correlation between channel density and maximum grounding line depth or ice shelf melt rate.

We used ICESat data product GLA12, Release 633 (http://nsidc.org/data/ICESat), applying the product saturation correction and Gaussian-centroid (GC) corrections [*Borsa et al.*, 2014]. Following Fricker and Padman (2006), we removed the applied tide correction and then "retided" the data using Circum-Antarctic Tidal Simulation (CATS [*Padman et al.*, 2002]). In

estimating channel incision rates, we addressed possible cross-track slope effects. Incision was estimated only at the lowest point in the channel. Cross-track variability at the base of the channel was then assessed using high-resolution Worldview-2 digital elevation models provided by the Polar Geospatial Center (http://www.pgc.umn.edu). Elevations were extracted for the deepest part of the channel for five kilometers. The difference between the minimum and maximum elevation was recorded in 200 m increments (cross-track distances in both cases were less than 200 m), every 100 m along the trace. The average and standard deviation of the differences were calculated, and the error bars in the main text Figure 3.2 D and Figure 3.14 represent the average plus one standard deviation on either side of the value. Finally, residual tidal effects and background thinning were eliminated by normalizing the track elevation to a location outside the channel that could be matched on all tracks.

Channel incision rates are calculated using the assumption that firn-air thickness does not change between the ICESat measurements from 2004 to 2007, or within the channel relative to the flanks. From hydrostatic equilibrium, we obtain an expression for change in ice thickness, ΔH, based on a given surface elevation change, ΔZ_s:

$$\Delta H = \Delta Z_s \Big/ \left(1 - \frac{\rho_i}{\rho_w}\right)$$

The basal elevation change is then $\Delta H - \Delta Z_s$. We used an ice density value ρ_i = 910 kg m^{-3} and a seawater density value ρ_w = 1026 kg m^{-3}.

3.4: Supplementary information

3.4.1. Identifying basal channels

Basal channels are identified as surface depressions visible in satellite imagery. Where data are available, we were also able to confirm the presence of identified channels as depressions on the ice shelf base using Operation IceBridge Multichannel Coherent Radar Depth Sounder (MCoRDS) radar data. Examples of this confirmation are shown in figures 3.4 and 3.5. This was found to be a consistent method: locations where a basal channel was suspected due to the presence of a surface feature always corresponded to a channel on the base of the shelf. Because these data were not available on all ice shelves, channels were never initially identified using basal topography; first identification was always made using satellite imagery.

Identified basal channels are divided into three categories. In the first category, subglacially-sourced channels are identified based on two criteria: 1. Channels begin immediately at the grounding line, and 2. Channel origins correspond to modeled subglacial outflow [*Brocq et al.*, 2009]. As noted in Le Brocq et al. (2013), as well as in observations from this study, subglacially-sourced channels may include abrupt changes in channel path, which are interpreted to signify reorganizations of subglacial hydrology. Aside from these shifts, subglacially-sourced channels tend to follow ice flow direction closely and dissipate gradually toward the ice edge.

In contrast, ocean-sourced channels are identified by the single criterion that they begin at a location downstream from the grounding line. Observations show that ocean-sourced channels roughly follow the direction of ice flow in most cases, but may be sinuous. They

frequently originate at or migrate towards ice shelf shear margins adjacent to islands and peninsulas. Ocean-sourced channels generally deepen toward the ice edge and sometimes terminate in persistent ice-edge polynyas (Section 3.4.4).

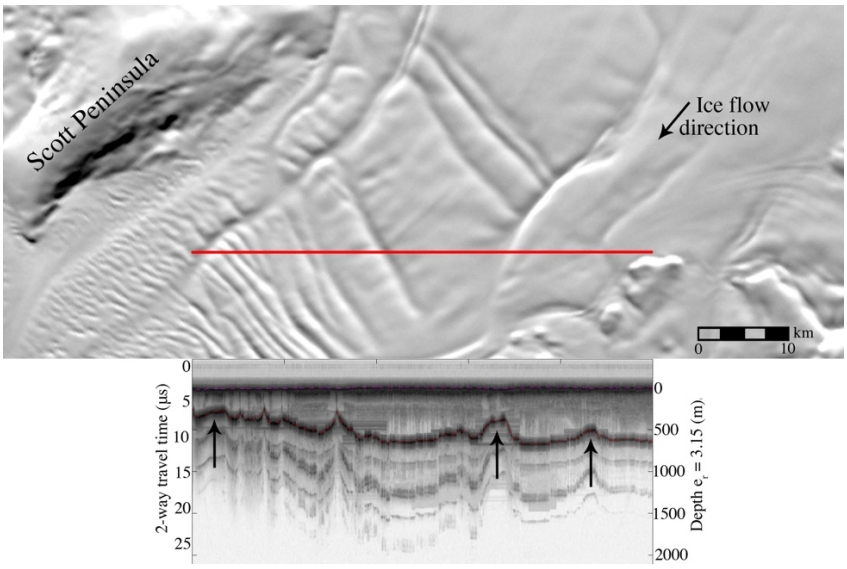

Figure 3.4 | Supplementary figure: Basal channels on the Getz Ice Shelf.
The red line shows the location of a November 2011 MCoRDS radar transect. Arrows on the radargram mark three prominent basal channels. Note that other surface depressions overlying incisions on the ice shelf base are formed by basal rifts rather than basal channels. These tend to have sharper basal profile peaks than basal channels. Radargram label $e_r = 3.15$ indicates the constant dielectric permittivity used to calculate depth.

Grounding-line-sourced channels have characteristics of both of the other categories. They originate immediately at the grounding line, like subglacially-sourced channels. However, they do not correspond to modeled subglacial outflow, suggesting that they are unrelated to subglacial hydrology, like ocean-sourced channels.

Though the criteria were created to make channel classification as clear as possible, instances still exist where identification is ambiguous. For example, figure 3.6 shows the

floating tongue of Pine Island Glacier (PIG), which was one of the most challenging locations for basal channel identification and classification. The basal channels on PIG have been examined in several other studies, using a combination of airborne radar and satellite techniques [*Bindschadler et al.*, 2011; *Mankoff et al.*, 2012; *Vaughan et al.*, 2012b; *Dutrieux et al.*, 2013] and Autosub observations of the ice shelf base [*Dutrieux et al.*, 2014b], which makes it possible to be more confident of basal channel locations. However, this kind of analysis is not available on all ice shelves around Antarctica. In order to maintain consistency in basal channel identification, we limit the basal channels measured on PIG to those that could be identified by our methods alone.

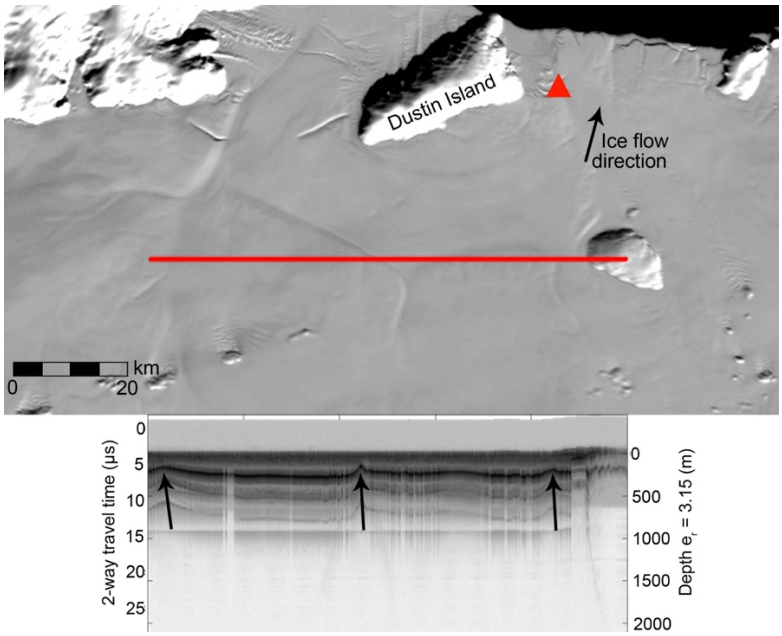

Figure 3.5 | Supplementary figure: Basal channels on the Abbot Ice Shelf.
IceBridge radargram from November 2009. Annotations following those in Figure 3.4. Red triangle is at the location of a persistent polynya, identified in images with fast ice at the ice tongue front (Section 3.3.4). Radargram label $e_r = 3.15$ indicates the constant dielectric permittivity used to calculate depth.

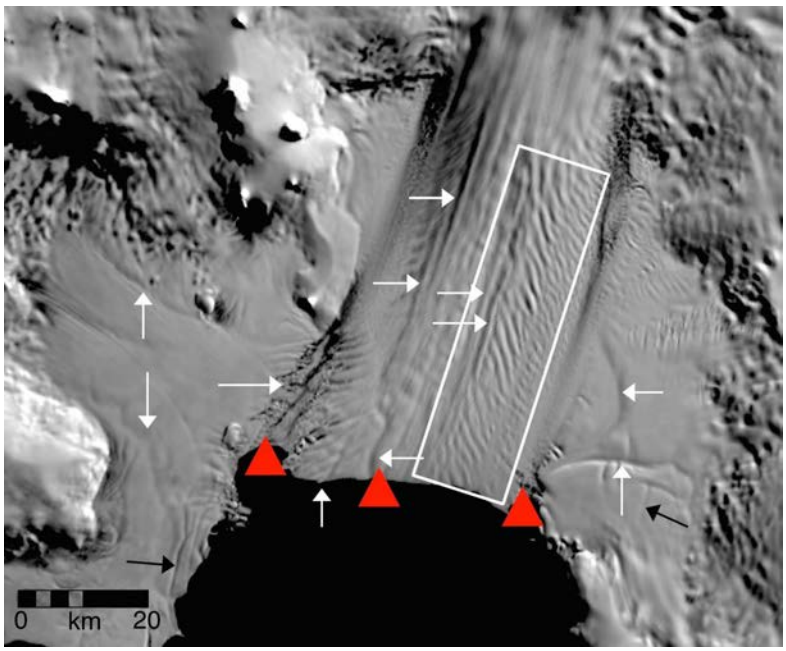

Figure 3.6 | Supplementary figure: Basal Channels on the Pine Island Glacier Ice Shelf. The floating tongue of Pine Island Glacier as shown in the 2009 MODIS Mosaic of Antarctica (MOA) image [*Scambos et al.*, 2007]. White arrows mark features identified as basal channels. The white box outlines an area of small, diagonal features identified as basal channels in other studies, but which are indistinguishable from small fractures by the methods used in this study. Black arrows mark examples of small fractures. Red triangles mark the locations of persistent polynyas identified in images with fast ice at the ice tongue front (Section 3.3.4).

Identification of basal channels on PIG is challenging for two main reasons. First, the floating ice tongue of PIG has several types of topographic features, including flowstripes (sometimes called 'streaklines' [*Glasser and Gudmundsson*, 2012]) and basal crevasses, both of which can have a surface morphology similar to basal channels. However, flowstripes can be traced above the grounding line, particularly using high-resolution Landsat 8 imagery. Only if a feature obviously deepens or widens on the ice shelf is it identified as a basal channel. This criterion is used on all ice shelves with flowstripes. Features identified as basal channels are marked with white arrows in figure 3.6.

Second, PIG has a line of small surface features running diagonal to ice flow, outlined in a white box in figure 3.6. These features have been identified as basal channels in other studies [*Dutrieux et al.*, 2014b], or as basal undulations that mirror ocean heat content patterns [*Bindschadler et al.*, 2011]. However, in our study, these features are indistinguishable from features identified as small fractures in the ice shelf base. Examples of these fractures are marked with black arrows in figure 3.6. Because of an inability to distinguish similar features on other ice shelves, these small features were not included in the statistical basal channel analyses. We do not refute that these features could represent basal channels; we only state that they cannot be positively identified by this method, and are left out of the analysis of the large basal channels identified for the sake of consistency.

In some cases, the identification of a feature as any type of basal channel is ambiguous. Figure 3.7 shows a portion of the Ross Ice Shelf at the MacAyeal Ice Stream. The red arrow identifies a subglacially-sourced channel. The area shown in the figure contains many flow lines that all have a similar visible morphology. In most cases, these flow lines can be easily traced to grounded features, and do not obviously deepen or widen beyond the grounding line. However, two features, marked with black arrows, are ambiguous. Because these features closely resemble the flow lines surrounding them but cannot be positively identified as flow lines because they cannot be traced back to grounded features, they are marked as “possible channels.” These possible channels are included in the statistical analyses.

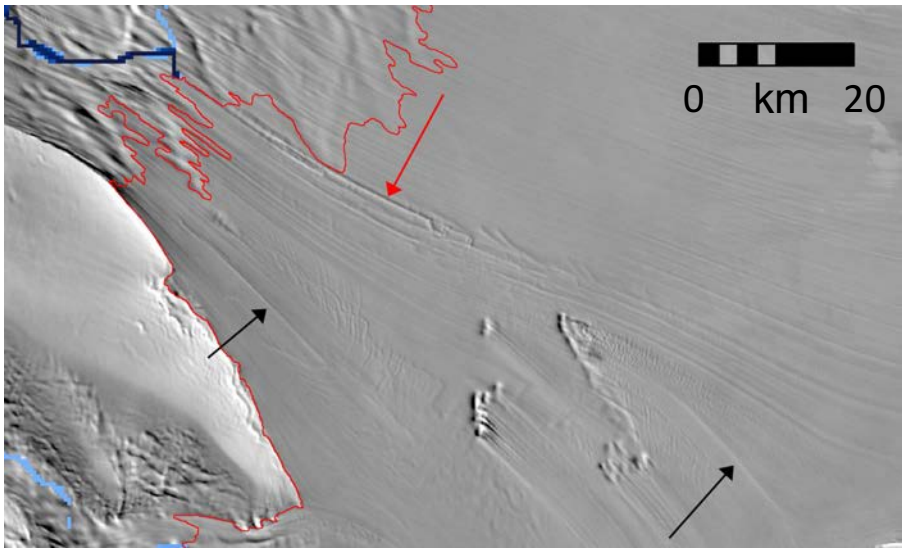

Figure 3.7 | Supplementary figure: Basal channels on the Ross Ice Shelf.
A portion of the Ross Ice Shelf at the MacAyeal Ice Stream as shown in the 2009 MOA image [*Scambos et al.*, 2007]. The red arrow marks a subglacially-sourced channel. Black arrows mark possible channels, which resemble nearby flow lines but cannot be positively traced to grounded features.

3.4.2. Basal channel origins

Of the three channel types discussed in the paper, the formation of subglacially-sourced channels is the most well-described [*Le Brocq et al.*, 2013] (Figure 3.8 A). Ocean-sourced and grounding-line-sourced channels are somewhat more speculative in origin, but are unlikely to be directly influenced by subglacial meltwater outflows. Their general correlation with the presence of warm seabed water temperatures and correlations with grounding line depth in the AB region strongly imply that the formation of these two channel types is driven by the presence of a deep layer of warm water in the sub-ice-shelf cavity, specifically CDW or modified CDW. Further supportive evidence comes from their association with persistent small polynas at the ice shelf front, which have been previously shown to be associated with warm sub-ice-shelf water presence [*Bindschadler et al.*, 2011; *Mankoff et al.*, 2012].

Because the formation of these two channel types is not tied to subglacial meltwater outflow, their exact formation locations are much less constrained. Just as streams on the land surface will form in low regions, determined by previously-carved features or random variations in landscape topography, plumes that form ocean-sourced and grounding-line-sourced channels are likely to flow in previously-carved high spots (the reverse of low spots, since these plumes rise with buoyancy rather than sink with gravity). These high spots may come from random variations in basal topography that were formed by inhomogeneity of basal melt or by features inherited from the grounding line [*Rignot and Steffen*, 2008; *Gladish et al.*, 2012]. Other high spots may be initiated by transverse shelf slopes accelerating plumes toward the margins [*Sergienko*, 2013]. Or, plumes may flow in previously-formed channels, such as troughs that began as subglacially-sourced channels or basal incisions caused by suture zones [*Fricker and Padman*, 2006].

Though these controls can determine the exact location of plume flow on a local scale, they do not explain what would initiate an ocean-sourced channel vs. a grounding-line-sourced channel in the first place. Any conceptual model explaining the formation of these two channel types must explain both the differences in grounding line proximity and the observation of ocean-sourced channels on the Getz Ice Shelf experiencing headward growth. Two possible mechanisms are presented here: the degree of interaction between an ice shelf and a deep layer of warm water, and the influence of tidally mixed zones near the grounding line. Both working models for the origins of ocean-sourced and grounding-line-sourced channels invoke warm water as the formation agent. A conclusive explanation of the difference between these

channel types is not possible due to the lack of observations within ice shelf cavities. Numerical modeling of these processes is beyond the scope of the current observational study.

Our first conceptual model, addressing the degree of interaction between an ice shelf and warm water, concerns variations in the depth to the CDW layer, thickness of the ice shelf, or presence of sills that limit the entry of CDW into the shelf cavity. CDW rarely rises above 300 m depth [*Jacobs et al.*, 2012]. If an ice shelf is relatively thin (Figure 3.8 B), or if it lies above a continental shelf area that is shallower than this depth, its interaction with CDW will be limited [*Padman et al.*, 2012]. However, for many Antarctic continental shelf areas, the distal shelf edge is at or near the depth of the CDW layer, sometimes as a sill, with gradually increasing depth from the shelf edge to the ice sheet grounding line (Figure 3.8 B1). Persistent changes in ocean circulation (e.g., driven by changes in mean wind pattern), or changes in the layer depth due to ocean climate changes, can cause CDW to intrude onto the continental shelf in some areas. Because CDW is denser than the polar water layer that forms the majority of the sub-ice-shelf water components, the intruded water will move down the seabed slope toward the grounding line, and into the deepest seabed channels beneath the shelf. This density-driven tendency for CDW to migrate as a thin layer to the deepest parts of seabed channels is our favored explanation for grounding-line-sourced basal channels in areas that do not correlate with a sub-glacial hydrologic exit. Channels will only be initiated at or near the grounding line, creating an abundance of grounding-line-sourced channels, or ocean-sourced channels that reach very close to the grounding line.

In order for ocean-sourced channels to form (Figure 3.8 C), the ice shelf must be thick enough and/or the warm water layer shallow enough for interaction over a significant area of

the shelf. Plumes may then initiate closer to the middle of the ice shelf, likely due to a distributed source of meltwater that flows into a topographic depression. If melting accelerates near the grounding line, a plume that has initiated in the middle of the shelf may grow headwards, as has been observed on the Getz Ice Shelf (main text Figure 3.2, Figures 3.11-3.12).

Our second explanation builds on the work of [*Holland*, 2008], which demonstrated that a homogeneously mixed zone is formed at ice shelf grounding lines due to tidal processes. The size of this relatively small feature depends on variables such as shelf slope, ocean temperature, and tidal velocities. Within the tidally mixed zone, melting is suppressed, insulating the grounding line from the full effects of warm water layers held offshore. Warm water plumes tend to initiate oceanward of the mixed zone boundary. Beneath an ice shelf with a relatively large mixed zone, basal channels will only initiate as ocean-sourced channels, at a point removed from the grounding line. Ice shelves with small or insignificant mixed zones may have basal channels that initiate at the grounding line. Changes in ocean temperature or ocean circulation may change the extent of a mixed zone, allowing for the growth of a channel towards the grounding line.

Both of these mechanisms are likely to act in combination to determine the type of channel that is formed by a sub-ice-shelf plume. Without extensive measurements within ice shelf cavities and/or numerical modeling studies, the details of these interactions cannot be confidently assessed.

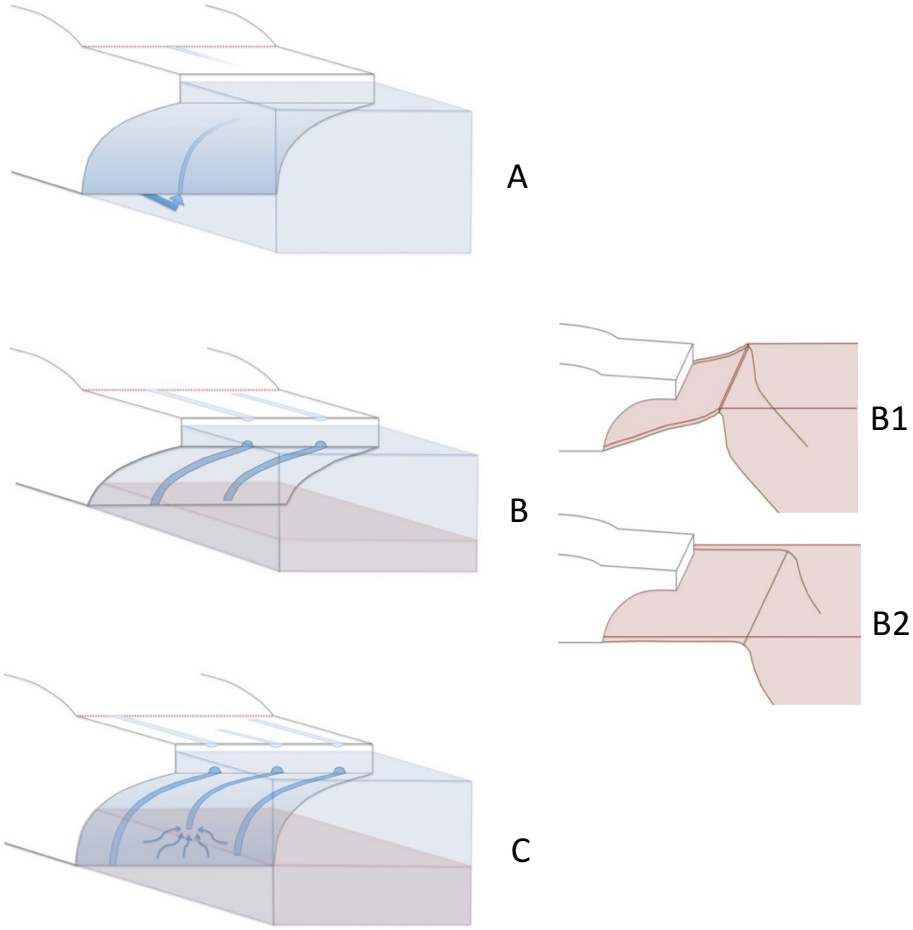

Figure 3.8 | Supplementary figure: Conceptual diagrams of the origins of all three channel types.
Not to scale. A) Subglacially-sourced channel. Blue arrow at ice shelf base represents the outflow of sub-ice-sheet meltwater. This water rises, entraining ocean water and carving a basal channel, which dissipates toward the ice edge. B) Grounding-line-sourced channels. The ice shelf interacts with a thin layer of warm water and/or has a shallow grounding line, limiting channel formation to at or near the grounding line. B1 shows one scenario causing the layer of warm water to be thin: the approximate depth of warm water on the distal shelf is at or near the elevation of the top of a sill, allowing a small amount of dense warm water to flow down the continental shelf to the ice shelf grounding line. B2 shows a second scenario, in which the warm water depth just barely clears the elevation of the continental shelf, again resulting in a thin layer of warm water interacting with the ice shelf grounding line C) Ocean-sourced and grounding-line-sourced channels. The ice shelf interacts with a thick layer of warm water and/or has a very deep grounding line, allowing channels to form at or near the grounding line or in the middle of the shelf.

3.4.3. Basal channel density and grounding line depth statistics

We took two steps to ensure the comparability of basal channel length data from all ice shelves in Antarctica. First, basal channel lengths were normalized to shelf area, creating a unit identified as "basal channel density," which is expressed as 100×km/km^2. This proxy represents basal channel presence while minimizing measurement error. Because channel edges are diffuse, measuring length allows for error only at the channel ends. If channel area were measured, error would accumulate on all edges. Second, because characteristics of ice-ocean interaction can reasonably be expected to vary across large shelves, shelves are subdivided into smaller sections. Initial shelf boundaries were defined using the MODIS Mosaic of Antarctica (MOA) 2009 grounding line, ice edge, and island products [*Scambos et al.*, 2007]. Section boundaries within these shelf regions are guided by flowstripes and drawn along major outflow boundaries, and no section has a shelf front length greater than 200 km. The resulting sections, numbered counterclockwise around Antarctica, are identified in figure 3.9. Shelves are also grouped into regions based on Antarctic seas [*Holland and Kwok*, 2012]. However, this grouping resulted in very few samples in some regions. Statistics were therefore calculated based on three broader groupings, yielding at least 30 samples in each group: the Amundsen/ Bellingshausen Sea region, the Ross Sea through Cooperation Sea region, and the Cosmonaut Sea through Weddell Sea region (Figure 3.9). A 95% confidence level was used to define significance for all statistical tests.

The first correlation we tested was between basal channel densities and basal melt rates [*Rignot et al.*, 2013] for all ice shelves. Because basal melt rates were published only for total ice shelf areas, we were not able to use the sub-sections we defined for this correlation. The

correlation was significant at the 95% confidence level (p = 0.004-0.006), showing that basal channels form more prevalently where warm ocean water presence leads to higher basal melt rates.

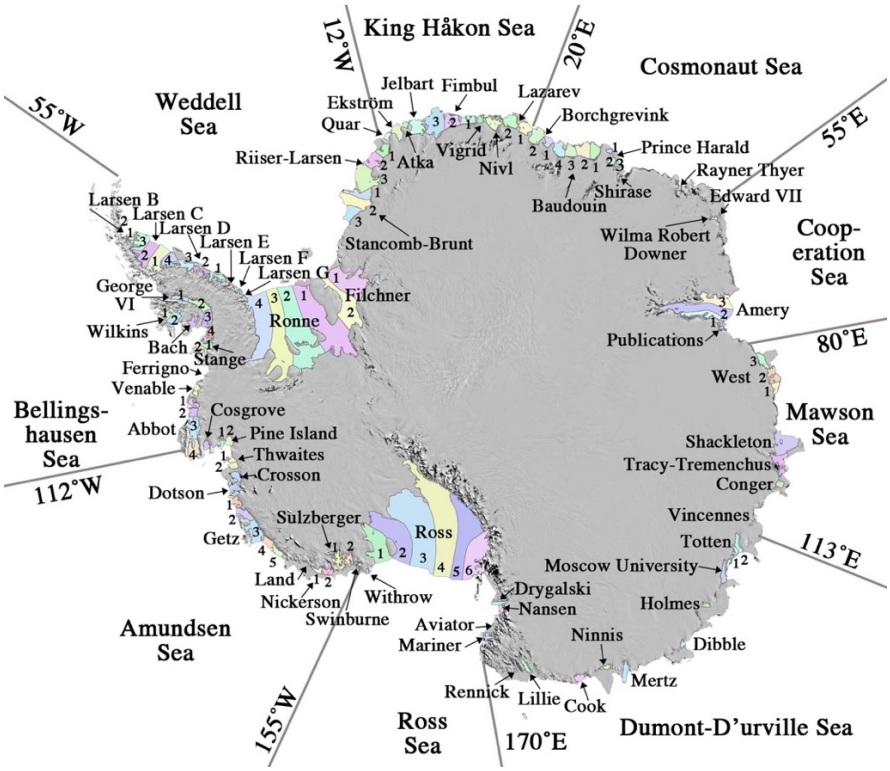

Figure 3.9 | Supplementary figure: Ice shelf subsections used for statistical analyses.

A visual inspection of the basal channel mapping (main text figure 3.1 A) suggested that the Amundsen/Bellingshausen Sea (AB) region had an especially high density of basal channels. The ice shelf area, basal channel length (including all three different types of basal channels), and basal channel density are recorded in Appendix 3. A Wilcoxon signed-rank test confirmed that the AB region has a higher basal channel density than the overall channel density mean for all Antarctic ice shelves at the 95% confidence level. A Wilcoxon test was also carried out on the other two broad regions. The Ross Sea through Cooperation Sea region had no statistically significant difference from the mean, while the Cosmonaut to Weddell Sea region has a basal

channel density significantly lower than the mean. The P-values for these Wilcoxon signed-rank tests are shown in table 3.1.

The high basal channel densities in the AB region suggested a link between basal channel density and Circumpolar Deep Water (CDW) presence. Circumpolar Deep Water is known to access and melt the bases of ice shelves in the Amundsen and Bellingshausen Seas [*Shepherd et al.*, 2004]. A link between high channel density and warm ocean water is qualitatively seen in the continental shelf ocean floor temperatures shown in main text Figure 1A. Note that these temperatures represent only the ocean water offshore of the ice shelves; CDW and other water mass influence beneath the shelves is not well-constrained. Additionally, the temperatures are limited to the continental shelf, which is very narrow in some regions. This leaves the nature of ocean water beneath some shelves, like the Sulzberger Ice Shelf, ambiguous based on offshore ocean floor temperature measurements alone.

However, it is possible to use proxy measurements where direct measurements are unavailable. CDW on the continental shelf tends to be close to the seafloor. If the base of an ice shelf is deep enough (typically at the grounding line, where ice shelves are thickest), the CDW will cause increased melt. The buoyant, freshened meltwater rises, entraining warm CDW and accelerating melting across the entire shelf base. We hypothesize that this accelerated melting also leads to increased basal channel density. If CDW is responsible for increased basal channel density, then there should be a correlation between grounding line depth and basal channel density, as CDW interacts more strongly with shelves with deep grounding lines. We hypothesize that this correlation should not be significant where warm water masses are not present at depth.

For each ice shelf section, a maximum grounding line depth was obtained using depths from Bedmap2 [*Fretwell et al.*, 2012] and the MOA 2009 grounding line product [*Scambos et al.*, 2007]. Because the basal channel density data were non-normally distributed, two different non-parametric correlation tests were performed, with the p-values recorded in table 3.1. For both tests, the correlation between grounding line depth and basal channel density is significant at the 95% confidence level in the AB region.

We also highlight the fact that statistics were not run individually for the three channel categories. This would not be physically valid, with the reasoning displayed in Figure 3.10. The channel outlined by two brackets is identified as a subglacially-sourced channel, because it intersects a subglacial meltwater outlet and begins at the grounding line. Subglacially-sourced channels typically shallow towards the ice edge, as has been shown in our observations and previous analyses [*Le Brocq et al.*, 2013]. Subglacially-sourced channels shallow because, without the plumes of warm ocean water that drive ocean-sourced and grounding-line sourced channels, the water in the channel eventually super-cools, causing freeze on. This area of typical shallowing is shown in the blue bracket in figure 3.10. However, this channel then continues in the area denoted by the green bracket, deepening towards the ice edge in a manner typical of an ocean- or grounding-line-sourced channel. This suggests that available warm water has been directed into an existing depression created by the sub-glacially-sourced channel. Had the sub-glacially-sourced channel not been present, it is likely that an ocean-sourced channel would have formed. Since the paths of ocean-sourced or grounding-line-sourced plumes can be funneled into sub-glacially-sourced channels in this manner, it is not possible to separate the channel types in statistical analyses.

Table 3.1 | Supplementary table: Statistics for all basal channels.
The Wilcoxon test refers to the difference from the overall mean for mean basal channel density in each broad region. The Spearman's and Kendall test refer to the correlation between basal channel density and maximum grounding line depth. Values in bold are significant at the 95% confidence level.

Shelf region	Mean channel density ($100*km/km^2$)	Wilcoxon test	Spearman's ρ	Kendall's τ
All shelves	1.73	N/A	0.11	0.13
Amundsen and Bellingshausen Seas	2.86	**0.00018**	**0.025**	**0.037**
Ross Sea to Cooperation Sea	1.67	0.31	0.15	0.14
Cosmonaut Sea to Weddell Sea	0.96	**0.032**	0.052	0.098

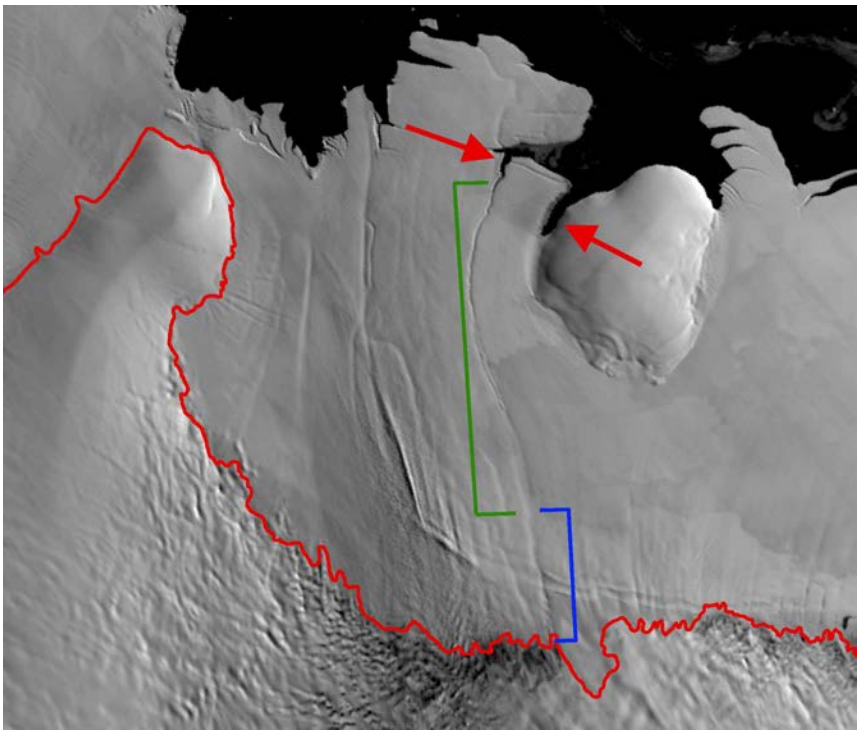

Figure 3.10 | Supplementary figure: Basal channels on the Roi Baudouin Ice Shelf.
A portion of the Roi Baudouin Ice Shelf, Queen Maud Land, East Antarctica, from the MODIS Ice Shelf Image Archive. Red line is the MOA 2009 grounding line. Brackets denote a basal channel, identified as subglacially-sourced. Blue bracket shows region of shallowing towards the ice edge, typical of subglacially-sourced channels. Green bracket shows region of deepening towards the ice edge, typical of ocean-sourced and grounding-line-sourced channels. Red arrows identify areas where the shelf edge is splitting along a basal channel.

3.4.4. Persistent polynyas

Persistent polynyas are identified using the MODIS ice shelf image archive available at http://nsidc.org/data/iceshelves_images/index_modis.html. These small features are identified as open-water regions in fast ice that occur in the same place during at least three summers. Polynyas are distinguished from leads because they are roughly circular, while leads are linear features that form when strong winds blow sea ice away from the continent. Because the polynyas that were found in the image archive almost always appear at the ends of visible basal channels, and because they are stationary, point-like features, we hypothesize that these polynyas form because water with a significant amount of remaining heat energy rises to the surface after exiting a basal channel, preventing the formation of fast ice at that location.

Of the 25 persistent polynyas identified (shown in Appendix 3), 22 of them are in the AB region. The three polynyas at the terminus of Pine Island Glacier have been previously identified in the literature [*Bindschadler et al.*, 2011; *Mankoff et al.*, 2012]. Large calving events can make the identification of persistent polynyas difficult because the exact polynya location shifts with the ice shelf terminus. If a polynya is clearly associated with the same basal channel following a calving event, it is considered to be the same polynya as before the calving event, even though the position has shifted with the terminus. This applied on Pine Island Glacier. However, in a case such as the Crosson Ice Shelf, where basal channels are not as obvious, polynyas had to be re-defined after a major calving event.

3.4.5. Basal channel growth and ICESat corrections

Observations of basal channel growth toward the grounding line were carried out by comparing the MODIS Mosaic of Antarctica (MOA) 2004 and 2014 images [*Scambos et al.*, 2007]. Four locations of channel growth were identified, with all of them on the Getz Ice Shelf in West Antarctica (Figures 3.11 and 3.12).

The fastest-growing channel was further analyzed using ICESat laser altimetry. Figure S10 shows the location of two ICESat tracks that cross the channel (main text figure 3.2). ICESat data were used to quantify the rate of deepening occurring within the channel. Results, shown in Figure 3.14, demonstrate that basal channels have the capacity for extremely rapid change under some circumstances. Between 2004 and 2007, the channel at track 1330 deepened by between 2.4 and 8.8 ma^{-1}. At track 0348, near the head of the channel where growth is actively occurring, deepening rates were between 8.8 and 14.7 ma^{-1} between 2005 and 2007.

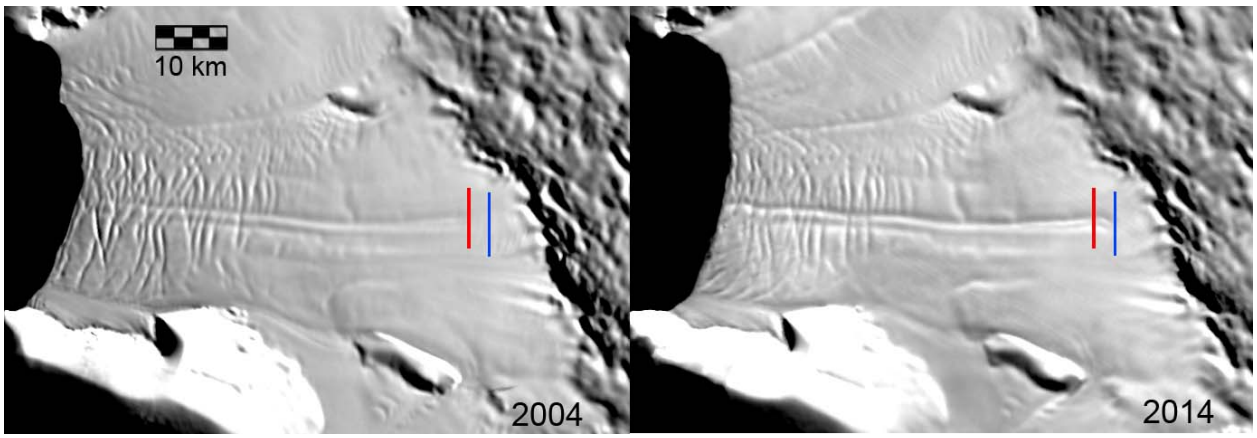

Figure 3.11 | Supplementary figure: Channel growth in the easternmost outflow of the Getz Ice Shelf.
MOA 2004 [*Scambos et al.*, 2007] and 2014 (in preparation; T. Scambos, T. Haran, M. Klinger) images, displaying a portion of the eastern end of the Getz Ice Shelf. Red and blue vertical marks show the approximate head of the channel in 2004 (red) and 2014 (blue). Vertical marks are in the same location in both images.

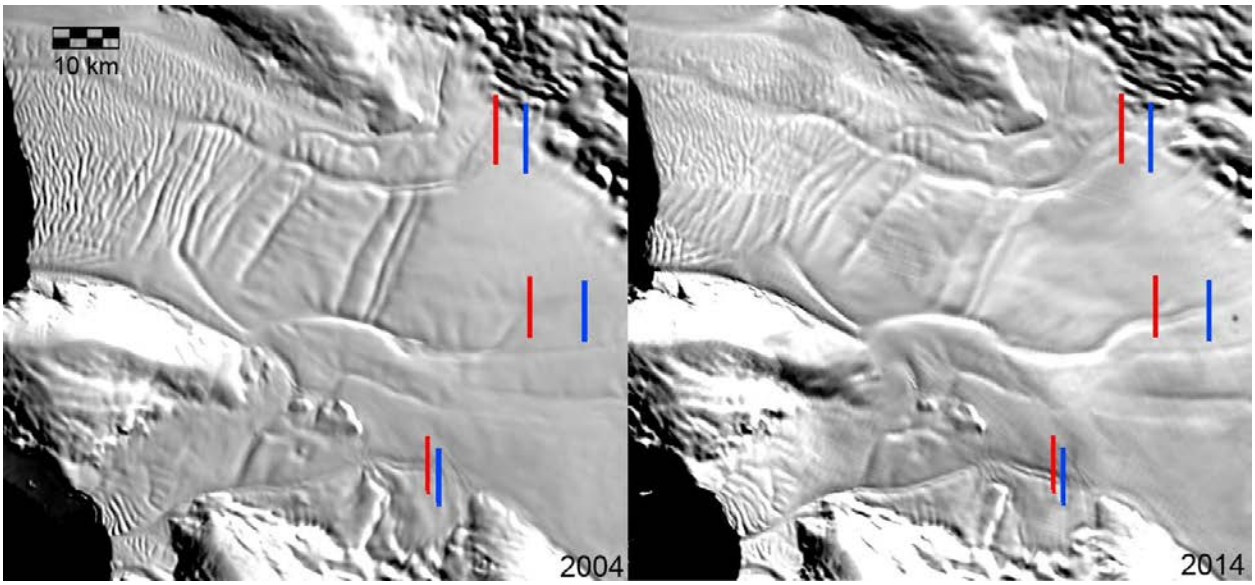

Figure 3.12 | Supplementary figure: Channel growth in the eastern Getz Ice Shelf.
MOA 2004 [*Scambos et al.*, 2007] and 2014 (in preparation; T. Scambos, T. Haran, M. Klinger) images just west of figure 3.11, showing three channels expanding toward the grounding line. Markings follow those in Figure 3.11. The middle channel is further analyzed in Figures 3.13-3.15.

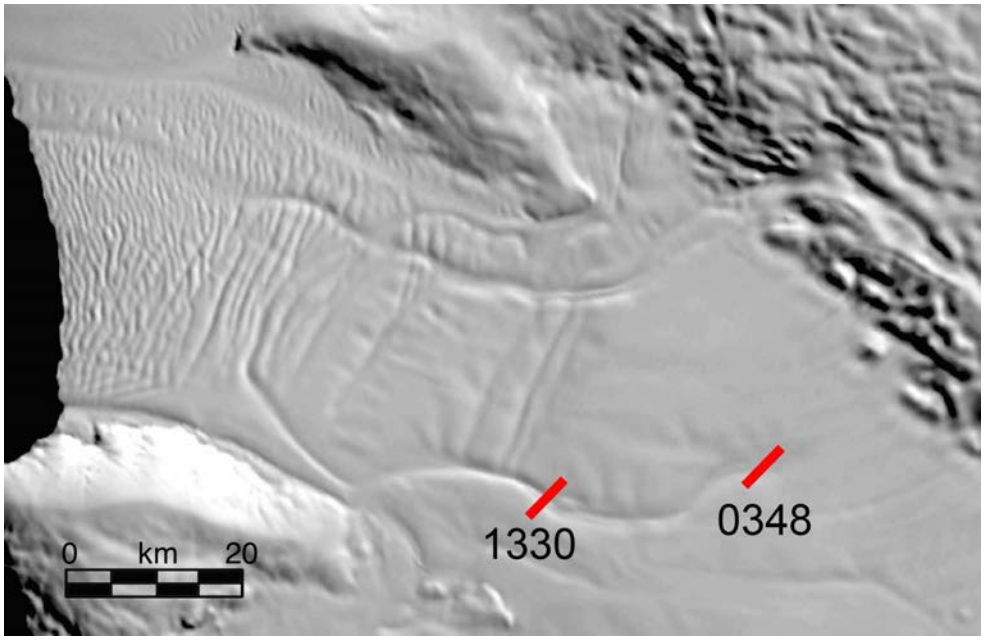

Figure 3.13 | Supplementary figure: ICESat tracks crossing a rapidly growing channel on the Getz Ice Shelf.
Background is the MOA 2009 image [*Scambos et al.*, 2007].

Figure 3.14 shows the data corrected using a product saturation correction and a Gaussian-centroid (GC) correction [*Borsa et al.*, 2014]. Data were "retided" using the Circum-Antarctic Tidal Simulation (CATS) [*Padman et al.*, 2002; *Fricker and Padman*, 2006]. Data are shown before and after elevation normalization to a point outside the channel. Because the Getz Ice Shelf is thinning across its whole area [*Pritchard et al.*, 2012; *Depoorter et al.*, 2013; *Rignot et al.*, 2013; *Paolo et al.*, 2015], the background thinning rate had to be removed to isolate the signal of channel deepening relative to the rest of the shelf. For both tracks, an elevation peak was chosen for normalization for two reasons. First, it was clear that the point was outside the channel, because elevation again decreased on the side away from the channel. Second, a peak is an easy location to match. Particularly for track 1330, advection of the sinuous channel led to a migration of the channel morphology over the measurement period. However, a clear peak outside of the channel remained that could be used to normalize all tracks. Though the data were already corrected for tides, the elevation normalization also ensures the removal of tidal effects.

The calculation of error bars to account for cross-track slope effects is described in the Methods section. These values are likely to be overestimates of error. First, the 200 m increment used is slightly larger than the cross-track slope distance, making it more likely to get a larger estimate of variability than exists across the track. Second, minimum and maximum values were extracted as points. ICESat has a ~70 m footprint, while the DEM from which the values were extracted has a 3 m pixel size. This makes it likely that some of the extremes would be averaged and reduced in the ICESat data. Finally, the extremes of the error bars assume that

the tracks are measured at the extremes of the cross-track variability, which is unlikely to be true.

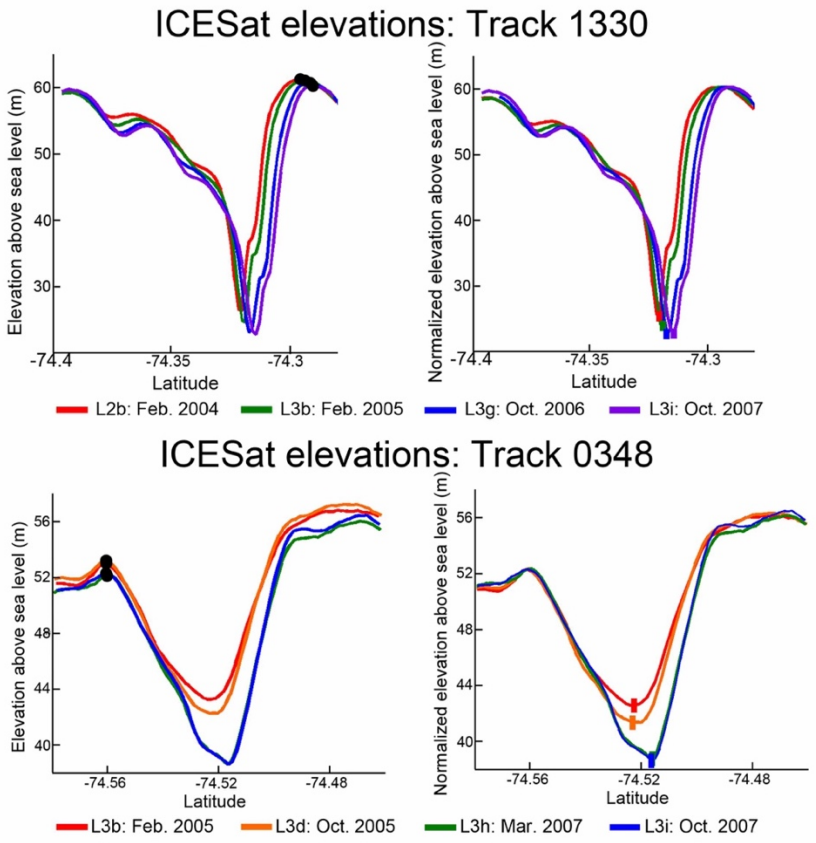

Figure 3.14 | Supplementary figure: ICESat profiles across a growing basal channel on the Getz Ice Shelf.
(see Figure 3.12, main text Figure 3.2). Black dots on the profiles in this column mark peak location used to normalize elevation. Graphs in the right-hand column have been normalized at the locations of the black dots to eliminate residual tidal effects and/or background thinning signals.

Five km of track were used to get sufficient samples for representative averages, but averages cannot yield exact values. In addition, the DEM available is from 2012, while the ICESat tracks are from 2004-2007. While we do not expect the average morphological

characteristics to change drastically during this time period, it is possible that the values we have obtained are not precisely representative of cross-track variability when ICESat tracks were collected.

In order to convert estimates of surface elevation change to basal deepening rates, an assessment of hydrostatic equilibrium is necessary. Equation 1 expresses the relationship between surface elevation and ice thickness of a volume of ice floating in hydrostatic equilibrium:

$$Z_s = \left(1 - \frac{\rho_i}{\rho_w}\right) H + \frac{\rho_i}{\rho_w} h_a \qquad (1)$$

where Z_s is the surface elevation (referenced to the WGS84 ellipsoid), ρ_i is the density of ice, ρ_w is the density of seawater, H is ice thickness, and h_a is equivalent air column thickness.

A visual inspection of data points taken from three IceBridge flight lines that crossed the channel (Figure 3.15) shows that the samples follow roughly a straight line on a graph of surface elevation vs. ice thickness, with some spread in the green dots. This is indicative of a rough hydrostatic equilibrium, because the relationship between surface elevation and ice thickness follows a predictable linear relationship. It is unsurprising that the green dots would deviate from this relationship because those data were collected near the shear margins where the shelf is expected to be out of hydrostatic equilibrium.

The plot in figure 3.15 also shows two black lines, which were calculated using equation 1. For both lines, ρ_i = 910 kg m^{-3} and ρ_w = 1026 kg m^{-3}. Fitting the data empirically gives h_a = ~16 m for the given ice density. This calculation is shown in the lower black line. The fact that the slope closely matches the data bolsters the assumption of rough hydrostatic equilibrium. The

upper line was calculated with h_a = 22 m, an average value for the region based on a firn model [*Ligtenberg et al.*, 2011]. With this higher value, it appears that no part of the shelf sampled is in hydrostatic equilibrium. This is an unreasonable assumption because samples include points well outside of the basal channels on flat, floating parts of the ice shelf that are generally expected to be hydrostatically adjusted. Because the sample points lie very close to a straight line to begin with, we judge it more accurate to rely on the empirical value for firn air thickness and conclude that points in and near the channel are in rough hydrostatic equilibrium.

Basal deepening rates were calculated based on the assumption of hydrostatic equilibrium, using equation 1. It is worth noting that, if the channels are not in hydrostatic equilibrium, basal deepening rates will be underestimates. This situation, where bridging stresses prevent complete hydrostatic relaxation, has been observed on some channels, particularly small ones [*Ligtenberg et al.*, 2011; *Drews*, 2015]. If elevation change is observed on a channel affected by bridging stresses, more deepening has taken place than is reflected in surface relaxation. Another important assumption made in the calculation of basal deepening rates is that firn air thicknesses are assumed to remain constant between ICESat measurements. That means the firn air thickness term cancels out of Equation 1 when change is calculated, and basal deepening rates depend only on the assumption of hydrostatic equilibrium and not on the value used for firn air thickness.

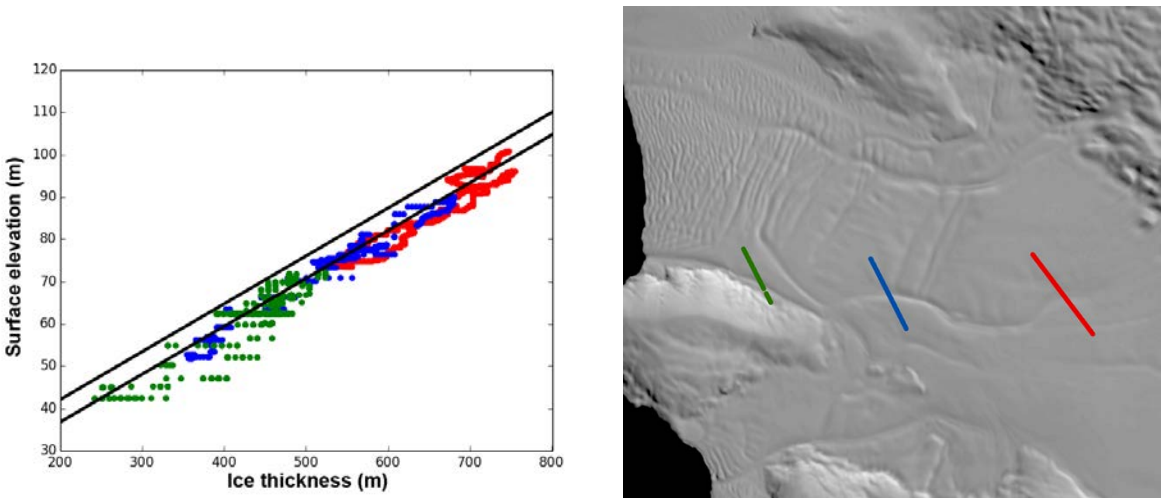

Figure 3.15 | Supplementary figure: Hydrostatic equilibrium in the growing channel on the Getz Ice Shelf.
Based on segments of three IceBridge flight lines collected November 10, 2010 (green), November 3, 2011 (blue), and October 16, 2009 (red). The plot on the left represents surface elevation from the Airborne Topographic Mapper, and ice thickness data from MCoRDS radar. Black lines are calculations of hydrostatic equilibrium using equation 1 with 22 m air thickness (upper line) and 16 m air thickness (lower line).

3.4.6. Basal channels and ice shelf stability

Our observations show a tendency for ocean-sourced and grounding-line-sourced channels to migrate towards the edges of islands and peninsulas, particularly in the AB region (where channel density is highest). Figure 3.16 shows the locations of these marginal channels. The locations and lengths of these features are recorded in Table 3.2. The tendency for channels to align with shear margins is most pronounced on the Getz and Sulzberger ice shelves, and it is a feature of basal channels predicted by numerical modeling [*Sergienko*, 2013].

Figure 3.10 and main text Figure 3.3 illustrate the importance of studying these channels that form along shear margins. Figure 3.10 shows a portion of the Roi Baudouin Ice Shelf. Red arrows mark two locations where the shelf is splitting along a basal channel. The arrow on the left denotes a portion of the middle of the shelf, while the arrow on the right indicates a split at

a shear margin. Main text Figure 3.3 shows an area at the confluence of two marginal basal channels where rifts are forming on the Getz Ice shelf. These observations combine with observational [*Rignot and Steffen*, 2008] and numerical modeling [*Vaughan et al.*, 2012b; *Sergienko*, 2013] studies that show that the presence of basal channels weaken ice shelves.

There is also evidence that shear zones tend to be weak areas on ice shelves to begin with. When the Larsen B Ice Shelf collapsed in 2002, extensive crevasses had formed along shear zones. Though the disintegration ultimately involved fracturing throughout the shelf, these shear zones were identified as zones of weakness that contributed to the collapse [*Khazendar et al.*, 2007].

If basal channels weaken ice shelves, and shear margins tend to already be weak areas on ice shelves, the formation of basal channels along islands and peninsulas, where shearing is often strong, is of significant concern to the stability of the ice shelf. We have no concrete evidence to show that these features are a threat to large-scale ice shelf stability. However, we do suggest that more work should be done on this subject.

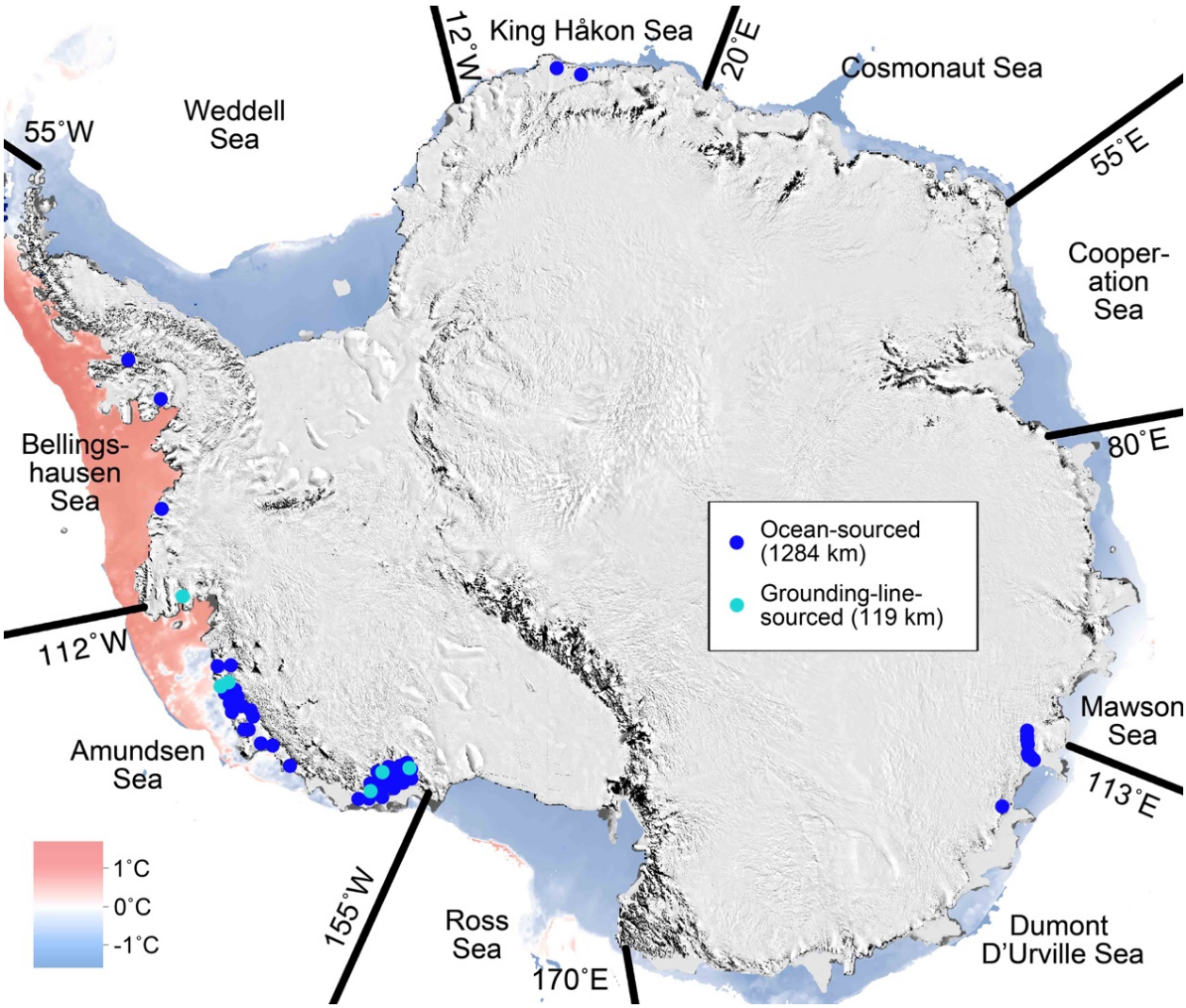

Figure 3.16 | Supplementary figure: Locations of channels that migrate towards the edges of islands and peninsulas.
Each dot represents 20 km of channel length. Note that the full length of these channels is included in the counts, not just the regions lying along islands and peninsulas. Ocean temperatures around the continent are the same as in figure 3.1.

Table 3.2 | Supplementary table: Lengths of channels that migrate towards the edges of islands and peninsulas.

Ice shelf name	Ocean region	Ocean-sourced channel length (km)	Grounding-line-sourced channel length (km)	Possible channel length (km)
Moscow University	Dumont D'Urville	24	0	0
Totten	Dumont D'Urville	181	0	0
Lazarev	King Håkon	0	0	14
Fimbul	King Håkon	43	0	0
Bach	Bellingshausen	31	0	0
George VI	Bellingshausen	37	0	0
Venable	Bellingshausen	30	0	0
Cosgrove	Amundsen	24	0	0
Dotson	Amundsen	57	0	0
Getz	Amundsen	354	42	0
Nickerson	Amundsen	125	0	0
Sulzberger	Amundsen	378	77	0
	Total	1284	119	14

Chapter 4:

Strain rates and Antarctic ice shelf flow dynamics

4.1: Introduction

In glaciology, strain is a measure of how much ice stretches, compresses, and deforms in all directions as it flows, and strain rates show how quickly these deformations occur. This tensor quantity is a fundamental measure of ice flow that is used in a variety of applications. Combined with Glen's Flow Law, strain rates can be used to calculate the stress state of flowing ice, and how that stress state has changed through time. In the case of ice shelves, these stress states are affected by factors such as ice velocity, ice thickness, and the influence of pinning points. Alongside surface and basal melt, strain rates are an important pillar of overall assessment of ice shelf stability.

The future work discussed in section 5.3 relies upon the calculation of strain accumulated by a parcel of ice as it travels through a glacier. In order to measure accumulated strain, we require a reliable method to calculate strain and strain rates from satellite-derived velocity grids. During the development of a suitable code, it became apparent that strain rates are calculated using widely varying methods and resolutions throughout the glaciological literature, complicating the direct comparison of strain rate values.

At the same time, the availability of velocity grids, most commonly derived from InSAR or velocity tracking on visible-band images, has increased. For example, Fahnestock et al. (2016) used multiple seasons of Landsat-8 image pairs to create a velocity grid covering the entire Antarctic continent. As the strain rate tensor is expressed as gradients in velocity, this creates the opportunity for more extensive calculations of strain rates than has been previously available.

In this chapter, we present an analysis of the accuracy and the differences between two commonly used strain calculation approaches. We also create a data product of Antarctic-wide strain rates derived from the Fahnestock et al. (2016) velocity grid. We determined that a numerical stake-tracking code calculating logarithmic strain rates is most accurate, and present a commented version of the code in the Appendix to Chapter 4 (hereafter Appendix 4).

Statement of contribution: We intend to submit a paper encompassing the material presented in this chapter, which will be authored by K. E. Alley, R. S. Anderson, H. Rajaram, T. A. Scambos, and A. Pope. K. E. Alley wrote the text of this chapter, performed all data analyses, wrote all codes, and created all figures, and will lead the writing of the paper. R. S. Anderson and H. Rajaram provided advice on algorithm development and validation. T. A. Scambos provided the LISA mosaic data used as the basis for the data product presented in section 4.8 and provided feedback on the algorithm. A. Pope assisted with coding and algorithm development. All authors will contribute to the writing and editing of the final paper.

4.2: Strain rate definitions

Linear strain is commonly defined as the change in length of an object or parcel divided by the original length of the parcel, while the strain rate is the rate of change of this quantity with time:

$$strain = e = \frac{L_f - L_o}{L_o} = \frac{\delta L}{L_o} \tag{1}$$

$$strain\ rate = \dot{e} = \frac{\delta L / L_o}{\delta t} \tag{2}$$

where L_f and L_o are the final and initial lengths, respectively. This definition of strain, often referred to as "engineering strain" or "nominal strain," is derived with the assumption that the change in length δL is very small compared to the original length of the object or parcel.

However, errors are introduced when this approximation is used for a parcel that is strained significantly and incrementally, such as an ice parcel flowing through a glacier. In this case, a different definition that essentially compares a length change to the current length, rather than the original length, is more appropriate, because the calculated strain will depend on the history of strain experienced by the parcel. This is an integrated quantity, and is known as "true strain" or "logarithmic strain:"

$$\int_{\Delta t} \dot{\epsilon} dt = \int_{L_o}^{L_f} \frac{\delta L}{L(t)} \tag{3}$$

$$\dot{\epsilon} = \frac{1}{\Delta t} \ln\left(\frac{L_f}{L_o}\right) \tag{4}$$

Engineering strain and logarithmic strain will be approximately equal if length change is less than 2% of the original length [*Rees*, 2006]. As ice parcels frequently experience more than a 2% strain, logarithmic strain can be used to take the strain history of the parcel into account.

A simple example can illustrate the relationship between engineering strain and logarithmic strain, which, under ideal conditions with exact integration of particle trajectories, must yield the same result. Assume that we have two particles moving in one dimension through a known velocity profile (Figure 4.1).

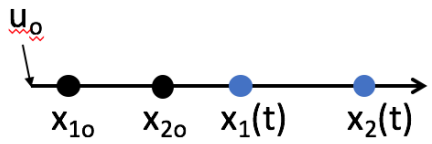

Figure 4.1 | The movement of two particles through a linear velocity field.

If the velocity profile is expressed by the linear equation $u = u_o + \alpha x$, where α is a constant, we can differentiate this equation to find the only component of the strain rate tensor:

$$\frac{du}{dx} = \alpha \tag{5}$$

Because the velocity is increasing linearly in space, the strain rate in this velocity field is spatially constant.

We have just found the strain rate of the velocity profile using the derivative of the velocity field, which is a direct application of the 1d strain rate tensor. A discretized solution would find the strain rate by differencing the velocities across some distance. Now we will derive the strain rate by asking how the distance between the particles changes as they move through the velocity field. This is an integration that uses the definition of logarithmic strain,

which takes into account the velocity history of each particle. In the case considered, the velocity profile is linear, making the integration very straightforward. The positions through time of each of the tracked particles are written:

$$x_1(t) \rightarrow \frac{dx_1}{dt} = u(x_1) = u_o + \alpha x_1 \tag{6}$$

$$x_2(t) \rightarrow \frac{dx_2}{dt} = u(x_2) = u_o + \alpha x_2 \tag{7}$$

Equations 5 and 6 describe the original particle positions sketched in Figure 4.1 when we apply the initial conditions $x_1 = x_{1o}$ and $x_2 = x_{2o}$.

At this point, we have defined the exact velocity profile that is experienced by each of the particles we are tracking. Now we wish to integrate over the domain to obtain the displacement of each particle. Following the first particle, we may separate equation 6 to become:

$$\int_{x_{1o}}^{x_1} \frac{dx}{u_o + \alpha x} = \int_0^t dt \tag{8}$$

$$t = \frac{1}{\alpha}[\ln(u_o + \alpha x_1) - \ln(u_o + \alpha x_{1o})] \tag{9}$$

We wish to know the position of the particle, so we solve for x_1:

$$\alpha t = \ln\left(\frac{u_o + \alpha x_1}{u_o + \alpha x_{1o}}\right) \tag{10}$$

$$\frac{u_o + \alpha x_1}{u_o + \alpha x_{1o}} = e^{\alpha t} \tag{11}$$

$$x_1(t) = \frac{(u_o + \alpha x_{1o})e^{\alpha t} - u_o}{\alpha} \tag{12}$$

Similarly, for $x_2(t)$, we have:

$$x_2(t) = \frac{(u_o + \alpha x_{2o})e^{\alpha t} - u_o}{\alpha} \tag{13}$$

We can find the initial length between the points through simple subtraction of the point locations:

$$L_o = x_{2o} - x_{1o} \tag{14}$$

Similarly, we can find the final length by subtracting the integrated equations (12) and (13):

$$L_f = x_2(t) - x_1(t) = \left(\frac{(u_o + \alpha x_{2o})e^{\alpha t} - u_o}{\alpha}\right) - \left(\frac{(u_o + \alpha x_{2o})e^{\alpha t} - u_o}{\alpha}\right) \tag{15}$$

This reduces to:

$$L_f = (x_{2o} - x_{1o})e^{\alpha t} \tag{16}$$

Now we can plug the initial and final lengths into the derivative of the logarithmic strain defined in equation (4). In this case, rather than writing a discrete time step, we will have taken an exact derivative of the strain with respect to time to obtain the strain rate:

$$\dot{\epsilon} = \mathrm{dln}\left(\frac{(x_{2o} - x_{1o})e^{\alpha t}}{x_{2o} - x_{1o}}\right)/dt \tag{17}$$

This reduces to:

$$\dot{\epsilon} = \frac{dln(e^{\alpha t})}{dt} = \frac{d(\alpha t)}{dt} = \alpha = \frac{\partial u}{\partial x} \tag{18}$$

Thus, where we can calculate exact derivatives, such as in an exactly linear velocity profile, the two definitions of strain rate yield the same result. However, errors may be introduced if finite differences are used without integration, as in the direct differencing of du/dx (the definition of the 1d strain rate tensor). Instead, the integrated logarithmic version should be used for large displacements to most accurately approximate true strain values in glacial ice.

4.3: Applications of strain rates in glaciology

Some of the first calculations of the strain rate tensor on a glacier were made by J.F. Nye as part of the 1956 Cambridge Austerdalsbre Expedition [*Nye*, 1959]. Nye's method calculated the surface strain rate at a point by measuring changes over time in a grid of five stakes. Multiple measurements were made between stakes to minimize error and take into account strain rate patterns averaged over a length scale of interest. The stakes were placed as shown in Figure 4.2, and measurements were taken of each labeled distance, as well as the angles between the stakes. Nye oriented the x-axis along-flow, and laid out the grid as close to a perfect square as possible.

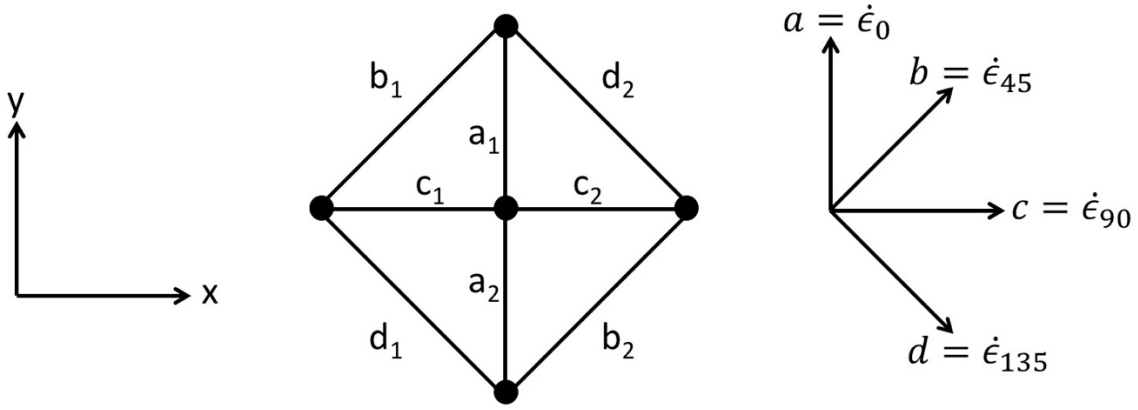

Figure 4.2 | Stake setup used by Nye (1959) to measure the strain rate tensor.

Returning after some period of time, the change in length of each segment defining the grid was recorded, and the initial and final lengths (L_o and L_f) were used, along with the time interval, to calculate the strain rate for each segment using the logarithmic strain equation (4). Each of the components was averaged with their corresponding component on the opposite

side of the grid in order to account for the variation of the strain rate tensor across the square. This resulted in four measured strain rates: a, b, c, and d, which correspond to $\dot{\epsilon}_0$, $\dot{\epsilon}_{45}$, $\dot{\epsilon}_{90}$, and $\dot{\epsilon}_{135}$. A least-squares method was used to estimate the longitudinal, transverse, and shear strains calculated from these averages (Section 4.3).

Nye (1959) measured strain rates in part to investigate the relationship between stresses and crevasse formation. Using the measured strain rates and a postulated flow law for ice, Nye calculated the principal stresses within the flowing ice. His results supported the hypothesis that crevasses would form perpendicular to the greatest tensile principal stress. He noted, however, that the stake locations were not well-placed to capture crevasses, and that many complexities remained in the study, such as accounting for advection of crevasses into regions with different principal stresses.

Nye's calculation of principal stresses is one of the most fundamental applications of strain rates in glaciology. At the time of Nye's 1959 paper, the flow law for ice, which has become known as Glen's Flow Law, had been only recently developed [*Nye*, 1953; *Glen*, 1955]. Glen's flow law is a power-law relation between strain rate and stress in ice. This law may be expressed in terms of the effective stress and strain rates (the second principal component of each tensor, respectively):

$$\dot{\epsilon}_{eff} = A\tau_{eff}^{n} \tag{19}$$

Or generalized to any tensor component:

$$\dot{\epsilon}_{jk} = A\tau_{eff}^{n-1}\tau_{jk} \tag{20}$$

For both equations, the coefficient *A* is the creep parameter, which indicates how easily the ice deforms. The creep parameter depends strongly on ice temperature, among other factors. The

exponent n is generally approximately equal to 3, but the value varies with the applied stress [*Cuffey and Paterson*, 2010]. Glen's Flow Law is an empirically derived relationship, and a single set of parameters is not appropriate for all scenarios. The choice of values for A and n can have large impacts on the results when the equation is inverted for stress. Despite the uncertainties associated with the choices of A and n, Glen's Flow Law remains the best constitutive relationship available describing the flow of ice, and is a fundamental component of ice flow models. In addition, if measurements of surface velocities are available, strain rates can be calculated and Glen's Flow Law can be inverted to derive estimates of A or of the basal shear stress [e.g. *De Rydt et al.*, 2015].

Although much can be discussed regarding the fundamental use of strain rates in ice flow models, this chapter is concerned with the calculation and use of strain rates from satellite-derived velocity grids. Many authors use these fields to gain a qualitative understanding of ice flow behavior. For example, Rignot et al. (2011) created an InSAR velocity grid of the Antarctic Ice Sheet, and used a map of effective strain rates to examine the inland penetration of shear margins, which indicate a high degree of coupling between inland ice and fast coastal ice streams. Strain rates also add dimension to descriptions of glacier surge cycles, showing clearly which areas have abruptly accelerated and decelerated and illustrating changes in the influence of tributary glaciers [e.g. *Murray et al.*, 2003; *Burgess et al.*, 2012].

Studies on surging glaciers also show the importance of strain rates for revealing other characteristics of glacier flow, such as ice thinning and thickening patterns. Ice thinning and thickening is generally expressed through vertical velocity, which is the product of vertical

strain rate and ice thickness. Assuming ice is incompressible, vertical strain rates are the result of divergence in horizontal velocity, and can be written:

$$\dot{\epsilon}_z = -\dot{\epsilon}_x - \dot{\epsilon}_y \tag{21}$$

Vertical velocities can then be written as the integral of equation (21):

$$w = -\int \dot{\epsilon}_x dz - \int \dot{\epsilon}_y dz \tag{22}$$

If we can assume that horizontal strain rates are constant throughout the ice thickness, which is approximately true on ice shelves and fast-flowing glaciers and ice streams, then the vertical velocity is simply the vertical strain rate (calculated from horizontal strain rates) multiplied by the ice thickness.

A qualitative picture of vertical strain rates can be useful for tracking the progression of a surging glacier [*Burgess et al.*, 2012]. Vertical strain rates can also be used more quantitatively to understand dynamic mass loss from glaciers that are out of equilibrium. For example, several glaciers feeding the Larsen B Ice Shelf accelerated significantly after its 2002 collapse, with concurrent increases in longitudinal strain rates. Immediately following the collapse, vertical strain rates indicated that feeder glaciers were thinning at rates of 10-25% annually [*Scambos et al.*, 2004]. Comparisons of strain rates with ICESat elevation profiles indicated that mass loss at this time was due primarily to the observed dynamic changes, rather than surface or basal mass balance.

Vertical strain rates – or, more explicitly, the divergence of horizontal velocity – are also inherent in assessments of mass balance at a given location. Again, if we assume that ice is incompressible, we can write the mass balance equation for flowing ice following Jenkins and Doake (1991):

$$\frac{\partial H}{\partial t} = \dot{\alpha}_s + \dot{\alpha}_b - \nabla \cdot (H\boldsymbol{u}) \tag{23}$$

In this equation, $\dot{\alpha}_s$ and $\dot{\alpha}_b$ are rates of surface and basal accumulation, respectively, H is the ice thickness, and t is time. $\boldsymbol{u}$ is a vector of horizontal velocities, which are assumed to be constant throughout the vertical column. Expansion using the chain rule makes the dependence on strain rates explicit:

$$\frac{\partial H}{\partial t} = \dot{\alpha}_s + \dot{\alpha}_b - H\left(\dot{\epsilon}_x + \dot{\epsilon}_y\right) + u\frac{\partial H}{\partial x} + v\frac{\partial H}{\partial y} \tag{24}$$

Because this requires the assumption of constant horizontal velocities in the vertical direction, it is best suited to ice with very little basal shear stress, such as ice shelves. Given independent estimates of $\partial H/\partial t$, surface mass balance ($\dot{\alpha}_s$), and ice thickness (H), velocity grids may be used to calculate horizontal strain rates which can be used with equation (24) to calculate rates of basal mass balance ($\dot{\alpha}_b$) on Antarctic ice shelves [*Rignot et al.*, 2013]. Since many ice shelves are losing mass rapidly due to melting from warm ocean waters, these calculations are important measures of the current state of the ice shelves and therefore of the Antarctic Ice Sheet.

In areas where basal shear stress is more significant, strain rates may reveal information about the character of the bed. Bindschadler et al. (1996) noted that positive vertical strain rates on Ice Streams D and E (Bindschadler and MacAyeal Ice Streams feeding the Ross Ice Shelf) correlate very well with areas of rough surface topography. It is unlikely that the surface topography is a simple reflection of basal topography, as this model would require vertical strain rates close to zero at all times. Instead, the authors hypothesize that the rough areas are caused by sticky spots in the ice stream beds. For example, a steep downward slope in the bed

may reduce basal water pressure, reducing lubrication and increasing the basal shear stress. This leads to flow convergence, which thickens the ice with positive vertical strain rates.

Although it remains difficult to constrain details, surface strain rates may also be used to learn about general characteristics of a sub-glacial hydrologic system and its effect on ice flow. For example, Rumrill (2009) used a network of GPS stations around Swiss Camp, Greenland, to analyze changes in flowline strain rates over two spring/summer seasons. Others have suggested [e.g. *Zwally*, 2002] that drainage of meltwater from the surface to the base of the ice sheet can cause widespread basal sliding and increases in velocity, which could potentially cause dynamic instability leading to very large mass losses if warming and surface melt continue to increase. Rumrill (2009) analyzed strain rates rather than velocities to assess the extent of sliding. The results showed large increases in strain rates concurrent with spring melting events. If sliding were widespread, strain rates would have stayed relatively constant, reflecting a uniform increase in velocity. The increase in strain rates indicates that sliding is limited to local regions, with velocity effects in the larger neighborhood driven by longitudinal coupling rather than by large regions of basal sliding. Therefore, at least in the study area, it is unlikely that increased surface melt could lead to a widespread sliding instability.

Howat et al. (2008) used a similar network of GPS stations on Breiðamerkurjökull in Iceland to observe glacier motion through several rainfall and enhanced melt events. In this study, observed surface horizontal strain rates were used to calculate vertical strain rates, which were in turn used to obtain an estimate of bed separation due to high basal water pressure during melt events. They also used the strain rates to estimate stress gradients along a flowline at the center of the glacier. Their results reveal a different glacier motion response

near the head and terminus of the glacier. Specifically, they suggest that less efficient drainage systems are found up-glacier, where a cavity system causes significant vertical uplift and increased velocities during melt events, and that more efficient drainage systems are found down-glacier where melt-event motion effects are less drastic. A significant longitudinal stress gradient is found between these regions. They also note that temporal evolution of the subglacial hydrologic system has large impacts on the measured values.

The detailed analyses described above used GPS installations to measure strain rates almost continuously, allowing them to capture short-term melt events and temporal evolution in hydrologic controls. As satellite observations are available only at much lower temporal resolutions, these detailed analyses are unlikely to be possible using satellite-derived strain grids. However, even monthly to seasonal changes may be captured by satellite imagery and could reveal features of the bed or the hydrologic system in areas where *in situ* data are unavailable.

Strain rates describe the stretching or compressing of ice as it flows. When stretched at great enough strain rates, ice can become brittle and form crevasses. Many authors have explored the relationships between strain rates and crevasse formation. As mentioned above, Nye (1959) showed that crevasses present in his study area were formed roughly perpendicular to the direction of greatest principal stress, which was calculated from the measured strain rates. Many other studies have demonstrated similar relationships [e.g. *Ambach*, 1968; *Bindschadler et al.*, 1996], although this relationship is far from exact in areas with complex dynamics [*Colgan et al.*, 2016]. Other studies have attempted to define a threshold failure criterion using strain and/or stress that could be used to predict areas of crevasse formation.

Vaughan (1993) compiled many of the datasets available at that time from locations in Antarctica, Canada, and Europe. The study compared strain rates and calculated stresses over locations with crevasses, without crevasses, and in close proximity to crevasses. The strain rates varied by a factor of 500 throughout the sites considered. However, when converted to stresses, which accounts in large part for temperature variations among other factors, the threshold variations were reduced to a factor of ~4. The study was hampered by data paucity, possible misidentification of crevasses in satellite imagery, and the inability to distinguish between new, actively forming crevasses and old, inactive crevasses.

Despite the widely varying strain failure criteria, strain rates continue to yield useful results relating to crevasse formation. Crevasses that penetrate deeply enough near the terminus of a glacier or ice shelf cause blocks of ice to calve; therefore, strain rates are often used in the formulation of calving laws. Alley et al. (2008) showed a predictable relationship between the calving velocity (v_c) at ice shelf fronts in Greenland and Antarctica and the product of longitudinal strain rate, ice thickness, and ice shelf half-width:

$$v_c = \dot{\epsilon}_{lon} \cdot H \cdot w \tag{25}$$

This very simple relationship is physically based due to its dependence on longitudinal stretching, which weakens the ice, and predicts calving velocity very well on the ice shelves examined. It is also advantageous because it takes into account the geometry of the ice shelf front.

Other authors choose to represent the effects of strain rates with more physical detail. For example, Benn et al. (2007), following Nye (1957), used a calving model for tidewater glaciers that predicts calving when crevasses penetrate deep enough to reach the water line.

The relation used for crevasse depth balances longitudinal strain rates with rates of creep closure:

$$d = \frac{2}{\rho_i g}\left(\frac{\dot{\epsilon}_*}{A}\right)^{\frac{1}{n}} \tag{26}$$

where d is crevasse depth, ρ_i is ice density, g is acceleration due to gravity, and A and n are ice flow law parameters. $\dot{\epsilon}_*$ is the strain rate above some critical threshold for ice fracture, which, as noted above, can be very hard to constrain. They modified this model for crevasse depth by adding the stress of water within crevasses, and found that it performed well in predicting calving rates and glacier terminus position.

A final application of strain rates that we wish to highlight, which is of particular relevance to this dissertation, is the use of strain rates in assessing the stability of ice shelves. Ice shelves are found in many geometries, but typically form in embayments where shear stresses from ice rises and embayment walls buttress the ice flowing off the continent. These partially free-floating features depend on a balance of internal dynamics for stable flow. Some of these internal dynamics may be revealed by examining the strain rates.

Doake et al. (1998) analyzed the principal strain rates on the Larsen B Ice Shelf on the Antarctic Peninsula shortly after the collapse of the more northerly Larsen A Ice Shelf. They noted that the least principal strain rate component was primarily extensile near the ice front but compressive over most of the inland areas of the ice shelf. They suggested that an unbroken band of compressive least principal strain rates – a "compressive arch" – must be present near the ice front to maintain ice shelf stability. If a calving event breaches the compressive arch, an irreversible ice shelf retreat may take place. Their predictions were

verified a few years later when the ice front of the Larsen B continued to retreat, breached the compressive arch, and led to catastrophic disintegration.

More recently, Kulessa et al. (2014) applied a similar analysis to the Larsen C Ice Shelf, which lies to the south of the Larsen B embayment. They carried out a very similar analysis to Doake et al. (1998), but used the second principal stress, rather than the second principal strain rate, to measure the position of the compressive arch. Their results suggest that, even if large blocks of ice were to calve off of the Larsen C, it is unlikely to retreat catastrophically in the near future.

The examples described above are only a few of the many applications of surface strain rates to glaciological problems. Because they are used so commonly in important, fundamental assessments of ice flow, it is essential that strain rates are measured as accurately and consistently as possible. In the following sections, we present two Matlab codes that calculate strain rates from satellite-derived velocity grids following two methods commonly used in the literature. We present an analysis of accuracy for the two methods, and suggest a preferred method for strain rate calculations. We then use this method to create a data product of strain rates across the Antarctic continent.

4.4: Calculating strain rates from satellite-derived velocity grids

Most modern satellite-based estimates of ice velocity are presented as regular raster grids. It is therefore easiest to first calculate strain rates relative to the regular grid, and then rotate them to a desired direction, such as orienting them relative to the flow direction.

We investigate two methods of calculating strain relative to regular raster grids. The first approach uses direct differencing of the strain rate tensor:

$$\dot{\epsilon} = \begin{bmatrix} \frac{\partial u}{\partial x} & \frac{1}{2}\left(\frac{\partial v}{\partial x} + \frac{\partial u}{\partial y}\right) \\ \frac{1}{2}\left(\frac{\partial v}{\partial x} + \frac{\partial u}{\partial y}\right) & \frac{\partial v}{\partial y} \end{bmatrix} \quad (27)$$

In this approach, x- or y-velocities are subtracted from velocities some length scale away, and the results are divided by the length scale and combined according to equation 27. This method calculates engineering or nominal strain.

Our second and more complicated approach is an adaptation of Nye's strain square method. In this approach, virtual "stakes" are placed in a square on the velocity grid and allowed to move through the velocity field. The distances between each pair of stakes is recorded throughout the movement and used to calculate the logarithmic strain experienced by each segment. The measurements are reduced to the strain rate tensor at the center of the square using a least squares approximation. Detailed descriptions of both approaches are included in the following sections, and the commented codes are provided in Appendix 4.

4.4.1 Differencing strain rate code

As shown in section 4.1, a 1d strain rate is correctly defined as the instantaneous change in velocity with distance, du/dx. However, to implement this definition, velocity differences have to be taken over some finite distance:

$$\frac{du}{dx} = \frac{u2 - u1}{\Delta x} \quad (28)$$

This quantity is frequently seen in the literature, generalized to 2d and calculated from a velocity grid. This method gives the same result as looking at the relative velocities of pairs of

stakes that are allowed to move for some period of time at a single velocity, which is the value of the velocity pixel at their starting points. This does not take into account the variation of velocity across the distance through which a stake travels. Where there are large gradients in strain, in areas such as ice falls and shear zones, this approximation can introduce significant error into the calculations. Further, strain calculations using this approach are likely to be strongly affected by any noise in the velocity field, as strain rates are based on the velocities of only two pixels at a time and are generally not averaged in any way, unless a smoothing filter is applied to the original velocity grid or the produced strain rates. The steps of the differencing code are described below.

Inputs:

1. Geotiffs or raster grids of x- and y-velocities
2. Pixel size
3. Length scale

Calculation steps:

1. Initialization

This code requires the user to define a length scale over which the calculations are made. The chosen length scale depends both on the geometry of the flowing ice and the aspect of ice flow being studied. For instance, large-scale viscous processes manifest over a length scale governed by longitudinal stress-gradient coupling, which tends to be about 1-3 times the ice thickness in temperate mountain glaciers and 4-10 times the ice thickness in colder, grounded ice sheets [*Cuffey and Paterson*, 2010]. The length scale increases if the bed is very

slippery or if the ice is not grounded, such as in an ice stream or ice shelf [*Gudmundsson*, 2013b]. However, brittle behavior may arise when velocity gradients occur over much shorter length scales relative to the ice thickness, and investigators might be interested in small-scale patterns, which would necessitate the use of a smaller length scale. Note that the user-defined length scale really operates as a half-length scale in the calculations, as it is the length from the center pixel to the points from which strain is being calculated. The initialization stage also includes the creation of grids into which the results are written.

2. Calculation of grid-oriented strains

$\dot{\epsilon}_x$ is calculated by subtracting a grid of x-velocities from a grid with velocities shifted by twice the length scale in the x-direction, and then dividing by twice the length scale. The same procedure is applied in the y-direction. Similar grids are created for the shift in y-velocities in the x-direction, and x-velocities in the y-direction. The strain component $\dot{\epsilon}_{xy}$ is calculated using $\dot{\epsilon}_{xy} = \frac{1}{2}(\dot{\epsilon}_{xy} + \dot{\epsilon}_{yx})$. Calculated strain-rate values are assigned to the pixel centered between the differenced pixels.

3. Measure the flow angle counter-clockwise from the x-axis

The flow angle, θ, is calculated at the center of each pixel by looping through each velocity pixel and using simple trigonometry: $\theta = \tan^{-1}(v_y/v_x)$. The resulting values are adjusted according to quadrant so that they range between 0˚ and 360˚ and are recorded in a grid.

4. Rotate the strain rate tensor to align with the local flow angle

Ultimately we want to calculate flow-oriented strain rate components, so we apply a tensor rotation at each pixel so that components are calculated relative to the local flow-oriented coordinate system. The rotation is applied following Bindschadler et al. (1996):

$$\begin{bmatrix} \dot{\epsilon}_{lon} & \dot{\epsilon}_{shear} \\ \dot{\epsilon}_{shear} & \dot{\epsilon}_{trans} \end{bmatrix} = \begin{bmatrix} cos\alpha & sin\alpha \\ -sin\alpha & cos\alpha \end{bmatrix} \begin{bmatrix} \dot{\epsilon}_x & \dot{\epsilon}_{xy} \\ \dot{\epsilon}_{xy} & \dot{\epsilon}_y \end{bmatrix} \begin{bmatrix} cos\alpha & -sin\alpha \\ sin\alpha & cos\alpha \end{bmatrix} \quad (29)$$

This reduces to a set of three equations for the flow-oriented strain components:

$$\dot{\epsilon}_{lon} = \dot{\epsilon}_x \cos^2 \alpha + 2\dot{\epsilon}_{xy} cos\alpha sin\alpha + \dot{\epsilon}_y \sin^2 \alpha \quad (30)$$

$$\dot{\epsilon}_{trans} = \dot{\epsilon}_x \sin^2 \alpha - 2\dot{\epsilon}_{xy} cos\alpha sin\alpha + \dot{\epsilon}_y \cos^2 \alpha \quad (31)$$

$$\dot{\epsilon}_{shear} = \left(\dot{\epsilon}_y - \dot{\epsilon}_x\right) cos\alpha sin\alpha + \dot{\epsilon}_{xy}(\cos^2 \alpha - \sin^2 \alpha) \quad (32)$$

We also calculate the effective strain rate, which is a measure of the total strain magnitude, and is defined as the square root of the second invariant of the strain rate tensor. For a 2d tensor, this quantity is defined as:

$$\dot{\epsilon}_{eff} = \sqrt{\dot{\epsilon}_x \dot{\epsilon}_y - \dot{\epsilon}_{xy}^2} \quad (33)$$

Outputs:

Geotiffs of the longitudinal, transverse, shear, and effective strain rates.

4.4.2 Least squares approximation derivation

In order to adapt Nye's strain square method to a regular velocity grid, we find values for two components oriented horizontally and vertically relative to the grid ($\dot{\epsilon}_x$ and $\dot{\epsilon}_y$, corresponding to the *c* and *a* components in the strain square in Figure 4.2), and the shear strain relative to those directions ($\dot{\epsilon}_{xy}$, which is measured twice corresponding to the *b* and *d* components in Figure 4.2). To calculate strain rates in any direction from these components, we

can write the system of n equations corresponding to n strain component measurements, with three coefficients, as shown below:

$$a_{n1}\dot{\epsilon}_x + a_{n2}\dot{\epsilon}_{xy} + a_{n3}\dot{\epsilon}_y = \dot{\epsilon}_n \tag{34}$$

The application of equation (34) to our system yields four equations corresponding to the four directions in Nye's strain square. The three coefficients in each of the four equations in our system can be constructed as a matrix A, which depends on the angles of the strain component measurements taken, relative to the coordinate system that defines the three components we want to calculate. We have deliberately oriented the strain square so that $\dot{\epsilon}_{90} = \dot{\epsilon}_x$ (the *c* component of the strain square) and $\dot{\epsilon}_0 = \dot{\epsilon}_y$ (the *a* component of the strain square), so the coefficients for these two equations, according to the form of the system of equations written above, are simply $[1\ 0\ 0]$ and $[0\ 0\ 1]$, respectively. The coefficients for $\dot{\epsilon}_{45}$ and $\dot{\epsilon}_{135}$ could be determined equally simply if our coordinate system were rotated by 45˚. Therefore, we perform a rotation on the strain rate tensor as shown below:

$$\begin{bmatrix} cos\alpha & sin\alpha \\ -sin\alpha & co\square\alpha \end{bmatrix} \begin{bmatrix} \dot{\epsilon}_{xx} & \dot{\epsilon}_{xy} \\ \dot{\epsilon}_{xy} & \dot{\epsilon}_{yy} \end{bmatrix} \begin{bmatrix} cos\alpha & -sin\alpha \\ sin\alpha & cos\alpha \end{bmatrix} \tag{35}$$

When the matrix multiplication is completed, the expression for $\dot{\epsilon}_{45}$ can be found in the upper left entry, and the expression for $\dot{\epsilon}_{135}$ is in the lower right entry. These expressions are:

$$\dot{\epsilon}_{45} = \dot{\epsilon}_{xx}\cos^2\alpha + \dot{\epsilon}_{xy}cos\alpha sin\alpha + \dot{\epsilon}_{yy}\sin^2\alpha \tag{36}$$

$$\dot{\epsilon}_{135} = \dot{\epsilon}_{xx}\sin^2\alpha - \dot{\epsilon}_{xy}cos\alpha sin\alpha + \dot{\epsilon}_{yy}\cos^2\alpha \tag{37}$$

If we substitute 45˚ for □, we get the relevant coefficients for the remaining rows of the matrix A, which are $\left[{}^1/_2\ 1\ {}^1/_2\right]$ and $\left[{}^1/_2\ -1\ {}^1/_2\right]$ for $\dot{\epsilon}_{45}$ and $\dot{\epsilon}_{135}$, respectively. Then the whole coefficient matrix can be constructed:

$$\boldsymbol{A} = \begin{bmatrix} 0 & 0 & 1 \\ 1/2 & 1 & 1/2 \\ 1 & 0 & 0 \\ 1/2 & -1 & 1/2 \end{bmatrix} \tag{38}$$

The ideal system we are trying to solve is then represented by the matrix equation:

$$\dot{\epsilon}_c = \boldsymbol{A}\dot{\epsilon} \tag{39}$$

where $\dot{\epsilon}_c$ is a column vector of the measured strain rate components $\dot{\epsilon}_0$, $\dot{\epsilon}_{45}$, $\dot{\epsilon}_{90}$, and $\dot{\epsilon}_{135}$, $\boldsymbol{A}$ is the matrix of coefficients that depends on the angles at which the measurements were taken, and $\dot{\epsilon}$ is a column vector of the three strain rate components we wish to derive: $\dot{\epsilon}_x$, $\dot{\epsilon}_{xy}$, and $\dot{\epsilon}_y$. We wish to invert this equation to solve for $\dot{\epsilon}$.

However, because we have four measurements to solve for three unknowns, and because the measurements reflect both random errors and real gradients in strain across the strain square, we take error into account in the calculation. Instead of solving an exact system, we solve the equation:

$$\boldsymbol{r} = \boldsymbol{A}\dot{\epsilon} - \dot{\epsilon}_c \tag{40}$$

where r is the error. In the least squares method, we wish to minimize the sum of the squared components of the error vector r. Therefore, we square this equation, which can be represented as a sum of the error for each equation in the system in matrix notation:

$$\sum \boldsymbol{r}^2 = R = \dot{\epsilon}^T \boldsymbol{A}^T \boldsymbol{A}\dot{\epsilon} - 2\dot{\epsilon_c}^T \boldsymbol{A}\dot{\epsilon} + \dot{\epsilon_c}^T \dot{\epsilon}_c \tag{41}$$

The sum of the squared error R will be minimized when the partial derivatives of each component, with respect to the unknowns, are equal to zero. Taking this partial derivative, we get:

$$\frac{\partial R}{\partial \dot{\epsilon}} = 2\boldsymbol{A}^T \boldsymbol{A}\dot{\epsilon} - 2\boldsymbol{A}^T \dot{\epsilon}_c = 0 \tag{42}$$

Therefore, when least squares are minimized, we can solve for the unknowns that minimize error, $\hat{\hat{\epsilon}}$, using the equation:

$$\hat{\hat{\epsilon}} = (\boldsymbol{A}^T\boldsymbol{A})^{-1}\boldsymbol{A}^T\dot{\epsilon}_c \quad (43)$$

4.4.3: Numerical stake-tracking strain rate code

Although differencing codes are easy to implement and commonly seen in the literature, the application of techniques introduced in Nye (1959) hold a number of advantages. Nye's method not only honors the incremental nature of strain in ice by applying the logarithmic definition of strain, but it also measures strains surrounding an area and mathematically determines the best estimate of the strain rate at the central point. By numerically tracking virtual "stakes" through a satellite-derived velocity field, our modified version avoids assumptions of constant velocities throughout a time step or linear differences in velocities between measurement locations. The technique also allows for flexibility regarding the length scale being used, which can be chosen based on available pixel size and the nature of the problem being considered.

Inputs:

1. Geotiffs or raster grids of x- and y-direction velocities
2. Pixel size
3. Length scale
4. Tolerance

Calculation steps:

1. Initialization

As in the differencing code, the numerical stake-tracking code requires the user to specify a length scale relevant to the problem being studied. Also during the initialization phase, initial lengths (L_o) are assigned to each segment in the strain square according to Figure 4.2. For efficiency in the code, all calculations are performed on local grids extracted around each strain square. Stakes are assigned initial local coordinates within this grid according to the length scale used. Grids are also initialized for recording grid-oriented strains and central ice flow directions.

2. For-loop

A nested for-loop is defined and moves through each pixel in the velocity grid. Virtual stakes are placed in a strain square around each pixel, and assigned initial pixel-center velocities from the input velocity grids. A running strain counter is initialized at zero for each strain rate segment in the strain square.

Two arrays are extracted with the current pixel at the center. The first is a "local grid" that is, by default, twice the size of the strain square. Stake tracking is performed only within this local grid, rather than on the entire input velocity grid, to improve the efficiency of the code. A second, smaller grid is extracted with the dimensions of twice the length scale assigned. This grid represents just the area over the strain square. The average x- and y-velocities within this strain square grid are calculated and used to assign a time scale over which the stakes are allowed to move. The default is the time it takes a stake to move one-tenth of the length scale at the average velocity of the strain square (Section 4.5.4). A time step and time tracker are also initialized at this point.

3. While-loop

Each virtual stake in the current strain square is allowed to move at its current velocity for one time-step, in a simple Euler-forward numerical formulation:

$$x_1^{n+1} = x^n + u^n \Delta t \tag{44}$$

where the superscripts indicate the relevant time step, with x^n representing the current time step and x^{n+1} representing the following time step. Assuming the stake does not move outside of the local grid, at the end of the time step, the lengths of each strain segment are updated (L_f) and the strain and strain rate during that time step are calculated using $\dot{\epsilon} = \frac{1}{\Delta t} \ln\left(\frac{L_f}{L_o}\right)$,.

After the time step has been completed, an accuracy check is performed. The Euler-forward method calculates the final stake positions by allowing the stakes to move at their initial velocity throughout the time step. However, in reality each stake's velocity should change continuously as it moves. If the time step and the velocity gradients are both small, the Euler-forward method should have very little impact on the final stake positions. However, in areas with large velocity gradients, a smaller time step may be required to maintain accuracy. Therefore, we use an adaptive time-stepping approach.

At the end of each time step, after each stake's position x^{n+1} is calculated, a second calculation of the new stake position is made using an improved Euler method. In this method, the averaged velocities at the beginning and approximate end positions are used to move the stakes:

$$x_2^{n+1} = x^n + \frac{1}{2}(u^n + u^*)\Delta t \tag{45}$$

where u^* is the velocity extracted at the final stake position x_1^{n+1} calculated by the Euler-forward method. The difference between the positions at the next time step, x_1^{n+1} and x_2^{n+1}, can be used as a metric to ensure that errors remain small in the final result. We choose to use a relative error metric:

$$\left|\frac{(x_1^{n+1} - x_2^{n+1})}{x_2^{n+1}}\right| \leq tol \tag{46}$$

where the tolerance criterion tol is set by the user (the default is 10^{-4}). If the error in any stake position during the time step exceeds the defined tolerance limit, the time step is reduced by half and the iteration is repeated. If all stake positions are within the tolerance limit, the final strain segment lengths are updated as the new initial lengths, and the running total of strain experienced by each segment is updated. If necessary, the time step is reset.

The stakes are also assigned new current velocities for the next time steps. These velocities are determined using a bilinear interpolation function (function "locInterp2," included in Appendix 4) that acts on the local grid. Note that velocities and stake movements are calculated using x- and y-components; therefore, changes in the direction of the stakes are automatically applied at each time step. Then the process repeats, moving the stakes according to their new velocities.

The loop is ended either when a stake would move outside the local grid (an occurrence only likely to happen in areas with very high velocity gradients, where the average velocities used to determine the time over which the stakes are allowed to move is radically lower than a stake velocity) or when the sum of the time steps exceeds the total time allowed for stake movement.

4. Calculation of four component strain rates

At each time step, a running total of strain accumulated by each pair of stakes is recorded. At the end of stake movement, the total strain experienced is divided by the total time elapsed to find the final strain rate. The strain rates calculated for each segment are then averaged into the four component strain rates: $\dot{\epsilon}_0 = \frac{1}{2}(a_1 + a_2)$, $\dot{\epsilon}_{45} = \frac{1}{2}(b_1 + b_2)$, $\dot{\epsilon}_{90} = \frac{1}{2}(c_1 + c_2)$, and $\dot{\epsilon}_{135} = \frac{1}{2}(d_1 + d_2)$.

5. Calculate strain rates relative to the x- and y-axes: $\dot{\epsilon}_x$, $\dot{\epsilon}_y$, and $\dot{\epsilon}_{xy}$

While Nye's strain square was oriented so that $\dot{\epsilon}_0$ was parallel to the flow direction, the above formulation simply orients $\dot{\epsilon}_0$ parallel to the y-axis, regardless of the flow direction. This deliberate orientation makes the calculation of three strain-rate components relative to the x- and y-axes straightforward, using the derived least squares equations (equation 43):

$$\dot{\epsilon_x} = -\frac{1}{4}\dot{\epsilon}_0 + \frac{1}{4}\dot{\epsilon}_{45} + \frac{3}{4}\dot{\epsilon}_{90} + \frac{1}{4}\dot{\epsilon}_{135} \tag{47}$$

$$\dot{\epsilon}_{xy} = \frac{1}{2}\dot{\epsilon}_{45} - \frac{1}{2}\dot{\epsilon}_{135} \tag{48}$$

$$\dot{\epsilon}_y = \frac{3}{4}\dot{\epsilon}_0 + \frac{1}{4}\dot{\epsilon}_{45} - \frac{1}{4}\dot{\epsilon}_{90} + \frac{1}{4}\dot{\epsilon}_{135} \tag{49}$$

These values are recorded for each pixel in strain rate grids that are updated at each step in the for-loop.

6. Measure the flow angle counter-clockwise from the x-axis

The local flow angle at each pixel, θ, is calculated in the same manner as in the differencing code. This is the last step carried out within the for-loop; the final calculations can be made on the grids containing the strain rates and flow angles.

7. Calculate final flow-oriented strain rates

The three coordinate-oriented strain-rate components are rotated to the local flow direction at each pixel in the same manner as in the differencing code, using equations (30)-(32). We also calculate the effective strain rate according to equation (33).

Outputs:

Geotiffs of the longitudinal, transverse, shear, and effective strain rates

4.5: Evaluation of code performance using simulated velocity fields

In order to test that the strain rate codes are producing reasonable results, we use velocity fields that have known analytical strain rates. This also gives us the opportunity to assess the amount of error introduced by the numerical methods. We use two fields for validation and evaluation: a pure strain field that is shown analytically to have constant strain rates, and a flow field around a Rankine half-body that is very similar to flow around a nunatak or ice rise.

4.5.1: Derivation of pure strain field

A non-divergent, non-rotating velocity field exhibits “pure strain.” The non-divergence condition, which also implies that a parcel will not change in volume, is:

$$0 = \nabla \cdot \vec{v} = \frac{du}{dx} + \frac{dv}{dy} \tag{50}$$

We can define a velocity field in (x', y') coordinates that satisfies this condition using the form:

$$u'(x', y') = \alpha x' \tag{51}$$

$$v'(x', y') = -\alpha y' \tag{52}$$

From this field, we also know that the shear strain components dv/dx and du/dy must both be equal to zero. That gives us the strain rate tensor:

$$\dot{\epsilon}' = \begin{bmatrix} \alpha & 0 \\ 0 & -\alpha \end{bmatrix} \tag{53}$$

Note that this yields a constant strain field only when measurements are oriented relative to the x- and y-directions, with $\dot{\epsilon}_x = \alpha$, $\dot{\epsilon}_y = -\alpha$, and $\dot{\epsilon}_{xy} = 0$.

We can make this velocity field more flexible by allowing rotation through an arbitrary angle θ to a new set of coordinates (x, y). With θ defined as positive in the counter-clockwise direction, we can relate (x', y') to (x, y) using a coordinate system transformation:

$$\begin{bmatrix} x' \\ y' \end{bmatrix} = \begin{bmatrix} cos\theta & sin\theta \\ -sin\theta & cos\theta \end{bmatrix} \begin{bmatrix} x \\ y \end{bmatrix} \tag{54}$$

We also need to obtain equations for (u, v), the components of the velocity field along the new coordinates (x, y). Therefore, we rotate the vector (u', v') through the angle θ:

$$\begin{bmatrix} u \\ v \end{bmatrix} = \begin{bmatrix} cos\theta & -sin\theta \\ sin\theta & cos\theta \end{bmatrix} \begin{bmatrix} u' \\ v' \end{bmatrix} \tag{55}$$

Now we solve for u and v in terms of θ and α in the (x, y) coordinate system. First, carry out matrix multiplication to obtain an expression for u:

$$u = u'cos\theta - v'sin\theta \tag{56}$$

Then substitute the velocity field in the original coordinate systems for u' and v':

$$u = \alpha x' cos\theta + \alpha v' sin\theta \tag{57}$$

Now we want to apply the coordinate system rotation to substitute for $x'$and y':

$$u = \alpha(xcos\theta + ysin\theta)cos\theta + \alpha(-xsin\theta + ycos\theta)sin\theta \tag{58}$$

This can be simplified using distribution and trig identities:

$$u = \alpha(x(\cos^2\theta - \sin^2\theta) + 2ysin\theta cos\theta) \tag{59}$$

$$u = \alpha(xcos2\theta + ysin2\theta) \tag{60}$$

A similar progression is used to derive an expression for v:

$$v = -\alpha(ycos2\theta - xsin2\theta) \tag{61}$$

Using the two final equations for u and v, we take the partial derivatives $\partial u/\partial x$, $\partial u/\partial y$, $\partial v/\partial y$, and $\partial v/\partial x$ to obtain the final strain rate tensor:

$$\dot{\epsilon} = \begin{bmatrix} \frac{\partial u}{\partial x} & \frac{1}{2}\left(\frac{\partial v}{\partial x} + \frac{\partial u}{\partial y}\right) \\ \frac{1}{2}\left(\frac{\partial v}{\partial x} + \frac{\partial u}{\partial y}\right) & \frac{\partial v}{\partial y} \end{bmatrix} = \begin{bmatrix} \alpha cos2\theta & \alpha sin2\theta \\ \alpha sin2\theta & -\alpha cos2\theta \end{bmatrix} \tag{62}$$

Note that we can also add a constant velocity β to the pure strain field at some arbitrary angle ϕ:

$$u = \alpha(xcos2\theta + ysin2\theta) + \beta cos\phi \tag{63}$$

$$v = -\alpha(ycos2\theta - xsin2\theta) + \beta sin\phi \tag{64}$$

Because the added velocity is constant, it does not change the derivatives that comprise the strain rate tensor.

4.5.2: Pure strain field results

The pure strain field is useful for verifying the code and understanding the applied sign conventions. Flow vectors for a constant strain field centered on the origin are shown in Figure

4.3. This field was built with α equal to 0.01 and θ, ϕ, and β equal to zero. The function used to produce this field is included in Appendix 4.

Using these parameters, the constant strain field yields theoretical values of $\dot{\epsilon}_x = 0.01$, $\dot{\epsilon}_y = -0.01$, and $\dot{\epsilon}_{xy} = 0$. Both the differencing and numerical codes reproduce these values. The numerical code introduces a small amount of error in the slowest sections (of order 10^-5 at the maximum); the differencing code is more accurate because its assumption of linear velocity change is accurate for this field. Error introduced by the codes is discussed in more detail in section 4.5.4 on a more realistic strain field.

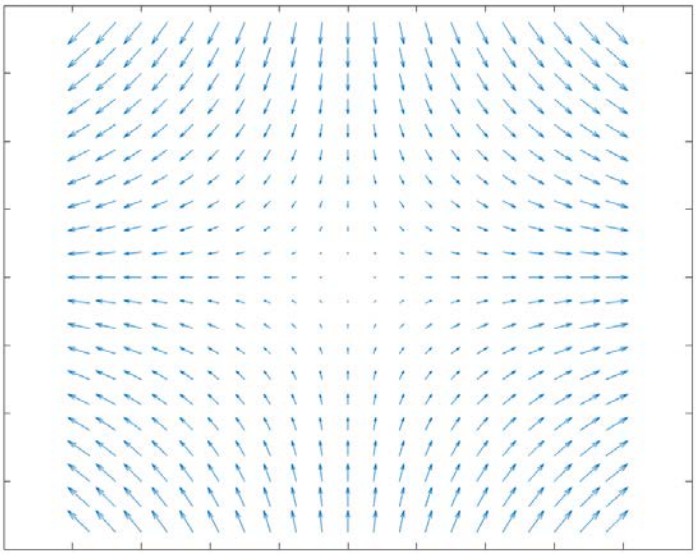

Figure 4.3 | Flow vectors for constant strain field.

Figure 4.4 shows results from the numerical code rotated to local flow directions, which can be understood using the flow vectors in figure 4.3. Figure 4.4A shows the longitudinal strain, with positive values between 315˚ and 45˚ as well as between 135˚ and 225˚, and negative values elsewhere. By following flow lines in Figure 4.3, it is evident that the regions

with positive longitudinal strain are areas where the velocity increases along a flow line; a parcel traveling in these regions will extend as it flows, conventionally referred to as positive longitudinal strain. Figure 4.4B is the transverse strain for the field, which measures stretching or compression across flow. In this case, the positive and negative values are reversed from the longitudinal strain field. In negative areas, flowlines approach each other, leading to transverse compression, while in positive areas the flow lines are spreading farther apart. Therefore, as with longitudinal strain, transverse strain is positive in extension.

Sign conventions for shear strain are more obscure. In Figure 4.4C, we see that the positive shear strains are found between 0˚ and 90˚, as well as between 180˚ and 270˚. If an imaginary parcel is placed in the field in one of these regions, the parcel would deform with the right-hand face moving downwards and the left-hand face moving up, relative to each other. This shear strain sign convention is maintained throughout this chapter.

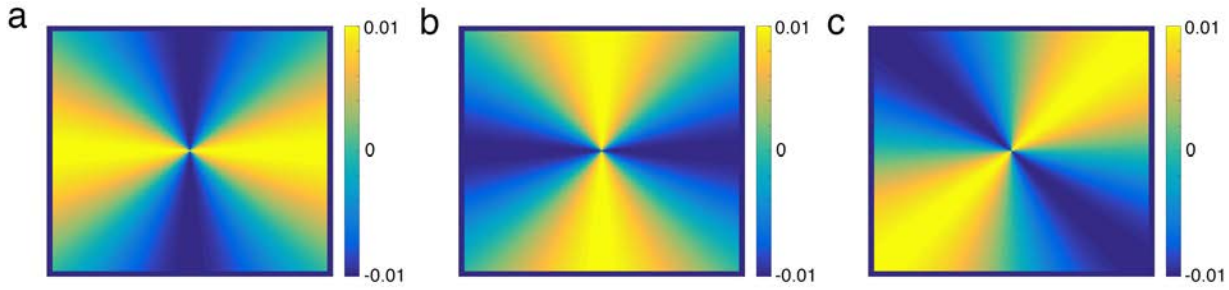

Figure 4.4 | Flow-oriented strain rate results for pure strain field.
a. Longitudinal strain. b. Transverse strain. c. Shear strain.

4.5.3: Derivation of strain field around a Rankine half-body

A pure strain field is useful for verifying and understanding the codes and sign conventions, but it is not realistic. In order to test the level of error in our codes, we create a strain field around a Rankine half-body, which yields patterns similar to flow around a nunatak

or ice rise within flowing ice. However, it is still likely to have smoother and more linear gradients than those found in the more complex systems of real glaciers and ice sheets.

We begin with a uniform flow in one direction. For convenience, we will limit this flow to the x-direction and give it a magnitude of U. Within this flow, we add a source point from which fluid is released evenly in all radial directions. We represent the source strength m as:

$$m = \frac{Q}{2\pi} \tag{65}$$

Then in Cartesian coordinates, the equation for flow from the point source can be represented in the x- and y-directions, respectively, as a simple sum of the uniform and source flows:

$$u = U + \frac{mx}{x^2 + y^2} \tag{66}$$

$$v = \frac{my}{x^2 + y^2} \tag{67}$$

Figure 4.5 shows the resulting flow vectors produced from these equations. Note that as x and y become very large, the velocity equations reduce to the far-field uniform flow, U. The stagnation point, shown as a red dot in Figure 4.5, is where all velocity goes to zero. As the uniform velocity field is only in the x-direction, we know that this stagnation point will occur directly in the x-direction from the source point, which we have placed at (0, 0), where the x-direction velocities cancel each other out. By setting $u = 0$ and solving for x with y equal to zero in equation (66), we find the x-coordinate of the stagnation point:

$$x_s = -\frac{Q}{2\pi U} \tag{68}$$

We also find the equation of the "surface streamline," which is the streamline passing through the stagnation point that outlines the surface of the Rankine half-body:

$$x = \frac{y}{\tan\left(\pi - \frac{2\pi U y}{Q}\right)} \tag{69}$$

To simulate an obstruction within the flow field, which has no flow through or across it, we simply set every value within the surface streamline to NaN.

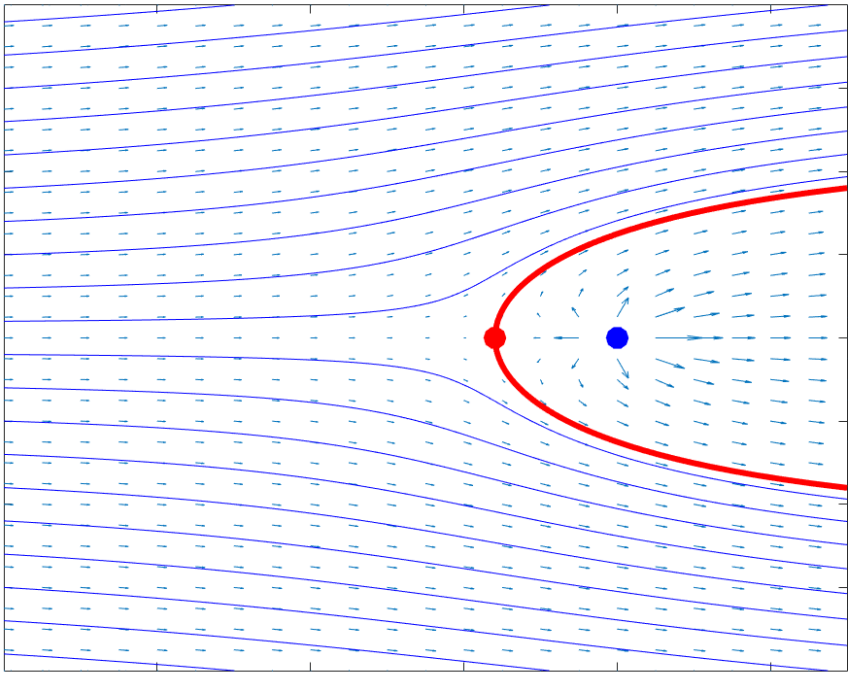

Figure 4.5 | Uniform flow field with fluid source (flow around a Rankine half-body). Arrows show direction of motion; length is proportional to speed. Blue lines are streamlines. Blue dot is fluid source. Red dot is fluid stagnation point. Red surface streamline outlines the Rankine half-body that may be treated as an obstruction in the flow field, similar to a nunatak or ice rise in a glacier or ice shelf.

From the velocity field equations, we can derive the analytical solutions for the components of the strain rate tensor:

$$\dot{\epsilon} = \begin{bmatrix} \frac{\partial u}{\partial x} & \frac{1}{2}\left(\frac{\partial v}{\partial x} + \frac{\partial u}{\partial y}\right) \\ \alpha\frac{1}{2}\left(\frac{\partial v}{\partial x} + \frac{\partial u}{\partial y}\right) & \frac{\partial v}{\partial y} \end{bmatrix} = \begin{bmatrix} \frac{m(y^2 - x^2)}{(x^2 + y^2)^2} & -\frac{2mxy}{(x^2 + y^2)^2} \\ -\frac{2mxy}{(x^2 + y^2)^2} & \frac{m(x^2 - y^2)}{(x^2 + y^2)^2} \end{bmatrix} \tag{70}$$

4.5.4 Rankine half-body error analysis

Because we can calculate an analytical solution for the $\dot{\epsilon}_x$, $\dot{\epsilon}_y$, $\dot{\epsilon}_{xy}$, and $\dot{\epsilon}_{eff}$ strain rates for the Rankine half-body flow field, we can develop some measure of accuracy for the two strain rate codes. It is important to note, however, that real strain rate fields are considerably more complicated and, particularly at shear margins, have much larger gradients in strain rates. Because this field only includes smooth, predictable changes that can be reasonably approximated in linear segments, we expect the differencing code to perform better than in more complex flow fields, where the logarithmic strain calculations and stake-tracking in the numerical code will be more important.

We use a simple measure of error to assess code accuracy: the mean of the absolute value of the difference between the calculated and theoretical strain fields. This is a single value that will not be representative of all areas. We chose a domain that encompasses the higher-strain regions near the tip of the Rankine half-body, but still includes large areas of very low strains where the differencing code is expected to perform better.

We also ran the codes on a smooth velocity field to which we added simulated noise in the form of a normally distributed perturbation with a mean of zero and a standard deviation of 2.5 m/yr, which is a low, though fairly reasonable, estimate for error associated with velocity grids derived from feature tracking in Antarctica.

Images of the results are shown in figure 4.6. In this scenario, we have used parameters similar to what might be found for a flow field around an island within an ice shelf, such as Berkner Island in the Filchner-Ronne Ice Shelf. The function used to create this field is included in Appendix 4. Both codes very closely reproduce the patterns expected from the theoretical

grids, and although random noise is very visible in the relevant images, the underlying patterns still closely represent the correct strain rates.

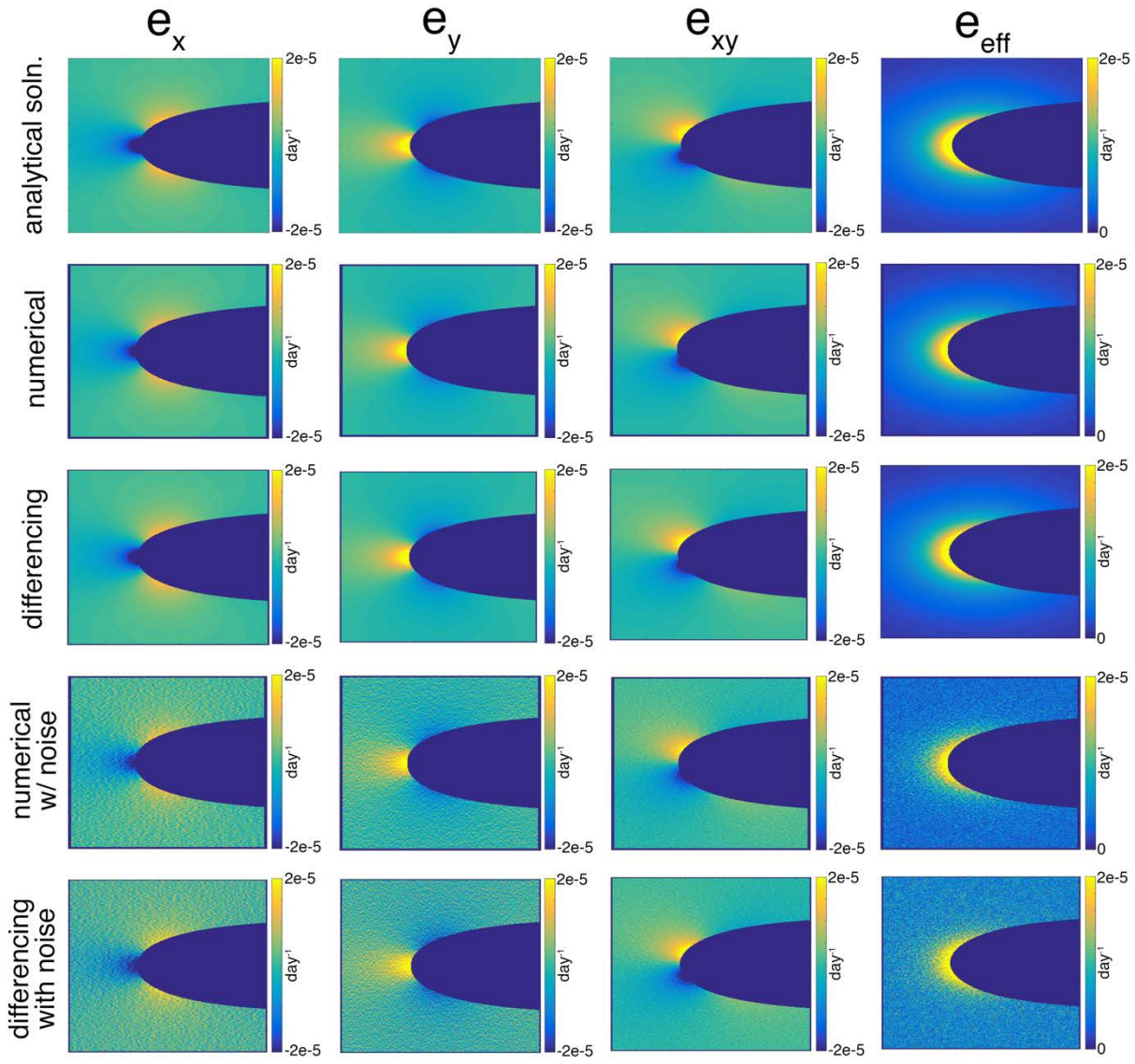

Figure 4.6 | Theoretical and calculated strain rate results for flow around a Rankine half-body.

Figure 4.7 shows the error associated with each code with and without Gaussian noise. Figure 4.7A shows that, without noise, the errors are generally on the order of 10^{-8} to 10^{-7},

which means they are generally between 0.1 and 1% of the actual values calculated for this scenario. The error for the differencing code stays almost constant regardless of length scale, because the smooth gradients in the velocity field are approximated well by linear assumptions regardless of differencing distance. The numerical code shows an increase in error with length scale, which is related to the error introduced by the number of times approximations are applied with every iteration. However, very few locations would rely on the larger length scales shown on the graph, and at maximum the error is less than 1% of typical values. The length scales more commonly used would yield even less error, at levels where the disparities between the differencing and numerical codes are not statistically significant.

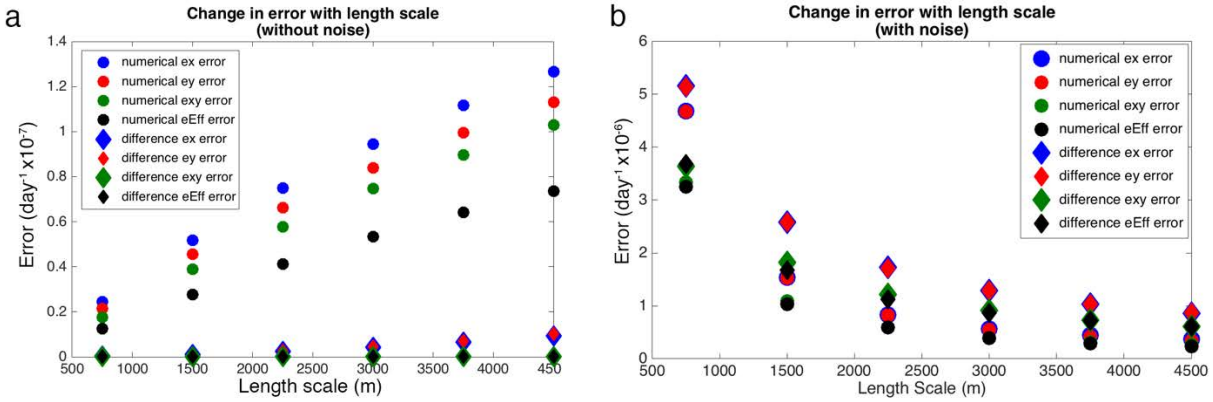

Figure 4.7 | Measure of error in Rankine half-body results at different length scales. Error measure is the mean of the absolute value of the difference between the calculated and analytical solutions. **a.** Error calculated without added noise. **b.** Error calculated with added Gaussian noise.

In addition, we conducted error tests on synthetic fields with added Gaussian noise, shown in figure 4.7B. In this case, error estimates were about an order of magnitude higher, yielding percentages roughly between 1% and 10%. This makes sense, as we have deliberately added some level of error to the original velocity grids. Furthermore, the results suggest that in

real data, any error added by larger numbers of iterations in the numerical code will be insignificant compared to any error in the data. With noise added, the numerical code has slightly lower levels of error. The reduced error is a consequence of the numerical code sampling over many pixels, which smooths out noisy measurements, whereas the differencing code calculates differences over just two measurements at a time, which can magnify error.

In contrast to the trends in error without noise, the fields with noise show a decrease in error as the length scale increases. This is due to a smoothing effect produced by spreading calculations over larger distances. The effect is slightly enhanced in the numerical code, which takes into account more of the velocity field, as it tracks stake velocities as they move. The differencing code relies on single points, which yield measurements more strongly affected by any error that happens to be associated with those individual points.

Overall, these tests show that both codes perform well on this relatively smooth strain field, both with and without added noise, and that error introduced by the numerical methods is insignificant. We also conclude, however, that the numerical code is more likely to be accurate when applied to a wide variety of real strain fields. Its use of logarithmic strain will make it more accurate in areas with high strain rates [*Rees*, 2006], and its numerical integration along stake paths makes it less sensitive to individual large errors. It also avoids the assumptions of linear changes in velocity inherit in the differencing code. We explore the impact of these differences on real data in section 4.6.

We performed a further error analysis on the numerical code to evaluate the impact of another relevant parameter: the amount of time the stakes are allowed to move. When Nye (1959) first developed his method to measure strain rates between stakes placed on a glacier,

the time interval between measurements was governed by the logistics of returning to the site. With the availability of a gridded velocity field, the options for stake movement time are much more flexible.

Figure 4.8 shows the error, calculated in the same manner as in Figure 4.7, associated with different time intervals for stake movement. We have measured the time intervals by using a "distance factor." In the code, the time a stake is allowed to move is determined relative to the average speed within the strain square. This standardizes the number of measurements in the velocity grid that are considered for each stake movement path. In this case, we have calculated the time interval as:

$$time\ interval = \frac{r * pixel\ size * distance\ factor}{average\ speed} \tag{71}$$

where r is the assigned length scale. Therefore, the distance factor approximately represents the number of length scales each stake is allowed to move.

Figure 4.8A shows the results for smooth fields with no added noise. As before, the error is very small, and increases with the distance factor, which is related to the repetition of the numerical approximation with larger numbers of iterations in the while loop. Figure 4.8B shows that, when a reasonable amount of Gaussian noise is added to the velocity fields, error decreases as a larger length scale is used. It appears that this decrease is generally asymptotic, although the differences in error are very small overall.

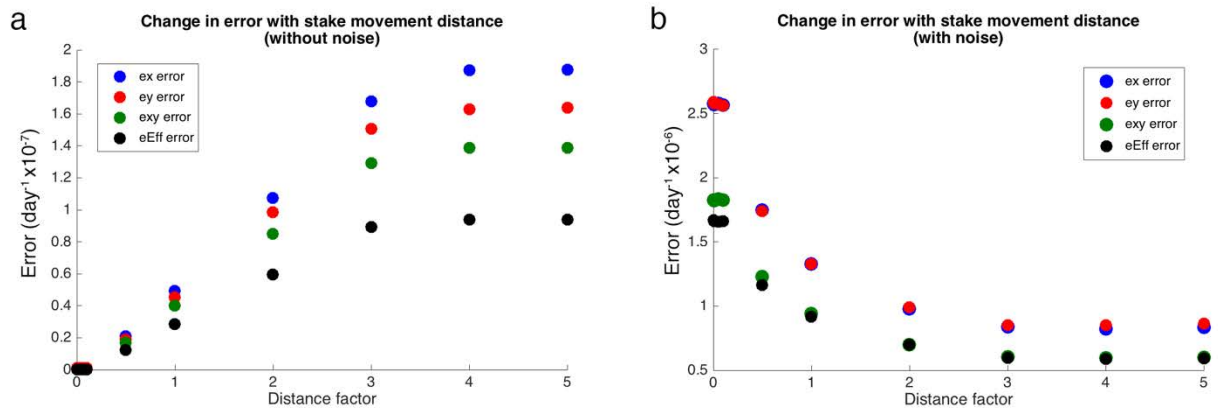

Figure 4.8 | Measure of error in Rankine half-body results for numerical code with different stake movement time intervals.
As in Figure 4.7, error measure is the mean of the absolute value of the difference between the calculated and analytical solutions. "Distance factor" is the number of length scales used to calculate how long stakes are allowed to move. **a.** Error calculated without added noise. **b.** Error calculated with added calculated Gaussian noise.

Since the choice of time interval does not introduce significant error regardless of distance factor, we choose a default distance factor of 0.1. That is, we allow the stakes around each center pixel to move for approximately one-tenth of a length scale. Although this causes slightly more error than a longer length scale, the differences are not statistically significant, and it helps minimize the code run-time. Over length scales used for Antarctica, this generally still allows stakes to move for many tens of meters.

However, in some situations it may be important to adjust this default. The calculation of strain rates using a velocity grid inherently assumes that the velocity field is constant. Over the time intervals considered, that is a good assumption in most cases. However, there may be situations, such as with surging glaciers, where it may be advisable to choose a smaller distance factor so that the signal of acceleration or deceleration between velocity grids is not obscured.

4.6: Impacts of code and length-scale choice on real-data results

In the above sections, we have derived two approaches for calculating strain rates from velocity grids: an approach that relies upon direct differencing of velocities, and a code that uses numerical methods to track virtual "stakes" as they move through the velocity field. Both of these codes extract velocities around a center point according to some length scale. Our tests on analytical velocity fields show that they successfully reproduce strain solutions with comparable accuracy, both with and without noise in the original fields. However, there are important differences between the codes that can impact accuracy, particularly in regions with large and complex strain-rate gradients where the linear approximations inherent in the differencing code are less appropriate. Although we can assume that the numerical code is more likely to produce accurate results in these scenarios, the following sections explore how much the differences in approach matter to the final results, as well as demonstrating the impacts of length-scale choice.

The results in the following sections are calculated using a pan-Antarctic velocity mosaic created from Landsat-8 image pairs [*Fahnestock et al.*, 2016]. This is also the mosaic used to produce our strain rate data products presented in section 4.7.

4.6.1: Impacts of code choice on real-data results

In order to explore the impacts of the calculation approach on real data, we extracted a section of the Fahnestock et al. (2016) Landsat-8 velocity mosaic around the Bindschadler and MacAyeal Ice Streams (also known as Ice Streams D and E) that feed the Ross Ice Shelf. We chose this region as representative of many areas of interest for strain rate calculations.

Although the strain rates are not the largest in Antarctica, they are still high at the shear margins, which is likely to highlight any differences between the codes. The ice streams also exhibit complex strain rate patterns between the shear margins. In addition, this is a region in which strain rates have been previously calculated [*Bindschadler et al.*, 1996] because they reveal important information about the ice stream flow patterns.

Figure 4.9 shows the percent difference between the results of the numerical and differencing codes for the region of interest. The percent difference is calculated as the absolute value of the difference between the two results divided by the absolute value of the results for the numerical code, multiplied by 100. As before, we have calculated effective, longitudinal, shear, and transverse strain rates. For this area, we have also added vertical strain rates, calculated following Bindschadler et al. (1996):

$$\dot{\epsilon}_z = -\dot{\epsilon}_{lon} - \dot{\epsilon}_{trans} \tag{72}$$

Vertical strain rates are of particular interest on ice streams and ice shelves because very low basal stresses mean that horizontal velocities are close to constant in the vertical. This means that vertical strain rates measured at the surface reasonably represent rates of thinning and thickening throughout the ice column.

Because we are showing differences as percentages, small differences in strain-rate results due either to code differences and/or random error in the original data yield much larger values in areas with very small strain rates, such as those generally found outside the ice streams. Therefore, most of the speckled values shown outside the ice streams can be treated as spurious noise. However, the areas within and along the edges of the ice streams show more reliable results, with the biggest errors found at shear margins. This is predictable, because

shear margins are typically where the largest strain rates, as well as the largest gradients in strain rates, occur, which leads to larger differences between engineering and logarithmic strain formulations.

The differences between the codes vary with the type of strain being calculated, but generally are not large, particularly within the ice streams. It is only in the narrow shear margins where significant errors are found. Very little difference is found at all for effective strain. Typical difference values in the shear margins for longitudinal and shear strains are below 10%, but can reach 20-30% in some areas. Vertical and transverse strains have much higher differences near the shear margins, typically above 10% and often reaching above 50% in areas that are not obviously noisy. There are also some significant differences within the ice streams for vertical and transverse strains, in areas of higher strain rates.

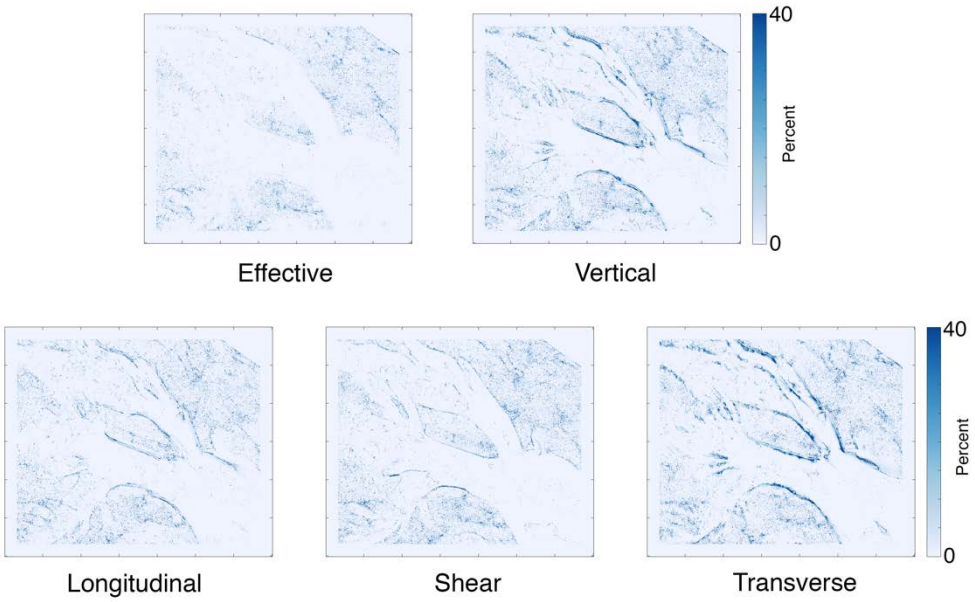

Figure 4.9 | Percent difference in strain rate calculations between the numerical and differencing codes for the Bindschadler and MacAyeal Ice Streams.
Both codes were run using a length scale of 3000 m, which means the effective averaging distance is ~6x the average ice thickness in this area. Percent difference is calculated as the absolute value of the difference between the two codes divided by the absolute value of the results of the numerical code, multiplied by 100.

As noted, we expect smaller differences between the codes, due to better performance from the differencing code, in areas with small strain-rate gradients where linear approximations between pixels are fairly accurate. There is also an interesting feedback in the strain rate calculations between differences in the codes, the local strain rate, and the length scale assigned. Rees (2006) noted that logarithmic strain formulations are significantly more accurate when an object strains more than ~2%. Although this sort of percentage measure is more obscure when differencing velocities, it is straightforward to understand in terms of the change in length of strain rate segments used in the numerical code. In an area with high strain rates, each strain rate segment will change length a relatively large amount during the designated time interval. So, we expect the numerical code with its logarithmic strain approach to perform better in areas with high strain rates. However, the length scale being used also becomes important. If a calculation is made with a larger length scale in an area with high strain rates, a comparable amount of absolute length change in a strain segment translates to a smaller percentage, and use of the logarithmic strain rate approach is not as important. Therefore, we expect smaller differences between the codes in areas with low strain rates and when using larger length scales.

Overall, we conclude that, in most locations, there is very little difference between the two approaches, and either code can be reasonably applied. However, if it is important to measure strain rates accurately at the shear margins or in other areas with high strain rates and/or high gradients in strain rates, there is a significant increase in accuracy associated with the use of the numerical code.

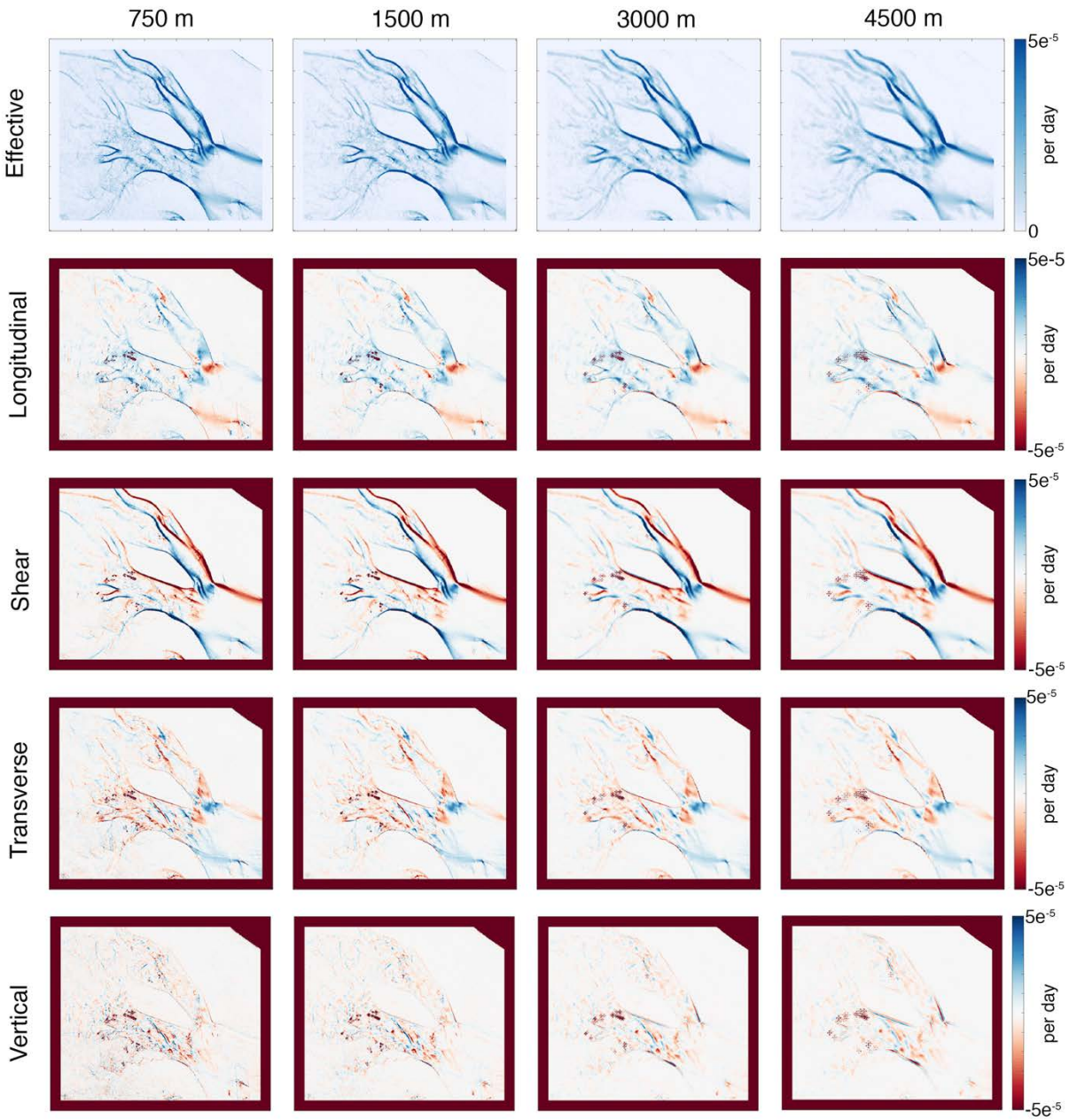

Figure 4.10 | Numerical code results for Bindschadler and MacAyeal Ice Streams at different length scales.
Labeled lengths are user-defined scales, representing half of the length scale used in the calculation.

4.6.2: Impacts of length scale on real-data results

Although differences between results produced by the two codes were relatively small, with significant differences confined to shear margins and areas of large strain, bigger differences are found associated with the use of different length scales. The use of a larger length scale has essentially a smoothing or averaging effect on the results, although this effect is achieved without applying any filters to the data. Figure 4.10 shows numerical code results for the MacAyeal/Bindschadler Ice Streams region at four different length scales. Close inspection of the images shows that shear margins and features within the ice streams tend to be thinner and more defined at smaller length scales, while at larger length scales shear margins spread to larger areas and some small-scale features are no longer visible.

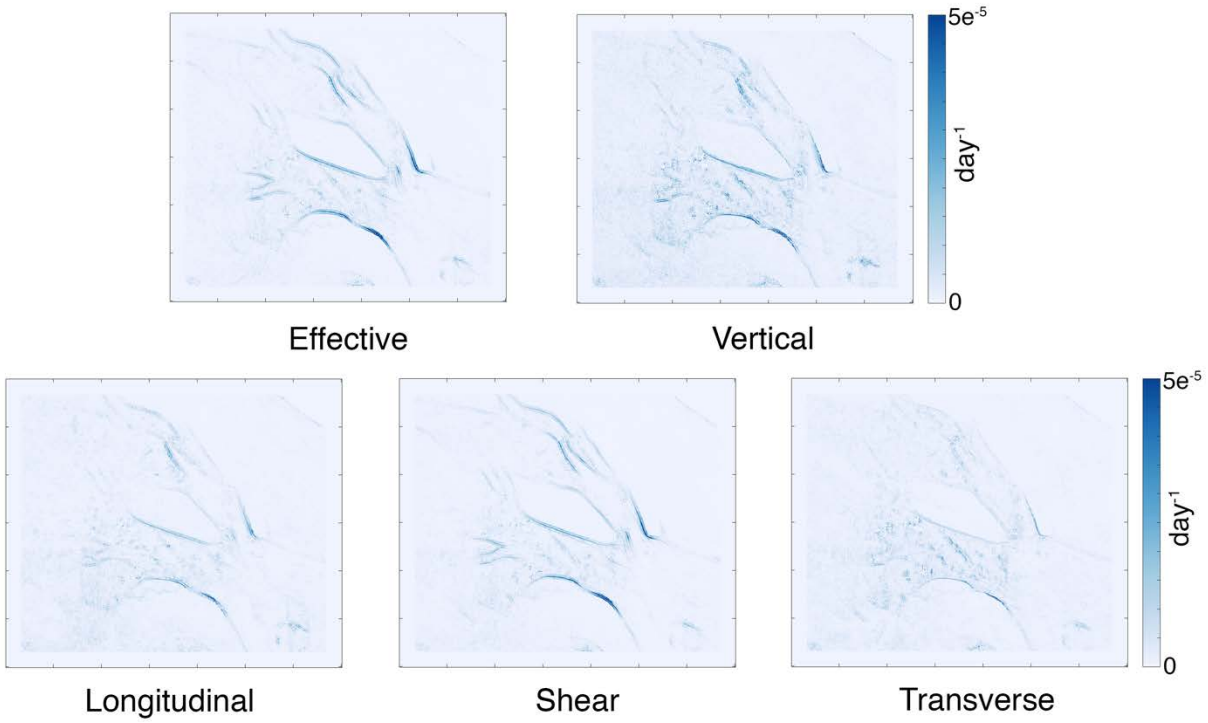

Figure 4.11 | Length-scale differences between numerical code strain rate calculations for the Bindschadler and MacAyeal Ice Streams.
Values shown are absolute values of differences. Half-length scales used are 1500 m and 3000 m.

Figure 4.11 shows the absolute value of the difference between the results at user-defined length scales of 1500 m and 3000 m (effective length scales of 3000 m and 6000 m). Note that the units used in this case are day^{-1}, and are the same units and order of magnitude as seen in the raw results in Figure 4.10. Though the magnitudes of the differences are smaller than the actual values, the fact that they are of the same order of magnitude indicates the importance of the choice of length scale in the resulting values.

As with the differences between the codes, the biggest differences are found at the shear margins. However, differences in length scale also cause differences of comparable magnitude in strain rates within the ice streams. Many of the strain rate patterns within the ice streams may reflect changes in basal shear stress around "sticky spots" in the bed [*Bindschadler et al.*, 1996]. Differences in the calculated strain rate values therefore translate to slightly different conclusions about the stickiness of those spots, particularly in relation to vertical velocities.

Unfortunately, deciding on a "correct" length scale is not straightforward. If large-scale features of the flow, such as thinning or thickening of the ice, are of interest, it is best to choose a length scale that reflects the viscous processes governing ice flow. Therefore, we seek a "longitudinal stress-gradient coupling" length that roughly indicates how far away a perturbation in one location can be felt by another ice parcel [*Cuffey and Paterson*, 2010]. Longitudinal coupling is governed by many factors such as effective viscosity, which relates strongly to ice temperature among other influences, ice thickness, and basal shear stress. Ice with higher viscosities, larger thicknesses, and lower basal shear stress exhibits longer longitudinal stress-gradient coupling lengths [*Cuffey and Paterson*, 2010; *Gudmundsson*,

2013b]. Additionally, crystal fabric orientation may make longitudinal coupling lengths anisotropic, putting our centered, isotropic approach to strain rate calculation at a disadvantage.

Of the major factors that govern longitudinal coupling length (effective viscosity, ice thickness, and basal shear stress), only ice thickness can currently be reasonably constrained across the Antarctic continent. Longitudinal coupling length scales in temperate mountain glaciers tend to be small because of high basal shear stresses and low ice viscosities, as well as small ice thicknesses, with length scales generally 1-3 times the ice thickness. Colder ice sheets have longitudinal coupling length scales that are typically 4-10 times the ice thickness [*Cuffey and Paterson*, 2010]. As ice sheets also tend to have much larger thicknesses, this leads to very large length scales for calculation. Since our strain rate data product covers the whole Antarctic continent, we choose to use viscous length scales that represent large-scale ice flow variations, and make a reasonable average estimate, related to ice thickness, for the length scales used throughout (Section 4.8).

If strain rate calculations are being made over smaller areas with known characteristics, a more accurate length scale may be determined. For the Bindschadler/MacAyeal Ice Streams region, we might consider typical ice thicknesses (~1000 m), basal shear stresses (very low), and ice viscosity (relatively high due to cold polar ice). Noting that the length scale defined in the code is really half of the length scale being averaged for a strain rate calculation, we might then choose to use a length scale of perhaps 5000 m, which would have an effective averaging length of ~10x the ice thickness. This would yield results close to those shown in the right-hand column in Figure 4.10, which shows strain rates at the margins affecting wide areas of ice flow,

and relatively smooth patterns of flow within the ice streams, although variations are still preserved.

If we are looking for effects that are related to brittle behavior, such as crevasse formation regions, or other small-scale features it may be better to consider strain rates over smaller length scales. Therefore, the selection of a length scale is both location- and application-dependent.

4.7: Error propagation and real-data error estimation

The following sections present two common ways to measure errors associated with the calculated strain rates. The first relies on a knowledge of the random error associated with the velocity grids, and propagates that error through the steps of the code. This method is included because it is commonly used, but we demonstrate that it gives unrealistic results in low-strain areas and that its strong dependence on the time the stakes are allowed to move is not reasonable. The second method, the calculation of standard error estimated through the least-squares approximation, is specific to the numerical stake-tracking formulation. If we assume that the error associated with the velocity grids is truly random, it can yield a fairly accurate estimate because it intrinsically accounts for the error present in the velocity grids according to the least-squares error minimization. However, error estimates increase in areas with high strain-rate gradients, which does not reflect an increase in random error.

4.7.1: Propagation of error estimated for the velocity grids

The calculation of velocity grids will always include some amount of random error. The relationship between the error in the velocity fields and the error in the output strain rate grids depends on factors like the local velocity and the amount of time stakes are allowed to move. Below we outline the application of standard error propagation rules to the random error in the velocity grids through the numerical stake-tracking code.

We will assume that a velocity grid has an associated random error magnitude of δv. Each stake in the grid is allowed to move for a certain amount of time Δt within the while-loop. The Euler-forward formulation moves stakes according to equation (44). In this formulation, the velocity is multiplied by a constant. We use the general error propagation rule for multiplication and division, when $R = X * Y$ or $R = X/Y$:

$$\delta R = |R| \sqrt{\left(\frac{\delta X}{X}\right)^2 + \left(\frac{\delta Y}{Y}\right)^2} \tag{73}$$

In the case of multiplication by a constant c, equation (73) simplifies to $\delta R = |c|\delta X$, or in our scenario:

$$\delta_{pos} = |\Delta t|\delta v \tag{74}$$

where δ_{pos} is the error associated with the new position of the stake at the end of the while-loop. We assume that the random error is isotropic, and therefore assign δ_{pos} as the error in both the x- and y-positions. Because each stake in a given strain square is allowed to travel for the same amount of time Δt, and because we are using a single value to represent the magnitude of random error across the velocity grid, we only need to calculate one value of δ_{pos} for each iteration.

We then use the old and new x- and y-positions to calculate the length of each strain segment, according to the distance formula:

$$l_f = \sqrt{(x_1 - x_2)^2 + (y_1 - y_2)^2} \tag{75}$$

This requires a combination of rules for error propagation. We have the same error δ_{pos} associated with all of the variables in the equation. We first apply error propagation for addition and subtraction within each set of parentheses; we will refer to this error as δ_{paren}:

$$\delta_{paren} = \sqrt{\delta_{pos}^2 + \delta_{pos}^2} = \sqrt{2\delta_{pos}^2} = \sqrt{2}\delta_{pos} \tag{76}$$

Then, the value inside each set of parentheses is squared. We use the error propagation rule for polynomial functions of one variable, such as $R = X^n$:

$$\delta R = |n| \frac{\delta X}{|X|} |R| \tag{77}$$

In this case, the error in δ_{paren}^2 is:

$$\delta_{xPos} = 2 \frac{\delta_{paren}}{|X_1 - X_2|} (X_1 - X_2)^2 \tag{78}$$

Note that here we reveal a dependence on the difference between the stake coordinate positions, which necessitates a separate error calculation for δ_{xPos} and δ_{yPos} for each of the strain rate segments.

Now we work within the square root sign, adding the errors for δ_{xPos} and δ_{yPos} according to:

$$\delta_{sqrt} = \sqrt{\delta_{xPos}^2 + \delta_{yPos}^2} \tag{79}$$

Finally, we need to find the error in the strain segment length by again using the error propagation rule for polynomials of one variable (equation 77), where the expression inside the square root sign is raised to one half:

$$\delta l_f = \frac{1}{2}\frac{\delta_{sqrt}}{(x_1 - x_2)^2 + (y_1 - y_2)^2} l_f \tag{80}$$

We will not back-substitute to show δl_f in terms of δv here, because the equations above comprise the progression used in code.

Once we have calculated the error δl_f for each strain rate segment, we have to propagate the error through the determination of logarithmic strain based on initial and final lengths (equation (3)). We do not have any error associated with the initial length, as we have defined that exactly based on the grid, and we are also assigning an exact time step. So, the only error we have to propagate through this equation is δl_f.

We first have division of the initial and final lengths within the natural logarithm, which uses a simplified version of equation 73 for division by a constant. Then we use the rule for error propagation through a natural logarithm $R = \ln(x)$:

$$\delta R = \frac{\delta X}{X} \tag{81}$$

In our case, the equation becomes:

$$\delta_{log} = \frac{\delta l_f}{l_f} \tag{82}$$

Finally, we again multiply by a constant Δt, which yields a value for the linear strain of each strain segment:

$$\delta_{strSeg} = \Delta t \delta_{log} = \Delta t \frac{\delta l_f}{l_f} \tag{83}$$

The linear strains calculated for each strain rate segment are not the final values produced by the code. There are several more calculation steps through which error continues to propagate. First, we average each pair of strain rate segments that measure in the same direction. For example, we would average the strain segments in the a_1 and a_2 directions to find $\dot{\epsilon}_0$, yielding the error estimate:

$$\delta\dot{\epsilon}_0 = \frac{1}{2}\sqrt{\delta\dot{\epsilon}_{a1}^2 + \delta\dot{\epsilon}_{a2}^2} \tag{84}$$

Then we calculate the coordinate-oriented strain rate values derived using the least-squares approximation (equations 47-49). This entails multiplication by constants and addition of errors:

$$\delta\dot{\epsilon}_x = \sqrt{\left(\frac{1}{4}\delta\dot{\epsilon}_0\right)^2 + \left(\frac{1}{4}\delta\dot{\epsilon}_{45}\right)^2 + \left(\frac{3}{4}\delta\dot{\epsilon}_{90}\right)^2 + \left(\frac{1}{4}\delta\dot{\epsilon}_{135}\right)^2} \tag{85}$$

$$\delta\dot{\epsilon}_{xy} = \sqrt{\left(\frac{1}{2}\delta\dot{\epsilon}_{45}\right)^2 + \left(\frac{1}{2}\delta\dot{\epsilon}_{135}\right)^2} \tag{86}$$

$$\delta\dot{\epsilon}_y = \sqrt{\left(\frac{3}{4}\delta\dot{\epsilon}_0\right)^2 + \left(\frac{1}{4}\delta\dot{\epsilon}_{45}\right)^2 + \left(\frac{1}{4}\delta\dot{\epsilon}_{90}\right)^2 + \left(\frac{1}{4}\delta\dot{\epsilon}_{135}\right)^2} \tag{87}$$

The coordinate-oriented strain rate components are used to create an estimate of error for the effective strain-rate field (equation 33), using similar applications of the rules noted above. We first calculate error for the multiplication of $\dot{\epsilon}_x$ and $\dot{\epsilon}_y$, along with the error for the squaring of $\dot{\epsilon}_{xy}$:

$$\delta\left(\dot{\epsilon}_x * \dot{\epsilon}_y\right) = \left|\dot{\epsilon}_x\dot{\epsilon}_y\right|\sqrt{\left(\frac{\delta\dot{\epsilon}_x}{\dot{\epsilon}_x}\right)^2 + \left(\frac{\delta\dot{\epsilon}_y}{\dot{\epsilon}_y}\right)^2} \tag{88}$$

$$\delta(\dot{\epsilon}_{xy}^2) = 2\frac{\delta\dot{\epsilon}_{xy}}{|\dot{\epsilon}_{xy}|}\dot{\epsilon}_{xy}^2 \tag{89}$$

Then an addition rule is applied to the error for each of these quantities:

$$\delta\dot{\epsilon}_{add} = \sqrt{\delta\left(\dot{\epsilon}_x * \dot{\epsilon}_y\right)^2 + \delta\left(\dot{\epsilon}_{xy}^2\right)^2} \tag{90}$$

Finally, a power rule is applied to find the error after the square root has been taken:

$$\delta\dot{\epsilon}_{eff} = \frac{1}{2}\frac{\delta\dot{\epsilon}_{add}}{|\dot{\epsilon}_x * \dot{\epsilon}_y - \dot{\epsilon}_{xy}^2|}\dot{\epsilon}_{e⍰f} \tag{91}$$

Errors are further adjusted when the strain rates are rotated relative to the local flow direction:

$$\delta\dot{\epsilon}_{lon} = \sqrt{(\delta\dot{\epsilon}_x \cos^2\alpha)^2 + \left(2\delta\dot{\epsilon}_{xy}\cos\alpha\sin\alpha\right)^2 + \left(\delta\dot{\epsilon}_y \sin^2\alpha\right)^2} \tag{92}$$

$$\delta\dot{\epsilon}_{trans} = \sqrt{(\delta\dot{\epsilon}_x \sin^2\alpha)^2 + \left(2\delta\dot{\epsilon}_{xy}\cos\alpha\sin\alpha\right)^2 + \left(\delta\dot{\epsilon}_y \cos^2\alpha\right)^2} \tag{93}$$

$$\delta\dot{\epsilon}_{shear} \tag{94}$$

$$= \sqrt{\left(\delta\dot{\epsilon}_y\cos\alpha\sin\alpha\right)^2 + (\delta\dot{\epsilon}_x\cos\alpha\sin\alpha)^2 + \left(\delta\dot{\epsilon}_{xy}\cos^2\alpha\right)^2 + \left(\delta\dot{\epsilon}_{xy}\sin^2\alpha\right)^2}$$

Errors for vertical strain rates are calculated from the errors for longitudinal and transverse strain rates:

$$\delta\dot{\epsilon}_z = \sqrt{\delta\dot{\epsilon}_{lon}^2 + \delta\dot{\epsilon}_{trans}^2} \tag{95}$$

4.7.2: Calculation of error from the least-squares approximation

Every strain rate calculated in the numerical stake-tracking code is determined using measurements within a strain square surrounding a center point, to which the results are assigned. We ultimately solve for three strain-rate components, which are found using four linear strain-rate directions. This is an over-determined system. If the data were perfect, we

would expect any set of three measurements to yield the same solution. Since the data are not perfect, the fourth measurement helps to distribute the measurements evenly in space around the center point and yield an average closer to the real value. The standard error associated with each strain square is a measure of the difference between results that should ideally yield the same answer. These differences are due in large part to random error in the velocity grids, though there is also a component due to large variations in strain rates around a center point, particularly when using larger length scales.

We derived the least-squares approximation (section 4.4.2) by minimizing the error vector r. We can calculate the components of a residual error matrix by using our original definition of $r = \boldsymbol{A}\dot{\epsilon} - \dot{\epsilon}_c$, and substituting in the formula we derived for calculating the strain rate components (equation 43) yielding:

$$\boldsymbol{r} = \boldsymbol{A}(\boldsymbol{A}^T\boldsymbol{A})^{-1}\boldsymbol{A}^T\dot{\epsilon}_c - \dot{\epsilon}_c \tag{96}$$

In our case, the quantity $\boldsymbol{A}(\boldsymbol{A}^T\boldsymbol{A})^{-1}\boldsymbol{A}^T$ is represented by the matrix:

$$\boldsymbol{A}(\boldsymbol{A}^T\boldsymbol{A})^{-1}A^T = \begin{bmatrix} 3/4 & 1/4 & -1/4 & 1/4 \\ 1/4 & 3/4 & 1/4 & -1/4 \\ -1/4 & 1/4 & 3/4 & 1/4 \\ -1/4 & -1/4 & 1/4 & 3/4 \end{bmatrix} \tag{97}$$

Then the whole matrix equation to calculate the error associated with each of the measured components of strain is:

$$\boldsymbol{r} = \begin{bmatrix} 3/4 & 1/4 & -1/4 & 1/4 \\ 1/4 & 3/4 & 1/4 & -1/4 \\ -1/4 & 1/4 & 3/4 & 1/4 \\ -1/4 & -1/4 & 1/4 & 3/4 \end{bmatrix} \begin{bmatrix} \dot{\epsilon}_0 \\ \dot{\epsilon}_{45} \\ \dot{\epsilon}_{90} \\ \dot{\epsilon}_{135} \end{bmatrix} - \begin{bmatrix} \dot{\epsilon}_0 \\ \dot{\epsilon}_{45} \\ \dot{\epsilon}_{90} \\ \dot{\epsilon}_{135} \end{bmatrix} \tag{98}$$

Each of the residuals will have the same absolute value for each strain square [*Nye*, 1959]. Then the standard error of the four measured strain rate components is:

$$r_s = \sqrt{4r^2}/(4-3) = 2|r| \tag{99}$$

where the denominator (4 – 3) represents the number of equations subtracted from the number of measurements. Using the same error propagation methods for multiplication by a constant and addition as used in section 4.7.1, we substitute $2|r_s|$ for the error values to calculate the standard errors for the grid-oriented strain-rate components. We find that $\dot{\epsilon}_x$ and $\dot{\epsilon}_y$ have standard errors of $\sqrt{3}|r_s|$, while the standard error of $\dot{\epsilon}_{xy}$ is $\sqrt{2}|r_s|$. Again following section 4.5.1, we can propagate the errors to the flow-oriented strain rates, the effective strain rates, and the vertical strain rates.

4.7.3: Comparison of error estimates

To compare the magnitudes and patterns of error estimate between the two approaches (error propagation and estimation of standard error through the least-squares method), we calculated both for the same region surrounding the Bindschadler and MacAyeal Ice Streams feeding the Ross Ice Shelf as used in section 4.6. For these calculations, we used a length scale of 5 times the ice thickness (which effectively averages over 10 times the ice thickness, a reasonable value for polar ice streams and ice shelves with very little basal shear stress), and an assumed δv of 5 m/yr or 0.0137 m/day.

The results are shown in Figure 4.12. Within the ice streams, with the selected set of parameters, both approaches calculate values of similar magnitude. The magnitudes are also similar to the strain-rate values themselves, indicating that errors are very large compared to

the measurements being made. This is a common feature of gradient measurements, which are very sensitive to error in the original data. Bindschadler et al. (1996) found comparable error magnitudes for this region. Without dramatic improvement in velocity calculation, errors in all gridded strain-rate measurements will remain large.

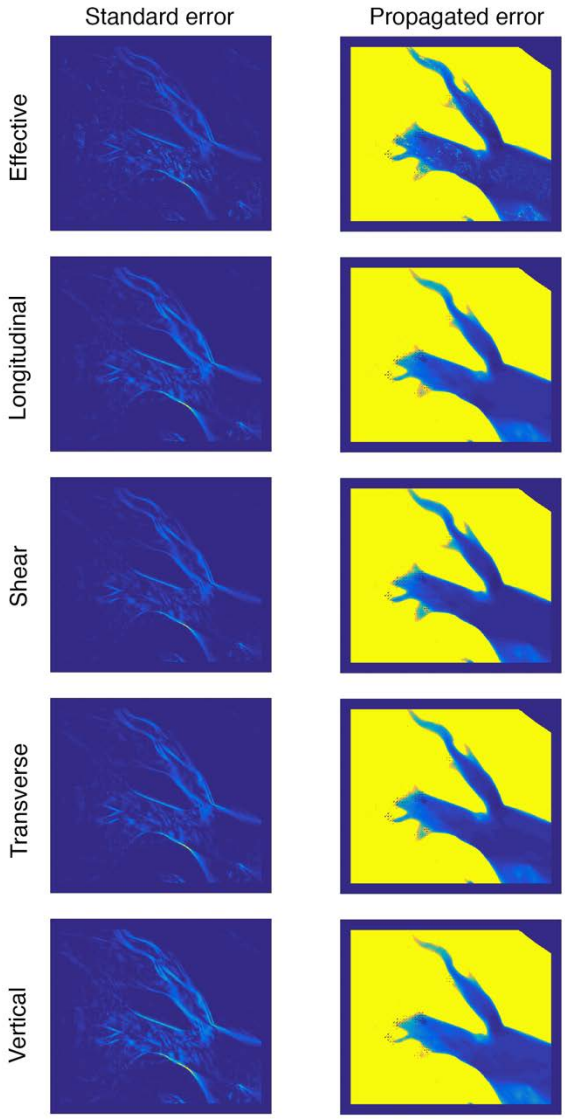

Figure 4.12 | Error estimate comparison for the Bindschadler and MacAyeal Ice Streams region. All units are per day, and color bars go from 0 to $10e^{-4}$.

However, both error estimates are unlikely to be realistic. As can be seen from equations (74) and (83), the propagated error depends very strongly on the time interval over which the stakes are allowed to move, with higher errors for larger stake movements. However, Figure 4.8 shows that, in our test fields, errors actually decrease when the stakes are allowed to move larger distances. In addition, areas outside the ice streams calculate with extremely high error values. This is due to the nature of the calculations

combined with the very low velocities and strain rates in these grounded areas. Because stake movement is governed by distance and local mean velocity, this means that the time factor is much larger in these areas. In addition, two of the calculations include division by the amount the stakes have moved in the x- and y-directions during the time interval. As the stakes move very little in slower areas, this value is very small, causing the error greatly increase. Finally, even small errors are large percentages in areas with very small calculated values.

Within the ice streams, the two methods of error calculation yield broadly similar patterns, though the standard error method includes considerably more detail. Particularly for estimates of standard error, areas of high error closely follow areas with high strain rate magnitudes. As the standard error is an estimate of the disagreement within the over-determined system solved within the strain square, it takes into account both the random error in the data and any real gradients in strain across the length scale being used. As real gradients in strain should not directly contribute to random error, the standard error is also not a good approximation of the error in the final strain rate fields.

We tested two modifications to the standard error approach to account for real gradients in strain across calculation regions. First, we fit the strain segment measurements taken around each pixel center to a plane, and subtracted the plane from real data to remove any linear trends. Though this method reduced error estimates slightly, the differences were not significant, which is probably due to the fact that a plane fits the data very poorly at shear margins. We also tried fitting a quadratic polynomial to the strain rate segment data. However, this method over-fit the data, yielding errors on the order of 10^{-17} day^{-1}, which are

unrealistically small values according to the tests we ran on synthetic strain fields with added noise.

We therefore suggest that empirical methods of error determination are most appropriate, such as Monte Carlo simulations (Section 4.8.2). Where Monte Carlo simulations are not feasible, such as over large areas where computing times become prohibitive, error may sometimes be estimated directly from the results. If an area has extremely low velocities, it is also expected to have very small strain rates, especially over short length scales. Therefore, the strain rates measured at these locations themselves give some estimate of error. However, estimating directly from the results does not take into account how error propagates through the code.

4.8: Antarctic strain-rate data product

4.8.1: Calculated strain values

We present four strain-rate data products derived from the Landsat Ice Speed of Antarctica (LISA) Mosaic (Fahnestock et al. 2016). The original velocity data are gridded with 750 m square pixels, and are assembled from Landsat-8 image pairs acquired during three austral summers between 2013 and 2016. We present results for effective, longitudinal, transverse and shear strain rates (Figures 4.13-4.16). Vertical strains may be calculated from the longitudinal and transverse strain rates using equation (72).

As the data products cover a large area, we choose a longitudinal coupling length representing large-scale viscous processes. Longitudinal coupling lengths are on the order of 4-10 ice thicknesses for polar ice [Cuffey and Paterson, 2006]. Because the data product includes

grounded ice, ice streams with very low basal shear stresses, and floating ice, an appropriate longitudinal coupling length might lie somewhere in the middle of this range. However, because most of the areas with complex strain rate patterns are found within ice streams and ice shelves, we chose a number at the upper end of the range that would favor ice that experiences little basal resistance. The effective length scale used in the data products is approximately 8x the ice thickness.

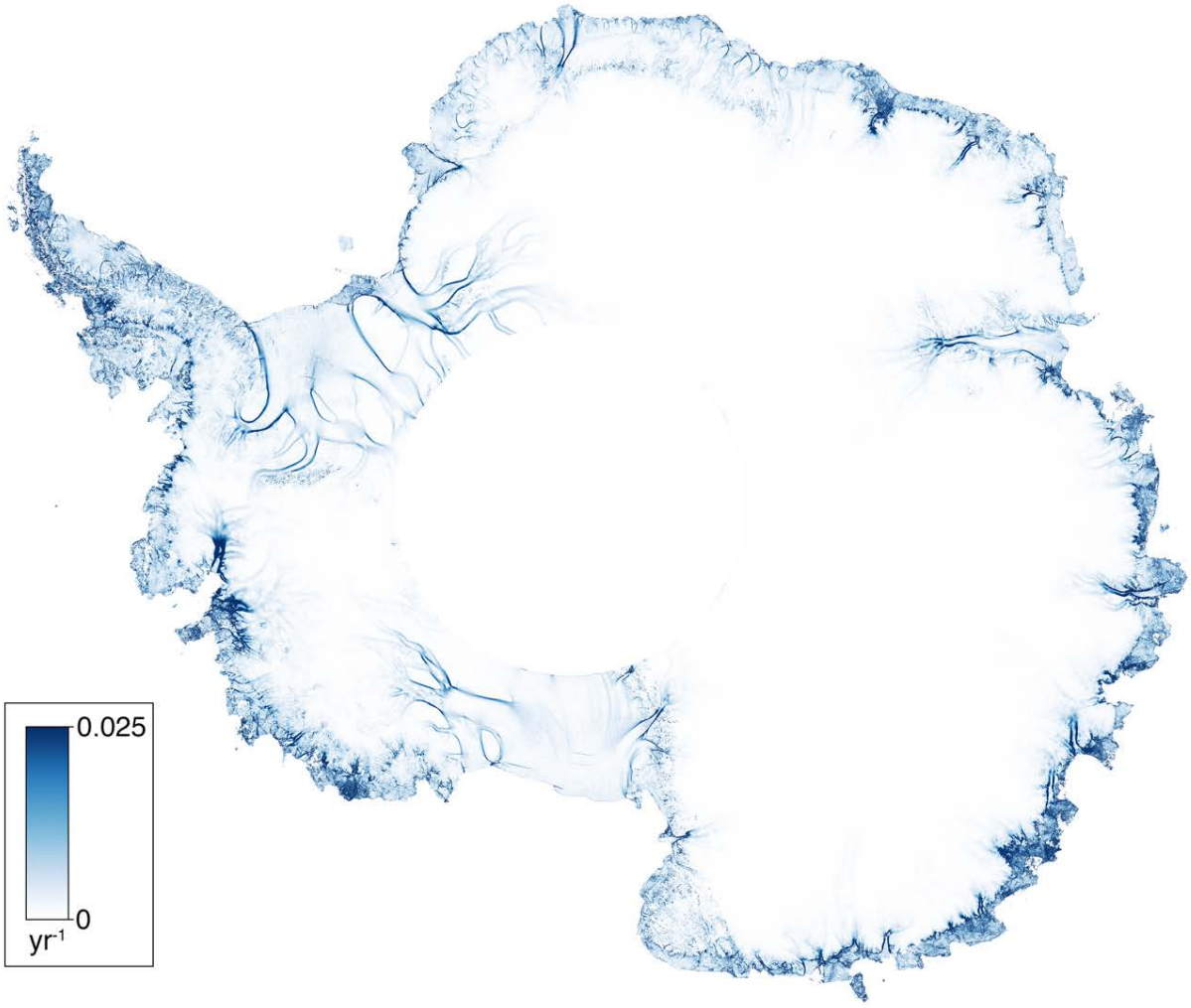

Figure 4.13 | Effective strain rate product

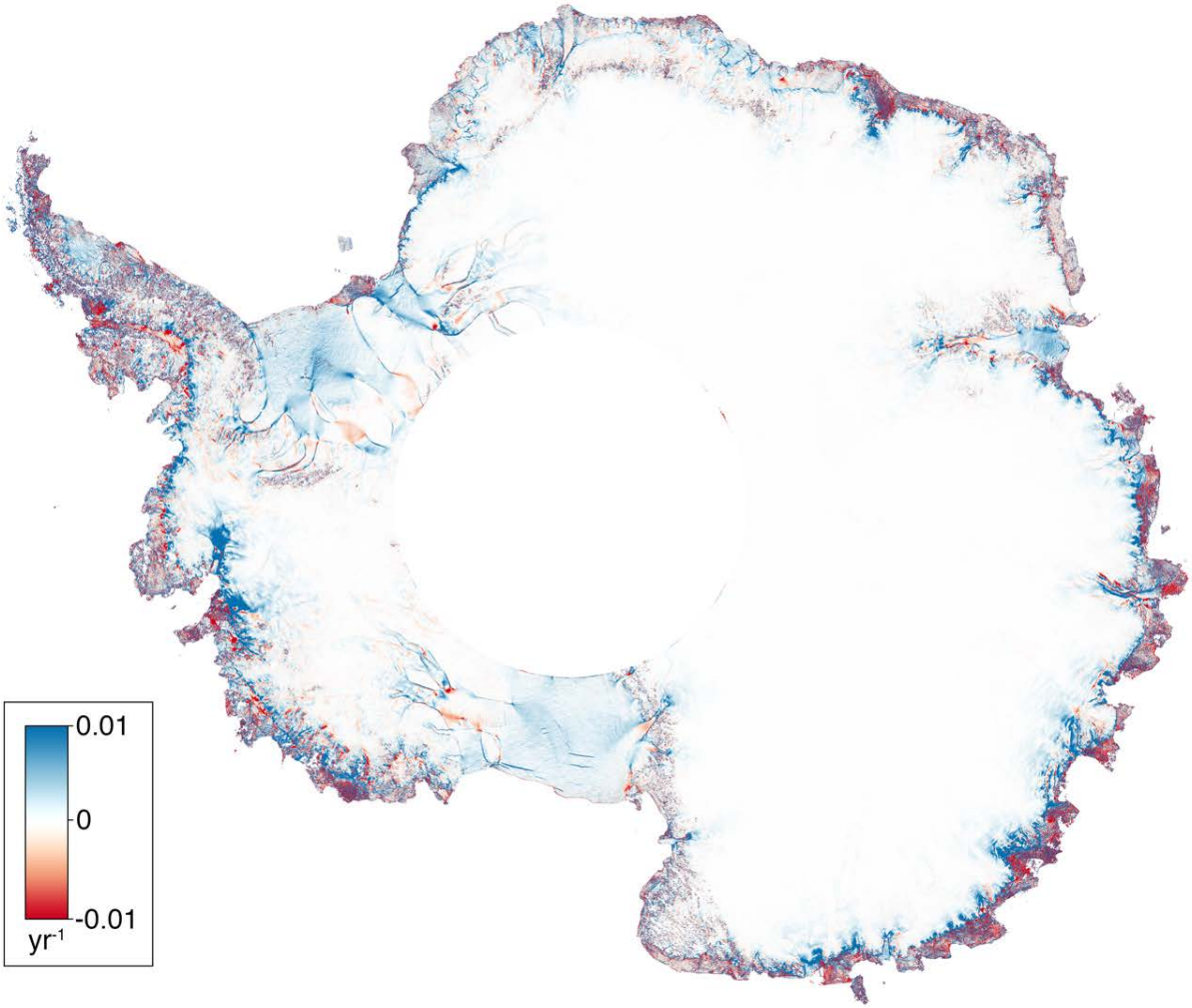

Figure 4.14 | Longitudinal strain rate product

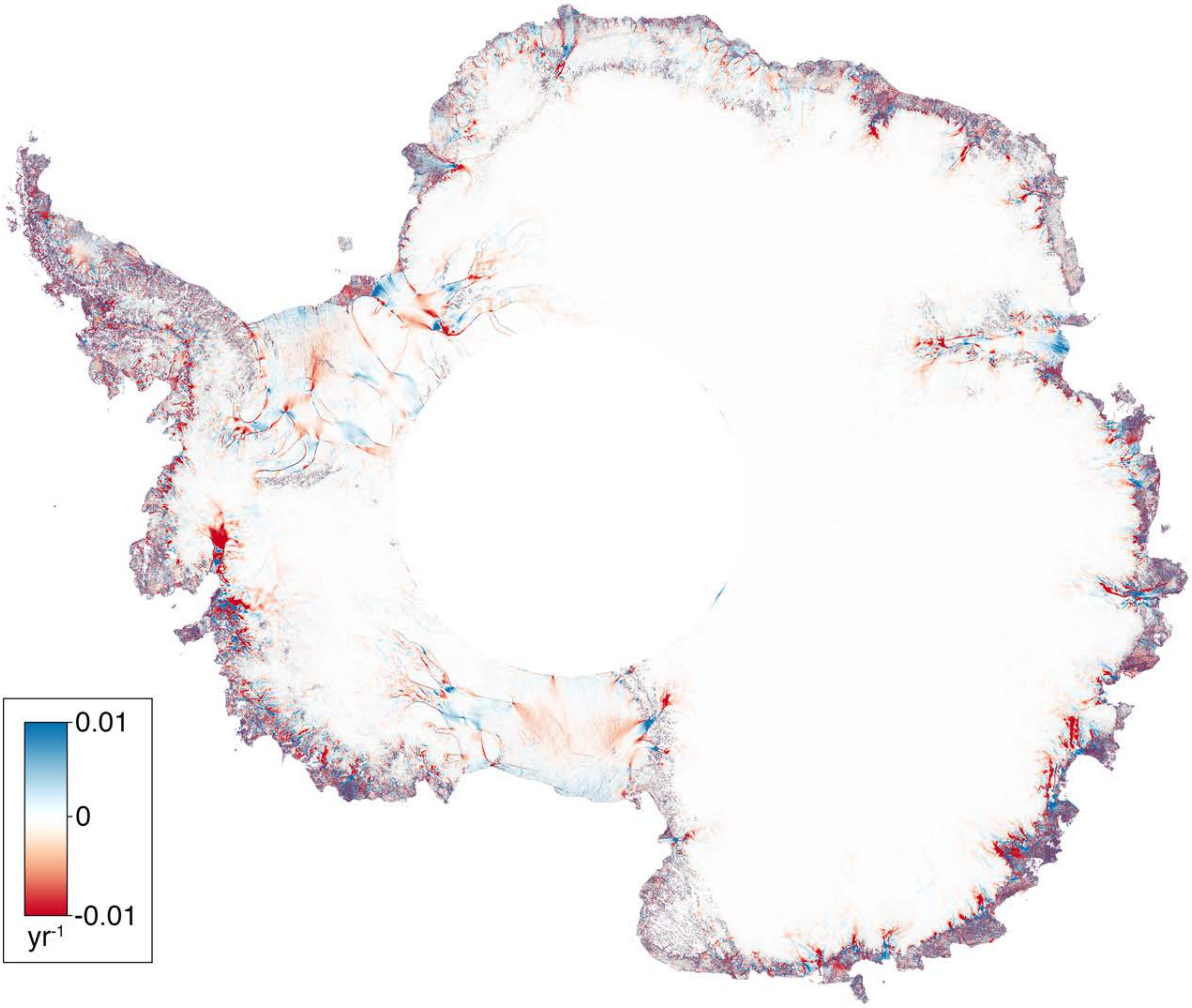

Figure 4.15 | Transverse strain rate product

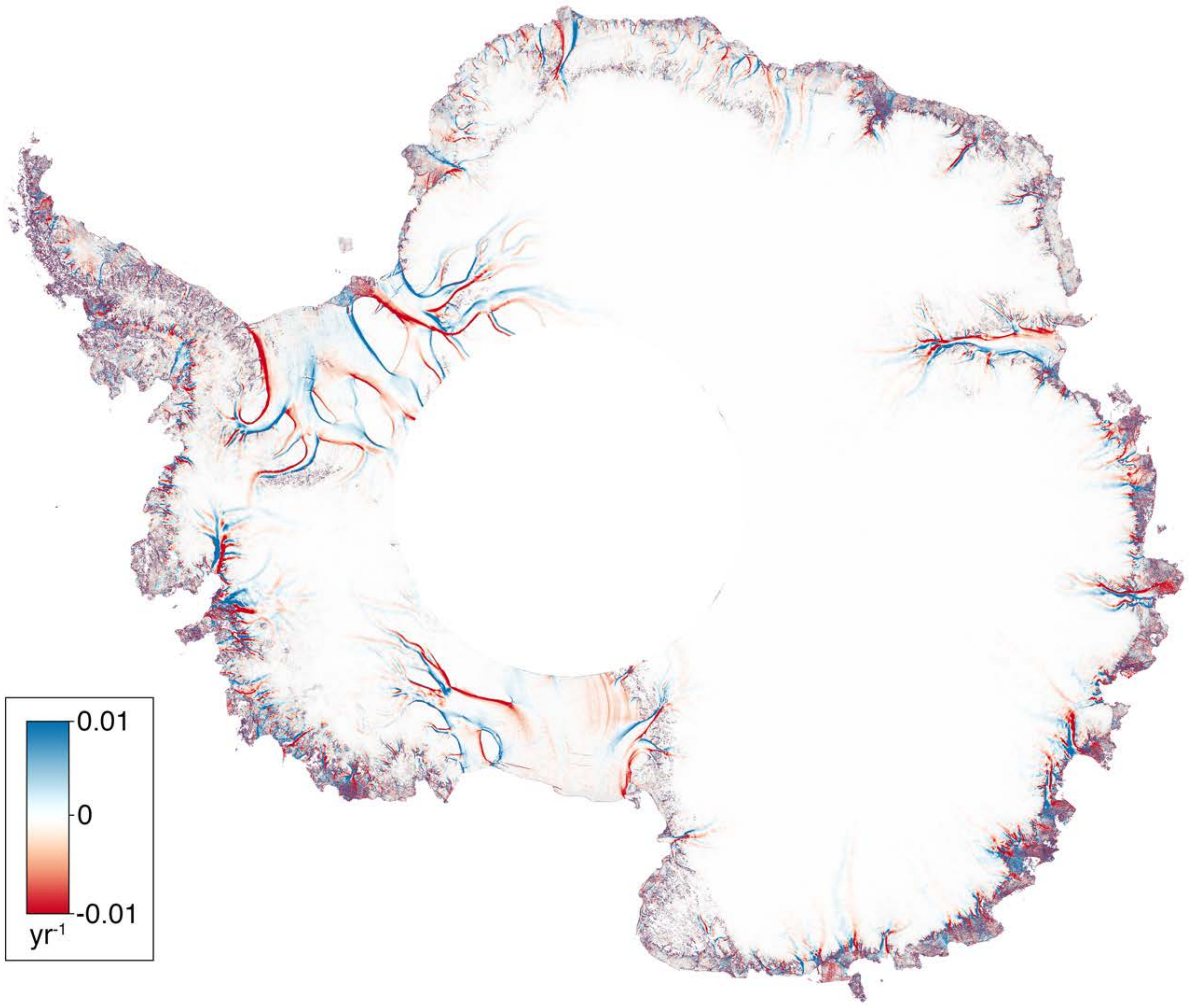

Figure 4.16 | Shear strain rate product

4.8.2: Estimated error

As discussed in section 4.7, standard methods of error propagation or estimates of the standard error associated with the least squares method yield unreasonable error estimates in the resulting strain rate field. We therefore rely on empirical methods to estimate error and understand how it propagates through the strain rate code. First, we assess error associated with the velocity fields. The feature tracking program used by Fahnestock et al. (2016) is accurate to about 0.1 times the pixel size, which is 15 m for Landsat 8 imagery. The accuracy in

velocity estimates is then tied to the time separation between the images and the amount of displacement observed, as well as geolocation errors in the imagery.

Because consistency is not predictable in geolocation errors across the velocity mosaic, and because error is hard to estimate directly in a mosaicked product, we make a rough and conservative estimate of error by using velocities in slow-moving areas of Antarctica. Table 4.1 shows statistics for the x- and y-velocities (vx and vy, respectively) in three slow-moving sample areas: Roosevelt Island on the Ross Ice Shelf, Berkner Island on the Filchner-Ronne Ice Shelf, and a grounded portion of interior East Antarctica. Although these areas move very slowly, they are still flowing; t-tests show that the mean velocities in these regions are significantly different from zero. Nonetheless, we will make the assumption that the velocities here should be zero, and treat the mean as an approximate measure of the standard error in the velocities. Since we know the means are not zero, this is likely to be an overestimate of the error in the velocity measurements.

Table 4.1 | Velocity statistics for slow-moving test regions.

Region	Mean of absolute values (m/day)	Standard deviation (m/day)
Roosevelt Island vx	0.0058	0.0015
Roosevelt Island vy	0.0065	0.0016
Berkner Island vx	0.0084	0.0018
Berkner Island vy	0.0063	0.0020
East Antarctica vx	0.0015	0.00023
East Antarctica vy	0.0017	0.00025
Mean vx	**0.0052**	**0.0012**
Mean vy	**0.0048**	**0.0013**

We wish to use this estimate of the magnitude of random error in the velocity measurements to understand how this error propagates through the strain rate calculations. To do this, we add a random error with a standard deviation of 0.005 m/day (the average of the means in Table 4.1) to the velocity fields before calculating strain rates, and repeat the procedure 100 times in a Monte Carlo simulation. Computing time prohibits the application of this procedure to all of Antarctica; therefore, we run it only on the Bindschadler/MacAyeal Ice Streams region used previously.

The standard deviation of the Monte Carlo simulation is a reasonable estimate of error in the strain rate calculations due to random error in the velocity measurements. The standard deviation results are shown in Figure 4.13. For the longitudinal, shear, and transverse strain rates, error magnitudes are clearly largest at the shear margins and other areas with large gradients in strain. The error associated with the effective strain rates is shown with a color bar an order of magnitude smaller than the others because its values are much smaller. Effective strain rate errors are much less significant on shear margins than in the other strain rate measurements.

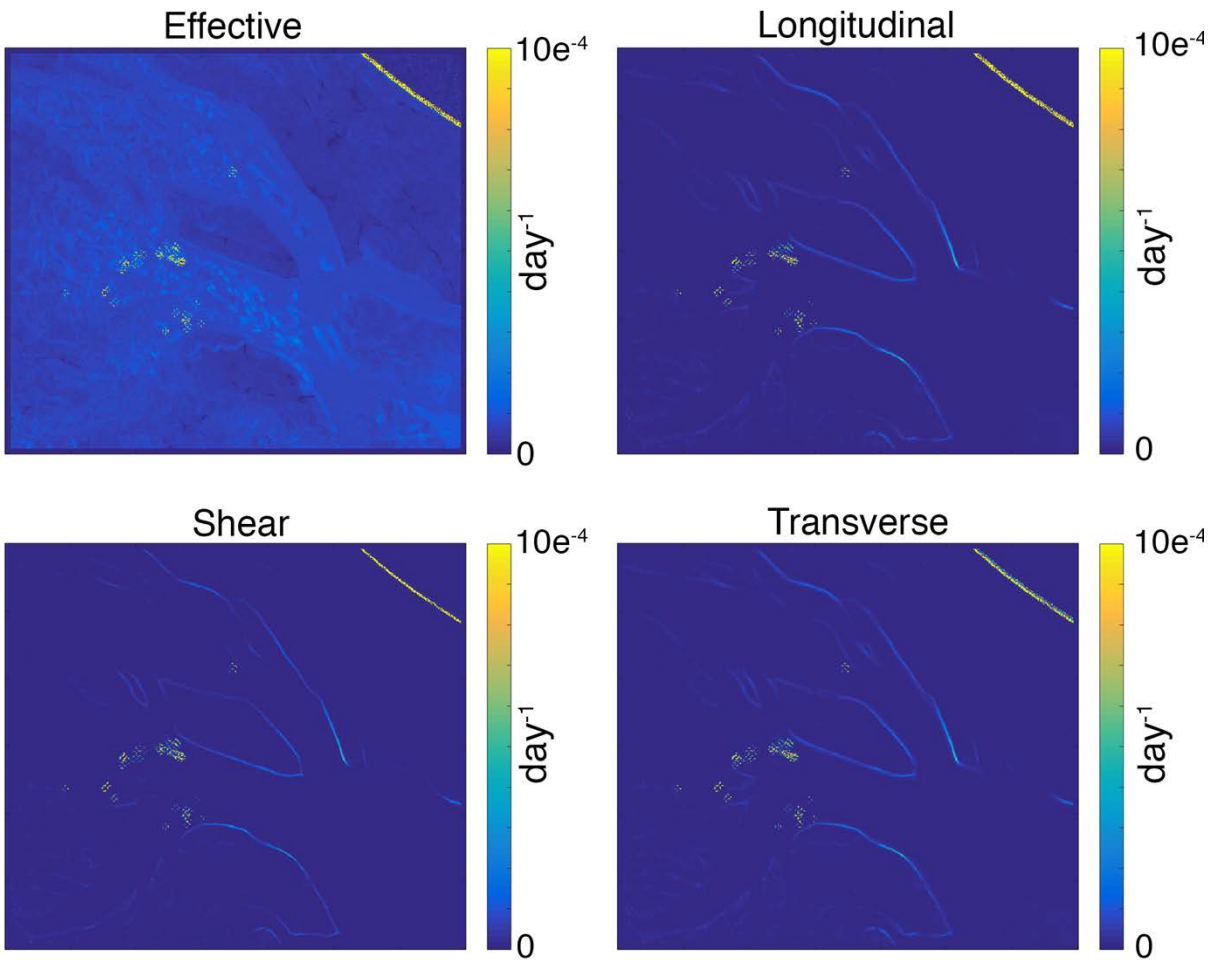

Figure 4.13 | Standard deviation of results in Monte Carlo simulation.

However, the significance of error can be more easily understood when expressed as a percentage of the measured strain rate values. Figure 4.14 shows these percentages. Errors within the ice streams are comparatively small; they are generally less than 10% of the measured strain rates. The large errors seen at shear margins in Figure 4.13 are shown to be insignificant when expressed as percentages. However, in slow-moving regions with very low strain rates, errors can be large compared to measurements. The magnitudes of these errors are typical compared to other published studies [e.g. *Bindschadler et al.*, 1996].

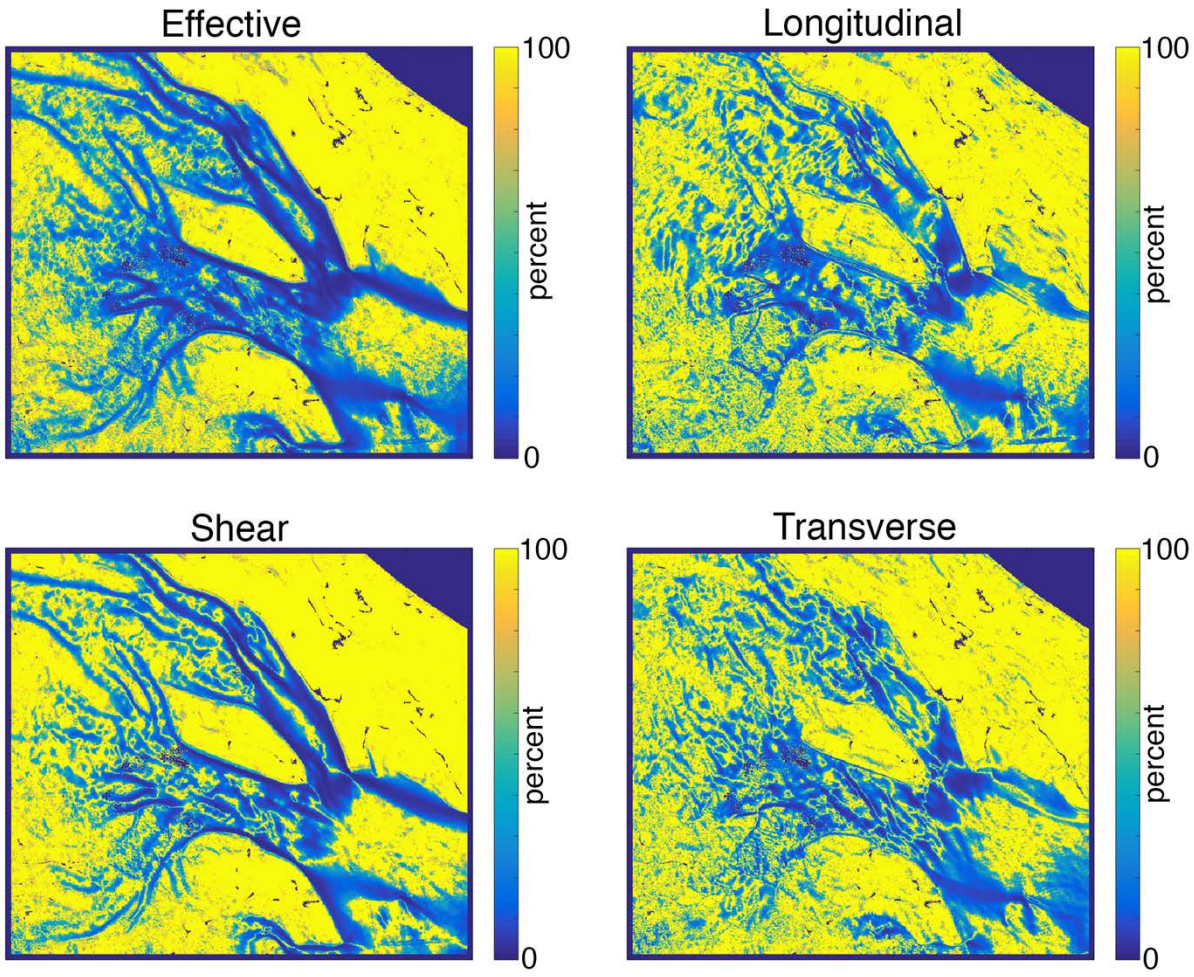

Figure 4.14 | Percent error as measured by results of the Monte Carlo simulation.

Although the percent errors are extremely high in areas with low strains, they are likely to only slightly impact quantitative calculations related to strain rates. Since the strains are small to begin with, the errors have small absolute values. It is only in areas with high strain rates that one can find, for example, significant vertical velocities. Even with errors of large percentages, vertical velocities calculated in low strain rate areas will still be very small, yielding very little impact on the interpretation of results.

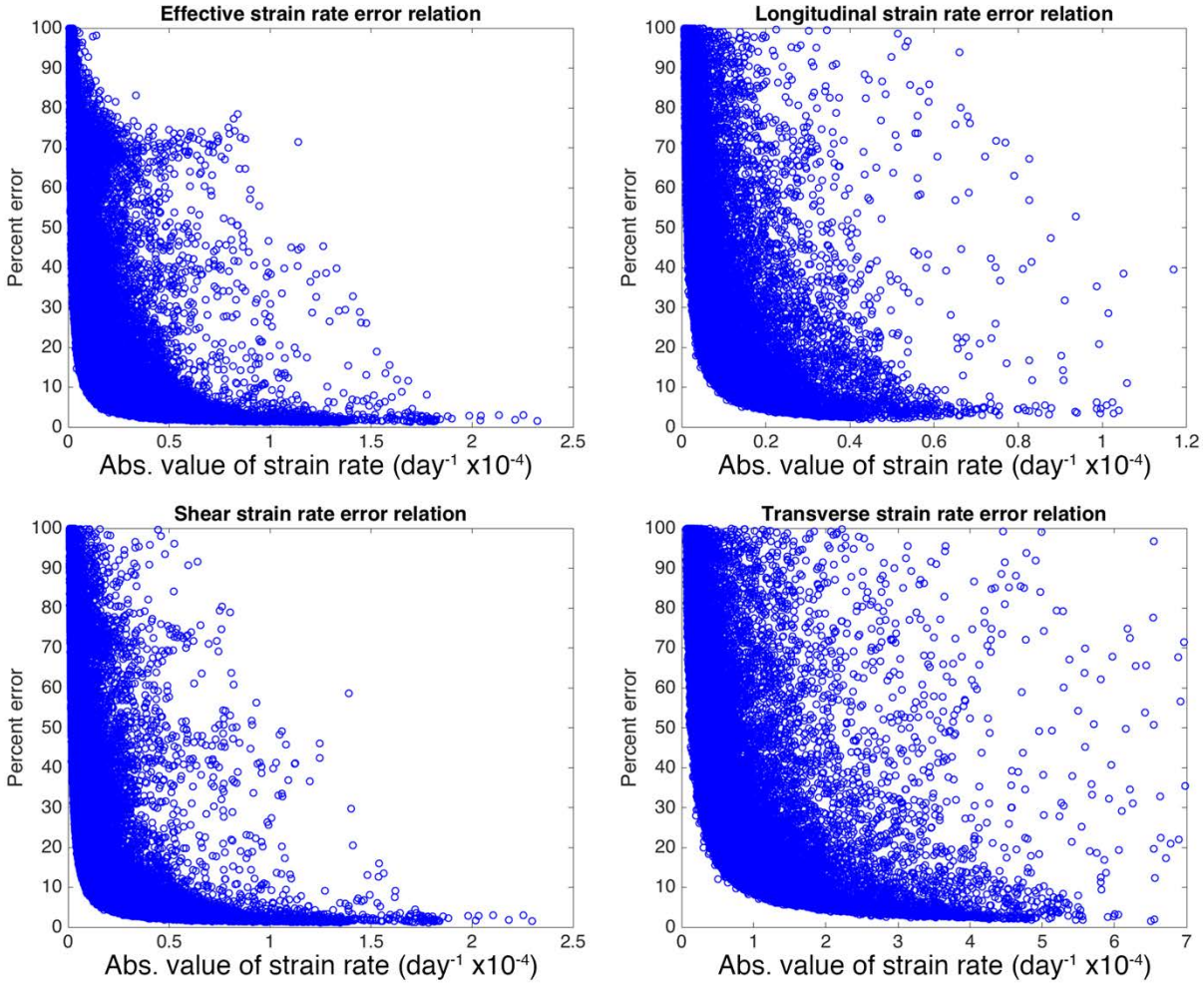

Figure 4.15 | Error relations for calculated strain rates.
Percent error is calculated from the standard deviation of the Monte Carlo simulations and the calculated strain rate values. All values are calculated for the Bindschadler and MacAyeal Ice Streams region.

The resulting Monte Carlo simulation revealed very strong relationships between the percent error and the absolute value of the strain rates (Figure 4.15). We fit a power law curve of the form $percent\ error = a * |strain\ rate|^b$ to each error relationship. The coefficients and R^2 values are shown in table 4.2. The high R^2 values indicate the reliability of these power laws. We used the calculated relations to estimate percent errors across the entire Antarctic

strain rate product, and then used the percentages to convert to absolute error values. The results are shown in figures 4.16-4.19.

Table 4.2 | Power law coefficients for error relations

Strain type	a	b	R^2
Longitudinal	0.001189	-0.8188	0.8699
Shear	0.001026	-0.8326	0.8761
Transverse	0.001111	-0.8240	0.8644
Effective	0.0009713	-0.8351	0.8838

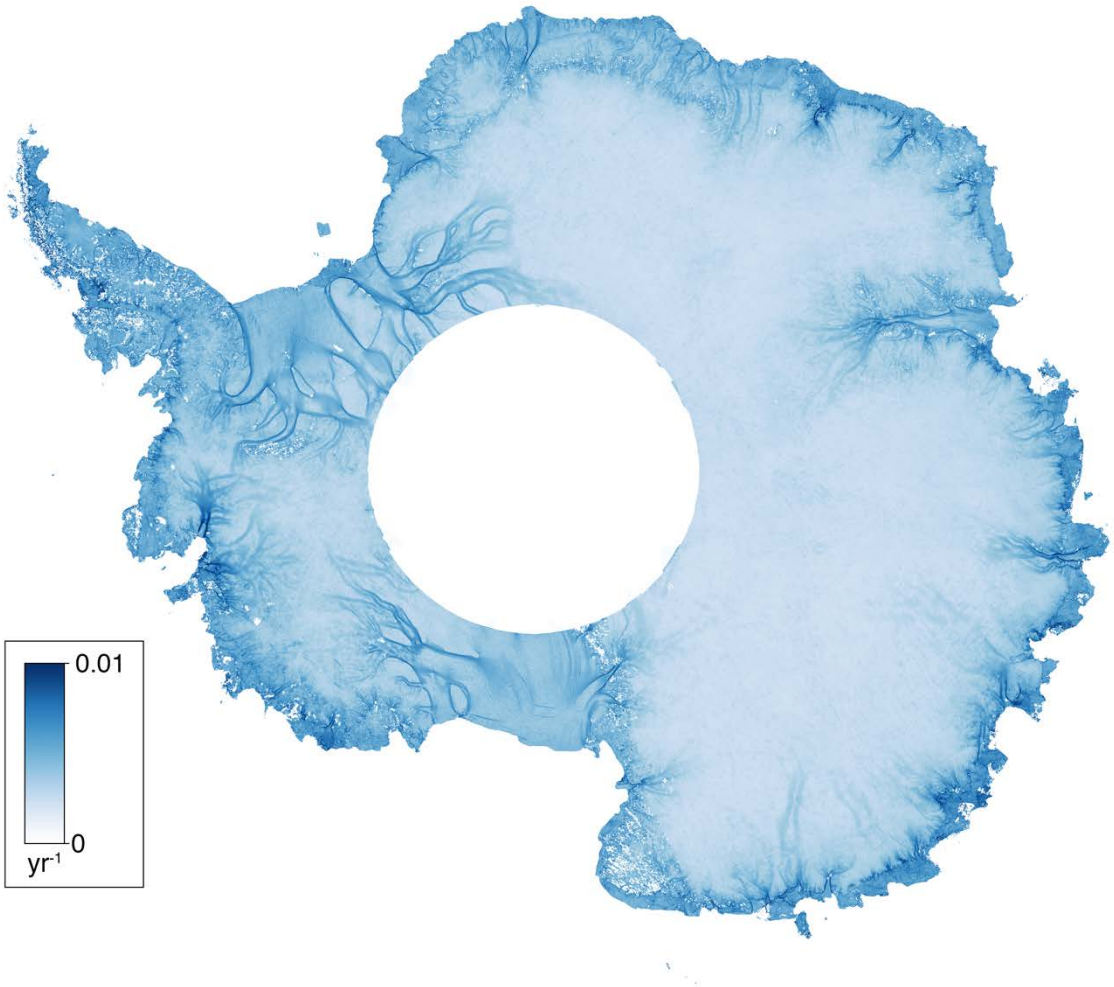

Figure 4.16 | Effective strain rate error.

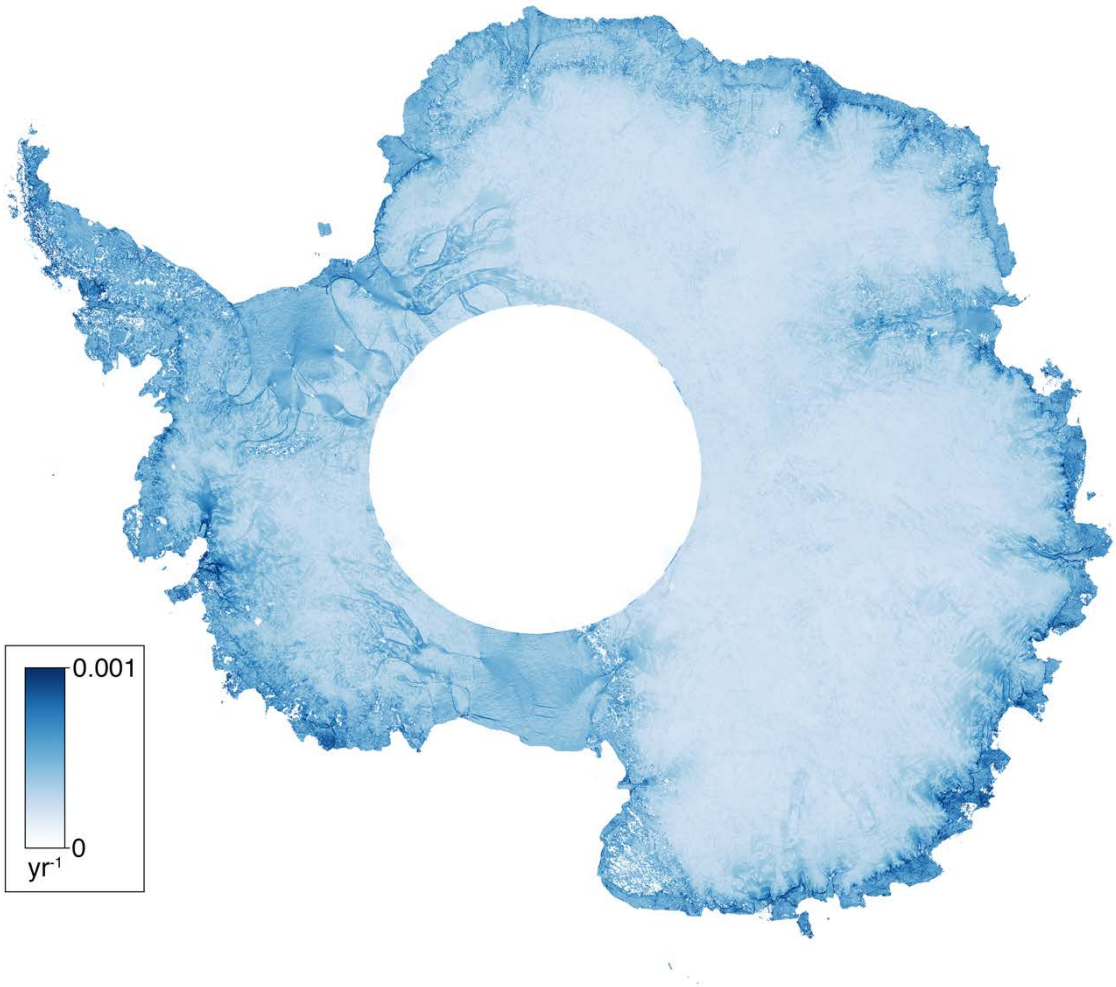

Figure 4.17 | Longitudinal strain rate error.

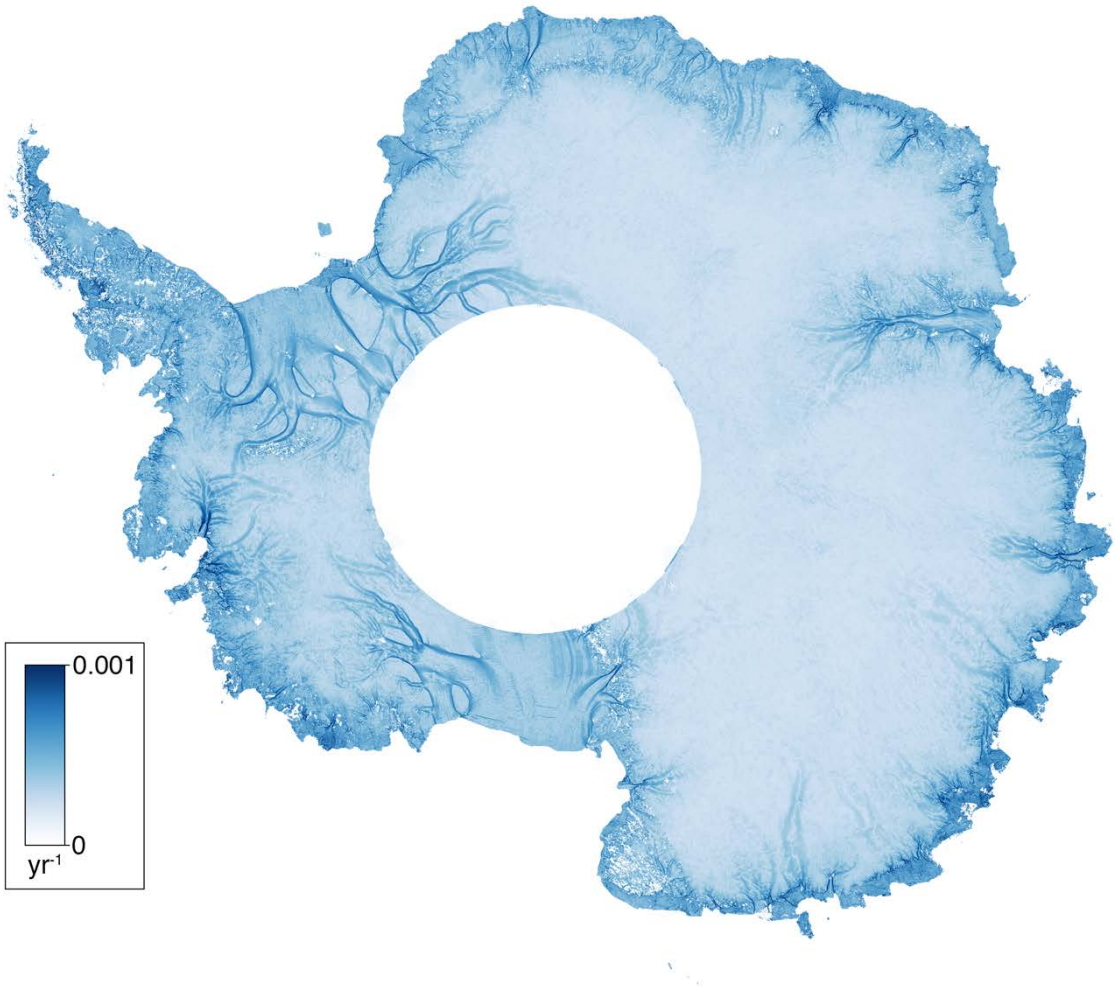

Figure 4.18 | Shear strain rate error.

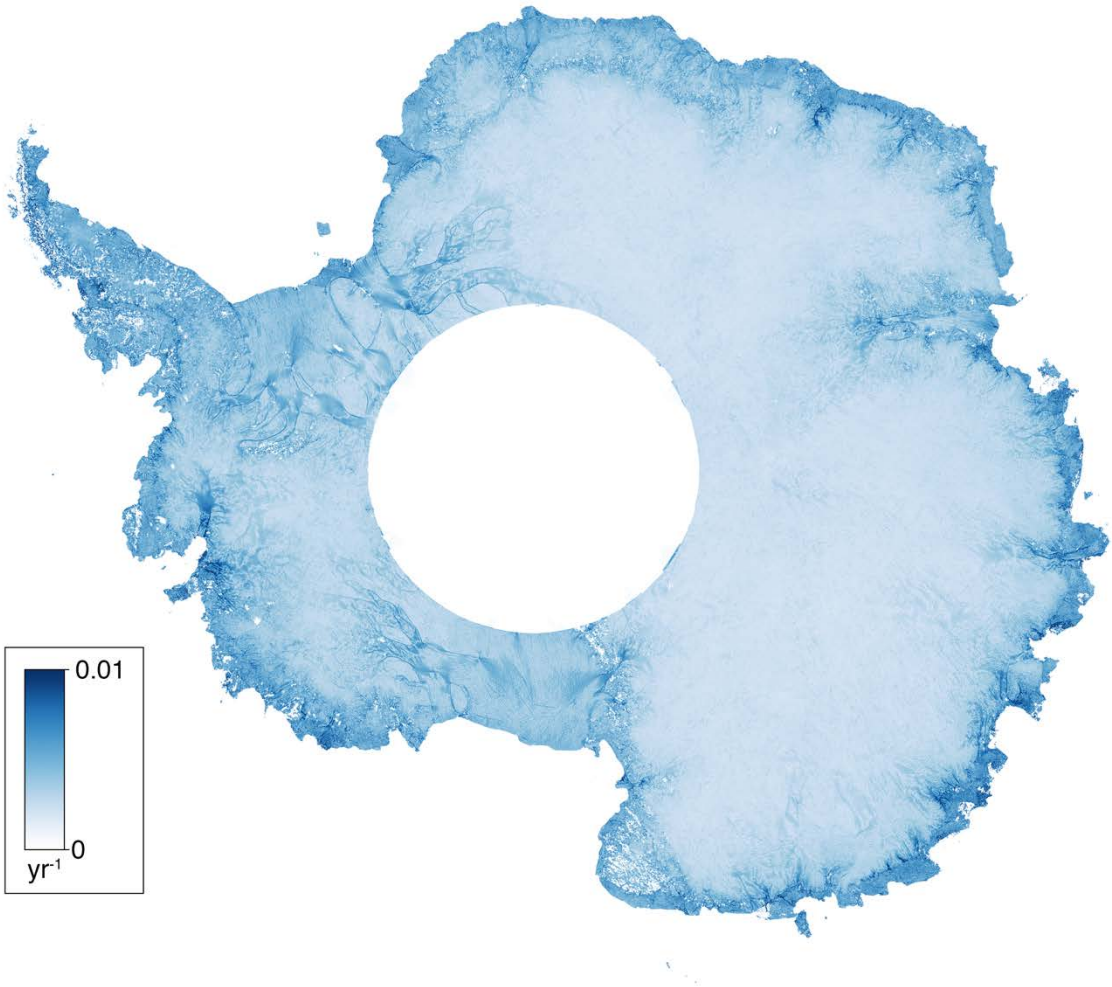

Figure 4.19 | Transverse strain rate error.

4.9 Impacts of strain rates on basal melt rate calculations

As discussed in section 4.3, the calculation of basal melt rates using mass continuity (equation (24)) is an example of an important application of strain rates for understanding ice shelf processes and stability. In section 4.6.2, we demonstrate that the length scale used can have a significant impact on calculated strain rates. In this section, we show that differences in length scale also significantly impact calculated basal melt rates on ice shelves.

For convenience, we restate equation 24:

$$\frac{\partial H}{\partial t} = \dot{\alpha}_s + \dot{\alpha}_b - H\left(\dot{\epsilon}_x + \dot{\epsilon}_y\right) + u\frac{\partial H}{\partial x} + v\frac{\partial H}{\partial y} \quad (24)$$

This mass balance equation states that the change in ice thickness with time at any given location on an ice shelf is equal to mass fluxes into and out of that location. These mass fluxes include surface mass balance, basal melt or freeze-on, and the advection of ice thickness through the location. In areas with high steady-state basal melt rates, the time-varying term $\partial H/\partial t$ and the surface mass balance term have relatively insignificant impacts on the calculated basal melt rates. The ice thickness and mass flux divergence, calculated from surface strain rates, have much larger impacts.

In order to carry out these calculations, we use several data sources. Ice shelf thicknesses (H) are derived at a 1 km resolution from Cryosat-II radar altimetry data collected between 2011 and 2014 [*Chuter and Bamber,* 2015]. All other data have been resampled to match this 1 km resolution. Surface mass balance ($\dot{\alpha}_s$) is derived from a 30-year average of RACMO-2.3 model output from 1984 to 2014 [*Van Wessem et al.*, 2014]. Ice thickness change ($\partial H/\partial t$) is calculated from an 18-year trend of satellite altimetry data between 1996 and 2014 [*Paolo et al.,* 2015]. We approximate ice thickness change from surface elevation change using a density of 917 kg/m^3 for ice and a density of 1023 kg/m^3 for seawater. Surface velocities (u, v) are from LISA mosaics derived from Landsat-8 data between 2013 and 2016 [*Fahnestock et al.,* 2016]. We were unable to find data sources collected during a single coincident time period; however, as mentioned previously, the data sources that have the largest impacts on the calculations are ice thickness and surface velocity, and the time periods of data collection for these overlap.

Because ice thickness and velocity measurements are not from precisely the same time period, local basal melt rates may be strongly affected by the advection of large rifts. These features are reflected in both the ice thickness measurements and the calculated strain rates. If the rift locations are offset between the two datasets, the basal melt calculation will falsely indicate parallel regions of very high basal melt and freeze-on. For this reason, we have assessed basal melt rates reasonable for each sample area and removed outliers that do not fall within a reasonable range.

Figure 4.20 shows the calculated basal melt rate results for several large ice shelves in Antarctica. We first calculated basal melt rates using strain rates computed at the smallest possible length scale, which in this case is a half-length scale of 1 km. This commonly used approach utilizes the highest resolution possible given the pixel size, and may be appropriate for assessments of small-scale patterns of basal melt rates on ice shelves with complex basal topography. Then basal melt rates were recalculated with strain rates determined using length scales of approximately 8x the ice thickness. These viscous-scale calculations might be appropriate for large-scale averages and for ice shelves with less complex basal topography. Finally, we compared the values in each calculation. We chose ice shelves that are not dominated by large rifts.

Table 2.3 gives a comparison of average basal melt rates for each calculation. For some ice shelves with low strain rates and low overall melt rates, such as on the Ross and Filchner-Ronne, there is a very small percent difference between the two methods. The Amery has a much larger percent difference, but the absolute value of the difference is still very small. Ice shelves that have large strain rates and strain-rate gradients as well as large overall melt rates,

such as the Dotson/Crosson and Pine Island Ice Shelves, yield significant differences between the two basal melt rate calculation methods. In these cases, the length scale used to calculate strain rates may have a significant impact on interpretation of ice shelf mass balance.

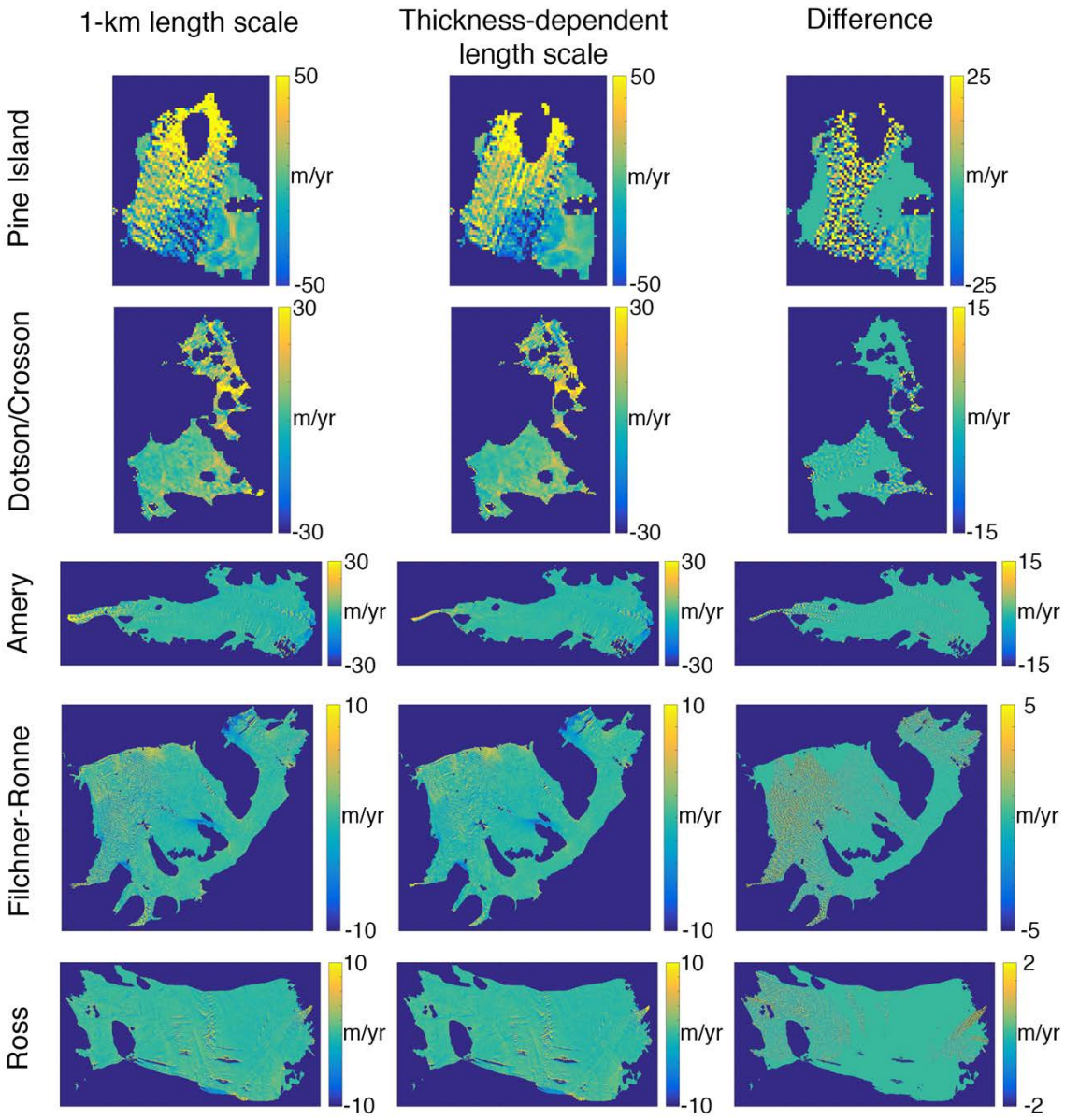

Figure 4.20 | Basal melt rates on ice shelves.
Basal melt rates calculated using equation 24. First column shows results with strain rates calculated at the smallest possible length scale according to the pixel size; second column shows results with strain rates calculated at a length scale of 8x the ice thickness. Third column is first column subtracted from second column.

Table 2.3 | Average basal melt rates for several Antarctic ice shelves.

Ice shelf	Avg. basal melt rate at 1-km length scale (m/yr)	Avg. basal melt rate at thickness-dependent length scale (m/yr)	Percent difference
Pine Island	11.1	10.1	9.9
Dotson/Crosson	6.5	4.1	58.5
Amery	1.5	1.3	15.4
Filchner-Ronne	-0.040	-0.041	2.4
Ross	0.22	0.21	4.8

4.10: Conclusions

Strain rates have been commonly calculated using both direct differencing of the strain rate tensor and adaptations of stake-tracking approaches. Our analyses show that both methods yield reliable results in most cases. The largest differences between methods are found in areas with high strain rates and high strain-rate gradients, such as at ice stream shear margins. The length scale over which strain rates are calculated is a more important factor, yielding differences both at shear margins and within ice streams. We suggest that the numerical stake-tracking approach, which utilizes a logarithmic strain formulation, is more likely to be accurate in areas with large strain rates. Errors can be most effectively estimated using empirical techniques.

As strain rate calculations are integral to many applications in glaciology, it is important to choose the length scale of calculation deliberately. For example, when calculating basal melt rates on ice shelves using mass continuity, strain rates are used to assess mass flux divergence and have a large impact on the results. The length scale used for the strain rate calculations may in some cases change the average estimated basal melt rate by more than 50%, which could significantly change the interpretation of results.

Chapter 5:

Conclusions and future work

5.1. Introduction

All of the studies presented in the last three chapters raise further interesting questions for follow-on work. This chapter briefly outlines future studies for just a few of the questions raised within this dissertation. The proposed studies include extended work on topics addressed previously in limited detail, the application of strain rates to glaciological problems, and the combination of results into meaningful assessments. The final section discusses overall conclusions derived from the studies presented in this dissertation.

5.2. Continuing work for Chapter 2: details of backscatter/melt days relationship in Greenland

Greenland's ice facies are relatively well-defined and much more predictable than similar regions in Antarctica. For this reason, a backscatter/melt days transect was extracted from Greenland that was known to cross all ice facies, giving a clear example of the basic shape expected in the backscatter/melt days relationship. However, a more comprehensive analysis of this relationship in different parts of Greenland reveals a lot of variations in this overall trend.

Figure 5.1 shows the backscatter/melt days relationship extracted between Summit Station in the dry snow facies and five locations on the Greenland coast. The Kangerlussuaq transect, shown in purple, is the transect used in Figure 2.1 in our paper. Figure 5.1 reveals a split in the relationship trajectories between transects. All the relationships begin near the same coordinates, but Thule, Kangerlussuaq, and Tasiilaq then follow a trajectory much lower on the graph, while backscatter for Nord and East increase much more quickly with average annual melt days. Kangerlussuaq and Nord clearly show the decrease in backscatter that occurs due to specular reflection at high melt days, while the others are not as obvious. Black and green pixels from the East and Thule transects are found far from the typical transect trajectories at very high average annual melt days.

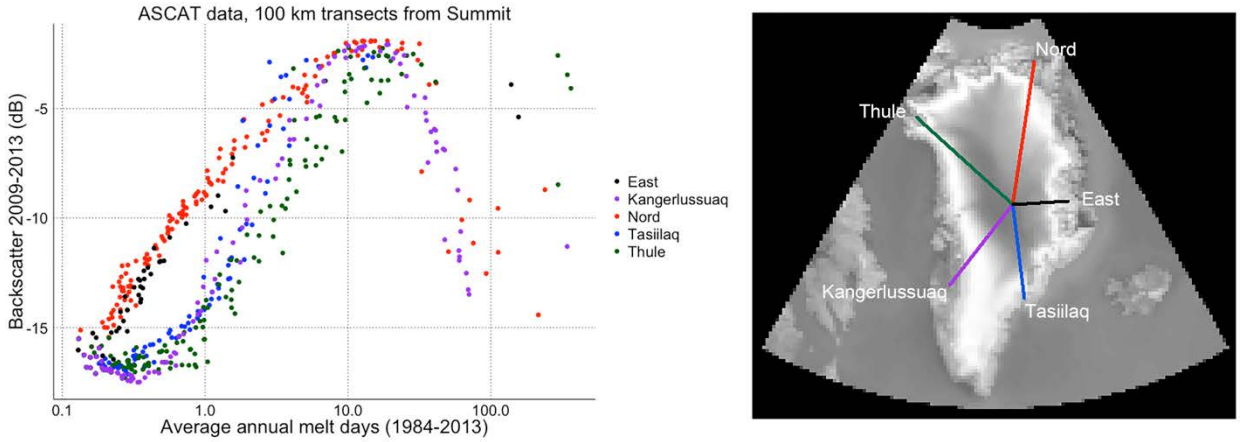

Figure 5.1 | Backscatter/melt days relationship for five Greenland transects.

As discussed in Chapter 2, many variables affect the backscatter signal, with impacts that are difficult to quantify. The split between transects that go south and west (Thule, Tasiilaq, and Kangerlussuaq) and transects that go north and east (Nord and East) suggests that there could be some sort of geometric control on the results, perhaps related to azimuthal variations. However, Tasiilaq falls on the other side of the ice divide from Thule or

Kangerlussuaq, so this may not be a viable explanation. In addition, some areas on Greenland, such as the areas crossed by the Tasilaaq transect, are affected by firn aquifers that hold liquid meltwater year round [*Forster et al.*, 2014].

A more detailed analysis could be carried out to understand the subtle variations in the backscatter/melt days relationship seen in Greenland. Because this relationship reveals important information on the the evolution of the upper layers of the ice sheet, analysis at a regional and/or interannual level could reveal valuable information about how surface melt impacts the ice sheet. In addition, because the relationship is relatively well-constrained, it may afford the opportunity to understand in more detail how some cryospheric variables impact scatterometry results.

5.3. Continuing work for Chapter 3: persistent polynyas and basal channel evolution

Chapter 3 and the Appendix to Chapter 3 discuss persistent polynyas, which are defined as small open-water regions found at ice shelf fronts that have been observed when fast ice is present during at least three summers. Of the 25 polynyas documented, 22 of them were found to be collocated with the terminus of a basal channel, suggesting that their formation may be tied to the flux and temperature of water flow through the channel. Although the study presented in Chapter 3 documents the association between channels and polynyas, it does not include details about polynya change or links to inter-annual variability.

A future study might focus on the temporal evolution of persistent polynyas, basal channels, and their correlation to factors such as ocean heat flux. The analysis could also include the use of thermal-band satellite imagery to identify water outflow from channels when fast ice is not present. As shown in appendix figure A.3.12, some polynyas form consistently each summer, while others may not be observed every year, even if fast ice is present. For example, Figure 5.2 shows the location of a persistent polynya (marked with an arrow) on the Cosgrove Ice Shelf in the Amundsen Sea, which forms at the terminus of an ocean-sourced channel. In the image on the left, collected in October of 2011, fast ice abuts the ice shelf edge tightly with no evidence of a polynya. In December of 2013, however, an open-water region is clearly visible at the channel terminus. This raises questions about the interannual variability of factors that could cause flow within a basal channel to vary.

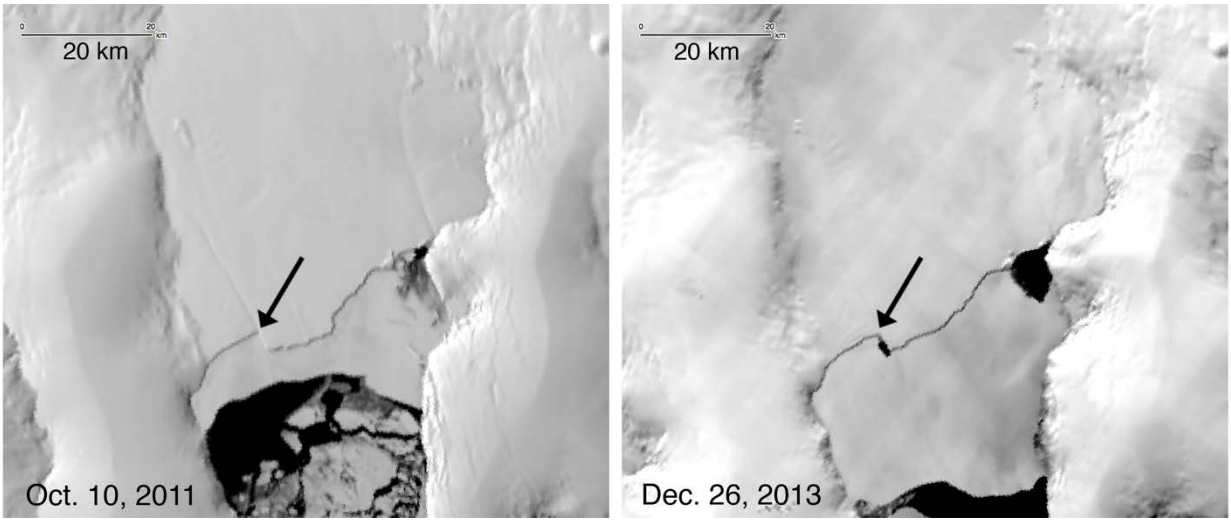

Figure 5.2 | Interannual variability in polynya presence on the Cosgrove Ice Shelf, Amundsen Sea.

Figure 5.3 shows polynya change within a single summer. The polynya shown is at the edge of the Getz Ice Shelf, coincident with the terminus of the rapidly growing ocean-sourced channel analyzed in Figure 3.2. In the first panel of Figure 5.3, near the beginning of the

summer season, the polynya is approximately 700 m in diameter. A month later, it has grown to 1.7 km. By the third image, just 15 days later, the polynya has reached a diameter of approximately 2.5 km. These very large changes in polynya size might be linked to changes in the amount or temperature of water carried through the channel and/or to changes in fast ice thickness. The fast ice in the first image appears to be very solid; by the third image, it has significantly broken out. The same flux or temperature of water that may be unable to maintain a large polynya when thick fast ice is present might form a larger polynya through thinner fast ice.

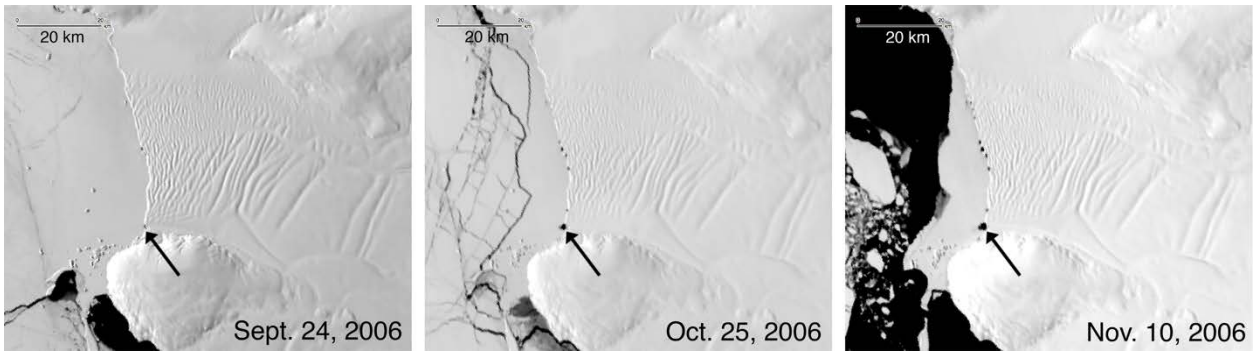

Figure 5.3 | Intraseasonal polynya growth on the Getz Ice Shelf, Amundsen Sea.

A combination of visible-band satellite imagery, such as data from the MODIS and Landsat sensors, may be used to create a detailed documentation of polynya presence and size through time, as well as observations of fast ice character and water temperature. The changes might correlate directly to variables such as local ocean heat flux, which can be derived from modelled or observed ocean properties. The correlation might also be enhanced by taking into account fast ice thickness, which could be measured using ICESat, IceBridge, or other altimeters.

In addition, as most of the observed ice-front polynyas are coincident with basal channel termini, the study could include observations of channel change over time. Figure 3.2 shows that the growing channel on the Getz Ice Shelf is not only growing in horizontal extent, but it is also deepening rapidly. Repeat ICESat tracks were used to document the rate of channel deepening. More extensive use may be made of ICESat and IceBridge altimetry to document channel geometry and changes in geometry with time. The links between changing polynyas and changing channels may illuminate in more detail the links between ocean circulation and basal channel impacts on ice shelves.

5.4. Continuing work for Chapter 4: Accumulated strain and calving rates

The material presented in Chapter 4 is primarily a methods study examining the approaches to strain rate calculations. But as discussed in sections 4.2 and 4.9, strain rates have many applications to glaciological problems. One of those problems is the determination of a relationship between strain rates and ice fracture, either within grounded ice or as calving on floating ice.

Many authors have shown a connection between strain rates and ice fracture. Vaughan (1993) used a variety of available datasets to empirically determine thresholds of strain rate and stress that, when exceeded, cause crevassing. However, that study was hampered by a lack of comprehensive data and the inability to accurately identify the locations of active crevasses. The availability of a continent-wide dataset of high-quality longitudinal strain rates, as was presented in Chapter 4, provides a much more comprehensive database of strain rates. In

addition, high-resolution visible-band imagery is also available for the whole Antarctic continent. This makes it possible to use automated methods to identify crevasse locations. The most reliable locations to measure strain rates leading to crevasse formation are likely to be in areas where crevasses are actively forming, which may be found at the upstream ends of trains of crevasses that have been advected downstream.

While high strain rates are likely to cause crevassing and/or calving, it is also possible that the longitudinal strain (or longitudinal strain above some threshold) accumulated by a parcel as it moves through its flow path – i.e. the total amount a given parcel of ice has stretched – may be a determinant for crevasse formation. In particular, we are interested in understanding how accumulated strain relates to ice shelf calving rates and calving front locations. To do this, we will calculate flow lines using the LISA velocity mosaics. We will then make pixel-by-pixel calculations of the strain accumulated by an ice parcel based on the amount of stretching it experiences during each time step as it moves along the calculated flow lines to each ice shelf edge.

The calculations may also take into account the healing of crevasses. Positive strain rates represent stretching, which will cause crevasses to open farther. In contrast, negative strain rates represent compression, which can cause crevasses to close. In addition, ice voids tend to fill in over time through ice creep. Ice healing is included implicitly in the calculation of accumulated strain, which takes into account both positive and negative strain rates. Crevasse healing may also be validated through the detection of crevasses using optical imagery and the quantification of where crevasses appear and disappear.

The strain rate code presented in Chapter 4 and the Appendix to Chapter 4 includes flexibility for the length scale used. The use of a large length scale related to large-scale viscous processes is likely to average out small-scale features, including local high strain rates that could lead to crevassing. It is likely that some experimentation will be required to empirically determine an appropriate length scale over which to measure strain rates that relate to brittle fracture in Antarctic ice.

5.5: Overall conclusions and combined assessments

Ice shelves are complicated systems, and a precise understanding of their current and future stability, along with the ability to predict the locations and timing of future ice shelf collapses, still eludes the glaciological community. However, the widespread availability of a variety of remotely sensed data products, increased numbers of field-based data products, and advances in numerical modeling have brought us to the point of being able to make larger-scale assessments of ice shelf stability.

The studies presented in this dissertation might be used alongside other datasets to predict ice shelf collapse vulnerability in the future. In Chapter 2, we showed that ice shelf vulnerability to hydrofracture may be quantified using information about surface mass balance and average annual surface melt. We might use the demonstrated relationship to parameterize vulnerability based solely on surface melt, which is a quantity that can be projected into the future using climate models. Based on projected climate changes, we might then ask how much melt would have to occur to overcome ice shelf stress regimes and cause hydrofracture collapse.

These stresses are determined in part by ice thickness, which is a quantity that is also evolving. In Chapter 3, we showed that small-scale variations in ice thickness, in the form of basal channels, can in some cases weaken ice shelf structures. Recent studies, such as Paolo et al. (2015), have identified trends in ice shelf thinning that may be used to create rough future projections of ice shelf thickness. We might make the assumption that basal channels will maintain about the same depth over the next several decades, while ice shelves continue to thin. If this is the case, the stresses caused by basal channel presence may ultimately lead to more widespread fracture of ice shelf surfaces.

Finally, the information in Chapter 4 and the presented strain rate products for Antarctica might be integrated into the results and future projections for both of the other studies. If ice shelves maintain about the strain rates they have now, how much stress would that impart on ice shelves that have thinned in the future? Do future scenarios of surface melt raise the stresses in surface ponds high enough to overcome the stresses supporting current ice shelf geometries? Will surface melt factors matter before stresses within basal channels lead to fracture due to basal melt? Numerical modeling combined with the comprehensive strain rate measurements presented here may be able to provide estimates that can answer these questions in more detail than has been available to date.

As with most glaciological studies, we have raised more questions than we have answered. However, we have also helped open the door a little further to estimating future ice shelf behavior in a detailed and accurate way. Future work that builds on these and and similar studies will help increase understanding of the future of our ice sheets, and therefore the future of sea level and our planet.

Bibliography

Alley, R. B., H. J. Horgan, I. Joughin, K. M. Cuffey, T. K. Dupont, B. R. Parizek, S. Anandakrishnan, and J. Bassis (2008), A Simple Law for Ice-Shelf Calving, *Science*, *322*(5906), 1344, doi:10.1126/science.1162543.

Ambach, D. D. W. (1968), The formation of crevasses in relation to the measured distribution of strain-rates and stresses, *Archiv für Meteorologie, Geophysik und Bioklimatologie Serie A*, *17*(1), 78–87, doi:10.1007/BF02250793.

Ashcraft, I. S., and D. G. Long (2001), Azimuth variation in microwave backscatter over the Greenland Ice Sheet, *Geoscience and Remote Sensing Symposia*, IEEE, 1779-1781, doi:10.1109/IGARSS.2001.977069.

Benn, D. I., N. Hulton, and R. H. Mottram (2007), 'Calving laws', 'sliding laws' and the stability of tidewater glaciers, *Annals of Glaciology*, *46*(1), 123–130, doi:10.3189/172756407782871161.

Benson, C. S. (1962), Stratigraphic studies in the snow and firn of the Greenland ice sheet, *Res. Rep. 70,* 93 pp., U. S. Army Cold Reg. Res. and Eng. Lab., Hanover, N. H. (Reprinted and updated in 1996.)

Berthier, E., T. A. Scambos, and C. A. Shuman (2012), Mass loss of Larsen B tributary glaciers (Antarctic Peninsula) unabated since 2002, *Geophys. Res. Lett.*, *39*(13), L13501, doi:10.1029/2012gl051755.

Bindschadler, R., D. G. Vaughan, and P. Vornberger (2011), Variability of basal melt beneath the Pine Island Glacier ice shelf, West Antarctica, *Journal of Glaciology*, *57*(204), 581–595, doi:10.3189/002214311797409802.

Bindschadler, R., P. Vornberger, D. Blankenship, T. Scambos, and R. Jacobel (1996), Surface velocity and mass balance of Ice Streams D and E, West Antarctica, *Journal of Glaciology*, *42*(142), 461-475, doi:10.1017/s0022143000003452.

Bingham, A. W., and M. R. Drinkwater (2000), Recent changes in the microwave scattering properties of the Antarctic ice sheet, *IEEE Transactions on Geoscience and Remote Sensing*, *38*(4), 1810–1820, doi:10.1109/36.851765.

Borsa, A. A., G. Moholdt, H. A. Fricker, and K. M. Brunt (2014), A range correction for ICESat and its potential impact on ice-sheet mass balance studies, *The Cryosphere*, *8*(2), 345–357, doi:10.5194/tc-8-345-2014.

Braithwaite, R. J., M. Laternser, and W. T. Pfeffer (1994), Variations of near-surface firn density in the lower accumulation area of the Greenland ice sheet, Pâkitsoq, West Greenland,

Journal of Glaciology, *40*(136), 477–485, doi:10.3198/1994JoG40-136-477-485.

Brown, R., C. Derksen, and L. Wang (2007), Assessment of spring snow cover duration variability over northern Canada from satellite datasets, *Remote Sensing of Environment*, *111*(2-3), 367–381, doi:10.1016/j.rse.2006.09.035.

Burgess, E. W., R. R. Forster, C. F. Larsen, and M. Braun (2012), Surge dynamics on Bering Glacier, Alaska, in 2008-2011, *The Cryosphere*, *6*(6), 1251–1262, doi:10.5194/tc-6-1251-2012.

Cape, M. R., M. Vernet, P. Skvarca, S. Marinsek, T. Scambos, and E. Domack (2015), Foehn winds link climate-driven warming to ice shelf evolution in Antarctica, *Journal of Geophysical Research: Atmospheres*, *120*(21), 11,037–11,057, doi:10.1002/2015JD023465.

Carsey, F. D. (1992), *Microwave remote sensing of sea ice*, American Geophysical Union, Washington DC, pp. 462.

Chuter, S. J., and J. L. Bamber (2015), Antarctic ice shelf thickness from CryoSat-2 radar altimetry, *Geophysical Research Letters*, *42*(24), 10721-10729, doi: 10.1002/2015GL066515.

Colgan, W., H. Rajaram, W. Abdalati, C. McCutchan, R. Mottram, M. S. Moussavi, and S. Grigsby (2016), Glacier crevasses: Observations, models, and mass balance implications, *Reviews of Geophysics*, *54*(1), 119–161, doi:10.1002/2015RG000504.

Cuffey, K. M., and W. S. B. Paterson (2010), *The Physics of Glaciers*, 4 ed., Elsevier, Burlington, MA, pp. 704.

De Rydt, J., G. H. Gudmundsson, H. Rott, and J. L. Bamber (2015), Modeling the instantaneous response of glaciers after the collapse of the Larsen B Ice Shelf, *Geophys. Res. Lett.*, *42*(13), 5355–5363, doi:10.1002/2015GL064355.

Depoorter, M. A., J. L. Bamber, J. A. Griggs, J. T. M. Lenaerts, S. R. M. Ligtenberg, M. R. van den Broeke, and G. Moholdt (2013), Calving fluxes and basal melt rates of Antarctic ice shelves, *Nature*, *502*(7469), 89–92, doi:10.1038/nature12567.

Dierking, W., S. Linow, and W. Rack (2012), Toward a robust retrieval of snow accumulation over the Antarctic ice sheet using satellite radar, *Journal of Geophysical Research*, *117*, D09110, doi:10.1029/2011JD017227.

Doake, C. S. M., H. F. J. Corr, H. Rott, P. Skvarca, and N. W. Young (1998), Breakup and conditions for stability of the northern Larsen Ice Shelf, Antarctica, *Nature*, *391*(6669), 778–780, doi:10.1038/35832.

Drews, R. (2015), Evolution of ice-shelf channels in Antarctic ice shelves, *The Cryosphere*, *9*(3), 1169–1181, doi:10.5194/tc-9-1169-2015.

Drinkwater, M. R., and X. Liu (2000), Seasonal to interannual variability in Antarctic sea-ice surface melt, *Special Issue of IEEE Transactions of Geoscience and Remote Sensing on "Emerging Scatterometer Applications"*, *38*(4), 1827–1842, doi:10.1109/36.851767

Drinkwater, M., D. Long, and A. Bingham (2001), Greenland snow accumulation estimates from satellite radar scatterometer data, *Journal of Geophysical Research, 106*(D24), 33935-33950, doi:10.1029/2001JD900107.

Dupont, T. K., and R. B. Alley (2005), Assessment of the importance of ice-shelf buttressing to ice-sheet flow, *Geophys. Res. Lett.*, *32*(4), L04503, doi:10.1029/2004GL022024.

Dutrieux, P., C. Stewart, A. Jenkins, K. W. Nicholls, H. F. J. Corr, E. Rignot, and K. Steffen (2014), Basal terraces on melting ice shelves, *Geophys. Res. Lett.*, *41*(15), 5506–5513, doi:10.1002/2014GL060618.

Dutrieux, P., D. G. Vaughan, H. F. J. Corr, A. Jenkins, P. R. Holland, I. Joughin, and A. H. Fleming (2013), Pine Island Glacier ice shelf melt distributed at kilometre scales, *The Cryosphere*, *7*(5), 1543–1555, doi:10.5194/tc-7-1543-2013.

Fahnestock, M., R. Bindschadler, R. Kwok, and K. C. Jezek (1993), Greenland ice sheet surface properties and ice dynamics from ERS-1 SAR imagery, *Science*, *262*(5139), 1530–1534, doi:10.1126/science.262.5139.1530.

Fahnestock, M., T. Scambos, T. Moon, A. Gardner, T. Haran, and M. Klinger (2016), Rapid large-area mapping of ice flow using Landsat 8, *Remote Sensing of Environment*, *185*, 84–94, doi:10.1016/j.rse.2015.11.023.

Foster, J. L., D. K. Hall, J. B. Eylander, G. A. Riggs, S. V. Nghiem, M. Tedesco, E. Kim, P. M. Montesano, R. E. J. Kelly, K. A. Casey, B. Choudhury (2011), A blended global snow product using visible, passive microwave and scatterometer satellite data, *International Journal of Remote Sensing*, *32*(5), 1371–1395, doi:10.1080/01431160903548013.

Forster R. R., J. E. Box, M. R. Van Den Broeke, C. Miege, E. W. Burgess, J. H. van Angelen, J. T. M. Lenaerts, L. S. Koenig, J. Paden, C. Lewis, S. P. Gogineni, C. Leuschen, J. R. McConnel (2014), Extensive liquid meltwater storage in firn within the Greenland ice sheet, *Nature Geoscience*, *7*(2), 95-98, doi:10.1038/ngeo2043.

Fretwell, P., H. D. Pritchard, and D. G. Vaughan (2012), Bedmap2: improved ice bed, surface and thickness datasets for Antarctica, *The Cryosphere*, *6*(5), 4305–4361, doi:10.5194/tcd-6-4305-2012.

Fricker, H. A., and L. Padman (2006), Ice shelf grounding zone structure from ICESat laser altimetry, *Geophys. Res. Lett.*, *33*(15), L15502, doi:10.1029/2006GL026907.

Fricker, H. A., R. Coleman, L. Padman, T. A. Scambos, J. Bohlander, and K. M. Brunt (2009), Mapping the grounding zone of the Amery Ice Shelf, East Antarctica using InSAR, MODIS

and ICESat, *Antarctic Science*, *21*(05), 515–532, doi:10.1017/S095410200999023X.

Fürst, J. J., G. Durand, F. Gillet-Chaulet, L. Tavard, M. Rankl, M. Braun, and O. Gagliardini (2016), The safety band of Antarctic ice shelves, *Nature Climate Change*, *6*, 479–482, doi:10.1038/nclimate2912.

Girard-Ardhuin, F., and R. Ezraty (2012), Enhanced Arctic Sea Ice Drift Estimation Merging Radiometer and Scatterometer Data, *IEEE Transactions on Geoscience and Remote Sensing*, *50*(7), 2639–2648, doi:10.1109/TGRS.2012.2184124.

Gladish, C. V., D. M. Holland, P. R. Holland, and S. F. Price (2012), Ice-shelf basal channels in a coupled ice/ocean model, *Journal of Glaciology*, *58*(212), 1227–1244, doi:10.3189/2012JoG12J003.

Glasser, N. F., and G. H. Gudmundsson (2012), Longitudinal surface structures (flowstripes) on Antarctic glaciers, *The Cryosphere*, *6*(2), 383–391, doi:10.5194/tc-6-383-2012.

Glen, J. W. (1955), The Creep of Polycrystalline Ice, *Proceedings of the Royal Society A: Mathematical, Physical and Engineering Sciences*, *228*(1175), 519–538, doi:10.1098/rspa.1955.0066.

Griggs, J. A., and J. L. Bamber (2011), Antarctic ice-shelf thickness from satellite radar altimetry, *Journal of Glaciology*, *57*(203), 485–498, doi:10.3189/002214311796905659.

Gudmundsson, G. H. (2013a), Ice-shelf buttressing and the stability of marine ice sheets, *The Cryosphere*, *7*(2), 647–655, doi:10.5194/tc-7-647-2013.

Haarpaintner, J. (2006), Arctic-wide operational sea ice drift from enhanced-resolution QuikScat/SeaWinds scatterometry and its validation, *IEEE Transactions on Geoscience and Remote Sensing*, *44*(1), 102–107, doi:10.1109/tgrs.2005.859352.

Haas, C. (2001a), The seasonal cycle of ERS scatterometer signatures over perennial Antarctic sea ice and associated surface ice properties and processes, *Annals of Glaciology*, *33*(1), 69–73, doi:10.3189/172756401781818301.

Haas, C., D. N. Thomas, and J. Bareiss (2001b), Surface properties and processes of perennial Antarctic sea ice in summer, *Journal of Glaciology*, *47*(159), 613–625, doi:10.3189/172756501781831864.

Hall, D. K., R. S. Williams, J. S. Barton, O. Sigurdsson, L. C. Smith, and J. B. Garvin (2000), Evaluation of remote-sensing techniques to measure decadal-scale changes of Hofsjökull ice cap, Iceland, *Journal of Glaciology*, *46*(154), 375–388, doi:10.3189/172756500781833061.

Hall, D. K., S. V. Nghiem, C. B. Schaaf, N. E. DiGirolamo, and G. Neumann (2009), Evaluation of surface and near-surface melt characteristics on the Greenland ice sheet using MODIS and

QuikSCAT data, *Journal of Geophysical Research*, *114*(F4), F04006, doi:10.1029/2009JF001287.

Hicks, B. R., and D. G. Long (2011), Inferring Greenland melt and refreeze severity from SeaWinds scatterometer data, *International Journal of Remote Sensing*, *32*(23), 8053–8080, doi:10.1080/01431161.2010.532174.

Holland, P. R. (2008), A model of tidally dominated ocean processes near ice shelf grounding lines, *Journal of Geophysical Research*, *113*(C11), C11002, doi:10.1029/2007JC004576.

Holland, P. R., H. F. J. Corr, H. D. Pritchard, D. G. Vaughan, R. J. Arthern, A. Jenkins, and M. Tedesco (2011), The air content of Larsen Ice Shelf, *Geophys. Res. Lett.*, *38*(10), L10503, doi:10.1029/2011GL047245.

Holland, P. R., and R. Kwok (2012), Wind-driven trends in Antarctic sea-ice drift, *Nature Geoscience*, *5*(12), 872–875, doi:10.1038/ngeo1627.

Holland, P. R., A. Brisbourne, H. F. J. Corr, D. McGrath, K. Purdon, J. Paden, H. A. Fricker, F. S. Paolo, and A. H. Fleming (2015), Oceanic and atmospheric forcing of Larsen C Ice-Shelf thinning, *The Cryosphere*, *9*(3), 1005–1024, doi:10.5194/tc-9-1005-2015.

Howat, I. M., S. Tulaczyk, E. Waddington, and H. Björnsson (2008), Dynamic controls on glacier basal motion inferred from surface ice motion, *J. Geophys. Res. Earth Surf.*, *113*(F3), doi:10.1029/2007JF000925.

Hubbard, B., A. Luckman, D. W. Ashmore, S. Bevan, B. Kulessa, P. K. Munneke, M. Philippe, D. Jansen, A. Booth, H. Sevestre, J. L. Tison, M. O'Leary, I. Rutt (2016), Massive subsurface ice formed by refreezing of ice-shelf melt ponds, *Nature Communications*, *7*, 1–6, doi:10.1038/ncomms11897.

Hughes, T. (1983), On the Disintegration of Ice Shelves: The Role of Fracture, *Journal of Glaciology*, *29*(101), 98–117, doi:10.1017/S0022143000005177.

Jacobs, S., A. Jenkins, H. Hellmer, C. Giulivi, F. Nitsche, B. Huber, and R. Guerrero (2012), The Amundsen Sea and the Antarctic Ice Sheet, *Oceanography*, *25*(3), 154–163, doi:10.5670/oceanog.2012.90.

Jenkins, A., and C. S. M. Doake (1991), Ice-ocean interaction on Ronne Ice Shelf, Antarctica, *Journal of Geophysical Research*, *96*(C1), 791–813, doi:10.1029/90JC01952.

Jezek, K. C., M. R. Drinkwater, J. P. Crawford, R. Bindschadler, and R. Kwok (1993), Analysis of synthetic aperture radar data collected over the southwestern Greenland ice sheet, *Journal of Glaciology*, *39*(131), 119–132, doi:10.3198/1993JoG39-131-119-132.

Jezek, K. C., P. Gogineni, and M. Shanableh (1994), Radar measurements of melt zones on the Greenland Ice Sheet, *Geophys. Res. Lett.*, *21*(1), 33–36, doi:10.1029/93GL03377.

Joughin, I., B. E. Smith, and B. Medley (2014), Marine Ice Sheet Collapse Potentially Under Way for the Thwaites Glacier Basin, West Antarctica, *Science*, *344*(6185), 735–738, doi:10.1126/science.1249055.

Joughin, I., W. Abdalati, and M. Fahnestock (2004), Large fluctuations in speed on Greenland's Jakobshavn Isbrae glacier, *Nature*, *432*(7017), 608–610, doi:10.1038/nature03130.

Khazendar, A., E. Rignot, and E. Larour (2007), Larsen B Ice Shelf rheology preceding its disintegration inferred by a control method, *Geophys. Res. Lett.*, *34*(19), L19503, doi:10.1029/2007GL030980.

Kulessa, B., D. Jansen, A. J. Luckman, E. C. King, and P. R. Sammonds (2014), Marine ice regulates the future stability of a large Antarctic ice shelf, *Nature Communications*, *5*, 3707, doi:10.1038/ncomms4707.

Kunz, L. B., and D. G. Long (2006), Melt Detection in Antarctic Ice Shelves Using Scatterometers and Microwave Radiometers, *IEEE Transactions on Geoscience and Remote Sensing*, *44*(9), 2461–2469, doi:10.1109/TGRS.2006.874138.

Langley, K., A. von Deschwanden, J. Kohler, A. Sinisalo, K. Matsuoka, T. Hattermann, A. Humbert, O. A. Nøst, and E. Isaksson (2014), Complex network of channels beneath an Antarctic ice shelf, *Geophys. Res. Lett.*, *41*(4), 1209–1215, doi:10.1002/2013GL058947.

Le Brocq, A. M. L., A. J. Payne, M. J. Siegert, and R. B. Alley (2009), A subglacial water-flow model for West Antarctica, *Journal of Glaciology*, *55*(193), 879–888, doi:10.3189/002214309790152564.

Le Brocq, A. M., N. Ross, J. A. Griggs, R. G. Bingham, H. F. J. Corr, F. Ferraccioli, A. Jenkins, T. A. Jordan, A. J. Payne, D. M. Rippin, and M. J. Siegert (2013), Evidence from ice shelves for channelized meltwater flow beneath the Antarctic Ice Sheet, *Nature Geoscience*, *6*(11), 945–948, doi:10.1038/ngeo1977.

Lenaerts, J., S. Lhermitte, R. Drews, S. R. M. Ligtenberg, S. Berger, V. Helm, C. J. P. P. Smeets, M. R. van den Broeke, W. J. van de Berg, E. van Meijgaard, M. Eijkelboom, O. Eisen, F. Pattyn (2016), Meltwater produced by wind-albedo interaction stored in an East Antarctic ice shelf, *Nature Climate Change*, *7*, 58-62, doi:10.1038/nclimate3180.

Ligtenberg, S. R. M., M. M. Heilsen, and M. R. van de Broeke (2011), An improved semi-empirical model for the densification of Antarctic firn, *The Cryosphere*, *5*(4), 809–819, doi:10.5194/tc-5-809-2011.

Lindell, D., and D. Long (2016), Multiyear Arctic Ice Classification Using ASCAT and SSMIS, *Remote Sensing*, *8*(4), 294–19, doi:10.3390/rs8040294.

Lindsley, R. D., and D. G. Long (2016), ASCAT and QuikSCAT Azimuth Modulation of Backscatter Over East Antarctica, *IEEE Geosci. Remote Sensing Lett.*, *13*(8), 1134–1138,

doi:10.1109/LGRS.2016.2572101.

Long, D. G., and M. R. Drinkwater (1994), Greenland ice-sheet surface properties observed by the Seasat-A scatterometer at enhanced resolution, *J Glaciol*, *40*(135), 213–230, doi:10.3198/1994JoG40-135-213-230.

Long, D. G., and M. R. Drinkwater (1999), Cryosphere applications of NSCAT data, *IEEE Transactions on Geoscience and Remote Sensing*, *37*(3), 1671–1684, doi:10.1109/36.763287.

Long, D. G., P. J. Hardin, and P. T. Whiting (1993), Resolution enhancement of spaceborne scatterometer data, *IEEE Transactions on Geoscience and Remote Sensing*, *31*(3), 700–715, doi:10.1109/36.225536.

MacAyeal, D. R., T. A. Scambos, C. L. Hulbe, and M. A. Fahnestock (2003), Catastrophic ice-shelf break-up by an ice-shelf-fragment-capsize mechanism, *Journal of Glaciology*, *49*(164), 22–36, doi:10.3189/172756503781830863.

Machguth, H., M. MacFerrin, D. van As, J. E. Box, C. Charalampidis, W. Colgan, R. S. Fausto, H. A. J. Meijer, E. Mosley-Thompson, and R. S. W. van de Wal (2016), Greenland meltwater storage in firn limited by near-surface ice formation, *Nature Climate Change*, *6*(4), 390–393, doi:10.1038/nclimate2899.

Mankoff, K. D., S. S. Jacobs, S. M. Tulaczyk, and S. E. Stammerjohn (2012), The role of Pine Island Glacier ice shelf basal channels in deep-water upwelling, polynyas and ocean circulation in Pine Island Bay, Antarctica, *Annals of Glaciology*, *53*(60), 123–128, doi:10.3189/2012AoG60A062.

Marsh, O. J., H. A. Fricker, M. R. Siegfried, K. Christianson, K. W. Nicholls, H. F. J. Corr, and G. Catania (2016), High basal melting forming a channel at the grounding line of Ross Ice Shelf, Antarctica, *Geophys. Res. Lett.*, *43*(1), 250–255, doi:10.1002/2015GL066612.

Meier, W. N., and J. Stroeve (2008), Comparison of sea-ice extent and ice-edge location estimates from passive microwave and enhanced-resolution scatterometer data, *Annals of Glaciology*, *48*(1), 65–70, doi:10.3189/172756408784700743.

Millgate, T., P. R. Holland, A. Jenkins, and H. L. Johnson (2013), The effect of basal channels on oceanic ice-shelf melting, *Journal of Geophysical Research*, *118*(12), 6951–6964, doi:10.1002/2013JC009402.

Mote, Thomas L. 2014. MEaSUREs Greenland Surface Melt Daily 25km EASE-Grid 2.0, [2004-2013]. Boulder, Colorado USA: NASA DAAC at the National Snow and Ice Data Center. doi:10.5067/measures/cryosphere/nsidc-0533.001.

Munneke, P. K., S. R. M. Ligtenberg, M. R. Van Den Broeke, and D. G. Vaughan (2014), Firn air depletion as a precursor of Antarctic ice-shelf collapse, *Journal of Glaciology*, *60*(220), 205–

214, doi:10.3189/2014JoG13J183.

Murray, T., T. Strozzi, A. Luckman, H. Jiskoot, and P. Christakos (2003), Is there a single surge mechanism? Contrasts in dynamics between glacier surges in Svalbard and other regions, *J. Geophys. Res.*, *108*(B5), 2237, doi:10.1029/2002JB001906.

Nghiem, S. V., and W. Y. Tsai (2001), Global snow cover monitoring with spaceborne K u-band scatterometer, *IEEE transactions on geoscience and remote sensing*, *39*(10), 2118–2134, doi:10.1109/36.957275&url_ctx_fmt=info:ofi/fmt:kev:mtx:ctx&rft_val_fmt=info:ofi/fmt:kev:mtx:journal&rft.atitle=Global.

Nghiem, S. V., K. Steffen, G. Neumann, and R. Huff (2005), Mapping of ice layer extent and snow accumulation in the percolation zone of the Greenland ice sheet, *Journal of Geophysical Research*, *110*(F2), F02017, doi:10.1029/2004JF000234.

Nghiem, S. V., K. Steffen, G. Neumann, and R. Huff (2007), Snow accumulation and snowmelt monitoring in Greenland and Antarctica, *Dynamic Planet*, Springer, 130(5), 31-38, doi: 10.1007/978-3-540-49350-1_5.

Nye, J. F. (1953), The Flow Law of Ice from Measurements in Glacier Tunnels, Laboratory Experiments and the Jungfraufirn Borehole Experiment, *Proceedings of the Royal Society A: Mathematical, Physical and Engineering Sciences*, *219*(1139), 477–489, doi:10.1098/rspa.1953.0161.

Nye, J. F. (1957), The Distribution of Stress and Velocity in Glaciers and Ice-Sheets, *Proceedings of the Royal Society A: Mathematical, Physical and Engineering Sciences*, *239*(1216), 113–133, doi:10.1098/rspa.1957.0026.

Nye, J. F. (1959), A method of determining the strain-rate tensor at the surface of a glacier, *Journal of Glaciology*, *Cambridge Austerdalsbre Expedition*(Paper No. 6), 409–419.

Padman, L. et al. (2012), Oceanic controls on the mass balance of Wilkins Ice Shelf, Antarctica, *Journal of Geophysical Research*, *117*(C1), C01010, doi:10.1029/2011JC007301.

Padman, L., H. A. Fricker, R. Coleman, S. Howard, and L. Erofeeva (2002), A new tide model for the Antarctic ice shelves and seas, *Annals of Glaciology*, *34*(1), 247–254, doi:10.3189/172756402781817752.

Paolo, F. S., H. A. Fricker, and L. Padman (2015), Volume loss from Antarctic ice shelves is accelerating, *Science*, *348*(6232), 327–331, doi:10.1126/science.aaa0940.

Partington, K. C. (1998), Discrimination of glacier facies using multi-temporal SAR data, *Journal of Glaciology*, *44*(146), 42–53, doi:10.3198/1998JoG44-146-42-53.

Perovich, D. K., S. V. Nghiem, T. Markus, and A. Schweiger (2007), Seasonal evolution and interannual variability of the local solar energy absorbed by the Arctic sea ice–ocean

system, *Journal of Geophysical Research*, *112*(C3), C03005–13, doi:10.1029/2006JC003558.

Pfeffer, W. T., M. F. Meier, and T. H. Illangasekare (1991), Retention of Greenland runoff by refreezing: Implications for projected future sea level change, *Journal of Geophysical Research*, *96*(C12), 22117–22124, doi:10.1029/91JC02502.

Picard, G., and M. Fily (2006), Surface melting observations in Antarctica by microwave radiometers: Correcting 26-year time series from changes in acquisition hours, *Remote Sensing of the Environment*, *104*(3), 325-336, doi:10.1016/j.rse.2006.05.010.

Pritchard, H. D., S. R. M. Ligtenberg, H. A. Fricker, D. G. Vaughan, M. R. van den Broeke, and L. Padman (2012), Antarctic ice-sheet loss driven by basal melting of ice shelves, *Nature*, *484*(7395), 502–505, doi:10.1038/nature10968.

Rees, D. (2006), *Basic Engineering Plasticity*, Elsevier, London, pp. 528, isbn:9780750680257.

Remund, Q. P., and D. G. Long (2000), Iterative estimation of Antarctic sea ice extent using SeaWinds data, *Geoscience and Remote Sensing Symposium Proceedings,* 24-28 July, 2000.

Remund, Q. P., and D. G. Long (2014), A Decade of QuikSCAT Scatterometer Sea Ice Extent Data, *IEEE Transactions on Geoscience and Remote Sensing*, *52*(7), 4281–4290, doi:10.1109/TGRS.2013.2281056.

Rignot, E., and K. Steffen (2008), Channelized bottom melting and stability of floating ice shelves, *Geophys. Res. Lett.*, *35*(2), L02503, doi:10.1029/2007GL031765.

Rignot, E., G. Casassa, P. Gogineni, W. Krabill, A. Rivera, and R. Thomas (2004), Accelerated ice discharge from the Antarctic Peninsula following the collapse of Larsen B ice shelf, *Geophys. Res. Lett.*, *31*(18), L18401, doi:10.1029/2004GL020697.

Rignot, E., J. Mouginot, and B. Scheuchl (2011), Ice Flow of the Antarctic Ice Sheet, *Science*, *333*(6048), 1427–1430, doi:10.1126/science.1208336.

Rignot, E., J. Mouginot, M. Morlighem, H. Seroussi, and B. Scheuchl (2014), Widespread, rapid grounding line retreat of Pine Island, Thwaites, Smith, and Kohler glaciers, West Antarctica, from 1992 to 2011, *Geophys. Res. Lett.*, *41*(10), 3502–3509, doi:10.1002/2014GL060140.

Rignot, E., S. Jacobs, J. Mouginot, and B. Scheuchl (2013), Ice-shelf melting around Antarctica, *Science*, *341*(6143), 266–270, doi:10.1126/science.1235798.

Rotschky, G., W. Rack, W. Dierking, and H. Oerter (2006), Retrieving snowpack properties and accumulation estimates from a combination of SAR and scatterometer measurements, *IEEE Transactions on Geoscience and Remote Sensing*, *44*(4), 943–956, doi:10.1109/TGRS.2005.862524.

Rott, H., P. Skvarca, and T. Nagler (1996), Rapid Collapse of Northern Larsen Ice Shelf,

Antarctica, *Science*, *271*(5250), 788–792, doi:10.1126/science.271.5250.788.

Rott, H., and W. Rack (1995), *Characterization of Antarctic firn by means of ERS-1 scatterometer measurements*, *Geosciences and Remote Sensing Symposium Proceedings,* 10-14 July, 1995.

Rott, H., K. Sturm, and H. Miller (1993), Active and passive microwave signatures of Antarctic firn by means of field measurements and satellite data, *Annals of Glaciology*, 17, 337-343, doi:10.3198/1993AoG17-1-337-343.

Rumrill, J. (2009), Analysis of Spatial and Temporal Variations in Strain Rates Near Swiss Camp, Greenland, *University of Vermont* Master of Science thesis, edited by T. A. Neumann and G. A. Catania.

Scambos, T. A., C. Hulbe, M. Fahnestock, and J. Bohlander (2000), The link between climate warming and break-up of ice shelves in the Antarctic Peninsula, *Journal of Glaciology*, *46*(154), 516–530, doi:10.3189/172756500781833043.

Scambos, T. A., J. Bohlander, C. A. Shuman, and P. Skvarca (2004), Glacier acceleration and thinning after ice shelf collapse in the Larsen B embayment, Antarctica, *Geophys. Res. Lett.*, *31*(18), L18402, doi:10.1029/2004GL020670.

Scambos, T. A., T. M. Haran, M. A. Fahnestock, T. H. Painter, and J. Bohlander (2007), MODIS-based Mosaic of Antarctica (MOA) data sets: Continent-wide surface morphology and snow grain size, *Remote Sensing of Environment*, *111*(2-3), 242–257, doi:10.1016/j.rse.2006.12.020.

Scambos, T., and C. Hulbe, and M. Fahnestock (2003), Climate-induced ice shelf disintegration in the Antarctic peninsula, in *Antarctic Peninsula Climate Variability: Historical and Paleoenvironmental Perspectives,* edited by E. Domack, A. Leventer, A. Burnett, R. Bindschadler, P. Convey, and M. Kirby, doi:10.1029/AR079p0079.

Schmidtko, S., K. J. Heywood, A. F. Thompson, and S. Aoki (2014), Multidecadal warming of Antarctic waters, *Science*, *346*(6214), 1227–1231, doi:10.1126/science.1256117.

Sergienko, O. V. (2013), Basal channels on ice shelves, *J. Geophys. Res. Earth Surf.*, *118*(3), 1342–1355, doi:10.1002/jgrf.20105.

Shepherd, A., D. Wingham, and E. Rignot (2004), Warm ocean is eroding West Antarctic Ice Sheet, *Geophys. Res. Lett.*, *31*(23), doi:10.1029/2004GL021106.

Smith, L. C., Y. Sheng, R. R. Forster, K. Steffen, K. E. Frey, and D. E. Alsdorf (2003), Melting of small Arctic ice caps observed from ERS scatterometer time series, *Geophys. Res. Lett.*, *30*(20), 2034, doi:10.1029/2003GL017641.

Swan, A. M., and D. G. Long (2012), Multiyear Arctic Sea Ice Classification Using QuikSCAT, *IEEE Transactions on Geoscience and Remote Sensing*, *50*(9), 3317–3326,

doi:10.1109/TGRS.2012.2184123.

Trusel, L. D., K. E. Frey, and S. B. Das (2012), Antarctic surface melting dynamics: Enhanced perspectives from radar scatterometer data, *J. Geophys. Res. Earth Surf.*, *117*(F2), F02023, doi:10.1029/2011JF002126.

Ulaby, F., and Long, D. (2014), Microwave Radar and Radiometric Remote Sensing, *University of Michigan Press*, Ann Arbor, Michigan, pp. 984.

Van Wessem, J. M., C. H. Reijmer, M. Morlighem, J. Mouginot, B. Medley, I. Joughin, B. Wouters, M. A. Depoorter, J. L. Bamber, J. T. M. Lenaerts, W. J. van de Berg, M. R. van den Broeke, E. van Meijgaard (2014), Improved representation of East Antarctic surface mass balance in a regional atmospheric climate model, *Journal of Glaciology*, *60*(222), 761–770, doi:10.3189/2014JoG14J051.

Vaughan, D. G. (1993), Relating the occurrence of crevasses to surface strain rates, *Journal of Glaciology*, *39*(132), 255–266, doi:10.1017/s0022143000015926.

Vaughan, D. G., H. F. J. Corr, R. A. Bindschadler, P. Dutrieux, G. H. Gudmundsson, A. Jenkins, T. Newman, P. Vornberger, and D. J. Wingham (2012a), Subglacial melt channels and fracture in the floating part of Pine Island Glacier, Antarctica, *J. Geophys. Res.*, *117*(F3), F03012, doi:10.1029/2012JF002360.

Wang, L., C. Derksen, and R. Brown (2008), Detection of pan-Arctic terrestrial snowmelt from QuikSCAT, 2000–2005, *Remote Sensing of Environment*, *112*(10), 3794–3805, doi:10.1016/j.rse.2008.05.017.

Wang, L., M. J. Sharp, B. Rivard, S. Marshall, and D. Burgess (2005), Melt season duration on Canadian Arctic ice caps, 2000-2004, *Geophys. Res. Lett.*, *32*(19), L19502, doi:10.1029/2005GL023962.

Willmes, S., C. Haas, and M. Nicolaus (2011), High radar-backscatter regions on Antarctic sea-ice and their relation to sea-ice and snow properties and meteorological conditions, *International Journal of Remote Sensing*, *32*(14), 3967–3984, doi:10.1080/01431161003801344.

Winebrenner, D. P., E. D. Nelson, R. Colony, and R. D. West (1994), Observation of melt onset on multiyear Arctic sea ice using the ERS 1 synthetic aperture radar, *Journal of Geophysical Research*, *99*(C11), 22425–22441, doi:10.1029/94JC01268.

Zwally, H. J. (2002), Surface Melt-Induced Acceleration of Greenland Ice-Sheet Flow, *Science*, *297*(5579), 218–222, doi:10.1126/science.1072708.

Appendix to Chapter 3

Appendix 3A: Basal channel data

Table A.3.1 | Appendix table: Basal channel data.
Area, basal channel length, and grounding line depth data for all ice shelves, ice shelf subsections, and Antarctic sea divisions.

Shelf name	Shelf area (km^2)	Subglacially-sourced channel length (km)	Ocean-sourced channel length (km)	Grounding-line-sourced channel length (km)	Possible channel length (km)	Total channel length (km)	Total channel density ($100*km/km^{2)}$	Minimum grounding line depth (m)
Withrow	650	0	0	0	0	0	0.00	-433
Ross 1	35259	96	73		53	222	0.63	-957
Ross 2	61913	72	0	0	184	256	0.41	-742
Ross 3	131266	147	0	0	0	147	0.11	-603
Ross 4	133113	59	0	149	0	208	0.16	-1004
Ross 5	74160	0	258	0	0	258	0.35	-737
Ross 6	46251	0	0	182	0	182	0.39	-1431
Ross total	481961	374	331	331	237	1273	0.26	
Drygalski	2424	0	22	0	0	22	0.91	-786
Nansen	2264	0	0	0	24	24	1.06	-538
Aviator	860	0	27	0	0	27	3.14	-515
Mariner	2714	0	0	16	0	16	0.59	-752
Ross Sea	490872	374	380	347	261	1362	0.28	
Lillie	572	0	60	0	0	60	10.48	-1284
Rennick	3121	0	134	50	0	184	5.89	-1131
Cook	3665	0	0	0	0	0	0.00	-806
Ninnis	2177	0	0	0	0	0	0.00	-936
Mertz	5706	0	0	0	0	0	0.00	-1090
Dibble	1550	0	51	27	0	78	5.03	-1062
Holmes	1861	0	32	0	0	32	1.72	-730
Moscow Univ	4947	0	217	105	0	322	6.51	-2046
Totten 1	3844	0	12	17	0	29	0.75	-1329
Totten 2	4428	0	270	238	0	508	11.47	-2093
Totten total	8273	0	282	255	0	537	6.49	
Dumont D'Urville Sea	31873	0	776	437	0	1213	3.81	
Vincennes	1150	0	0	0	0	0	0.00	-1468
Conger	2499	0	0	0	0	0	0.00	-173
Tracy-Tremenchus	9843	0	0	0	0	0	0.00	-1388
Shackleton	22357	0	0	0	0	0	0.00	-601
West 1	3551	0	25	0	0	25	0.70	-835
West 2	7892	0	0	0	0	0	0.00	-869
West 3	5470	0	0	0	0	0	0.00	-876
West total	16912	0	25	0	0	25	0.15	

Shelf name	Shelf area (km^2)	Subglacially-sourced channel length (km)	Ocean-sourced channel length (km)	Grounding-line-sourced channel length (km)	Possible channel length (km)	Total channel length (km)	Total channel density ($100*km/km^{2)}$	Minimum grounding line depth (m)
Mawson Sea	52761	0	25	0	0	25	0.05	
Publications	1279	0	0	0	0	0	0.00	-541
Amery 1	11436	0	0	0	0	0	0.00	-860
Amery 2	31814	0	0	0	0	0	0.00	-2010
Amery 3	18384	0	0	0	0	0	0.00	-752
Amery total	61634	0	0	0	0	0	0.00	
Wilma-Robert-Downer	1066	0	80	0	0	80	7.50	-928
Edward VIII	469	0	0	0	0	0	0.00	-494
Cooperation Sea	64449	0	80	0	0	80	0.12	
Rayner-Thyer 1	891	0	0	0	0	0	0.00	-794
Rayner-Thyer 2	495	0	0	0	0	0	0.00	-406
Rayner-Thyer total	1386	0	0	0	0	0	0.00	
Shirase	690	0	0	0	0	0	0.00	-929
Prince Harald 1	862	0	0	0	0	0	0.00	-259
Prince Harald 2	2787	45	0	127	0	172	6.17	-436
Prince Harald 3	1703	0	44	83	0	127	7.46	-498
Prince Harald total	5352	45	44	210	0	299	5.59	
Baudouin 1	7509	0	0	0	0	0	0.00	-499
Baudouin 2	10547	0	0	171	0	171	1.62	-613
Baudouin 3	6877	0	0	0	0	0	0.00	-670
Baudouin 4	8293	362	73	221	0	656	7.91	-746
Baudouin total	33226	362	73	392	0	827	2.49	
Borchgrevink 1	4170	0	55	0	45	100	2.40	-823
Borchgrevink 2	10473	0	0	106	62	168	1.60	-717
Borchgrevink total	14643	0	55	106	107	268	1.83	
Cosmonaut Sea	55297	407	172	708	107	1394	2.52	
Lazarev 1	7197	0	0	0	14	14	0.19	-745
Lazarev 2	8654	0	0	0	0	0	0.00	-539
Lazarev total	15850	0	0	0	14	14	0.09	
Nivl	7362	0	0	0	0	0	0.00	-628
Vigrid	2028	0	0	0	23	23	1.13	-564
Fimbul 1	6127	0	0	64	19	83	1.35	-721
Fimbul 2	10093	0	19	0	0	19	0.19	-444
Fimbul 3	23798	56	24	113	0	193	0.81	-664
Fimbul total	40018	56	43	177	19	295	0.74	
Jelbart	11017	0	0	46	0	46	0.42	-1078
Atka	2008	0	0	0	0	0	0.00	-454
Ekstrom	6964	0	0	18	0	18	0.26	-869

Shelf name	Shelf area (km^2)	Subglacially-sourced channel length (km)	Ocean-sourced channel length (km)	Grounding-line-sourced channel length (km)	Possible channel length (km)	Total channel length (km)	Total channel density ($100*km/km^{2)}$	Minimum grounding line depth (m)
Quar	2233	0	17	0	23	40	1.79	-607
King Håkon Sea	87480	56	60	241	79	436	0.50	0.43
Riiser-Larsen 1	6427	0	0	0	0	0	0.00	-522
Riiser-Larsen 2	10729	0	0	0	16	16	0.15	-852
Riiser-Larsen 3	25048	0	167	94	0	261	1.04	-910
Riiser-Larsen total	42203	0	167	94	16	277	0.66	
Stancomb-Brunt 1	9885	0	0	0	0	0	0.00	-479
Stancomb-Brunt 2	17156	0	0	0	0	0	0.00	-772
Stancomb-Brunt 3	9725	0	0	0	0	0	0.00	-368
Stancomb-Brunt total	36766	0	0	0	0	0	0.00	
Filchner 1	45088	55	0	97	0	152	0.34	-1588
Filchner 2	39440	97	0	38	0	135	0.34	-1337
Filchner total	84528	152	0	135	0	287	0.34	
Ronne 1	100001	315	0	0	124	439	0.44	-1790
Ronne 2	96995	141	0	0	0	141	0.15	-1154
Ronne 3	73242	60	214	0	0	274	0.37	-1590
Ronne 4	65215	91	0	144	0	235	0.36	-1642
Ronne total	335454	607	214	144	124	1089	0.32	
Larsen G	456	0	0	0	0	0	0.00	-312
Larsen F	824	0	0	0	25	25	3.03	-505
Larsen E	1387	0	25	0	54	79	5.70	-590
Larsen D 1	5019	0	25	0	13	38	0.76	-751
Larsen D 2	3686	0	0	0	0	0	0.00	-499
Larsen D 3	5722	0	0	0	0	0	0.00	-554
Larsen D 4	9039	0	0	0	0	0	0.00	-582
Larsen D total	23467	0	25	0	13	38	0.16	
Larsen C 1	18549	0	0	0	0	0	0.00	-822
Larsen C 2	17677	0	0	0	0	0	0.00	-524
Larsen C 3	11582	0	0	0	0	0	0.00	-567
Larsen C total	47808	0	0	0	0	0	0.00	
Larsen B 1	1839	0	0	0	0	0	0.00	-574
Larsen B 2	779	0	0	0	0	0	0.00	-90
Larsen B total	2618	0	0	0	0	0	0.00	
Weddell Sea	575511	759	431	373	232	1795	0.31	
Wordie	101	0	0	0	0	0	0.00	-598
Wilkins 1	5036	0	70	0	0	70	1.39	-281
Wilkins 2	7518	0	25	0	0	25	0.33	-554
Wilkins total	12553	0	95	0	0	95	0.76	
George VI 1	3544	0	46	0	0	46	1.30	-393
George VI 2	7501	0	81	0	23	104	1.39	-600

Shelf name	Shelf area (km^2)	Subglacially-sourced channel length (km)	Ocean-sourced channel length (km)	Grounding-line-sourced channel length (km)	Possible channel length (km)	Total channel length (km)	Total channel density ($100*km/km^{2)}$	Minimum grounding line depth (m)
George VI 3	8687	0	147	0	0	147	1.69	-750
George VI 4	3313	0	52	0	0	52	1.57	-596
George VI total	23045	0	326	0	23	349	1.51	
Bach	4452	0	128	0	0	128	2.87	-388
Stange 1	4091	0	130	0	0	130	3.18	-810
Stange 2	3776	0	125	0	0	125	3.31	-718
Stange total	7866	0	255	0	0	255	3.24	
Ferrigno	250	0	0	18	0	18	7.20	-668
Venable	3169	0	199	0	0	199	6.28	-708
Abbot 1	3072	0	135	0	0	135	4.39	-496
Abbot 2	4070	0	34	0	0	34	0.84	-450
Abbot 3	12823	0	246	0	0	246	1.92	-701
Abbot 4	9570	0	118	0	0	118	1.23	-391
Abbot total	29534	0	533	0	0	533	1.80	
Bellingshausen Sea	80972	0	1536	18	23	1577	1.95	
Cosgrove	2885	0	112	24	0	136	4.71	-575
Pine Island 1	2009	0	56	24	0	80	3.98	-470
Pine Island 2	3640	0	289	0	0	289	7.94	-1153
Pine Island total	5649	0	345	24	0	369	6.53	
Thwaites 1	2141	21	28	9	0	58	2.71	-795
Thwaites 2	3002	36	0	0	22	58	1.93	-845
Thwaites total	5143	57	28	9	22	116	2.26	
Crosson	3862	0	62	0	0	62	1.61	-850
Dotson	5137	0	174	0	0	174	3.39	-1025
Getz 1	3799	0	125	64	0	189	4.98	-602
Getz 2	7350	0	538	0	0	538	7.32	-894
Getz 3	12888	0	285	28	0	313	2.43	-743
Getz 4	4844	0	14	0	0	14	0.29	-526
Getz 5	3599	0	49	0	0	49	1.36	-839
Getz total	32479	0	1011	92	0	1103	3.40	
Land	715	0	42	0	0	42	5.87	-651
Nickerson 1	2325	0	22	0	0	22	0.95	-496
Nickerson 2	4200	0	103	0	0	103	2.45	-773
Nickerson total	6525	0	125	0	0	125	1.92	
Sulzberger 1	7587	0	288	67	0	355	4.68	-681
Sulzberger 2	4397	0	171	20	0	191	4.34	-839
Sulzberger total	11984	0	459	87	0	546	4.56	
Swinburne	846	0	0	0	0	0	0.00	-690
Amundsen Sea	75227	57	2358	236	22	2673	3.55	

Appendix 3B: Persistent polynya data

Table A.3.2 | Appendix table: Persistent polynya data.
Locations and years of observed persistent polynyas near Antarctic ice shelves. Numbers correspond to following 11 figures.

Ice Shelf	Figure number	Polynya # (see figs.)	# of summers w/ images and fast ice	# of summers polynya observed	Years observed	Channel type
Wilkins	B S1	1	11	11	2003-2014	None
Bach	B S1	2	5	5	2003, 2004-2007, 2013	Ocean-sourced
George VI	B S2	1	12	12	2003-2014	Ocean-sourced
George VI	B S2	2	12	11	2003-2006, 2007-2013	None
George VI	B S2	3	12	10	2003-2005, 2007-2014	Ocean-sourced
Abbot	B S3	1	12	11	2002-2003; 2004-2014	Ocean-sourced
Abbot	B S3	2	11	11	2002-2008, 2010-2014	Ocean-sourced
Venable	B S3	3	12	9	2003-2005, 2007-2012	Ocean-sourced
Cosgrove	B S4	1	7	7	2002, 2004, 2006-2007, 2011-2014	Grounding-line-sourced
Cosgrove	B S4	2	7	3	2006-2007, 2013-2014	Ocean-sourced
Pine Island	B S5	1	5	5	2003-2007	Ocean-sourced
Pine Island	B S5	2	5	4	2003-2007	Ocean-sourced
Pine Island	B S5	3	5	5	2003-2007	Ocean-sourced
Crossen	B S6	1	6	6	2008-2013	Ocean-sourced
Thwaites	B S6	2	12	12	2002-2014	Ocean-sourced
Thwaites	B S6	3	11	10	2002-2011, 2013-2014	Ocean-sourced
Getz	B S7	1	12	11	2004-2014	Ocean-sourced
Getz	B S7	2	12	11	2002-2004, 2005-2010, 2012-2013	Ocean-sourced
Getz	B S7	3	9	7	2003, 2006-2008, 2009-2012	Ocean-sourced
Getz	B S7	4	11	10	2004-2013	Ocean-sourced
Sulzberger	B S8	1	8	6	2006-2007, 2009, 2011-2014	Ocean-sourced
Sulzberger	B S8	2	8	6	2006-2007, 2009-2014	Ocean-sourced
Lillie	B S9	1	3	3	2011-2014	Ocean-sourced
Lillie	B S9	2	3	3	2011-2014	Ocean-sourced
Totten	B S10	1	12	12	2002-2014	Ocean-sourced

Figure A.3.1 | Appendix figure: Polynyas on the Wilkins and Bach Ice Shelves. Polynya 2 is found at the end of an ocean-sourced channel.

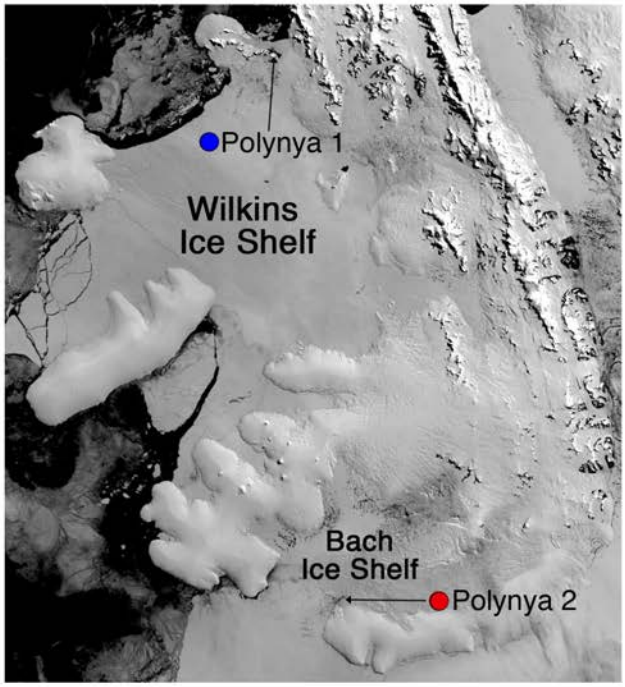

Figure A.3.2 | Appendix figure: Polynyas on the George VI Ice Shelf. Polynyas 1 and 3 are found at the ends of ocean-sourced channels.

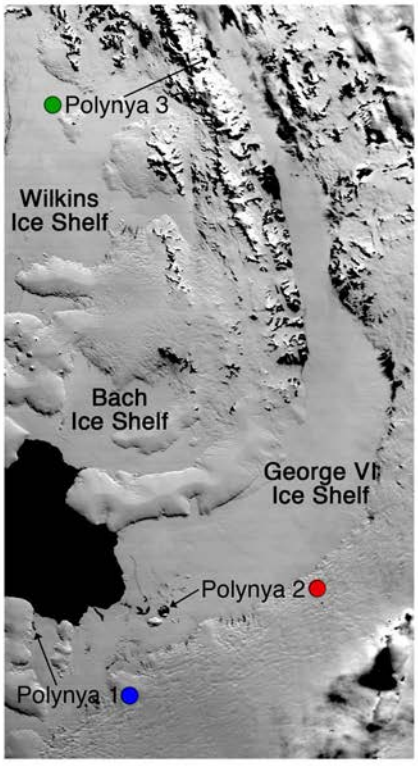

Figure A.3.3 | Appendix figure: Polynyas on the Abbot and Venable Ice Shelves.
All three polynyas are found at the ends of ocean-sourced channels.

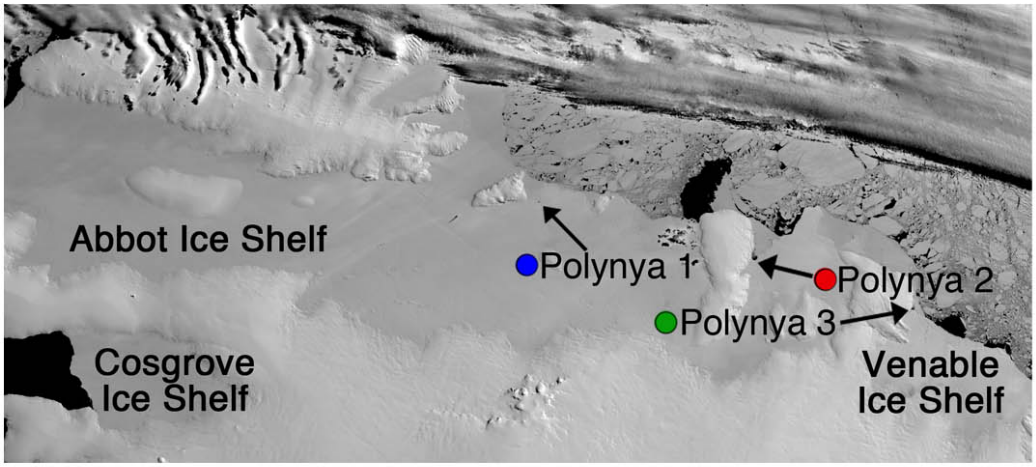

Figure A.3.4 | Appendix figure: Polynyas on the Cosgrove Ice Shelf.
Polynya 1 is found at the end of a grounding-line-sourced channel, and polynya 2 is found at the end of an ocean-sourced channel.

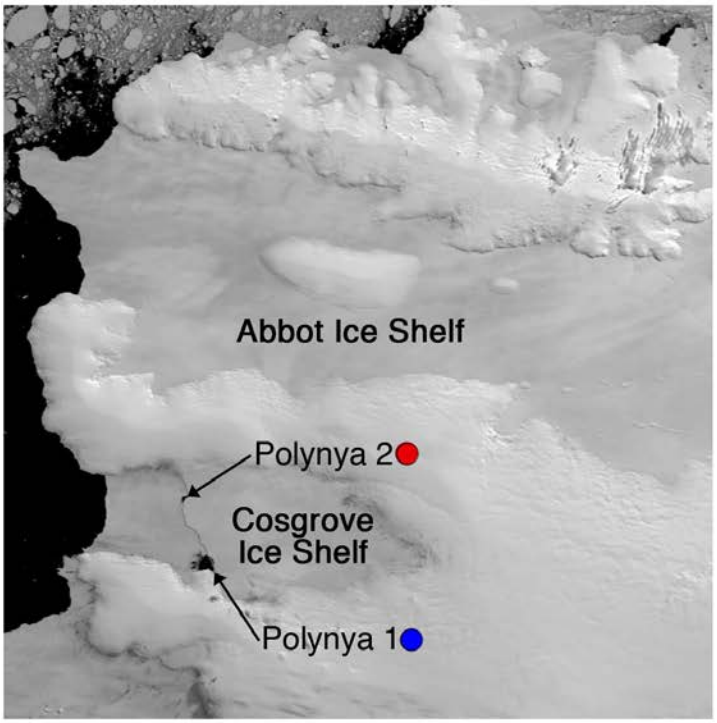

Figure A.3.5 | Appendix figure: Polynyas on the Pine Island Ice Shelf.
All three polynyas are found at the ends of ocean-sourced channels.

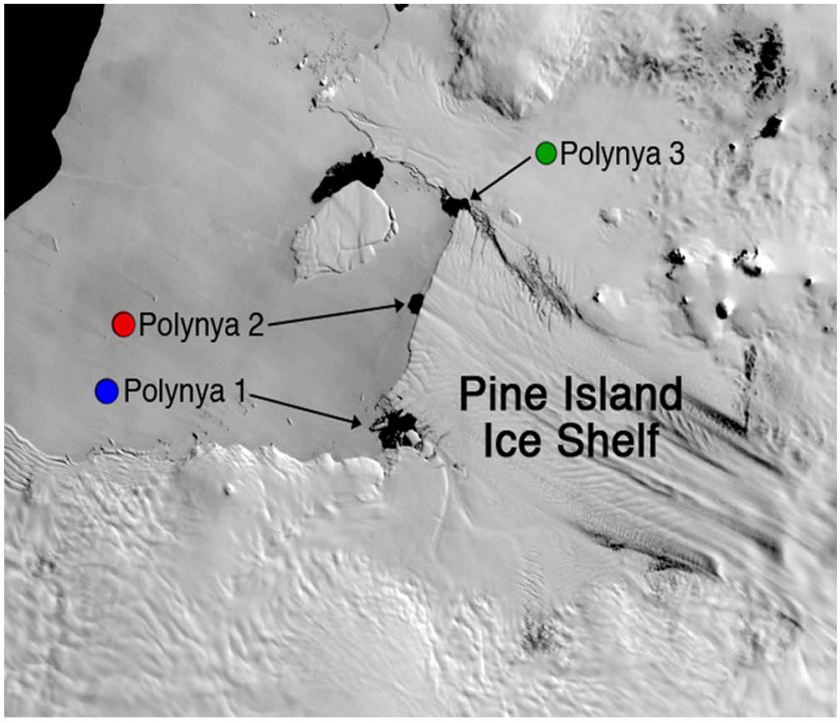

Figure A.3.6 | Appendix figure: Polynyas on the Thwaites and Crosson Ice Shelves.
All three polynyas are found at the ends of ocean-sourced channels.

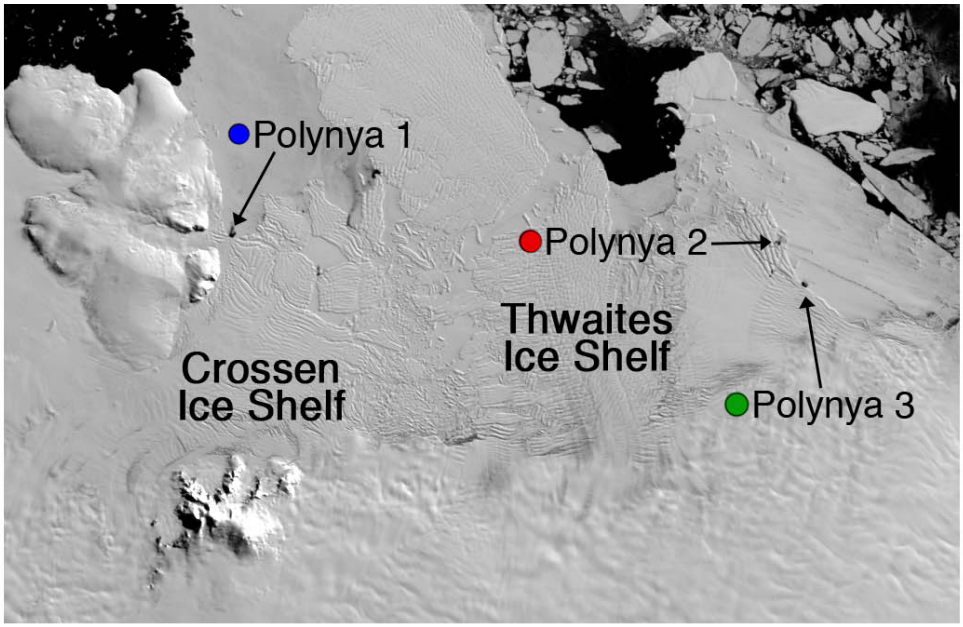

Figure A.3.7 | Appendix figure: Polynyas on the Getz Ice Shelf.
All four polynyas are found at the ends of ocean-sourced channels.

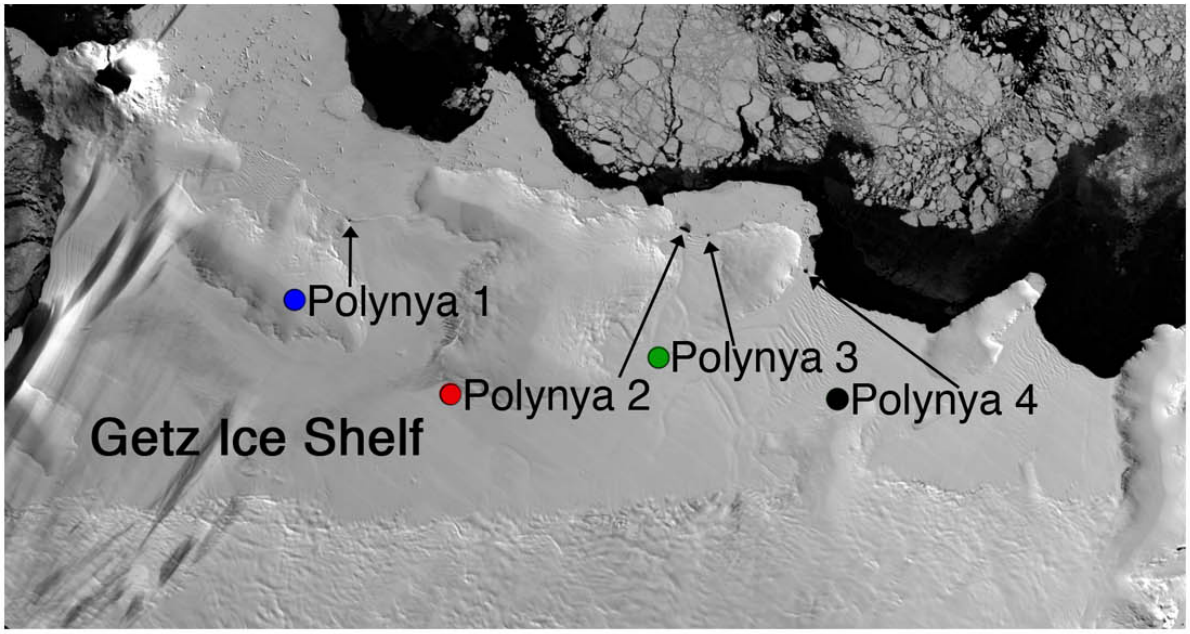

Figure A.3.8 | Appendix figure: Polynyas on the Sulzberger Ice Shelf.
Both polynyas are found at the ends of ocean-sourced channels.

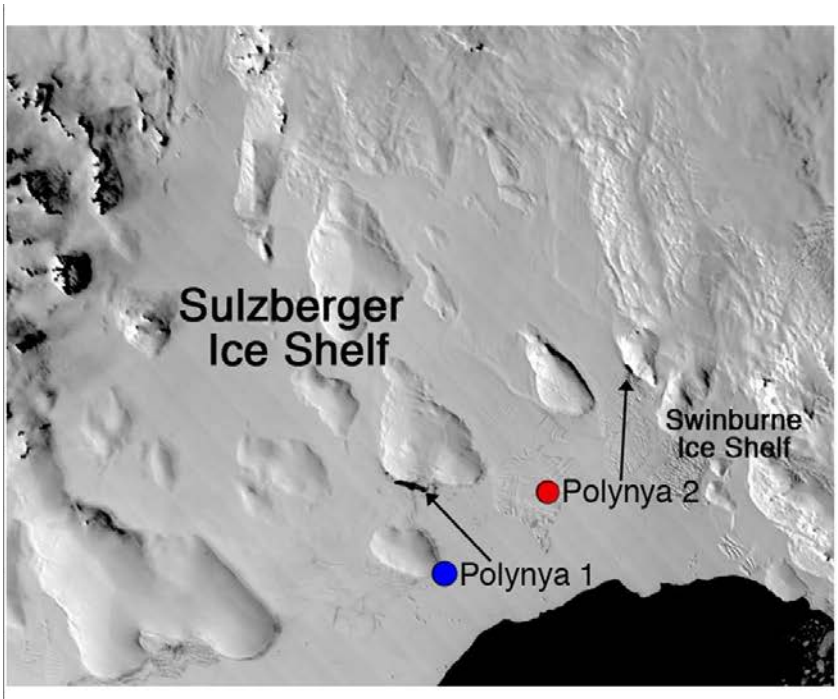

Figure A.3.9 | Appendix figure: Polynyas on the Lillie Ice Shelf.
Both polynyas are found at the ends of ocean-sourced channels.

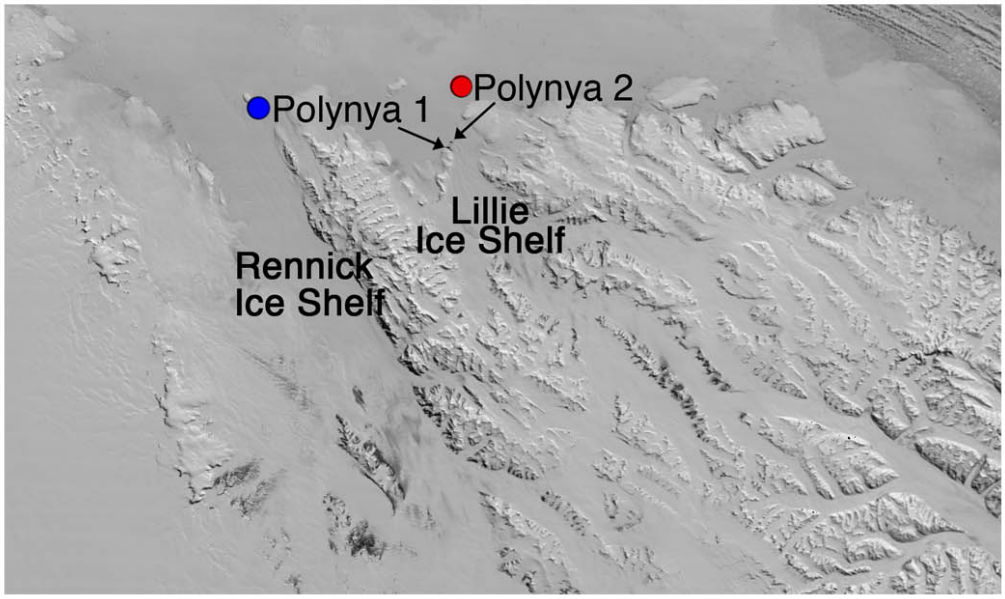

Figure A.3.10 | Appendix figure: Polynya on the Totten Ice Shelf.
The polynya is found at the end of an ocean-sourced channel.

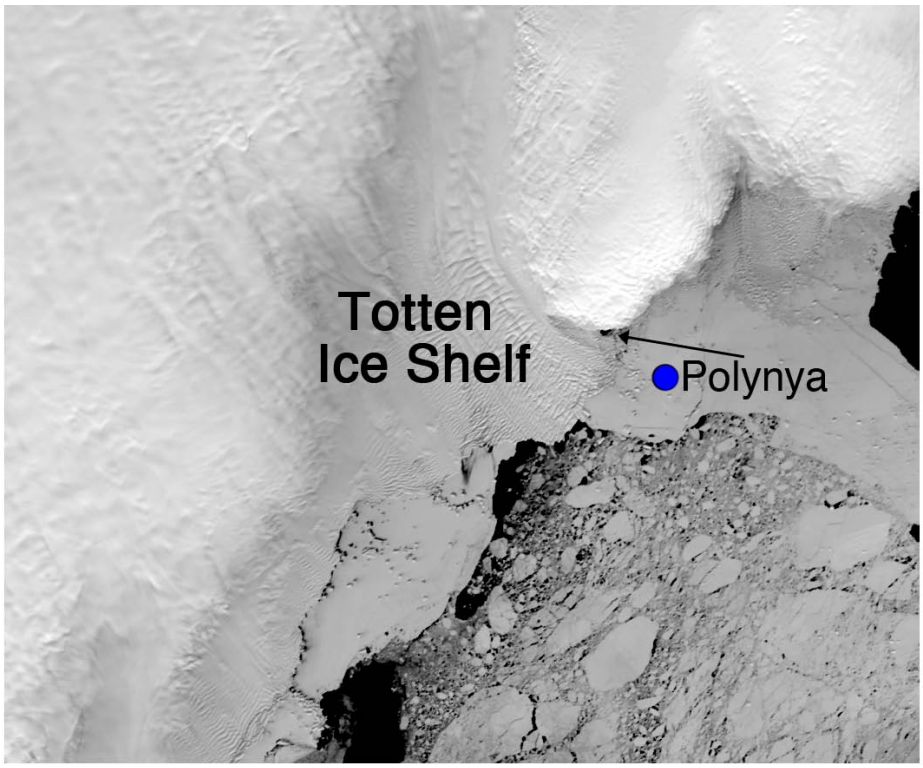

Figure A.3.11 | Appendix figure: Locations of figures showing persistent polynyas.
Numbers correspond to supplementary information appendix B figure numbers 1-10.

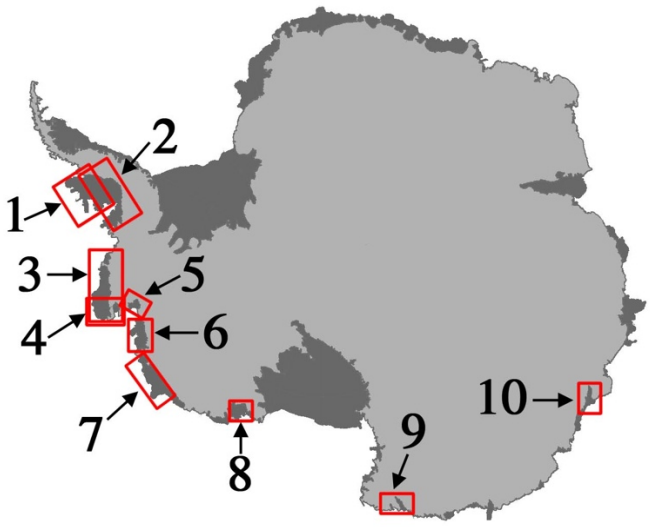

Figure A.3.12 | Appendix figure: Years in which polynyas are present.
Symbol meanings are shown below. Colors correspond to label colors in figures B S1-B S10.

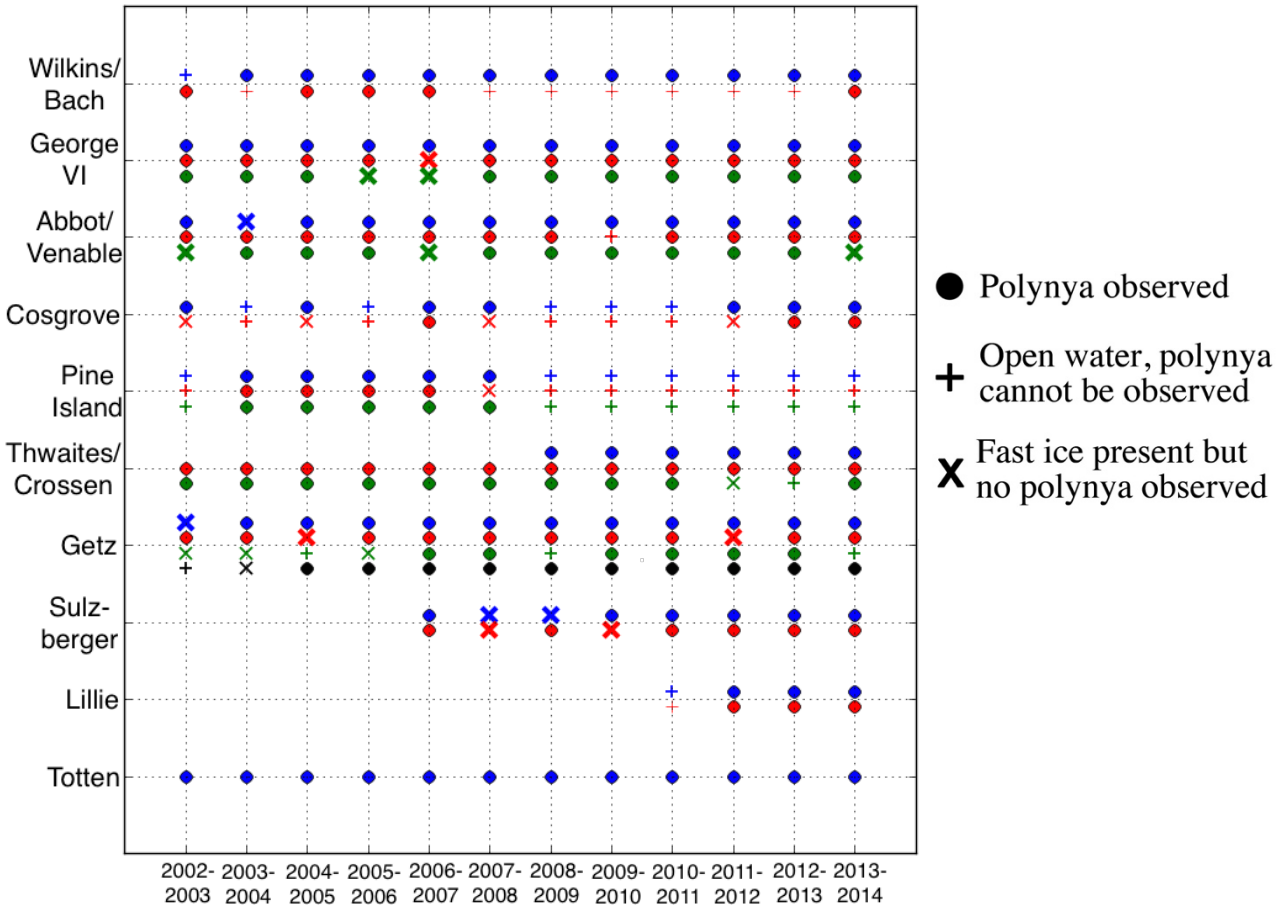

Appendix to Chapter 4

Appendix 4A: Numerical stake-tracking code

```
%% Define input files and set user-defined parameters

% Read in velocity geotiffs
 [vx, vx_info] = geotiffread('lisavx_pig.tif'); % x-component of velocity
[vy, vy_info] = geotiffread('lisavy_pig.tif'); % y-component of velocity
tiffinfo=geotiffinfo('lisavx_pig.tif'); % info from either geotiff

 % Read in ice thickness geotiff, if using
 % If not using ice thickness, comment out next two lines
 [thick, thick_info] = geotiffread('bedmap_pig.tif');
 thickinfo=geotiffinfo('bedmap_pig.tif');

% Define values that represent no data; if there are no relevant values,
% leave default of NaN
vxNoData = 99;
vyNoData = 99;
thickNoData = thick(10,10);

% Set grid parameters
pixel_size = 750; % Pixel size in distance units
tol = 10^-4; % Tolerance for error in adaptive time-stepping scheme; value
% is the percent difference between the two stake position estimates
% divided by 100

ydir = 1; % Set to 1 if positive y-velocities go up; -1 if down
thick_grid = 0; % Set to 1 if using an ice thickness grid, 0 if not
thick_multiplier = 4; % If using an ice thickness grid, the length scale is
% defined as thick_multiplier*ice_thickness, rounded to the  nearest pixel
% size multiple (this is effectively a half-length scale)
length_scale = 3000; % If not using an ice thickness grid, define a single
% length scale to be used throughout
maxR = 4; % Set a maximum value for r
% If using a single length scale, set it as length_scale/pixel size;
% If using a thickness grid, choose a reasonable estimate. Smaller maximum
% values speed up the script but cut off the length scale in areas with
% very thick ice. A maximum value is necessary for determining where the
% for-loop should start in the grid
```

```
time_max = 0.1*maxR*pixel_size/0.01;

%% Define output filenames
elonOut = 'meas_elon_align.tif';
eshearOut = 'meas_eshear_align.tif';
etransOut = 'meas_etrans_align.tif';
eEffOut = 'meas_eEff_align.tif';
ezOut = 'meas_ez_align.tif';

%% Finish setting parameters

r = round(length_scale/pixel_size); % Finds the nearest number of pixels to the given length
scale;
if r == 0 % If the length scale rounds to 0, set it to 1
   r = 1;
end
r = cast(r,'double');

% The actual length scale used will be r*pixel_size

% Remove erroneous thickness values
 thick(thick<0)=0;

 % Set no data values to NaN
 vx(vx==vxNoData)=NaN;
vy(vy==vyNoData)=NaN;
thick(thick==thickNoData)=NaN;

% Local square dimensions
locMult = 2;
% This sets the dimensions of the local square extracted at each time step;
% the default dimensions are 2*locMult*length_scale

%% Initialize calculations

% Create arrays that the calculated values will be written into
centerAlphas = zeros(size(vx));
curXVels = zeros(1,5);
curYVels = zeros(1,5);
checkXVels = zeros(1,5);
checkYVels = zeros(1,5);
checkRowCoords = zeros(1,5);
checkColCoords = zeros(1,5);
errorCriteriaX = zeros(1,5);
```

```
errorCriteriaY = zeros(1,5);
newRowCoords = zeros(1,5);
newColCoords = zeros(1,5);
exGrid = zeros(size(vx)) + NaN;
exyGrid = zeros(size(vx)) + NaN;
eyGrid = zeros(size(vx)) + NaN;
rGrid = zeros(size(vx)) + NaN;

dHdx = zeros(size(vx)) + NaN;
dHdy = zeros(size(vx)) + NaN;

[rows,cols] = size(vx);

% Define the lengths of the segments at the beginning of each calculation
l0a1 = r;
l0a2 = r;
l0b1 = r*sqrt(2);
l0b2 = r*sqrt(2);
l0c1 = r;
l0c2 = r;
l0d1 = r*sqrt(2);
l0d2 = r*sqrt(2);

% Local square dimensions
locDim = (2*locMult*r)+1;
locCent = ceil(locDim/2);

% Assign local coordinates to the stakes around each strain square
rowCoords = [locCent,locCent-r,locCent,locCent+r,locCent];
colCoords = [locCent,locCent,locCent+r,locCent,locCent-r];
% (In order, these are the center point, the top point, the right-hand
% point, the bottom point, and the left-hand point. In other words, it
% starts from the center and then moves clockwise from the top point.)

%% Loop through the velocity grids
for i=locMult*maxR+1:rows-locMult*maxR
   for j=locMult*maxR+1:cols-locMult*maxR
   %% Assign a local length scale if using an ice thickness grid
   if thick_grid==1
      h = thick(i,j);
      length_scale = thick_multiplier*h;
      r = round(length_scale/pixel_size); % Finds nearest number of pixels to given length scale;
      if isnan(h)==1
         continue
```

```
    end
    if r == 0 % If the length scale rounds to 0, set it to 1
        r = 1;
    elseif r > maxR
        r = maxR;
    end
    r = cast(r,'double');
    rGrid(i,j) = r;

    % Define the lengths of the segments at the beginning of each calculation
    l0a1 = r;
    l0a2 = r;
    l0b1 = r*sqrt(2);
    l0b2 = r*sqrt(2);
    l0c1 = r;
    l0c2 = r;
    l0d1 = r*sqrt(2);
    l0d2 = r*sqrt(2);

    % Local square dimensions
    locDim = (2*locMult*r)+1;
    locCent = ceil(locDim/2);

    % Assign local coordinates to the stakes around each strain square
    rowCoords = [locCent,locCent-r,locCent,locCent+r,locCent];
    colCoords = [locCent,locCent,locCent+r,locCent,locCent-r];
end

%% Initialize calculations for each center pixel
    % Set the initial strain experienced by each strain segment to zero
    stota1 = 0;
    stota2 = 0;
    stotb1 = 0;
    stotb2 = 0;
    stotc1 = 0;
    stotc2 = 0;
    stotd1 = 0;
    stotd2 = 0;

    % Set the current length of each strain segment to the original
    % lengths comprising the strain square
    lLasta1 = l0a1;
    lLasta2 = l0a2;
    lLastb1 = l0b1;
```

```
lLastb2 = l0b2;
lLastc1 = l0c1;
lLastc2 = l0c2;
lLastd1 = l0d1;
lLastd2 = l0d2;

% Set the current rows and columns to the coordinates of the strain
% square
curRows = rowCoords;
curCols = colCoords;

% Extract an array around the center point (i,j) that represents
% twice the dimensions of the strain square in order to make later
% calculations. This is the "local grid"
sqVx = vx((i-(locMult*r)):(i+(locMult*r)),(j-(locMult*r)):(j+(locMult*r)));
sqVy = vy((i-(locMult*r)):(i+(locMult*r)),(j-(locMult*r)):(j+(locMult*r)));
sqThick = thick((i-(locMult*r)):(i+(locMult*r)),(j-(locMult*r)):(j+(locMult*r)));

% Extract an array around the center point (i,j) that represents
% just the strain square in order to calculate the average velocity
% at the center point and determine a reasonable time interval
sqVxmean = vx((i-r):(i+r),(j-r):(j+r));
sqVymean = vy((i-r):(i+r),(j-r):(j+r));
[sqRows,sqCols] = size(sqVx);
% Calculate mean velocity
meanX = nanmean(nanmean(sqVxmean));
meanY = nanmean(nanmean(sqVymean));
meanVel = sqrt(meanX^2+meanY^2);

% Let the stakes move by approximately one tenth of the length scale
time = 0.1*r*pixel_size/meanVel;
time = min(time, time_max);

dtOrig = pixel_size/meanVel*.05; % Initialize time step as the time it takes to move
% a twentieth of the pixel length, according to the average velocity
dt = dtOrig;
t = 0; % Initialize time tracker

% Extract the x- and y-velocities at the original stake positions
for k = 1:5
   curXVels(k) = sqVx(rowCoords(k),colCoords(k));
   curYVels(k) = sqVy(rowCoords(k),colCoords(k));
end
if any(isnan([curXVels,curYVels]))==1
```

```
    continue
    % Go to the next pixel in the for-loop if any of the current
    % velocities are NaNs
end

%% Let the stakes move and measure strain rates
    while t<time
        % Move the stakes according to the x- and y-velocities and the
        % time step. Calculate the new column and row positions.
        % Also calculate the column and row positions according to
        % the improved Euler method to check for accuracy.
        t = t+dt;
        for k = 1:5
            newRowCoords(k) = curRows(k) - ydir*curYVels(k)*dt/pixel_size;
            newColCoords(k) = curCols(k) + curXVels(k)*dt/pixel_size;
            [checkXVels(k),checkYVels(k)] = locInterp2(curRows(k),curCols(k),sqVx,sqVy);
            checkRowCoords(k) = curRows(k) –
                ydir*0.5*(curYVels(k)+checkYVels(k))*dt/pixel_size;
            checkColCoords(k) = curCols(k) + 0.5*(curXVels(k)+checkXVels(k))*dt/pixel_size;
            errorCriteriaY(k) = abs((checkRowCoords(k)-
                newRowCoords(k))/checkRowCoords(k));
            errorCriteriaX(k) = abs((checkColCoords(k)-newColCoords(k))/checkColCoords(k));
        end
        if any(isnan([checkXVels,checkYVels]))==1
            break
        end
        %% Adaptive time stepping
        if any([errorCriteriaY,errorCriteriaX] >= tol)==1
            t = t-dt; % Reverse the time to what it was before
            dt = dt/2; % Make a smaller time step
            % We leave the current rows, columns, and velocities the
            % same
        else
        %% Make final calculations
        % Check to be sure that the stakes haven't moved outside of the
        % local grid
            if max(newRowCoords) <= sqRows && max(newColCoords) <= sqCols &&
                min(newRowCoords)>=1 && min(newColCoords)>=1
                % Calculate the current length
                lfa1 = sqrt((newRowCoords(1) - newRowCoords(2))^2+(newColCoords(1)-
                    newColCoords(2))^2);
                lfa2 = sqrt((newRowCoords(1) - newRowCoords(4))^2+(newColCoords(1)-
                    newColCoords(4))^2);
                lfb1 = sqrt((newRowCoords(2) - newRowCoords(5))^2+(newColCoords(2)-
```

```
  newColCoords(5))^2);
lfb2 = sqrt((newRowCoords(3) - newRowCoords(4))^2+(newColCoords(3)-
  newColCoords(4))^2);
lfc1 = sqrt((newRowCoords(1) - newRowCoords(5))^2+(newColCoords(1)-
  newColCoords(5))^2);
lfc2 = sqrt((newRowCoords(1) - newRowCoords(3))^2+(newColCoords(1)-
  newColCoords(3))^2);
lfd1 = sqrt((newRowCoords(2) - newRowCoords(3))^2+(newColCoords(2)-
  newColCoords(3))^2);
lfd2 = sqrt((newRowCoords(4) - newRowCoords(5))^2+(newColCoords(4)-
  newColCoords(5))^2);

% Calculate the current strains and strain rates
stra1 = log(lfa1/lLasta1);
stra2 = log(lfa2/lLasta2);
strb1 = log(lfb1/lLastb1);
strb2 = log(lfb2/lLastb2);
strc1 = log(lfc1/lLastc1);
strc2 = log(lfc2/lLastc2);
strd1 = log(lfd1/lLastd1);
strd2 = log(lfd2/lLastd2);

ea1 = stra1/dt;
ea2 = stra2/dt;
eb1 = strb1/dt;
eb2 = strb2/dt;
ec1 = strc1/dt;
ec2 = strc2/dt;
ed1 = strd1/dt;
ed2 = strd2/dt;

% Update the new rows and columns as current
curRows = newRowCoords;
curCols = newColCoords;

% Update the current lengths as the previous
% lengths
lLasta1 = lfa1;
lLasta2 = lfa2;
lLastb1 = lfb1;
lLastb2 = lfb2;
lLastc1 = lfc1;
lLastc2 = lfc2;
lLastd1 = lfd1;
```

```
            lLastd2 = lfd2;

            % Update the running total of strain for each
            % segment
            stota1 = stota1 + stra1;
            stota2 = stota2 + stra2;
            stotb1 = stotb1 + strb1;
            stotb2 = stotb2 + strb2;
            stotc1 = stotc1 + strc1;
            stotc2 = stotc2 + strc2;
            stotd1 = stotd1 + strd1;
            stotd2 = stotd2 + strd2;

            % Calculate final strain rate components
            ea1f = stota1/t;
            ea2f = stota2/t;
            eb1f = stotb1/t;
            eb2f = stotb2/t;
            ec1f = stotc1/t;
            ec2f = stotc2/t;
            ed1f = stotd1/t;
            ed2f = stotd2/t;

            % Reset the time step
            dt = dtOrig;

            % Set the current velocities to those calculated at
            % the end of the time step
            curXVels = checkXVels;
            curYVels = checkYVels;

        else
            break
        end
        % If a stake has moved outside the strain square, leave the
        % current rows and columns and current velocities the same
        % as the previous time step, and simply move on to
        % calculating the strain rate components. This will be the
        % final value for this strain square. Change the time to
        % kick it out of the while loop
    end
end
if t<.5*time % Don't calculate values if the stakes have been
    % allowed to move for less than half of the designated time
```

```
    % increment
    exGrid(i,j) = nan;
    eyGrid(i,j) = nan;
    exyGrid(i,j) = nan;
    centerAlphas(i,j) = nan;
else
%% Create strain rate grids

% Average the strain rate components
ea = (ea1f + ea2f)/2;
eb = (eb1f + eb2f)/2;
ec = (ec1f + ec2f)/2;
ed = (ed1f + ed2f)/2;

% Calculate coordinate-oriented strain values
exGrid(i,j) = .25*(eb + ed - ea) + .75*ec;
exyGrid(i,j) = .5*eb - .5*ed;
eyGrid(i,j) = .75*ea + .25*(eb + ed - ec);


%% Calculate flow orientation
% Calculate a grid of flow directions so that the grid-oriented
% strain rates can be rotated outside of the for-loop to align with
% local flow directions
centerVelX = vx(i,j);
centerVelY = vy(i,j);
if centerVelX>0 && centerVelY>0
    centerAlphas(i,j) = atand(centerVelY/centerVelX);
elseif centerVelX<0 && centerVelY>0
    centerAlphas(i,j) = atand(centerVelY/centerVelX)+180;
elseif centerVelX<0 && centerVelY<0
    centerAlphas(i,j) = atand(centerVelY/centerVelX)+180;
elseif centerVelX>0 && centerVelY<0
    centerAlphas(i,j) = atand(centerVelY/centerVelX)+360;
elseif centerVelX>0 && centerVelY==0
    centerAlphas(i,j) = 0;
elseif centerVelX==0 && centerVelY>0
    centerAlphas(i,j) = 90;
elseif centerVelX<0 && centerVelY==0
    centerAlphas(i,j) = 180;
elseif centerVelX==0 && centerVelY<0
    centerAlphas(i,j) = 270;
end
end
```

```
    end

end

%% Rotate strains and finalize grids
elon = exGrid.*cosd(centerAlphas).^2 + 2*exyGrid.*sind(centerAlphas).*cosd(centerAlphas) +
        eyGrid.*sind(centerAlphas).^2;
etrans = exGrid.*sind(centerAlphas).^2 –
        2*exyGrid.*sind(centerAlphas).*cosd(centerAlphas)+eyGrid.*cosd(centerAlphas).^2;
eshear = (eyGrid-exGrid).*sind(centerAlphas).*cosd(centerAlphas) +
        exyGrid.*(cosd(centerAlphas).^2-sind(centerAlphas).^2);

eEff = sqrt(abs(exGrid.*eyGrid-exyGrid.^2));
ez = -elon-etrans;

geotiffwrite(elonOut, elon, vx_info,
        'GeoKeyDirectoryTag',tiffinfo.GeoTIFFTags.GeoKeyDirectoryTag);
geotiffwrite(eshearOut, eshear, vx_info,
        'GeoKeyDirectoryTag',tiffinfo.GeoTIFFTags.GeoKeyDirectoryTag);
geotiffwrite(etransOut, etrans, vx_info,
        'GeoKeyDirectoryTag',tiffinfo.GeoTIFFTags.GeoKeyDirectoryTag);
geotiffwrite(eEffOut, eEff, vx_info,
        'GeoKeyDirectoryTag',tiffinfo.GeoTIFFTags.GeoKeyDirectoryTag);
```

Appendix 4B: Local 2d interpolation function

```
function [intXVel,intYVel] = locInterp2(rowCoord,colCoord,sqVx,sqVy)
% This function carries out a bilinear interpolation at the points
% (rowCoord, colCoord) within a local square. In this case, it is written
% to give back the interpolated values withing a local square of
% x-direction and y-direction velocity values.

ULxVel = sqVx(floor(rowCoord),floor(colCoord));
URxVel = sqVx(floor(rowCoord),ceil(colCoord));
LLxVel = sqVx(ceil(rowCoord),floor(colCoord));
LRxVel = sqVx(ceil(rowCoord),ceil(colCoord));

ULyVel = sqVy(floor(rowCoord),floor(colCoord));
URyVel = sqVy(floor(rowCoord),ceil(colCoord));
LLyVel = sqVy(ceil(rowCoord),floor(colCoord));
LRyVel = sqVy(ceil(rowCoord),ceil(colCoord));
```

```
topInterp = colCoord - floor(colCoord);
sideInterp = rowCoord - floor(rowCoord);

topxVel = ULxVel + (URxVel-ULxVel)*topInterp;
botxVel = LLxVel + (LRxVel-LLxVel)*topInterp;

topyVel = ULyVel + (URyVel-ULyVel)*topInterp;
botyVel = LLyVel + (LRyVel-LLyVel)*topInterp;

intXVel = topxVel + (botxVel-topxVel)*sideInterp;
intYVel = topyVel + (botyVel-topyVel)*sideInterp;
```

Appendix 4C: Differencing code

```
% Define parameters
pixel_size = 750; % Pixel size in distance units
length_scale = 4500;     % Using the same units as pixel size. Note that this is
% really a half-length scale - pixels are selected one length scale away on
% all sides of a central pixel, and the calculated strain rate is applied
% to the central pixel
ydir = 1; % Set to -1 if the positive y-direction is down, +1 if up
r = round(length_scale/pixel_size); % Finds the nearest number of pixels to the given length
scale;
if r == 0 % If the length scale rounds to 0, set it to 1
   r = 1;
end
lenSc = r*pixel_size; % The actual length scale used will be r*pixel_size

% Read in geotiffs
 [vx, vx_info] = geotiffread('lisa750_vx_v16_v02_2013182_2016182.tif');
 [vy, vy_info] = geotiffread('lisa750_vy_v16_v02_2013182_2016182.tif');
 tiffinfo=geotiffinfo('lisa750_vx_v16_v02_2013182_2016182.tif');

% Specify if there is a no data value in the Geotiffs, and set any instance
% of that value to NaN
 nodata = 99;
 vx(vx==nodata)=NaN;
 vy(vy==nodata)=NaN;
```

```
[rows,cols] = size(vx);

% Create arrays that the calculated strain rates will be written into
centerAlphas = zeros(size(vx))+NaN;
exGrid = zeros(size(vx))+NaN;
eyGrid = zeros(size(vx))+NaN;
exyGrid = zeros(size(vx))+NaN;
eshearGrid = zeros(size(vx))+NaN;
elonGrid = zeros(size(vx))+NaN;
etransGrid = zeros(size(vx))+NaN;
exGridMatch = zeros(size(vx))+NaN;
exyGridMatch = zeros(size(vx))+NaN;
eyGridMatch = zeros(size(vx))+NaN;


% Calculate strain rates relative to the grid, using a differenced version
% of ex = du/dx, dy = dv/dy, and exy = 1/2(du/dx+dv/dy)
vxup = vx(r+1:end-r,r*2+1:end);
vxdown = vx(r+1:end-r,1:end-r*2);
vxdiff = vxup - vxdown;
exGridMid = vxdiff/(2*r*pixel_size);
exGrid(r+1:end-r, r+1:end-r) = exGridMid;

vyup = vy(1:end-2*r,r+1:end-r);
vydown = vy(2*r+1:end,r+1:end-r);
vydiff = ydir*(vyup - vydown);
eyGridMid = vydiff/(2*r*pixel_size);
eyGrid(r+1:end-r, r+1:end-r) = eyGridMid;

vxyup = vx(1:end-2*r,r+1:end-r);
vxydown = vx(2*r+1:end,r+1:end-r);
vxydiff = ydir*(vxyup - vxydown);
exinyGrid = vxydiff/(2*r*pixel_size);

vyxup = vy(r+1:end-r,r*2+1:end);
vyxdown = vy(r+1:end-r,1:end-r*2);
vyxdiff = ydir*(vyxup - vyxdown);
eyinxGrid = vyxdiff/(2*r*pixel_size);

exyGridMid = .5*(exinyGrid+eyinxGrid);
exyGrid(r+1:end-r, r+1:end-r) = exyGridMid;

[gridRows,gridCols] = size(exGrid);
```

```
for i = 2*r+1:gridRows-2*r
   for j = 2*r+1:gridCols-2*r
      % Calculate a grid of flow directions so that the grid-oriented
      % strain rates can be rotated outside of the for-loop to align with
      % local flow directions
      centerVelX = vx(i,j);
      centerVelY = vy(i,j);
         if centerVelX>0 && centerVelY>0
            centerAlphas(i,j) = atand(centerVelY/centerVelX);
         elseif centerVelX<0 && centerVelY>0
            centerAlphas(i,j) = atand(centerVelY/centerVelX)+180;
         elseif centerVelX<0 && centerVelY<0
            centerAlphas(i,j) = atand(centerVelY/centerVelX)+180;
         elseif centerVelX>0 && centerVelY<0
            centerAlphas(i,j) = atand(centerVelY/centerVelX)+360;
         elseif centerVelX>0 && centerVelY==0
            centerAlphas(i,j) = 0;
         elseif centerVelX==0 && centerVelY>0
            centerAlphas(i,j) = 90;
         elseif centerVelX<0 && centerVelY==0
            centerAlphas(i,j) = 180;
         elseif centerVelX==0 && centerVelY<0
            centerAlphas(i,j) = 270;
         end
    end
end

% Transform the strain rate calculations according to the local flow
% direction
elon = exGrid.*cosd(centerAlphas).^2 + 2*exyGrid.*sind(centerAlphas).*cosd(centerAlphas) +
          eyGrid.*sind(centerAlphas).^2;
etrans = exGrid.*sind(centerAlphas).^2 –
          2*exyGrid.*sind(centerAlphas).*cosd(centerAlphas)+eyGrid.*cosd(centerAlphas).^2;
eshear = (eyGrid-exGrid).*sind(centerAlphas).*cosd(centerAlphas) +
          exyGrid.*(cosd(centerAlphas).^2-sind(centerAlphas).^2);

eEff = sqrt(abs(exGrid.*eyGrid-exyGrid.^2));
 ez = -elon-etrans;

geotiffwrite(elonOut, elon, vx_info,
          'GeoKeyDirectoryTag',tiffinfo.GeoTIFFTags.GeoKeyDirectoryTag);
geotiffwrite(eshearOut, eshear, vx_info,
          'GeoKeyDirectoryTag',tiffinfo.GeoTIFFTags.GeoKeyDirectoryTag);
geotiffwrite(etransOut, etrans, vx_info,
```

```
        'GeoKeyDirectoryTag',tiffinfo.GeoTIFFTags.GeoKeyDirectoryTag);
geotiffwrite(eEffOut, eEff, vx_info,
        'GeoKeyDirectoryTag',tiffinfo.GeoTIFFTags.GeoKeyDirectoryTag);
```

Appendix 4D: Function to create a constant strain field

```
function [vx, vy, X, Y, exTheor, eyTheor, exyTheor] = constant_strain(pixel_size, xmin, xmax,
ymin, ymax, alpha, theta, beta, phi)
% This function creates a flow field with constant strain

% Inputs:
% pixel_size: The pixel size of the grid, in grid units
% xmin, xmax, ymin, ymax: The dimensions of the domain, in grid units
% alpha: The gradient in velocity, which will be multiplied by the x- and
% y-coordinates to calculate a velocity grid
% theta: The angle of the velocities, in degrees
% beta: A uniform constant velocity added to the velocity grid
% phi: The angle of the uniform constant velocity, in degrees


xs = xmin:pixel_size:xmax; ys = ymin:pixel_size:ymax;
[X,Y] = meshgrid(xs, ys);
Y = -Y; % This velocity field depends on the defined X- and Y-values (a
% real velocity field does not). Since the Y-values are automatically
% created with the positive direction going down, the y-velocities will end
% up going in the negative y-direction unless Y is flipped.
vx = alpha*(X.*cosd(2*theta)+Y.*sind(2*theta)) + beta*cosd(phi);
vy = -alpha*(Y.*cosd(2*theta)-X.*sind(2*theta)) + beta*sind(phi);

exTheor = alpha*cosd(2*theta);
eyTheor = -alpha*cosd(2*theta);
exyTheor = alpha*sind(2*theta);
```

Appendix 4E: Function to create flow around a Rankine half-body

```
function [vx,vy,X,Y,m] = uniform_source(pixel_size, U, radius, xmin, xmax, ymin, ymax)
%% Flow around a Rankine half-body
% Also known as uniform flow with a fluid source; the region within the
% "surface streamline," which passes through the stagnation point, has
% values converted to NaN's to represent an island with no through-flow.
```

```
% The surface streamline is also known as the streamline outlining the
% Rankine half-body.

% Inputs:
% pixel_size: The pixel size of the velocity grid
% U: Uniform far-field velocity
% radius: The distance from the source point to the stagnation point, which
% is roughly the radius of the curved front of the island. It's also very
% similar to the half-width of the island
% xmin, xmax, ymin, ymax: Dimensions of the domain

% Outputs:
% vx and vy: x- and y-components of the produced velocity field
% X and Y: Coordinates of the grid points
% m: Parameter

x=xmin:pixel_size:xmax; y=ymin:pixel_size:ymax;
[X,Y]=meshgrid(x,y);
Y = -Y; % This velocity field depends on the defined X- and Y-values (a
% real velocity field does not). Since the Y-values are automatically
% created with the positive direction going down, the y-velocities will end
% up going in the negative y-direction unless Y is flipped.

xs = -radius; % x-coordinate of the stagnation point, defined based on how
% big we want our "island" to be. In this case, it's the approximate half-
% width of Roosevelt Island on the

Q = -2*pi*xs; % Define Q based on how big we want our "island" to be
%Q = 10;
m = Q/(2*pi);

vx= U + m*X./(X.^2+Y.^2);
vy=m*Y./(X.^2+Y.^2);

for i = 1:length(y)
   for j = 1:length(x)
   if X(i,j)>(Y(i,j)/(tan(pi-(2*pi*U.*Y(i,j)/Q)))) & Y(i,j)>(-Q/(2*U)) & Y(i,j)<(Q/(2*U))
      vx(i,j) = NaN;
      vy(i,j) = NaN;
      X(i,j) = NaN;
      Y(i,j) = NaN;
   end
   if Y(i,j) == 0 & X(i,j)>(-Q/(2*pi*U))
      vx(i,j) = NaN;
```

```
        vy(i,j) = NaN;
        X(i,j) = NaN;
        Y(i,j) = NaN;
    end
    end
end
```